Exploring Emergence in Interconnected Ferromagnetic Nanoring Arrays

Richard William Staveley Dawidek

A thesis submitted in partial fulfilments of the requirements for the Degree of Doctor of Philosophy

Department of Materials Science and Engineering

The University of Sheffield

April 2020

Abstract

Emergent interactions in periodic, artificial ferromagnetic nanostructures is well explored for magnetic systems such as artificial spin ices (ASI). This work presents a novel approach of an interconnected array of ferromagnetic nanorings to harness emergence in a dynamic system for functionality.

Magnetic nanorings have two preferred configurations of magnetisation – 'vortex' that contains no domain walls (DWs) and 'onion' state with two DWs. In-plane applied rotating fields move DWs around a ring. The junction between interconnected rings presents a pinning potential that must be overcome to continue DW motion. In an ensemble, such as an array of interconnected rings, a sufficiently high field gives unimpeded DW motion. Under a sufficiently low field, no DWs de-pin. Both conserve DW population. Between these limits, de-pinning is probabilistic and field dependent. When one DW in an 'onion' state is pinned and the other de-pins, annihilation of DWs will occur and rings convert from 'onion' to 'vortex'. Micromagnetic modelling also shows a DW de-pinning from a junction adjacent to a 'vortex' ring repopulates it with DWs.

Analytical modelling of DW population revealed an equilibrium that varies non-monotonically with de-pinning probability and varies with array size and geometry. Polarised neutron reflectometry (PNR) and MOKE magnetometry measured arrays of permalloy nanorings. Magnetisation as a function of applied rotating field strength confirmed a non-monotonic response.

Magnetic force microscopy (MFM) and photoemission electron microscopy (PEEM) allowed direct observation of DW configurations, revealing: highly ordered arrangements of 'onion' states at saturation; minor changes in DW population with low and high strength rotating fields; DW loss and breakdown in long-range order with intermediate fields. Imaging showed junctions produce behaviour analogous to emergent vertex configurations in ASIs.

Interconnected nanoring arrays show good candidacy for novel computing architectures, such as reservoir computing, given their dynamic tuneability, non-linear response to an external stimulus, scalability, fading memory and repeatability.

Publications and Presentations

"Emergent Behaviour in Interconnected Nanoring Arrays" – MMM2017 (Oral Presentation, Pittsburgh, USA)

"Emergent Behaviour in Interconnected Nanoring Arrays" – Magnetism 2018 (Poster Presentation, Manchester, UK)

"Emergent Properties of a Dynamically Driven Nanomagnetic System" – R.W.S. Dawidek, et al. (2020)

List of Common Abbreviations

ASI – Artificial spin ice

DW – Domain wall

PNR – Polarised neutron reflectometry

MOKE – Magneto-optic Kerr effect

MFM – Magnetic force microscopy

PEEM – Photoelectron emission microscopy

MRAM – Magnetic random access memory

Py – Permalloy

EM – Electromagnetic

H2H – Head-to-head

T2T – Tail-to-tail

TDW – Transverse domain wall (uTDW – up TDW, dTDW – down TDW)

VDW – Vortex domain wall

MTXM – Magnetic transmission x-ray microscopy

LLG – Landau-Lifshitz-Gilbert

(X)MCD – (X-ray) magnetic circular dichroism

EBL – Electron beam lithography

PMMA – Polymethylmethacrylate

AFM – Atomic force microscopy

SEM – Scanning electron microscopy

List of Symbols

In order of appearance

τ – Torque (experienced by a magnetic dipole moment)

$\boldsymbol{m}$ – Atomic magnetic dipole moment

$\boldsymbol{B}$ – Magnetic flux density

$\boldsymbol{M}$ – Magnetisation

V – Volume

χ – Magnetic susceptibility

H – Applied magnetic field

H_d – Demagnetising field

N_d – Shape factor

$E_{magnetostatic}$ – Magnetostatic energy

E_k – Magnetocrystalline anisotropy energy

K_n – Material specific anisotropy constant

μ_0 – permeability of free space

E_{ex} – Exchange energy

J_{ex} – Exchange integral

S_i, j – Spin vectors

M_S – Saturation magnetisation

l_{ex} – Exchange length

K_u – Uniaxial anisotropy constant

a – Lattice constant

γ – Electron gyromagnetic ratio

q_z - Neutron scattering vector

W_{eq} – Equilibrium domain wall population

P_{de-pin} – Probability of a domain wall de-pinning from a junction to continue motion

C_{end} – Proportion of 'end' rings (such as the end of a linear chain)

C_{centre} – Proportion of 'centre' rings in a linear chain

P_n – Proportion of a rings of a given type that have n junctions to de-pin from to annihilate

$C_{fixed\ corner}$ – Proportion of 'fixed corner' rings in a square array

$C_{annihilating\ corner}$ – Proportion of 'annihilating corner' rings in a square array

C_{bulk} – Proportion of rings in the bulk of a square array

C_{edge} – Proportion of rings on the edges of a square array

$C_{trigonal\ bulk}$ – Proportion of rings in the bulk of a trigonal array

$C_{trigonal\ edge}$ – Proportion of rings on the edges of a trigonal array

C_{rest} – Proportion of rings that are not an annihilating corner in a defect array

P_{vortex} = Proportion of rings that are in vortex state

P_{mobile} = Proportion of rings that have mobile DWs in an applied rotating field

P_{pinned} = Proportion of rings that have DWs pinned at junctions in an applied rotating field.

S_{p-p} – Peak to peak amplitude of a measured Kerr signal

$S_{average}$ – Average measured Kerr signal

k_B – Boltzmann constant

f_0 – Attempt frequency

$E(B)$ - Energy barrier height

T – Temperature

$M_{normalised}$ – Calculated normalised magnetisation

$N_{red\ pixels}$ – Measured number of red pixels from a X-PEEM colour contrast image

$N_{total\ pixels}$ – Total measured number of pixels from a X-PEEM image

$N_{blue\ pixels}$ – Measured number of blue pixels from a X-PEEM colour contrast image

Acknowledgements

My first and biggest thanks must go to my supervisor, Professor Dan Allwood. There may not in this final work be much that followed on from my undergraduate project but instead we have explored a new area and devised an approach that may one day lead to some extraordinary science in neuromorphic computing. Thank you for the opportunity, the support and the many hours you have put in to help.

I must also profusely thank my second supervisor, Dr Tom Hayward, for the sterling effort put in to provide assistance during the programme – especially with the simulation side of this research.

I particularly pay tribute to Dr TJ Broomhall and Dr Rene Dost for the huge help they have been academically in moving various experiments along. Aidan Mullen and Stefan Kyle are also deserving of thanks for taking part in the October 2018 visit to Diamond to ensure 24-hour data collection was possible.

From J11, special mention must go to: Dr Jonathan Wood for the 3 B's (beers, brews, bogus transportation); Dr Qayes Al-Dulaim for teaching me 'interesting' Arabic phrases and gestures and for being very, very entertaining when times were difficult; Dr Adam Baggott for the reminders that there's probably plenty of time. Mackie, Wynny, Ghaiath, Matt W, Robin, Saturi, Alaa, Zhao, Aris, Weigang, Ruth, the girl who spent 2 weeks in J11 and never spoke to anyone – you've all played your part in my life the past four years and I wish everyone all the best.

I'd like to shout out to my good friends who have helped support me along the way. Particularly Matt Richardson, Sam Armistead, Alex Harvey and Tom Gout. Whether it was as my housemate, touring the curry circuit of Sheffield or via Messenger, you four have kept me sane and thoroughly entertained through difficult spells.

But also, to my pals Hugo Lynch, Kai Wolff, Ella Sexton, Shaun Colley, Robbie Schofield, Yash Patel, Luke Brennan-Scott, Ben Howell– thank you for the good times we've shared over the course of this work. There are others I've doubtless forgotten to mention – I'm so sorry!

Sheffield University Rowing Club will always have a special place in my heart. It is responsible for me getting to the end as well as keeping me from being at the end. Thank you to all of those involved with the club for giving me some of the greatest moments in my life.

To my extended family, thank you for believing in me. The Sweetnams, my Auntie Helen and Uncle Peter, the Lallys and Caves, the Davis' and Bartletts; if this page is the only one you humoured me by reading then the gist is it's all about tiny magnets.

To my close family, Mum, Dad, Charlotte – I can't thank you enough. You have been with me every step of the way and have supported me through everything. I love you and this work that I hope you will read, or at least attempt to, is only possible because of you.

To Holly, you have made everything worthwhile. The greatest result I have obtained in the last four years is meeting you.

"If you're going through hell, keep going" – Winston S. Churchill

Dedicated to my grandfather

Contents

Chapter 1- Introduction

"The beginning is the most important part of the work" – Plato

1.1 Research context

The advent of advanced lithographic techniques has allowed for the creation of electronic devices and structures that manipulate the non-trivial behaviour of magnetism at micro- and nanoscales. The use of magnetic materials for data storage is already prevalent and has been at the forefront of modern computing applications for decades with floppy disks, magnetic tape, and hard disk drives. Hard disk drives take advantage of giant magnetoresistive spin-based electronic (spintronic) effects in a sensor flying above the disk to read the magnetisation of nanoscale regions of the disk.

An exciting development in magnetic digital technology was the proposition of using "magnetic domain-wall racetrack memory" [1] , where columns of magnetic nanowires contained a 'train' of magnetic domain walls (DW) coded to a digital 1 or a 0. This train could be moved around the 'racetrack' of wires through externally applied inputs such as an applied magnetic field. Pinning sites that helped define this coding present an energy barrier that impedes motion of DWs [2], [3]. Overcoming the energy barrier with an applied field is known to be a probabilistic process following Arrhenius-Néel type behaviour [4].

The lack of reliability, or stochasticity, of this de-pinning has prevented the proliferation of disruptive magnetic racetrack type memory devices. Stochasticity of de-pinning is further enhanced by the dynamic considerations of DW motion in nanowires [5]–[8] especially with curved elements and fabrication roughness [9]–[11].

Whilst stochasticity continues to prevent advances in magnetic memory applications, there exists the possibility to harness the rich nature of the emergent stochasticity in magnetic nanodevices. This is a particularly prevalent feature of artificial spin ice [12]

systems wherein the stochastic interactions between constituent parts gives quantifiable global behaviour [13], [14].

This thesis explores how systems of interacting magnetic nanoelements with local stochastic behaviour can show emergent properties while being driven continuously.

Work before this research programme had studied lithographically patterned soft ferromagnetic nanorings [15], and especially DW behaviour within them [2], [16]–[20] or as a method of realising MRAM devices [21], [22]. The nanoring is particularly useful as it has two stable, low energy states of either two magnetic domains and two DWs (known as the 'onion' state) or a 'vortex' state of flux-closed, circumferentially-oriented magnetisation and no DWs (Fig. 1.1).
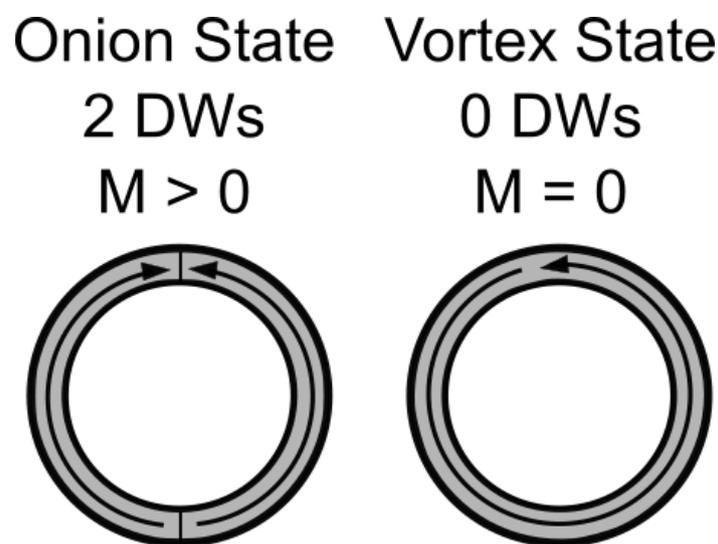
Figure 1.1. Representation of two stable states in ferromagnetic nanorings – the 'onion' and 'vortex' states. The onion state has two domains and thus two DWs, and has a non-zero net magnetisation, M. The vortex state is flux-closed with no DWs and zero net magnetisation. Arrows indicate the general orientation of magnetic dipole moments and DWs are shown in the 'onion' state by vertical lines at '12 o' clock' and '6 o'clock.'

DWs in nanorings have been studied dynamically under rotating applied fields [16], [17] and as stresses were applied to the pattern substrate [23]. Previous research overlapping nanorings considered the dipolar interactions of DWs in nanorings in close proximity [24], [25] and transport of DWs in 2D periodic square arrays of these connected nanorings [26].
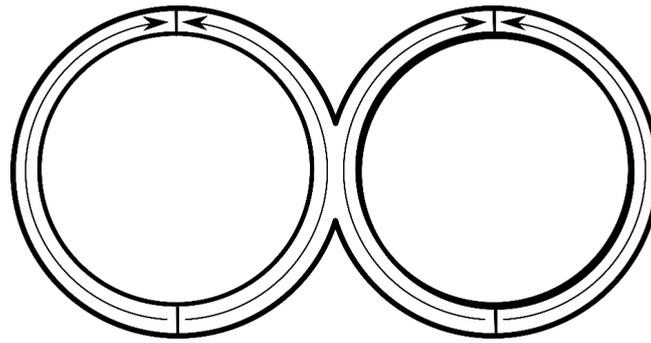
Figure 1.2. Schematic of two interconnected nanorings, both in the 'onion' state. Magnetic domains are denoted by curved lines with arrows (indicating magnetisation direction), and the four domain walls present shown by lines across the ring tracks.

Fig. 1.2 schematically shows two interconnected nanorings. Changes in local geometry in soft ferromagnetic nanowires are known to present a barrier for unimpeded DW motion [11], [27]–[31] and the same can be expected of the ring junction in Fig. 1.2. Overcoming this potential barrier will probably be stochastic and dependent on parameters such as applied magnetic field strength, temperature and wire geometry. A DW pinned by such a barrier would be annihilated by the arrival of a DW with opposing magnetic charge. This thesis considers how in a large array of interconnected nanorings, stochastic DW pinning and transport of DWs at wire junctions leads to equilibrium DW population in the array.

In this thesis these emergent interactions at junctions were probed through modelling and experimentally. Modelling used analytical approaches and micromagnetic simulations. Experimental magnetometry was conducted using polarised neutron reflectometry (PNR) and magneto-optic Kerr effect (MOKE) measurements. Complementing this was magnetic imaging using X-ray photoemission electron (X-PEEM) microscopy and magnetic force microscopy (MFM) to study the detailed magnetic configurations in wire rings.

The emergent behaviour seen here could support future applications in the field of non-linear computing. New paradigms such as reservoir computing [32]–[38] (a recurrent neural network based computing approach) can allow for more parallelism and networking of computation, inspired by the approach neural systems take to processing large amounts of data. This may be a way to realise low-power computing on complex, time-varying data, which is a particularly relevant application as demand for computational power grows exponentially greater. It the near future, as 5G data

transfer and 4K streaming becomes prevalent and mainstream, it is forecast that computational power will be responsible for nearly 20% of global power consumption [39]. Reducing the impact of this is vital for the sustainability of the internet-age economy as well as the planet.

1.2 Thesis Outline

The following seven chapters contained in this thesis are briefly as follows:
Chapter 2 starts with a description of the underlying scientific theory of magnetic behaviour at the nanoscale and various experimental techniques of relevance here.

Chapter 3 reviews previous research relevant to this thesis. DW motion in magnetic nanowires and ferromagnetic nanorings is discussed to create a foundation to this work. The nature and emergent properties of artificial spin ice systems are then described. Reservoir and bioinspired computing are also briefly explored to give a context to the motivations for this work.

Chapter 4 surveys the experimental techniques used. It starts with the fundamental principles of each technique and then presents the details of how technique was applied in the course of this work.

Chapter 5, 6 and 7 are the three research chapters. Whilst separated into distinct chapters, the sequence forms the story of hypothesising, demonstrating and then understanding the origin of emergent behaviour in interconnected nanoring arrays.

Chapter 5 presents modelling of magnetic nanoring array behaviour. Micromagnetic modelling demonstrates three basic behaviours of DW motion in two and then three connected rings. Various geometric dependencies on behaviours and DW motion are explored. Micromagnetic modelling of small arrays of connected rings is also presented. An analytical model to describe the equilibrium behaviour of ring arrays is then introduced and the non-linear, field-dependent predictions it makes of DW population are discussed.

Chapter 6 presents PNR and MOKE magnetometry experiments of the magnetic response of whole arrays. The observed field-dependent behaviour is compared with the model predictions from Chapter 5. Time-dependent MOKE measurements show an interesting 'fading memory' response that is important for the system's use in future reservoir computing applications.

Chapter 7 is dedicated to magnetic imaging techniques of interconnected nanoring arrays. MFM is presented to show the magnetic configuration of ring arrays in detail. Finally, PEEM is presented to show wider field-of-view images of larger arrays than seen with MFM and understand the nature of DW motion through the ring arrays generally.

Chapter 8 summarises this work and proposes the direction of future research that is opened by the results of this thesis.

1.3 References

[1]   S. S. P. Parkin, M. Hayashi, and L. Thomas, "Magnetic Racetrack Memory," *Science*, vol. 320, no. 5873, pp. 190–194, 2008.

[2]   M. Kläui *et al.*, "Domain Wall Pinning in Narrow Ferromagnetic Ring Structures Probed by Magnetoresistance Measurements," *Phys. Rev. Lett.*, vol. 90, no. 9, p. 4, 2003.

[3]   M. Hayashi, L. Thomas, C. Rettner, R. Moriya, X. Jiang, and S. S. P. Parkin, "Dependence of current and field driven depinning of domain walls on their structure and chirality in permalloy nanowires," *Phys. Rev. Lett.*, vol. 97, no. 20, 2006.

[4]   W. Wernsdorfer *et al.*, "Nucleation of magnetization reversal in individual nanosized nickel wires," *Phys. Rev. Lett.*, vol. 77, no. 9, pp. 1873–1876, 1996.

[5]   N. L. Schryer and L. R. Walker, "The motion of 180° domain walls in uniform dc magnetic fields," *J. Appl. Phys.*, vol. 45, no. 12, pp. 5406–5421, 1974.

[6]   S. K. Kim, J. Y. Lee, Y. S. Choi, K. Y. Guslienko, and K. S. Lee, "Underlying mechanism of domain-wall motions in soft magnetic thin-film nanostripes beyond the velocity-breakdown regime," *Appl. Phys. Lett.*, vol. 93, no. 5, pp. 91–94, 2008.

[7]   M. T. Bryan, T. Schrefl, D. Atkinson, and D. A. Allwood, "Magnetic domain wall propagation in nanowires under transverse magnetic fields," *J. Appl. Phys.*, vol. 103, no. 7, 2008.

[8]   A. Mougin, M. Cormier, J. P. Adam, P. J. Metaxas, and J. Ferré, "Domain wall mobility, stability and Walker breakdown in magnetic nanowires," *EPL*, vol. 78, no. 5, 2007.

[9]   X. Jiang *et al.*, "Enhanced stochasticity of domain wall motion in magnetic racetracks due to dynamic pinning," *Nat. Commun.*, vol. 1, no. 3, pp. 1–5, 2010.

[10]   D. A. Allwood, G. Xiong, C. C. Faulkner, D. Atkinson, D. Petit, and R. P. Cowburn, "Magnetic domain-wall logic," *Science.*, vol. 309, no. 5741, pp. 1688–1692, 2005.

[11]   E. R. Lewis *et al.*, "Magnetic domain wall pinning by a curved conduit," *Appl. Phys. Lett.*, vol. 95, no. 15, p. 152505, 2009.

[12]   R. F. Wang *et al.*, "Artificial 'spin ice' in a geometrically frustrated lattice of nanoscale ferromagnetic islands," *Nature*, vol. 439, no. 7074, pp. 303–306, 2006.

[13]   A. Farhan *et al.*, "Emergent magnetic monopole dynamics in macroscopically degenerate artificial spin ice," *Sci. Adv.*, vol. 5, no. 2, 2019.

[14]   W. R. Branford, S. Ladak, D. E. Read, K. Zeissler, and L. F. Cohen, "Emerging Chirality in Artificial Spin Ice," *Science.*, vol. 335, no. 6076, pp. 1597 LP – 1600, Mar. 2012.

[15]   C. A. F. Vaz *et al.*, "Ferromagnetic nanorings," *J. Phys. Condens. Matter*, vol. 19, no. 25, p. 255207, 2007.

[16]   M. Negoita, T. J. Hayward, and D. A. Allwood, "Controlling domain walls velocities in ferromagnetic ring-shaped nanowires," *Appl. Phys. Lett.*, vol. 100, no. 7, p. 072405, 2012.

[17]   M. Negoita, T. J. Hayward, J. A. Miller, and D. A. Allwood, "Domain walls in ring-shaped nanowires under rotating applied fields," *J. Appl. Phys.*, vol. 114, no. 1, p. 013904, 2013.

[18]   M. Negotia *et al.*, "Linear transport of domain walls confined to propagating 1-D potential wells," *J. Appl. Phys.*, vol. 114, 2013.

[19]   M. Kläui *et al.*, "Domain wall motion induced by spin polarized currents in ferromagnetic ring structures," *Appl. Phys. Lett.*, vol. 831, no. 10, 2003.

[20]   M. Kläui, C. A. F. Vaz, A. Lapicki, T. Suzuki, Z. Cui, and J. A. C. Bland, "Domain wall pinning in ferromagnetic structures fabricated by focused ion beam," in *Microelectronic Engineering*, 2004,

vol. 73–74, pp. 785–789.

[21] X. F. Han, Z. C. Wen, and H. X. Wei, "Nanoring magnetic tunnel junction and its application in magnetic random access memory demo devices with spin-polarized current switching (invited)," *J. Appl. Phys*, vol. 103, pp. 7–933, 2008.

[22] M. Kläui, C. A. F. Vaz, J. A. C. Bland, W. Wernsdorfer, G. Faini, and E. Cambril, "Controlled magnetic switching in single narrow rings probed by magnetoresistance measurements," *Appl. Phys. Lett.*, vol. 81, no. 1, pp. 108–110, 2002.

[23] J. D. Wheelwright, "Strain Based Control of Magnetic Domain Walls," University of Sheffield, 2016.

[24] Q. Ye, S. Chen, K. Zhong, and Z. Huang, "Magnetic properties for cobalt nanorings: Monte Carlo simulation," *Phys. B Condens. Matter*, vol. 407, no. 4, pp. 790–794, 2012.

[25] Y. Ren, S. Jain, A. O. Adeyeye, and C. A. Ross, "Magnetization states in coupled Ni80Fe20 bi-ring nanostructures," *New J. Phys.*, vol. 12, no. 11pp, p. 93003, 2010.

[26] G. Bordignon *et al.*, "Analysis of magnetoresistance in arrays of connected nano-rings," *IEEE Trans. Magn.*, vol. 43, no. 6, pp. 2881–2883, 2007.

[27] D. Petit, A. V. Jausovec, D. Read, and R. P. Cowburn, "Domain wall pinning and potential landscapes created by constrictions and protrusions in ferromagnetic nanowires," *J. Appl. Phys.*, vol. 103, no. 11, 2008.

[28] H. Y. Yuan and X. R. Wang, "Domain wall pinning in notched nanowires," *Phys. Rev. B*, vol. 89, p. 54423, 2014.

[29] M. Kläui, "Head-to-head domain walls in magnetic nanostructures," *J. Phys. Condens. Matter*, vol. 20, no. 31, p. 313001, 2008.

[30] M. Kläui *et al.*, "Domain wall behaviour at constrictions in ferromagnetic ring structures," in *Physica B: Condensed Matter*, 2004, vol. 343, no. 1–4, pp. 343–349.

[31] K. A. Omari and T. J. Hayward, "Chirality-based vortex domain-wall logic gates," *Phys. Rev. Appl.*, vol. 2, no. 4, 2014.

[32] G. Tanaka *et al.*, "Recent advances in physical reservoir computing: A review," *Neural Networks*, vol. 115, pp. 100–123, 2019.

[33] G. Van Der Sande, D. Brunner, and M. C. Soriano, "Advances in photonic reservoir computing," *Nanophotonics*, vol. 6, no. 3, pp. 561–576, 2017.

[34] C. Gallicchio, A. Micheli, and L. Pedrelli, "Deep reservoir computing: A critical experimental analysis," *Neurocomputing*, vol. 268, pp. 87–99, 2017.

[35] N. Soures, C. Merkel, D. Kudithipudi, C. Thiem, and N. McDonald, "Reservoir Computing in Embedded Systems," *IEEE Consumer Electronics Magazine*, July 2017, pp. 67–73, 2017.

[36] D. Prychynenko *et al.*, "Magnetic Skyrmion as a Nonlinear Resistive Element: A Potential Building Block for Reservoir Computing," 2018.

[37] D. Kudithipudi, Q. Saleh, C. Merkel, J. Thesing, and B. Wysocki, "Design and Analysis of a Neuromemristive Reservoir Computing Architecture for Biosignal Processing," *Front. Neurosci.*, vol. 9, no. February, p. 502, 2015.

[38] J. Torrejon *et al.*, "Neuromorphic computing with nanoscale spintronic oscillators," *Nature*, vol. 547, no. 7664, pp. 428–431, Jul. 2017.

[39] N. Jones, "How to stop data centres from gobbling up the world's electricity," *Nature*, vol. 561, pp. 163–166, 2018.

Chapter 2 – Theory

"A valid scientific theory is predictive, verifiable, and replicable. To me, that's beautiful" –
Dean Ornish

2.0 Background

This chapter gives an introduction to magnetism and magnetic materials, focussing on the energies driving ferromagnetic behaviour. This leads on to the origin of magnetic domains and domain wall (DW) formation in ferromagnetic materials, with literature review further exploring these as well as the dynamics behind DW motion. Finally, the origin of magneto-optic effects is introduced here prior to a description of application for magneto-optic Kerr effect magnetometry in Experimental Techniques.

2.1 Magnetic Materials

To the layman, magnetism is traditionally associated with the bar magnet as seen in school Physics lessons. These comprise of a bar of metal with a north and south pole with magnetic field lines flowing from the former to the latter. Bearing in mind this simple analogy, the more complex atomic magnetic dipole can be thought of as an atomic scale bar magnet.

The magnetic dipole will experience a torque in an applied magnetic field dependent on its orientation in and the strength of an applied magnetic field. The magnetic dipole can therefore be represented as a vector quantity – the atomic magnetic dipole moment.

$$\tau = \boldsymbol{m} \times \boldsymbol{B} \qquad\qquad \textit{Equation } 2.1$$

where τ is the torque experienced, $\boldsymbol{m}$ is the atomic magnetic (dipole) moment and $\boldsymbol{B}$ is the applied magnetic field.

The density of atomic magnetic dipole moments in a material gives the magnetisation, *M*, of a material, i.e the magnetic moment per unit volume

$$M = \frac{m}{V}$$ *Equation* 2.2

where V is the subject volume.

The origin of atomic dipole moment arises from the motion of electrons around the nucleus. It is formed from contributions from the angular momentum of the negatively charged electron orbiting the nucleus and the angular momentum or 'spin' of the electron itself. These effects produce their own magnetic fields that interact, leading to spin-orbit coupling. In atoms with more than one electron, coupling can occur between spins, orbits and spin-orbits. In an atom with multiple electrons, total magnetic moment depends on spin-orbit coupling and spin-spin/orbit-orbit coupling between different electrons. Therefore, only electrons that can couple will influence the total magnetic moment of a material.

Different elements exhibit different magnetic behaviours depending on their electron interactions. The electronic orbital structure of Cr, Mn, Fe, Co, Ni and Cu are considered here to demonstrate the origins of these behaviours. Electronic configurations for those elements are as follows:

Cr: $[Ar]4s^13d^5$

Mn: $[Ar]4s^23d^5$

Fe: $[Ar]\ 4s^23d^6$

Co: $[Ar]\ 4s^23d^7$

Ni: $[Ar]4s^23d^8$

Cu: $[Ar]4s^13d^{10}$

The spin of an electron is its angular momentum in one of two directions – 'up' or 'down'. By the Pauli exclusion principle [1], electrons cannot exist in the same electronic orbital with the same angular momentum so will pair in the same orbital with opposing spins. This means that fully completed electron pairs, with equal and opposite atomic dipole moments, will not contribute to the total magnetisation of a material.

The electron orbital schematic of preferential (i.e. more stable) configurations of electrons in the elements listed above are as follows:

Cr   [Ar]   4s   3d

Mn   [Ar]   4s   3d

Fe   [Ar]   4s   3d

Co   [Ar]   4s   3d

Ni   [Ar]   4s   3d

Cu   [Ar]   4s   3d
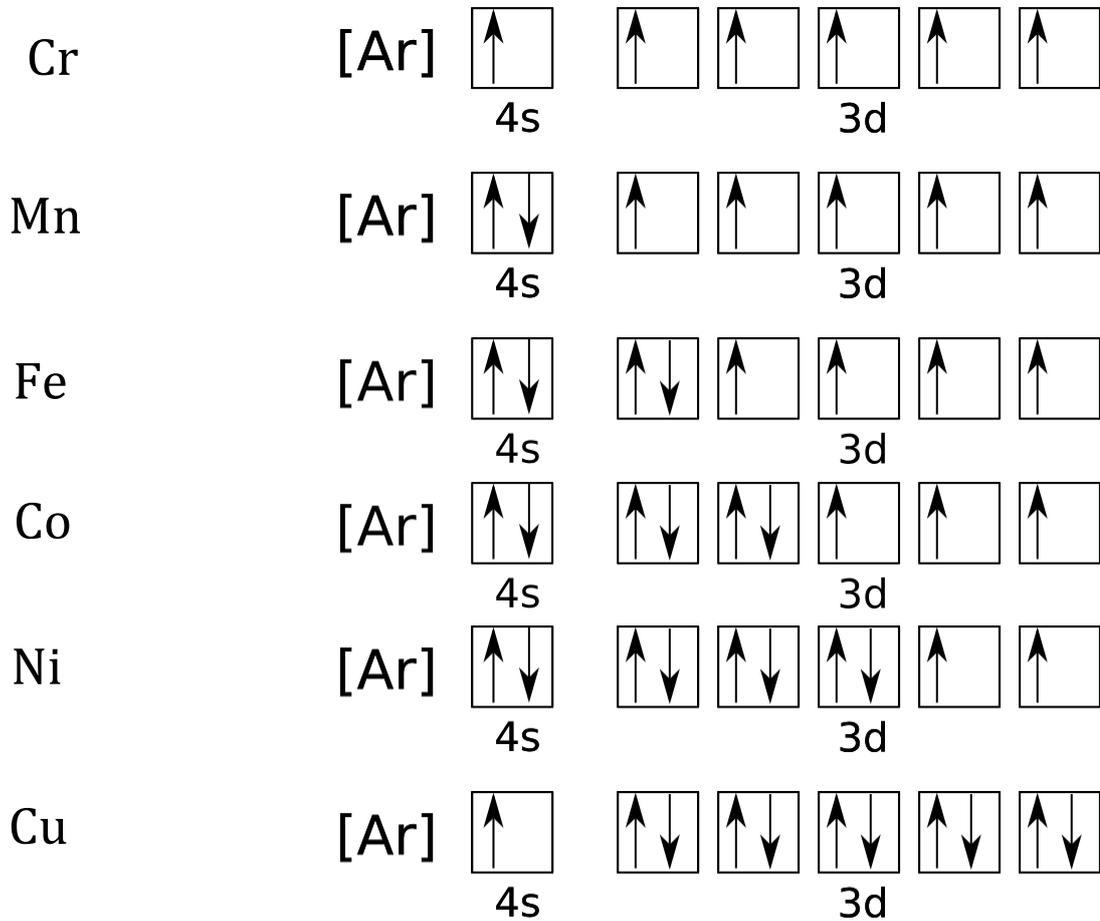
Figure 2.1. Schematic electron configurations of the ferromagnetic elements Mn, Fe, Co, Ni and Cu. Not that Cr and Cu are non-trivial in its structure as a 4s electron has been excited into the 3d orbital where it is more energetically favourable to exist.

Free electrons in the outer d-orbitals lend themselves to *ferromagnetic* behaviour in the classic ferromagnets of Fe, Co and Ni. However there are further quantum mechanical considerations to the origin of ferromagnetism beyond free-electron presence as evidenced by Mn being a *paramagnet.* In Mn, the vector sum of atomic dipole moments gives a net moment of approximately zero. An applied external field can align these dipole moments, but with the removal of this field the orientations of dipoles are free to relax to a net zero configuration. In ferromagnets, there is a driving force to retain magnetisation such that with the removal of an external field, the orientation of dipoles retain parallel alignment with each other. In addition, at a distance of 0.1nm from a moment with $1\mu_B$ is approximately 1T, which is orders of magnitude lower than the effective magnetic fields of 100T of a ferromagnet.

This arises from the consequences of the *exchange interaction* which reflects electrostatic repulsion of negatively charged electrons in overlapping orbitals to reach a more energetically favourable state. The Pauli exclusion principle affects the quantum state of two electrons in overlapping orbitals. As two electrons with, say, 'up' spin cannot exist in the same location, their distribution of electric charge in space is minimised when they are parallel (i.e. their electric charges are further apart). This also lowers the electrostatic energy of the system on an order much greater than aforementioned atomic dipole coupling.

To outline the quantum mechanical origin of the exchange interaction, the hydrogen molecule H_2 is considered as it is a simple case with one s-orbital and one free electron. In each molecule, the wavefunction of the two electrons can be represented as:

$$\Phi(1,2) = -\Phi(2,1) \qquad\qquad \textit{Equation 2.3}$$

These wavefunctions are products of space coordinates $\Psi(\boldsymbol{r_1}, \boldsymbol{r_2})$ and spin coordinates $\chi(s_1, s_2)$. Considering these wavefunctions in the hydrogen molecules 1s orbitals there are two potential molecular orbits – one with aligned spins antiparallel that is spatially symmetric, Ψ_S, and the other with spins parallel that is spatially antisymmetric, Ψ_A.

The symmetric space function is a multiple of the antisymmetric spin function and vice versa. For each electron, the wavefunctions are:

$$\Phi_1 = \Psi_S(1,2)\chi_A(1,2), \qquad \Phi_2 = \Psi_A(1,2)\chi_S(1,2) \qquad \textit{Equation 2.4}$$

With the Hamiltonian $H(\boldsymbol{r_1}, \boldsymbol{r_2})$, the energy levels of these wavefunctions can be expressed as:

$$E_{1,2} = \int \Psi_{S,A}^*(\boldsymbol{r_1}, \boldsymbol{r_2})\mathcal{H}(\boldsymbol{r_1}, \boldsymbol{r_2})\Psi_{S,A}(\boldsymbol{r_1}, \boldsymbol{r_2})d\boldsymbol{r_1}\boldsymbol{r_2} \qquad \textit{Equation 2.5}$$

These energy levels are degenerate such that $E_{1,2} = E_0$, but if excited then $E_1 = E_0 - 2J_{ex}$ and $E_2 = E_0 + 2J_{ex}$ where J_{ex} is the exchange integral.

The spin-dependent energy in the H_2 molecule can be written in the form

$$E = -2\left(\frac{J'_{ex}}{\hbar^2}\right).\boldsymbol{s_1}.\boldsymbol{s_2} \qquad\qquad \textit{Equation 2.6}$$

where J'_{ex} is the energy splitting between antiparallel and parallel spin states and $\hbar$ is the Planck constant over 2π. This was generalised in the hydrogen molecule by Heisenberg [2] into a Hamiltonian:

$$\mathcal{H} = -2J_{ex}\boldsymbol{S}_1.\boldsymbol{S}_2 \qquad\qquad Equation\ 2.7$$

Where $\boldsymbol{S}_1$ and $\boldsymbol{S}_2$ are cumulative electron atomic spins. Where J_{ex} is positive this is a ferromagnetic interaction with parallel alignment of spins and where this is negative, anti-parallel alignment of spins gives *antiferromagnetic* behaviour. The latter is seen in Cr which is an antiferromagnet and also causes moment alignment in *ferrimagnets*. Later, it will be seen that this Hamiltonian is used for describing the exchange energy of a ferromagnet, which is minimised by maintaining parallel or antiparallel alignment of spins.

The crystal lattice distributions of atoms can also affect whether a material is ferromagnetic or paramagnetic, such as where a phase transition to austenitic Fe will lose its ferromagnetic properties. The extent of the exchange interaction is dependent on interatomic spacing for electrons to be able to overlap and lead to ferromagnetic alignment of spins. This accounts for the origin of paramagnetism in Mn, despite having more free electrons than Ni, Fe and Co.

In summary, the ferromagnetic response in Ni, Fe and Cu occurs from the exchange interaction when electrons in d-orbitals overlap and minimise energy by aligning moments parallel.

The final example from Fig. 2.1 is Cu, where in the presence of an applied field the current loops formed from completed outer shells tend to align their spins anti-parallel to an applied field. This behaviour is typical of *diamagnets*.

These behaviours can be compared with reference to their magnetic susceptibility, as this varies characteristically for each magnet type. Magnetic susceptibility is defined from the relation between magnetisation and applied field;

$$\boldsymbol{M} = \chi\boldsymbol{H} \qquad\qquad Equation\ 2.8$$

where χ is the magnetic susceptibility.

2.1.1 Diamagnetism

Diamagnetism is the response to an applied external magnetic field as electron orbits are altered from an electromagnetic induction opposing the applied field. This leads to a repulsion from the source of the applied field and thus the susceptibility of a diamagnet is negative. Most materials have such a weak diamagnetic effect that this repulsion is negligible. When the applied field is removed, a diamagnet has no net magnetic moment. Superconductors are 'perfect diamagnets' as the Meissner effect [3] means all of their magnetic field is repelled. This leads to an easy visualisation of diamagnetism in levitating superconductors, such as shown in Fig. 2.2.
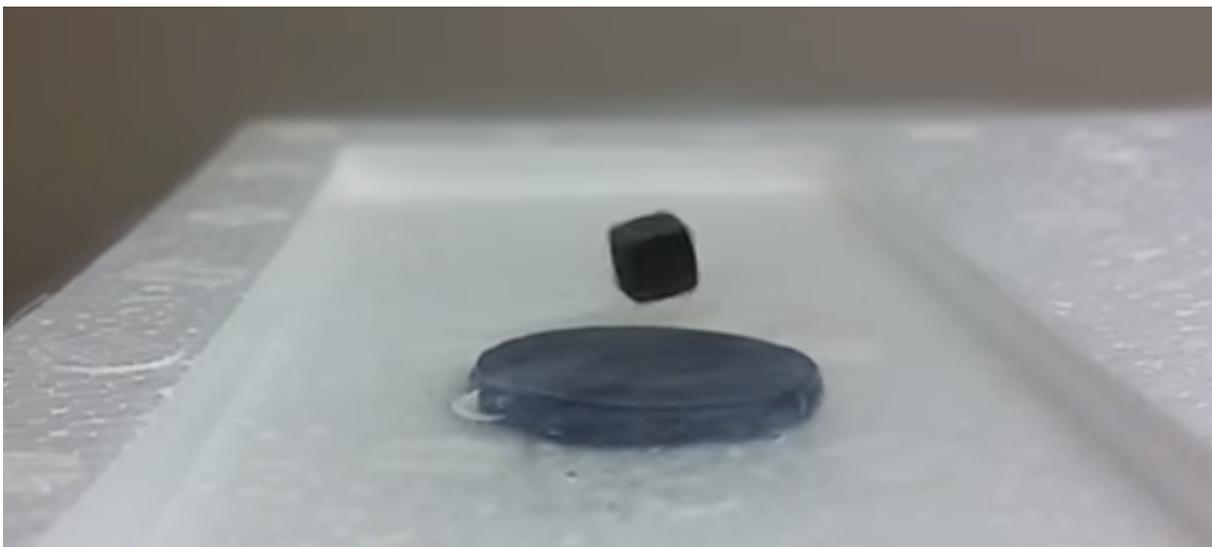
Figure 2.2. Image from a typical video freely available on Youtube of a levitating superconductor demonstrating the origin of their nickname of perfect diamagnets [4]

Examples of particularly diamagnetic materials (i.e. showing a stronger response than -1×10^{-5}) are silver, mercury, bismuth and pyrolytic carbon.

2.1.2 Paramagnetism

Paramagnetic materials contain atoms with a spontaneous magnetic moment that are randomly aligned such that in the absence of an applied field, magnetic moments are so

randomly distributed that net magnetisation is zero. Random orientation is possible because of thermal effects overcoming inherently weak interactions between moments. With enough thermal energy all moment-moment interactions can be overcome and paramagnetism is observed above a characteristic threshold temperature.

With application of a field, moments tend to align with the external field direction. The response of paramagnetic materials to an applied magnetic field is relatively weak and worsens with increasing temperature towards the characteristic threshold. This results in low, positive values of susceptibility. Figure 2.3 shows the response of magnetic dipole moments in a paramagnet as an external field is applied.
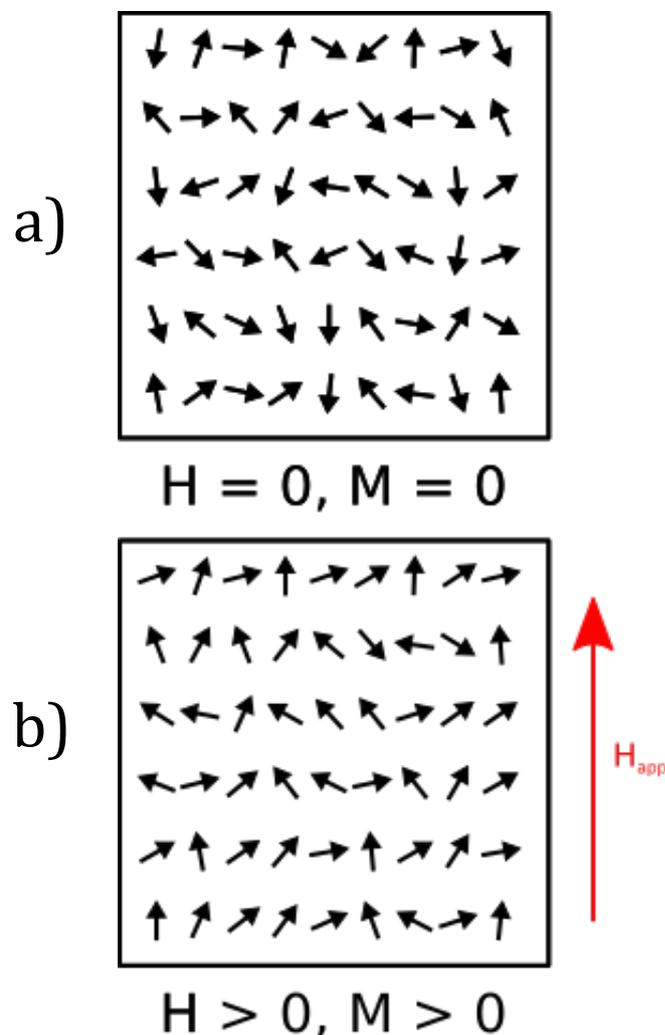
Figure 2.3. General behaviour of dipoles within a paramagnet with a) no applied field and b) an applied magnetic field. Random orientation of spontaneous magnetic dipole moments gives no net magnetisation in a). With the application of an applied field, H_{app} in b), there is slight ordering towards the direction of the applied field leading to an observable magnetisation.

2.1.3 Ferromagnetism

Ferromagnetic materials that have a magnetic field applied will orient atomic dipole moments parallel to that field. This orientation is generally maintained with the removal of the applied field. Figure 2.4 outlines the spontaneous magnetisation of a ferromagnetic material that has had a field applied and then reversed to 0.

$$H = 0, M \neq 0$$
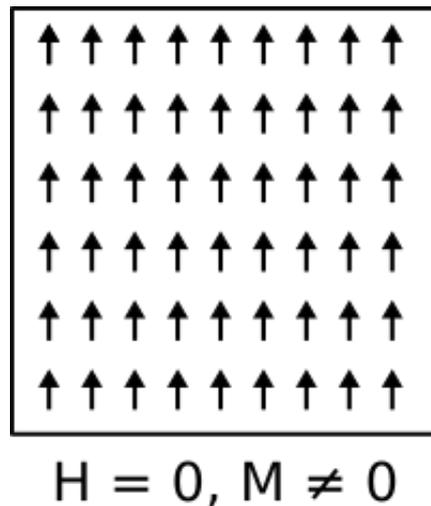
Figure 2.4. General behaviour of a ferromagnetic material after application of an external field. Ferromagnets retain their spontaneous magnetisation.

Ferromagnets often demonstrate magnetic hysteresis, in that the process by which magnetisation changes (usually in response to an applied field) is irreversible. Hysteretic responses are inherent to other ferroic materials from similar irreversibility in their properties.

A simplified, typical M-H hysteresis loop for a ferromagnetic material immediately following fabrication is shown in Fig. 2.5.
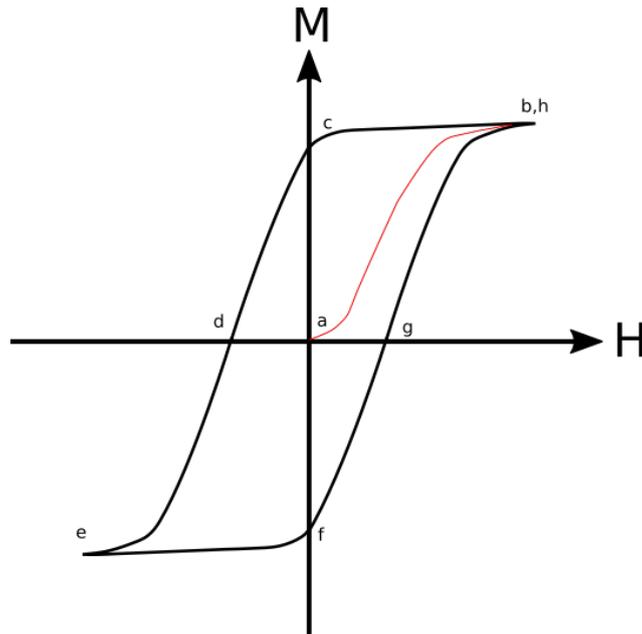
Figure 2.5. A simple plot of M-H for a ferromagnetic material following fabrication. The red line shows the initial response when the material has not previously been magnetised.

In general, starting at **M** = 0 the magnetisation of the ferromagnet increases in size with applied field until a point at which further increases in applied field produce no further increases in **M**. The external magnetic field is then applied in the opposing direction which initiates a decrease in magnetisation, passing through $M = 0$, until a point is reached again at which further increases in field no longer increase the magnitude of **M.** In a second reversal (i.e. the same direction as initially applied), magnetisation increases along a different path to the initial one. The initial path becomes inaccessible because of the hysteretic properties of the loop.

The key points in this sequence are labelled **a-h**. Point **b** is the saturation magnetisation, M_S – where further increases in H produce no further changes in M the ferromagnet is deemed to have reached saturation.

When the applied field is reversed to $H = 0$, there is often a relaxation from saturation. At this point, **c**, the magnetisation that remains is called the 'remanence' or M_R.

From **c-d-e**, magnetic field is applied opposite to the direction of saturation. Point **d** is significant as this is the field required to induce zero net magnetisation in the material. This is the field required to coerce the net alignment of magnetic dipole moment to orientations such that $M = 0$. This field (and its corresponding field for the other direction of applied field) is the coercive field $\pm H_C$.

Point **e** is also a saturation magnetisation in the opposite direction to that at **b** and has magnetisation of $-M_S$. Similarly, **f** is opposing remanence with magnetisation equal to $-M_R$ and **f-g-h** is analogous to **c-d-e** in the reverse direction.

The key point for ferroic materials that have hysteresis loops, is that the presence of remanence means the material retains its magnetisation/polarisation/strain when the external input is removed.

In this thesis, measurements are made using minor hysteresis loops that differ from the simple case (major loops) outlined here. These are loops where applied field values are less than saturation magnetisation. An example hysteresis loop made for work in §5 is shown in Fig. 2.6. The 'kink' demonstrates the presence of vortex state nanorings (expanded in §3.1.5 and Fig. 3.5).
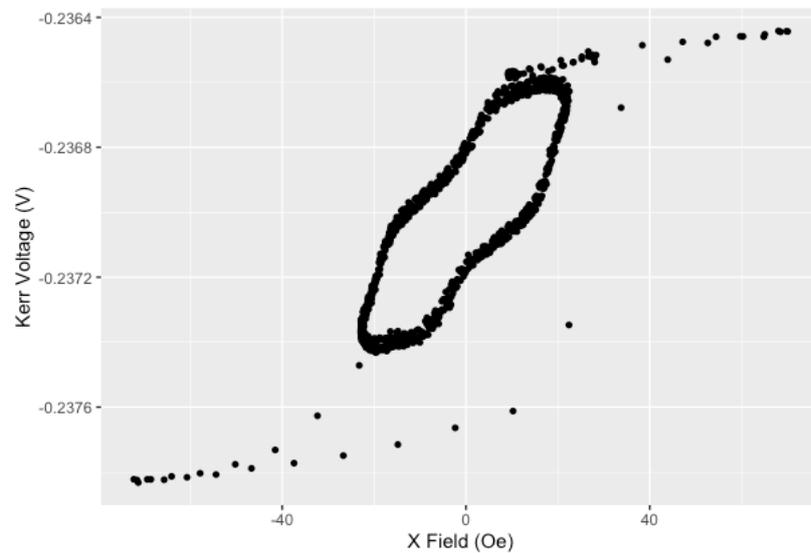
Figure 2.6. Sample hysteresis loop from this thesis showing the characteristic of a minor loop within the major loop defined by the saturation magnetisation. There are 25 cycles within the minor loop, hence the relative abundance of points to the major loop.

2.1.4 Antiferromagnetism

In antiferromagnets, local ordering is again present; however adjacent moments of identical magnitude are aligned antiparallel. This gives a net zero magnetisation, as

demonstrated in Fig. 2.7. Moments in an antiferromagnet are of equal magnitude such that the net magnetisation of the material is zero. Antiferromagnetic materials are weakly sensitive to applied magnetic fields, with low susceptibilities (10^{-3} – 10^{-5}).
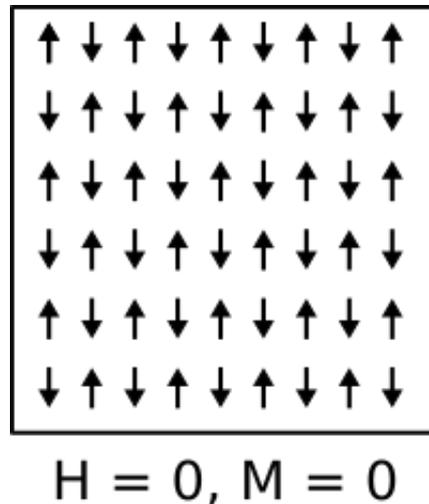
Figure 2.7. General behaviour of dipoles within an antiferromagnetic material. Net magnetisation is zero as all magnetic dipoles aligned in one direction have an equal proportion of dipoles aligned anti-parallel.

Typical antiferromagnets are Cr and oxides of transition metals such as, MnO and CoO as well as alloys like FeMn.

Antiferromagnetic materials are widely used as a coupling layer in spin valves [5]–[7] with practical uses in magnetic sensors, hard drive read heads and magnetic random-access memory (MRAM) [8] .

2.1.5 Ferrimagnetism

Ferrimagnetism is similar to antiferromagnetism in that they have antiparallel moments but these are not of equal magnitude. Instead, there are two sublattices of different magnetic moments which lead to a net spontaneous magnetisation. This is shown in Fig. 2.8. Ferrimagnetism can be found in materials with different ions such as ferrites or magnetic garnets (that have different ions of iron, e.g. Fe2+ and Fe3+)
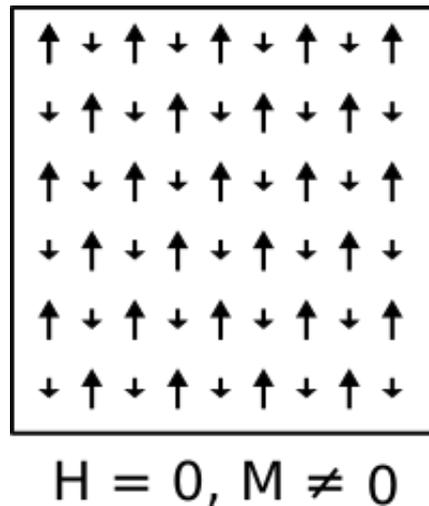
Figure 2.8. General behaviour of magentic dipoles in a ferrimagnetic material. Moments are spontaneously aligned antiparallel and of non-equal magnitude giving an observable magnetisation.

At low magnetic fields, ferrimagnetic materials show a hysteresis type response like that in ferromagnets (Fig. 2.5) but usually with a lower saturation magnetisation. The opposite alignment of moments is approximately maintained but higher magnetic fields can force full parallel alignment to reach the true saturation field of the material.

To compare relative behaviour of types of magnetic materials, a simplified plot of *M-H* for various magnets provides an insight into their behaviour is shown in Fig. 2.9.
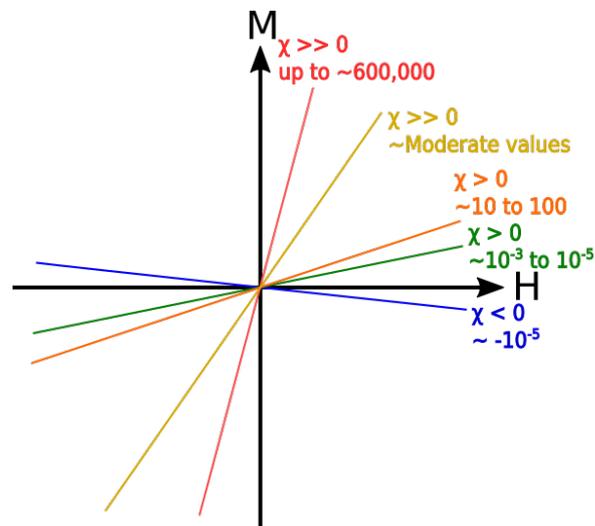
Figure 2.9. General plot (not to scale) of different types of magnetic behaviour. Red – Ferromagnetic, Yellow – ferrimagnetic, orange – antiferromagnetic, green – paramagnetic, blue – diamagnetic.

2.2 Magnetic Energy Terms

Most of the magnetic material types expressed some tendency for coupling of alignment, but all dipoles do not completely align without an external input. This is particularly noticeable when considering the proportion of dipoles that are aligned at different points on a hysteresis loop. To understand the mechanisms that drive these behaviours, four types of magnetic energy are introduced in this section. These will be fundamental for understanding interactions of magnetic dipole moments in magnetic nanostructures in this thesis.

2.2.1 Magnetostatic Energy

Magnetostatic energy can be described by considering a simple bar magnet or uniformly magnetised material. A demagnetising field is present around the block in the direction of North-South pole. This is demonstrated in Fig. 2.10.
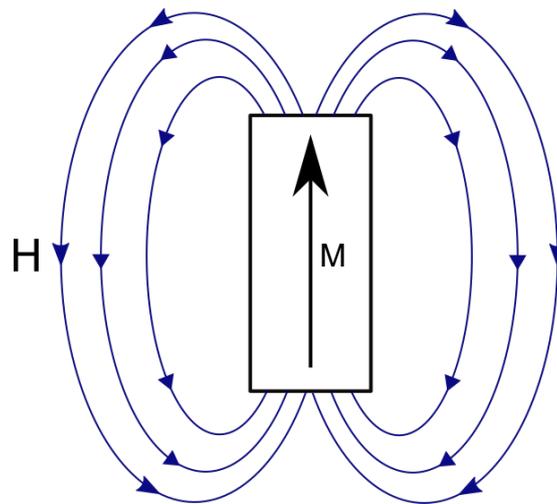
Figure 2.10. Schematic of the magnetic field around a single domain object such as a bar magnet

These single domain objects have an internal field opposite to the magnetisation of the sample, the demagnetising field, H_d, which can be visualised as the virtual field lines within the magnet that run from opposing surface charges. Figure 2.11a) demonstrates this in the same single domain object as Fig. 2.10 and also includes a visualisation of the same effect if the surface charges were along the longer axis of the asymmetric uniform domain in Fig 2.11 (b).
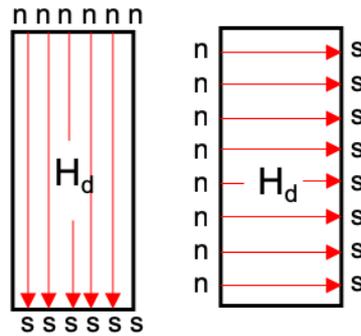
Figure 2.11.(a) Schematic of the demagnetising field in a single domain object such as Fig. 2.10, visualised by the extension of field lines from north to south poles at the surface. (b) Schematic of the demagnetising field in the theoretical single domain object from Fig. 2.10 that has magnetisation perpendicular to the long axis.

The energy of a system due to its own demagnetising field is the magnetostatic energy. This can be defined with the following equation:

$$E_{Magnetostatic} = -\frac{1}{2}\mu_0 \int_V \boldsymbol{H}_d . \boldsymbol{M} \, dV \qquad\qquad Equation\ 2.9$$

where dV is the infinitesimal volume of the system and μ_0 is the permeability of free space.

The demagnetising field depends on both the shape of a magnetic material and the direction of magnetisation within it. This can be described by:

$$\boldsymbol{H}_d = -N_d \boldsymbol{M} \qquad\qquad Equation\ 2.10$$

Where N_d is the 'shape factor' that depends on a material shape and magnetisation direction. This can be substituted into equation 2.9 as follows:

$$E_{Magnetostatic} = \frac{1}{2}\mu_0 \int_V N_d . M^2 \, dV$$

and for uniform magnetisation

$$E_{Magnetostatic} = \frac{1}{2}\mu_0 N_d M^2 V \qquad\qquad Equation\ 2.11$$

where $E_{magnetostatic}$ is the magnetostatic energy term. This can be minimised through minimisation of the shape factor. For a 2D material, this will be smaller when this

demagnetising field is aligned parallel to a longer axis. Recall in Fig. 2.11b) that there was a greater demagnetising effect from larger surface charge area when demagnetising field was perpendicular to the long axis, thus increasing magnetostatic energy.

Extending this to three dimensions, the shape factor can be considered as having three different orthogonal components: N_x , N_y and N_z. that sum to 1. For quasi 2D objects, in plane terms N_x and N_y tend to 0 due to the extended nature of that plane. This creates a shape dependent preference of magnetisation in films to lie in the film plane. Extended 1D objects, such as wires, will have only the axial shape factor tending to zero, which will cause magnetisation to prefer to lie along the wire length.

2.2.2 Magnetocrystalline Anisotropy Energy

The crystal structure of a magnetic material can create an energetic preference on magnetisation direction via spin-orbit coupling (see §2.1). For structures such as body centred cubic (BCC), face centred cubic (FCC) and hexagonal close packed (HCP), the 'easy' (most energetically favourable) axis is the line along which atoms are closest. Spin-orbit coupling is favourable along these easy axes and is proportional to the effective nuclear charge, Z_{eff}.

For uniaxial anisotropic materials, for example HCP cobalt which has an easy axis on the crystallographic c-axis, the magnetocrystalline anisotropy energy density is given by

$$\frac{E_k}{V} = K_0 + K_1 Sin^2\theta + K_2 Sin^4\theta + \cdots \qquad Equation\ 2.12$$

where E_k is the magnetocrystalline anisotropy energy, K_n are material specific constants and θ is the angle between **M** and the easy axis. Orders higher than $Sin^4\theta$ are usually neglected.

For cubic anisotropic materials with equivalent directions that are favourable this equation becomes:

$$\frac{E_k}{V} = K_0 + K_1(\alpha^2\beta^2 + \beta^2\gamma^2 + \gamma^2\alpha^2)Sin^2\theta + K_2(\alpha^2\beta^2\gamma^2)Sin^4\theta + \cdots \qquad Equation\ 2.13$$

where α, β and γ are directional cosines of M and the co-ordinate axis of the crystal lattice such that $\boldsymbol{M} = M_S(\alpha, \beta, \gamma)$ where M_S is the saturation magnetisation.

The magnetic material $Ni_{80}Fe_{20}$ or 'permalloy' (Py) has anisotropy constants that are approximately zero [9]. Py is the only magnetic material used in this thesis, with one reason being the lack of a unique easy axis giving a uniform response from the material to external fields.

Returning to a general perspective, magnetocrystalline anisotropy energy is minimised by alignment of moments parallel to an easy axis.

2.2.3 Zeeman Energy

This can be defined as the sum of work done turning a magnetic moment, m, by the angle $d\theta$ against an applied magnetic field.

$$dE = \mu_0 mH sin\theta d\theta \qquad \qquad Equation\ 2.14$$

Where θ is the angle made between magnetic moment and applied field prior to rotation.

(N.B. This defines the energy of a magnetic dipole as zero when perpendicular to the applied field, $\theta = \frac{\pi}{2}$).

This is called the Zeeman energy, E_Z, and can be further calculated as:

$$\therefore E_{Zeeman} = \int_{\frac{\pi}{2}}^{\theta} \mu_0 mH sin\theta d\theta \qquad \qquad Equation\ 2.15$$

$$= -\mu_0 mH cos\theta$$

$$= -\mu_0 \boldsymbol{m}.\boldsymbol{H} \qquad \qquad Equation\ 2.16$$

Across a unit volume, the magnetisation, M, is needed and equation 2.12 becomes

$$\frac{E_Z}{V} = -\mu_0 \boldsymbol{M}.\boldsymbol{H}$$
<div align="right">*Equation* 2.17</div>

From this equation it can be seen that minimisation of Zeeman energy is achieved by alignment of magnetisation parallel to an applied field.

2.2.4 Exchange Energy

The reorientation of electrons to give relative alignment of adjacent spins is dependent on the exchange energy. For two electrons,

$$E_{ex} = -2J_{ex}S_i.S_j \cos\theta$$
<div align="right">*Equation* 2.18</div>

where E_{ex} is the exchange energy, J_{ex} is the exchange integral (previously described in §2.1), θ the angle between spins and $S_{i,j}$ are the spin vectors. J can be positive or negative which dictates whether spins align parallel or anti-parallel leading to ferromagnetism or anti-ferromagnetism/ferrimagnetism respectively.

The exchange length, l_{ex} [10], the distance over which the strength of the exchange interaction and therefore local magnetisation is approximately constant is described as:

$$l_{ex} = \sqrt{\frac{A}{K_u + \frac{1}{2}\mu_0 M_s^2}}$$
<div align="right">*Equation* 2.19</div>

$$\approx \sqrt{\frac{A}{\frac{1}{2}\mu_0 M_s^2}}$$

where A is exchange constant, M_S is saturation magnetisation and K_u is the uniaxial anisotropy constant.

As an example, for pure Fe with $A = 10^{-11}\frac{J}{m}$ and $M_s = 1.71 \times 10^6 \frac{A}{m}$, $l_{ex} \approx 2.3nm$.

2.2.6 Magnetic Energies in Summary

The total energy of the system from the contributions can be generalised as:

$$E_{total} = E_{magnetostatic} + E_{anisotropic} + E_{Zeeman} + E_{exchange}$$ *Equation* 2.20

These energies are often described as MAZE energies from the acronym of their names.

A stable or metastable ground state is reached when E_{total} is minimsed. The minimisation of one term alone, however, often leads to an increase in another. Achieving a minimum in E_{total} is therefore a competition between constituent MAZE terms to minimise themselves.

2.3 Magnetic Domains and Domain Walls

A magnetic domain is a region within a magnetic material where magnetisation is uniform. A magnetic material (usually) spontaneously contains many domains that are magnetised in different directions. Magnetisation can be considered as the vector sum of all magnetisations of domains in a material.

Barkhausen discovered magnetisation reversal of a magnetic material is a non-continuous process characterised by discontinuities, now referred to as Barkhausen jumps or Barkhausen noise [11]. Later Langmuir [12], and confirmed by Sixtus and Tonks [13], who concluded these jumps are spatially inhomogeneous and are the propagation of a boundary between domains. This boundary, or wall, between domains of different magnetisation directions was investigated by Bloch (e.g. [14]) and Néel [15], who found walls to be a gradual change in dipole directions across the boundary on the order of a few lattice constants. The types of wall described by Bloch (and by Landau/Lifshitz [16]) (Bloch wall) and Néel (Néel wall) are described in §2.3.2.

Depending on the type of ferromagnet and its susceptibility, domains can flip their alignment at different applied fields. For low susceptibility ferromagnets this leads to a low gradient in the response. These materials are termed 'soft' ferromagnets. 'Hard' ferromagnets have large gradients/susceptibilities and virtually simultaneous flipping in moment alignment within the material. The terms 'hard' and 'soft' are foibles of their

history of discovery – the first hard ferromagnets were hard materials (mechanically) leading to this differentiation between the two.

With the introduction here of the concept of a domain wall that separates individual domains, the origin of domains can be explained with reference to the magnetic energy terms.

2.3.1 Formation of domains

Being regions of uniform magnetisation, domains have minimal exchange energy. However, in real magnetic structures this leads to large magnetostatic energies at interfaces such as physical edges and grain boundaries, especially those where the direction of uniform magnetisation is perpendicular to these. This occurs from the demagnetising field in this single, uniform domain being relatively large, as described by equation 2.9.

The intrinsic energy cost with creating a magnetic field can therefore be reduced by reducing the volume of the single domain and lessening the influence of demagnetising field. By creating two oppositely magnetised domains from the uniformly magnetised region, one can see the difference in surface charge area. Following from Fig. 2.9 and 2.10, the demagnetising field in this object is also reduced.
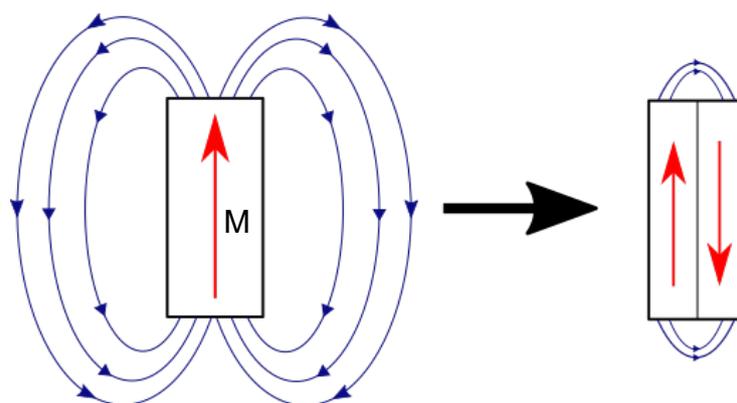
Figure 2.12. Schematic showing minimisation of magnetostatic energy at the surface of a block magnet by creation of two, oppositely magnetised domains.

Splitting the uniform domain from Fig. 2.12 into two roughly halves $E_{magnetostatic}$. Further splitting into more domains further reduces the magnetostatic energy such that, for even values of the number of domains, N:

$$E_{magnetostatic} = \frac{E_1}{N} \qquad\qquad Equation\ 2.21$$

where E_1 is the magnetostatic energy of the uniformly magnetised configuration. From this, it can be concluded that domain formation is preferred to minimise the ground state energy of the system, and there is a driving force towards infinite domain formation, in order to effectively neutralise the magnetostatic energy cost of the system.

The bidomain state shown in Fig. 2.12 still has a component of M perpendicular to the surface (shown by field lines) that can be minimised further still with the creation of a 'flux-closed' state. In the rectangular element considered here, this is achieved with additional end domains with magnetisation parallel to the element ends, as shown in Fig. 2.13. This eliminates surface magnetostatic interactions and therefore the only contribution to magnetostatic energy in the system comes from the interface between domains.
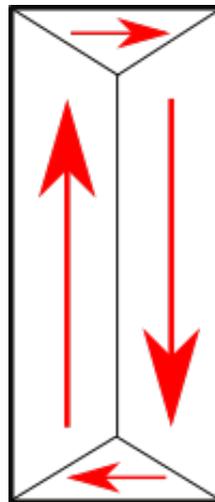
Figure 2.13. Schematic of the flux-closed state in a block magnet by the formation of domains. There is no significant contribution to magnetostatic energy from the outer surfaces in this configuration.

These interfaces between domains, or domain walls (DW) are explored in detail in the next section.

2.3.2 Domain Walls

DWs represent a change in the direction of magnetisation between regions, usually 90° or 180°. Within walls there exists gradual changes in spin alignment across the wall to minimise the exchange energy cost. To illustrate this, Fig. 2.14 considers two types of DW - Bloch and Néel. In each of these, the plane of rotation of spins are different.
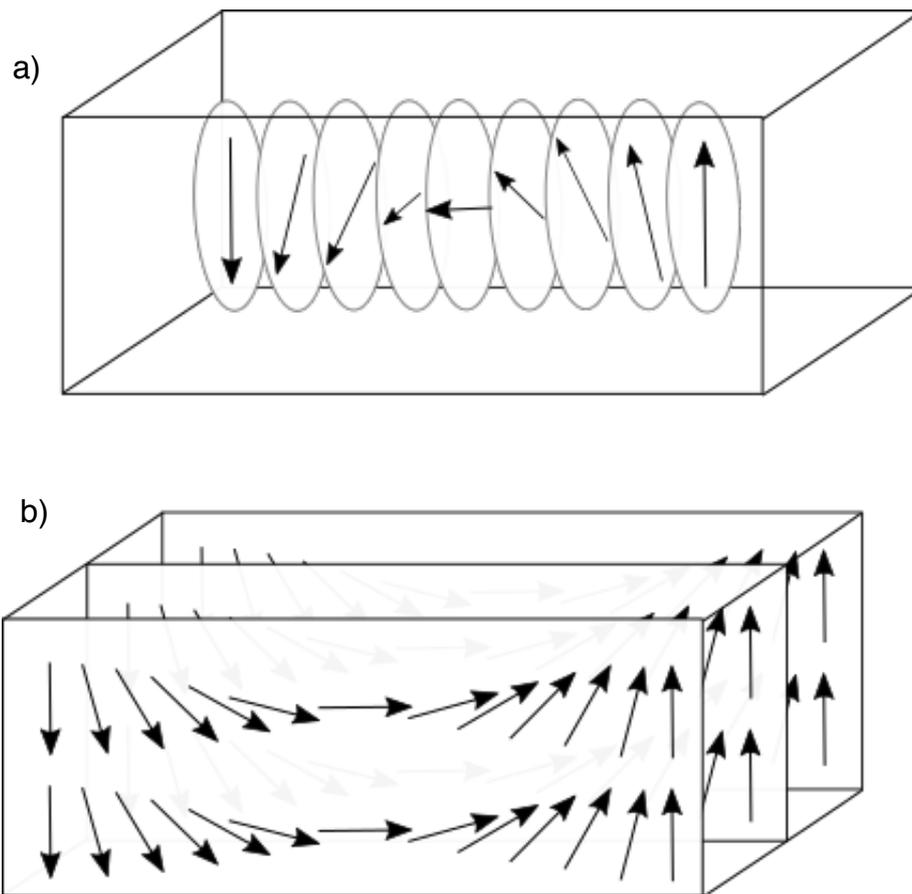
Figure 2.14. Schematic of change in orientation of dipole moments in two types of domain wall. a) Bloch wall b) Néel wall.

Domain walls are a balance between magnetostatic, magnetocrystalline and exchange effects. To minimise exchange, infinitely sized walls would be required to reduce the gradient of rotation in dipole moments across the wall. Magnetocrystalline energy increases for spins that are not aligned with an easy axis, and the "stray field" (i.e. the demagnetising field) of the domain wall will increase with the size of the DW, increasing the magnetostatic energy.

An expression for optimum wall width in ferromagnets in general can be made using equations 2.9 and 2.15 (originally derived by [17], with adaptation from [18]).

In a 180° Bloch wall, the exchange energy cost of reversal of magnetisation is

$$E_{ex} = 2J_{ex}S^2 \cos\theta$$

With S^2 used from the opposing spin alignment in domains of opposite magnetisation.

Each dipole moment will make an angle with its neighbour of $\theta = \frac{\pi}{N}$, where N is the lattice spacing width of the wall. The increment in exchange energy between neighbouring dipole moments is:

$$\Delta E_{ex} \approx E_{ex} - E_{ex}^{\theta=0} = -2JS^2 \cos\theta + 2JS^2 \qquad Equation\ 2.23$$

where the small angle approximation for $\cos\theta$, $(1 - \frac{\theta^2}{2})$ reduces this equation to the following

$$\approx 2JS^2 \frac{\theta^2}{2} = \frac{JS^2\pi^2}{N^2} \qquad Equation\ 2.24$$

Using the lattice constant, a, the exchange energy cost per unit area of the Bloch wall is:

$$\sigma_{DW}^{ex} = \frac{\sum_{DW} \Delta E_{ex}}{a^2} = \frac{JS^2\pi^2}{a^2 N} \qquad Equation\ 2.25$$

as the sum of exchange energy changes across the lattice spacing width of the wall is $N.\Delta E_{ex}$.

Equation 2.23 demonstrates an infinitely large wall (N tends to infinity) is preferable to minimise the energy cost of the wall.

From equation 2.9, magnetic anisotropy energy in the same wall is approximately

$$E_a \approx K_u \sin^2\theta$$

$$E_a^{total} \approx \sum_{i=1}^{N} K_u \sin^2\theta_i \approx \frac{1}{d\theta} K_u \int_0^{\pi} \sin^2\theta d\theta = \frac{\frac{1}{\frac{\pi}{N}} K_u \frac{1}{2}}{2}\pi = \frac{NK_u}{2} \qquad Equation\ 2.26$$

Assuming constant anisotropy per unit volume then the magnetocrystalline anisotropy energy per unit area is:

$$\sigma_a^{total} = \frac{NK_u}{2}\frac{a^3}{a^2} = \frac{NK_u a}{2} \qquad \textit{Equation 2.27}$$

Summing equations 2.23 and 2.25, the total energy cost per unit area of a Bloch wall is:

$$\sigma_{DW} = \sigma_{DW}^a + \sigma_{DW}^{ex} = \frac{NK_u a}{2} + \frac{JS^2\pi^2}{a^2 N} \qquad \textit{Equation 2.28}$$

The number of lattice spacings that will minimise this can be found by differentiating equation 2.26 with respect to N.

$$\frac{d\sigma_{DW}}{dN} = \frac{K_u a}{2} - \frac{JS^2\pi^2}{a^2 N^2} \qquad \textit{Equation 2.29}$$

And as $\frac{d\sigma_{DW}}{dN} \rightarrow 0$

$$N = \pi S \sqrt{\frac{2J}{K_u a^3}}$$

Wall width, δ, is then found by multiplying this minimum by the lattice constant such that

$$\delta = Na = \pi S \sqrt{\frac{2J}{K_u a}} \qquad \textit{Equation 2.30}$$

However, for materials such as those in this thesis created with Py ($K_u \approx 0$) then the magnetostatic cost of a domain wall becomes particularly relevant.

The preference of a wall to be infinitely narrow to minimise energy can be seen from equation 2.6 where a narrow wall will reduce the volume over which magnetostatic energy is relevant to approximately zero.

The competition between these two effects gives domain walls a non-infinite width but will also influence the form of domain wall type.

2.3.3 Nanostructured magnetic devices

A magnetic nanostructure is (typically) an artificially patterned region of magnetic material with geometries close to the exchange length of the material. This complicates the competition between magnetostatic, anisotropic and exchange energy considerations but can simplify the magnetic configurations.

Advances in lithographic techniques allow fabrication of nanostructures with features on the order of 10nm [19].

Various shapes of ferromagnetically soft nanostructures (i.e. those with low magnetocrystalline anisotropy [20]) such as squares, triangles and hexagons and their hysteresis profiles were studied experimentally in 1999 by Cowburn *et al.* [21]. That work identified circular nanomagnets as functionally attractive as their symmetry means there is no in-plane shape anisotropy or configurational anisotropy (so called from different energies at different configurations. For example fourfold or sixfold symmetry have four and six configurations - [22]).

Figure 2.15 shows Kerr hysteresis loops obtained from permalloy nanodisks of different diameter (d) and thickness (t) by Cowburn *et al* [23]. Different geometries will give two configurations of magnetic dipole moments – for example 'vortex' and 'single domain' for nanodisks of $d = 300nm, t = 10nm$ and $d = 100nm, t = 10nm$ respectively.
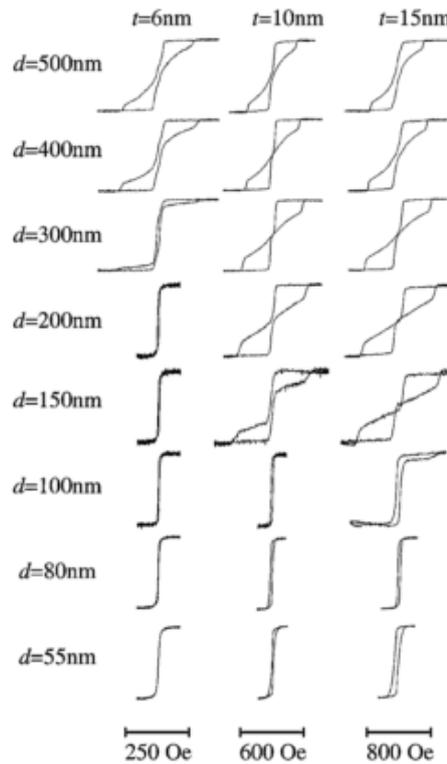
Figure 2.15. Hysteresis loops obtained via Kerr microscopy for arrays of circular NiFe nanomagnets (nanodisks) at given diameters (d) and thickness (t). From Cowburn et al [23]

Vortex state configuration brings the magnetostatic energy contribution down as magnetic dipole moments are circumferentially aligned leading to flux-closure at the edge but increases the exchange energy. The exchange energy increase is less significant the more gradual the moment rotation occurs, so vortices are preferred in disks with larger diameters. The curling of moments in a vortex is present throughout a disk except for the centre. Here, orientation by gradual alignment to a circle is not possible and an out of plane rotation will occur, perpendicular to the structure at the exact centre of the disk. This 'vortex-core' has a polarity dependent on whether the out of plane component is towards or away from an observer looking top-down at the structure [14], [24]. The magnetisation reversal of a vortex state is through a hysteresis loop as seen in larger diameter nanodisks in Fig. 2.15.

Smaller diameter disks are unable to support the vortex structure due to the tight moment curvature involved and the high exchange energy that results from this. Instead, single domains are preferred in which all moments align approximately uniformly [23]. This results in an increased magnetostatic energy but with little to no exchange energy contribution. These have hysteresis loops that alternate between

oppositely oriented uniformly magnetised states as there is no accessible metastable intermediate orientation. When thickness is increased, out of plane rotation is possible for energy minimisation leading to some off-axis rotation in the plane of the structure and hence wider hysteresis loops. These features are reflected in the hysteresis loops for thinner and smaller disks in Fig. 2.15. Figure 2.16 sketches the arrangement of magnetic dipoles on the surface of these disks following the measurements made in Fig. 2.15.
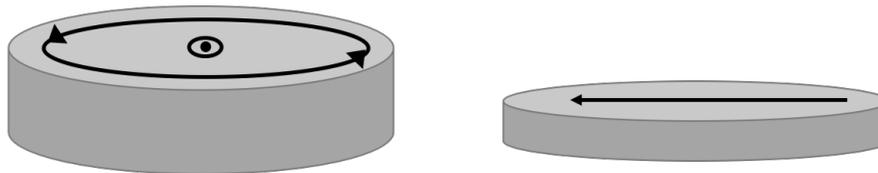
Figure 2.16. Schematic of 200nm diameter NiFe nanodisks at thicknesses of (left) 15nm and (right) 6nm showing surface arrangement of magnetic dipole moments, with a vortex (and core) in the 15nm disk and single domain arrangement in the 6nm disk.

There have been many other studies on the behaviour of similar nanodisks [25]–[29]. Here, they demonstrate the influence of geometry at the nanoscale on the resulting magnetic behaviour.

2.3.4 Domain walls in magnetic nanowires

A magnetic nanowire is a high aspect ratio strip of magnetic material. These are typically 5-70 nm thick, 100 nm – 1 μm wide and several micrometres in length. The small thickness compared with other dimensions means that soft ferromagnetic materials have a strong preference for in-plane magnetisation [30]. The high aspect ratio between wire width and length creates a large in-plane shape anisotropy, which leads to a strong preference for soft ferromagnetic materials to align parallel to the wire long axis. Magnetisation reversal in a nanowire usually proceeds through nucleation of a domain wall (DW) at a wire end followed by its rapid propagation through the wire [31]. DWs are interface regions through which magnetisation changes direction between two neighbouring magnetic domains. In soft ferromagnetic nanowires, the domains are usually oppositely aligned and the DWs stretch directly across the wire

width. The DWs are usually described as either 'head-to-head' (H2H) or 'tail-to-tail' (T2T), depending on the orientation of the domains either side (Fig. 2.17) [30].
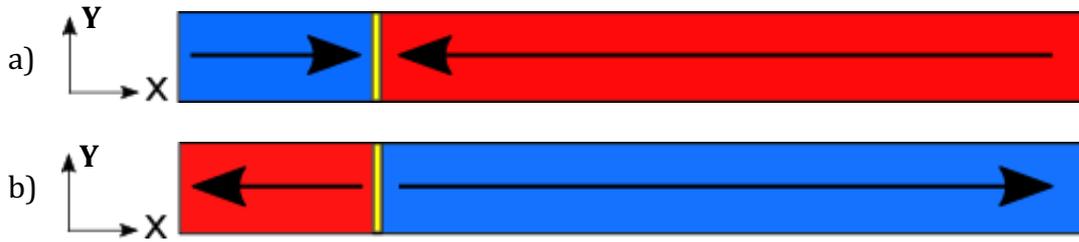
Figure 2.17. Schematic of a (a) head-to-head DW and (b) a tail-to-tail DW in a ferromagnetic nanowire

If an H2H DW is brought into contact with a T2T DW, annihilation of both walls will usually occur (e.g. as seen in [32]) as the entire nanowire becomes uniformly magnetised in the direction of the domains on the outer sides of the DW pairing (for the DWs to have been brought into contact, the domain between them must have been reduced in size until deletion). Alternatively, two 180° DWs in magnetic systems generally can meet to form a 360° DW [33]. This is a very unstable form of magnetic configuration as the reversed domain at the centre of the new DW is never removed and may grow again rapidly once an appropriate magnetic field is applied [34].

Finite difference modelling reveals a geometrical dependence of wires upon DW type [35], for example in Fig. 2.18 modelling by McMichael and Donahue showed the transition between transverse and vortex domain wall as the wire width was increased.
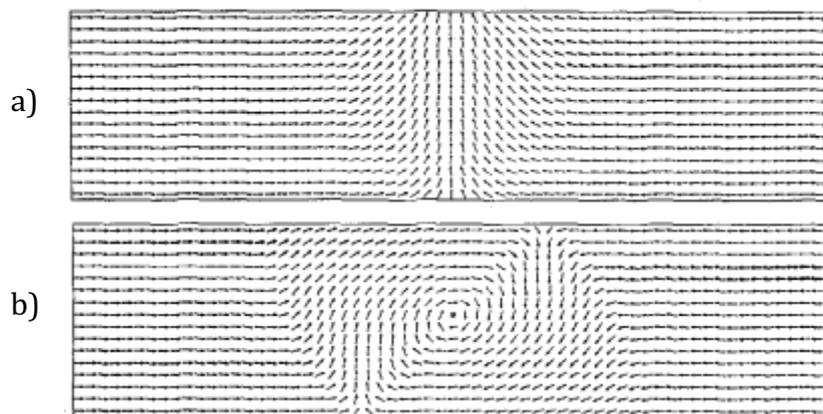
Figure 2.18 – Simulated domain wall in a ferromagnetic nanowire at different thicknesses. a) Transverse domain wall type. b) (clockwise) Vortex domain wall type [35].

A transverse wall has magnetic dipoles rotating in the plane of the wire. The direction of the moment rotation is uniform through any cross-section of the wall. The side of the

transverse wall that has a magnetic charge opposite to that of the surrounding wire domains is always shorter than the other side, which creates a triangular profile. This configuration reduces the magnetostatic energy of the system. The triangle can point in either y-direction (depending on the DW's magnetisation direction itself) giving rise to 'up' and 'down' transverse domain walls (uTDW and dTDW). This DW type arises particularly in thin and narrow nanowires where tight in-plane vortices and out-of-plane rotation of dipoles are energetically unfavourable [36].

Vortex domain walls (VDWs) have a central point at which magnetisation is out of the nanowire plane (i.e. parallel to the z-axis). Within the rest of the DW magnetisation curls around the central point which leads to two types of VDW – anti clockwise (aCW) and clockwise (CW), depending on the profile created in the plane of the wire. These walls are preferred in wires with larger cross-sections.

Each of these walls has different exchange and magnetostatic energy contributions. TDWs have a larger magnetostatic energy due to its simple magnetisation rotation resulting in significant stray field from the nanowire. VDWs have a large exchange energy because of the relatively tight magnetisation rotation through its structure.

The form that the domain wall will take will depend on the cross-sectional wire dimension. Smaller wire thicknesses cause out of plane magnetisation to become more unfavourable due to the increased magnetostatic energy this creates, and narrower wires increase the exchange energy cost of circular magnetic moment configurations within the wire. Both concepts are similar to the effects of length scale in nanodisks, discussed above.

The computational phase diagram of domain wall type in Fig. 2.19 was derived from an analytical model of stability of DW configuration. This model shows that in thinner and narrow nanowires, TDW formation is dominant and, with more space for reorientation of moments to minimise exchange energy, thicker and wider nanowires contain VDWs.
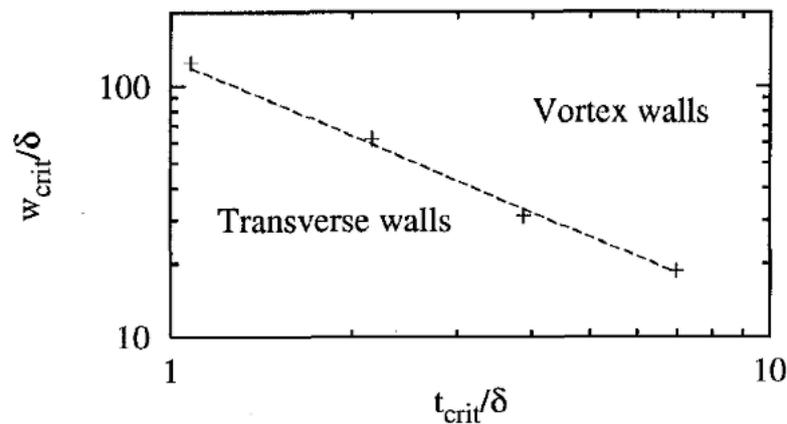
Figure 2.19 - Analytically derived phase diagram of DW type as varies by thickness and width in Permalloy nanowires by Donahue and McMichael [35]

Experimentally, DW types were investigated in ferromagnetic nanorings (itself a special case of a nanowire) by Kläui et al [37]. This work found good agreement with the analytical model but found two regions of stability in experimentally observed TDWs. There was also a metastable region between the transition from TDW to VDW wherein thermal fluctuations are a sufficient energy input to convert from one to the other. Ferromagnetic nanorings, being integral to this work, are further explored in §3.1.

Nakatani *et al.* [38] characterised the possible DW form in this metastable region as asymmetric TDW, where an elongation and tilt of the TDW in the nanowire is obtained. The various DW types are sketched in Fig. 2.20 and the simulated phase diagram of DW type in soft Permalloy nanowires shown in Fig. 2.21.
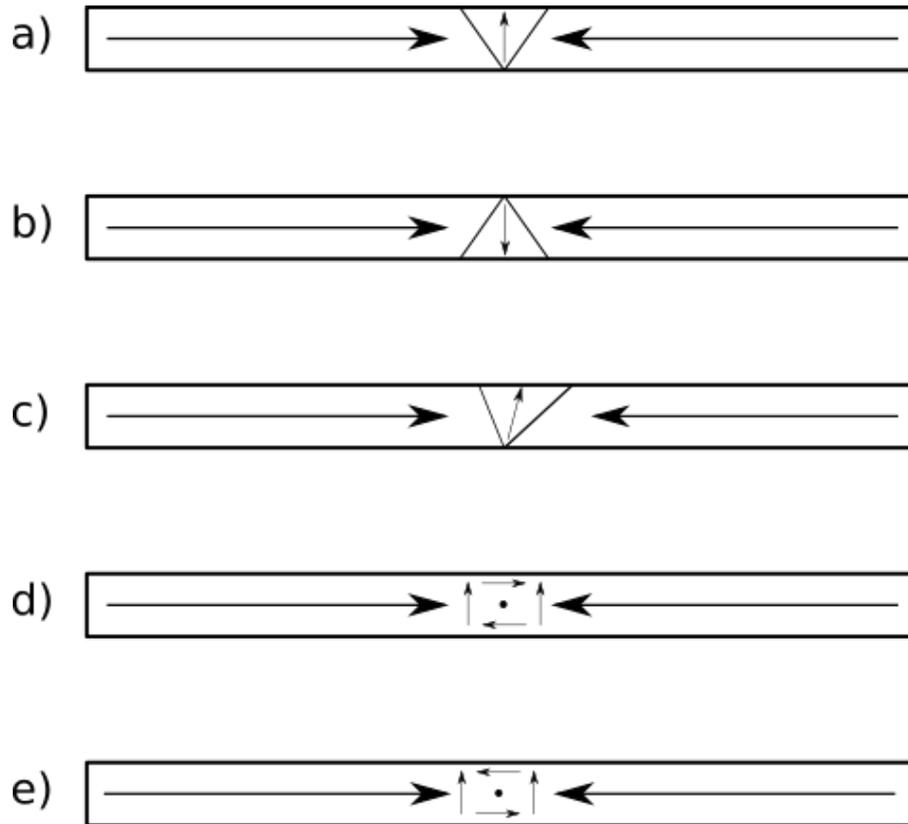
Figure 2.20. Schematic summary of DW types in soft ferromagnetic nanowires. a) up TDW b) down TDW c) asymmetric TDW d) clockwise VDW e) anticlockwise VDW.
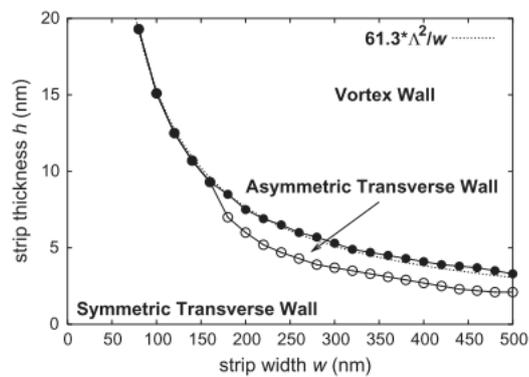
Figure 2.21. Phase diagram of DW type showing metastable asymmetric transverse DW region for soft Permalloy nanowires. Taken from [38]**.**

Literature here establishes the relationship between geometry and DW type in nanowires, which is relevant to this thesis in the selection of dimensions of width and thickness. As this thesis primarily explores the ferromagnetic nanoring, these are expanded upon in greater detail later on.

2.4 Magneto-optic Kerr effect

Magneto-Optic Kerr Effect (MOKE) magnetometry is a well-established optical technique measuring the magnetic response of thin films and nanostructures [23], [39]– [47] to external stimuli, such as magnetic field [32], [48] or electric current [49]. In addition to being useful and straightforward to obtain hysteresis loops for magnetic materials, it is an effective tool for characterising domain wall (DW) behaviour in nanostructured magnetic media e.g. [50], when using focussed optical spots.

A laser is usually used as the illumination due to their good beam intensity. The laser beam is first polarised in a desired state and then reflected from the magnetic sample and passes through an analyser (another polariser) before being incident on a photodiode to measure the beam intensity.

Critical to MOKE magnetometry is the measurement of change in intensity at the photodiode from rotations of optical polarisation when reflected from the magnetic sample. A study by Allwood et al. [39] derived a useful expression for quantifying the rotation in polarisation and investigated the maximisation of this, which is summarised as follows.

Polar and longitudinal MOKE configurations produce an orthogonal Kerr reflection component, whereas transverse MOKE changes the amplitude of polarisation. A vector diagram of the reflected components for polar or longitudinal as they travel to the analyser is as shown in Fig. 2.22.
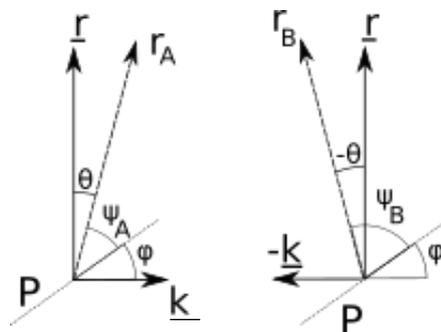
Figure 2.22. Vector diagrams of polarised light as they are reflected from a magnetic sample surface. P is the polarisation axis, $\underline{r}$ is the Fresnel amplitude of incident light, k is the Kerr vector induced from reflection with a magnetic surface, $\underline{r}_A$ is the Fresnel amplitude of reflected light which is the vector sum of $\underline{r}$ and $\underline{k}$, φ, ψ and θ are the angles between these axes and vectors.

$\underline{r}$ is the Fresnel amplitude reflected component of polarised light, and the Kerr vector, the contribution from magnetic interaction with the sample surface, is $\underline{k}$. The magnitude of $\underline{k}$ is determined by the sample magnetisation and the vectoral sum of $\underline{r}$ and $\underline{k}$ gives the total reflected amplitude component from a magnetised surface, r_A. The angle of rotation from the unmodified beam to the actual reflected beam is θ, the Kerr rotation angle. The analyser can be defined as having a polarisation axis that makes an angle of φ to the Kerr vector will have an angle of ψ with the reflected beam. The equivalent vectors for a beam reflected from the same surface magnetised in the opposite direction are given by the equivalent components $r_B, -\underline{k}, -\theta$ and φ_B etc.

Therefore, the transmitted optical amplitudes, t_A and t_B, through the analyser (ignoring any reflection losses in the analyser), are:

$$t_A = r_A \cos(90 - \varphi - \theta) = r_A \sin(\varphi + \theta) \qquad \qquad Equation\ 2.31$$
$$t_B = r_B \sin(\varphi - \theta) \qquad \qquad Equation\ 2.32$$

Optical intensity is proportional to the square of amplitude, so the transmitted intensities, I_A and I_B through the analyser are:

$$I_A = I_0 \sin^2(\varphi + \theta) \qquad \qquad Equation\ 2.33$$
$$I_B = I_0 \sin^2(\varphi - \theta) \qquad \qquad Equation\ 2.34$$

The average of these intensities, $\bar{I}$, for small angle Kerr rotations is:

$$\bar{I} = \frac{I_0}{2}(1 - cos2\varphi cos2\theta) \approx I_0 \sin^2 \varphi \qquad \qquad Equation\ 2.35$$

and the difference between them (the MOKE signal) is:

$$\Delta I = I_0\ sin2\varphi sin2\theta \qquad \qquad Equation\ 2.36$$

The intensity of the reflected beam is the useful experimental output. Using a photodetector to measure this intensity and changes in it can directly be used to track changes in magnetisation of the sample.

The fractional MOKE signal, $\frac{\Delta I}{\bar{I}}$, is sensitive to these changes in the Kerr rotation angle for the reflected beam:

$$\frac{\Delta I}{\bar{I}} = \frac{2 \sin 2\varphi \sin 2\theta}{1 - \cos 2\varphi \cos 2\theta} \qquad \qquad Equation\ 2.37$$

2.5 References

[1] W. Pauli, ".," *Z. Phys*, vol. 31, 1925.

[2] W. Heisenberg, "Zur Theorie des Ferromagnetismus," *Zeitschrift für Phys.*, vol. 49, no. 9, pp. 619–636, 1928.

[3] W. Meissner and R. Ochsenfeld, "No Title," *Naturwissenschaften*, vol. 21, p. 787, 1933.

[4] "No Title." [Online]. Available: https://www.youtube.com/watch?v=l0jEbWfFAXU. [Accessed: 27-Apr-2019].

[5] S. Parkin, X. Jiang, C. Kaiser, A. Panchula, K. Roche, and M. Samant, "Magnetically engineered spintronic sensors and memory," *Proc. IEEE*, vol. 91, no. 5, pp. 661–679, 2003.

[6] P. Grünberg, R. Schreiber, Y. Pang, M. Brodsky, and H. Sowers, "Layered Magnetic Structures: Evidence for Antiferromagnetic Coupling," *Phys. Rev. Lett.*, vol. 57, no. 19, pp. 2442–2445, 1986.

[7] S. S. P. Parkin, "Giant Magnetoresistance in Magnetic Nanostructures," *Annu. Rev. Mater. Sci.*, vol. 25, pp. 357–388, 1995.

[8] S. Bhatti, R. Sbiaa, A. Hirohata, H. Ohno, S. Fukami, and S. N. Piramanayagam, "Spintronics based random access memory: a review," *Materials Today*, vol. 20, no. 9. pp. 530–548, Nov-2017.

[9] J. M. D. Coey, *Magnetism and Magnetic Materials.* Cambridge University Press, 2010.

[10] G. S. Abo, Y. K. Hong, J. Park, J. Lee, W. Lee, and B. C. Choi, "Definition of magnetic exchange length," *IEEE Trans. Magn.*, vol. 49, no. 8, pp. 4937–4939, 2013.

[11] H. D. Bush and R. S. Tebble, "The Barkhausen Effect," *Proc. Phys. Soc.*, vol. 60, no. 4, p. 370, 1948.

[12] I. Langmuir and K. J. Sixtus, "Regions of Reversed Magnetization in Strained Wires," *Phys. Rev.*, vol. 38, no. 11, p. 2072, Dec. 1931.

[13] K. J. Sixtus and L. Tonks, "Propagation of Large Barkhausen Discontinuities," *Phys. Rev.*, vol. 37, no. 8, pp. 930–958, Apr. 1931.

[14] A. Hubert and R. Schafer, *Magnetic Domains: The Analysis of Magnetic Microstructures.* Springer, 1998.

[15] L. Néel, "Remarques sur la théorie des propriétés magnétiques des couches minces et des grains fins," *J. Phys. Radium*, vol. 17, pp. 250–255, 1956.

[16] L. Landau and E. Lifshits, "On the Theory of the Dispersion of Magnetic Permeability in Ferromagnetic Bodies," in *Collected Papers of L.D. Landau*, vol. 8, 1965, pp. 101–114.

[17] K. H. Stewart, *Ferromagnetic Domains.* Cambridge University Press, 1954.

[18] P. Anikeeva, G. Beach, and N. Holten-Andersen, "Massachusetts Institute of Technology: MIT OpenCourseWare," *3.024 Electronic, Optical and Magnetic Properties of Materials*, 2013. [Online]. Available: https:ocw.mit.edu.

[19] M. A. Mohammad, M. Muhammad, S. K. Dew, and M. Stepanova, "Fundamentals of electron beam exposure and development," in *Nanofabrication: Techniques and Principles*, Vienna: Springer Vienna, 2012, pp. 11–41.

[20] K. H. J. Buschow and F. R. de Boer, "Soft-Magnetic Materials," in *Physics of Magnetism and Magnetic Materials*, Boston, MA: Springer US, 2003, pp. 147–163.

[21] R. P. Cowburn, "Property variation with shape in magnetic nanoelements," *J. Phys. D. Appl. Phys.*, vol. 33, no. 1, pp. R1–R16, 1999.

[22] R. P. Cowburn, A. O. Adeyeye, and M. E. Welland, "Configurational Anisotropy in Nanomagnets," *Phys. Rev. Lett.*, vol. 81, no. 24, pp. 5414–5417, Dec. 1998.

[23]   R. P. Cowburn, D. K. Koltsov, a. O. Adeyeye, and M. E. Welland, "Single-Domain Circular Nanomagnets," *Phys. Rev. Lett.*, vol. 83, no. 5, pp. 1042–1045, 1999.

[24]   T. Shinjo, "Magnetic Vortex Core Observation in Circular Dots of Permalloy," *Science (80-.).*, vol. 289, no. 5481, pp. 930–932, 2000.

[25]   S. H. Chung, R. D. McMichael, D. T. Pierce, and J. Unguris, "Phase diagram of magnetic nanodisks measured by scanning electron microscopy with polarization analysis," *Phys. Rev. B - Condens. Matter Mater. Phys.*, vol. 81, no. 2, 2010.

[26]   V. Cambel *et al.*, "The influence of shape anisotropy on vortex nucleation in Pacman-like nanomagnets," *J. Magn. Magn. Mater.*, vol. 336, pp. 29–36, Jun. 2013.

[27]   T. Taniuchi, M. Oshima, H. Akinaga, and K. Ono, "Vortex-chirality control in mesoscopic disk magnets observed by photoelectron emission microscopy," *J. Appl. Phys.*, vol. 97, no. 10, pp. 1–4, 2005.

[28]   Q. F. Xiao, J. Rudge, B. C. Choi, Y. K. Hong, and G. Donohoe, "Dynamics of vortex core switching in ferromagnetic nanodisks," *Appl. Phys. Lett.*, vol. 89, no. 26, pp. 1–4, 2006.

[29]   R. P. Cowburn, "Spintronics: Change of direction," *Nat. Mater.*, vol. 6, no. 4, pp. 255–256, 2007.

[30]   R. D. McMichael and M. J. Donahue, "Head to head domain wall structures in thin magnetic strips," *IEEE Trans. Magn.*, vol. 33, no. 5, pp. 4167–4169, 1997.

[31]   R. P. Cowburn, D. a. Allwood, G. Xiong, and M. D. Cooke, "Domain wall injection and propagation in planar Permalloy nanowires," *J. Appl. Phys.*, vol. 91, no. 10 I, pp. 6949–6951, 2002.

[32]   D. A. Allwood, G. Xiong, C. C. Faulkner, D. Atkinson, D. Petit, and R. P. Cowburn, "Magnetic domain-wall logic," *Science (80-.).*, vol. 309, no. 5741, pp. 1688–1692, 2005.

[33]   A. M. Polyakov and A. A. Belavin, "Metastable States of Two-Dimensional Isotropic Ferromagnets," *JETP Lett.*, vol. 22, pp. 245–248, 1975.

[34]   J. Dean *et al.*, "The formation mechanism of 360 domain walls in exchange-biased polycrystalline ferromagnetic films," *J. Appl. Phys.*, vol. 110, no. 7, p. 73901, 2011.

[35]   R. D. McMichael and M. J. Donahue, "Head to head domain wall structures in thin magnetic strips," *IEEE Trans. Magn.*, vol. 33, no. 5, pp. 4167–4169, 1997.

[36]   Y. Nakatani, A. Andre´thiaville, and J. Miltat, "Head-to-head domain walls in soft nano-strips: a refined phase diagram," *J. Magn. Magn. Mater.*, pp. 750–753, 2005.

[37]   M. Kläui, "Head-to-head domain walls in magnetic nanostructures," *J. Phys. Condens. Matter*, vol. 20, no. 31, p. 313001, 2008.

[38]   Y. Nakatani, A. Thiaville, and J. Miltat, "Head-to-head domain walls in soft nano-strips: A refined phase diagram," *J. Magn. Magn. Mater.*, vol. 290-291 PA, pp. 750–753, 2005.

[39]   D. A. Allwood, G. Xiong, M. D. Cooke, and R. P. Cowburn, "Magneto-optical Kerr effect analysis of magnetic nanostructures," *J. Phys. D. Appl. Phys.*, vol. 36, no. 18, pp. 2175–2182, 2003.

[40]   A. O. Adeyeye, J. A. C. Bland, and C. Daboo, "Magnetic properties of arrays of 'holes' in Ni80Fe20films," *Appl. Phys. Lett.*, vol. 70, no. 23, pp. 3164–3166, 1997.

[41]   T. A. Moore, T. J. Hayward, D. H. Y. Tse, J. A. C. Bland, F. J. Castaño, and C. A. Ross, "Stochastic switching in individual micrometre-sized Permalloy rings," *Phys. B Condens. Matter*, vol. 372, no. 1–2, pp. 164–167, 2006.

[42]   J. Ferré, J. Jamet, and P. Meyer, "Magneto-Optical Studies of Magnetic Ultrathin Film Structures," *Phys. Status Solidi*, vol. 175, pp. 213–223, 1999.

[43]   R. P. Cowburn, D. K. Koltsov, A. O. Adeyeye, and M. E. Welland, "Probing submicron nanomagnets by magneto-optics," *Appl. Phys. Lett.*, vol. 73, no. 26, p. 3947, Dec. 1998.

[44]   M. Negotia *et al.*, "Linear transport of domain walls confined to propagating 1-D potential wells," *J.*

Appl. Phys., vol. 114, 2013.

[45]   M. Negoita, T. J. Hayward, and D. A. Allwood, "Controlling domain walls velocities in ferromagnetic ring-shaped nanowires," *Appl. Phys. Lett.*, vol. 100, no. 7, p. 072405, 2012.

[46]   K. Omari *et al.*, "Ballistic rectification of vortex domain wall chirality at nanowire corners," *Appl. Phys. Lett.*, vol. 107, no. 22, p. 222403, Nov. 2015.

[47]   Q. A. Abbas and N. A. Morley, "Fabrication and characterization of magnetostrictive amorphous FeGaSiB thin films," *J. Magn. Magn. Mater.*, vol. 439, pp. 353–357, Oct. 2017.

[48]   I. Polenciuc *et al.*, "Domain wall pinning for racetrack memory using exchange bias," *2015 IEEE Int. Magn. Conf. INTERMAG 2015*, vol. 162406, no. October, 2015.

[49]   U. Bauer, S. Emori, and G. S. D. Beach, "Voltage-controlled domain wall traps in ferromagnetic nanowires," *Nat. Nanotechnol.*, vol. 8, no. 6, pp. 411–416, 2013.

[50]   M. Negoita, T. J. Hayward, J. A. Miller, and D. A. Allwood, "Domain walls in ring-shaped nanowires under rotating applied fields," *J. Appl. Phys.*, vol. 114, no. 1, p. 013904, 2013.

Chapter 3 – Literature Review

3.0 Introduction

For the research undertaken in this thesis, a greater understanding of the state of the art and historical context in several topics is required in order to appreciate the context and themes around the results. These are artificial spin ice systems, ferromagnetic nanorings and neuromorphic computing techniques, including reservoir computing.

3.1 Applications of Magnetic Nanostructures

3.1.1 Magnetic nanodevices

The use of nanostructures and domain phenomena for functionality is a key driver in magnetic materials research. Magnetic recording media are commonplace – the use of the giant magnetoresistive effect for reading hard disk drives has enabled their widespread use in commercial computing. Here, a spin valve [1] has a layer of ferromagnetic Ni-Fe free to orient to stray field from the recording media. The free layer is part of a multi-layer stack of materials, which has a resistance that is a strong function of the free layer orientation. Magnetic recording devices use patterned media with bits comprised of individual magnetic elements such as dots or islands where in the orientation of the magnetic dipole moment or the chirality of the magnetic vortex are assigned a digital 1 or digital 0 [2], [3]. Experiments have shown that vortex chirality and the central magnetic dipole moment can be combined to increase the information density per bit and is a common advantage of magnetic nanodots for storage [4], [5]. By the latter, it is meant that the polarity of the out-of-plane component is also a measurable quantity with which various attempt have been made to harness functionality [6]–[11].

Propagating domain walls have also been used as information carriers. As far back as 2000 [12], DW-based magnetic random access memory (MRAM) devices were proposed in which geometrically-defined traps were used to specify the stable positions for a single memory cell. However, this work purely used micromagnetic models of materials at 0 K and did not consider the effects of thermal perturbations.

DW propagation through extended nanowire circuits has allowed magnetic DW logic [13] and magnetic racetrack memory [14] to be developed.

Magnetic DW logic circuits, as with conventional electronic devices, perform Boolean logic operations with magnetic DWs instead of electronic charge by driving them through various wire junctions with an in-plane rotating magnetic field. Logical "1" and "0" are represented by opposite magnetisation within nanowires. NOT, AND, fan out (splitting of DWs to create duplicates in multiple nanowires) and crossover of wires (to allow DWs to cross perpendicular wires) were replicated from CMOS architectures using magnetic nanowire arrangements. Fig. 3.1a) shows a focussed ion beam image from this work of these four elements and Fig 3.1b) shows MOKE traces at locations indicated by asterix (traces II and III are inferred from trace I) when the circuit is subject to a global counterclockwise rotating applied field, demonstrating the correct required output. The outlook for magnetic DW logic was a simplification of CMOS-based logic operations by reduction in the number of elements and potential advantages in power consumption. A limiting factor with the operation of logic circuits was the extent of in-plane field-space that gave correct operation [15].
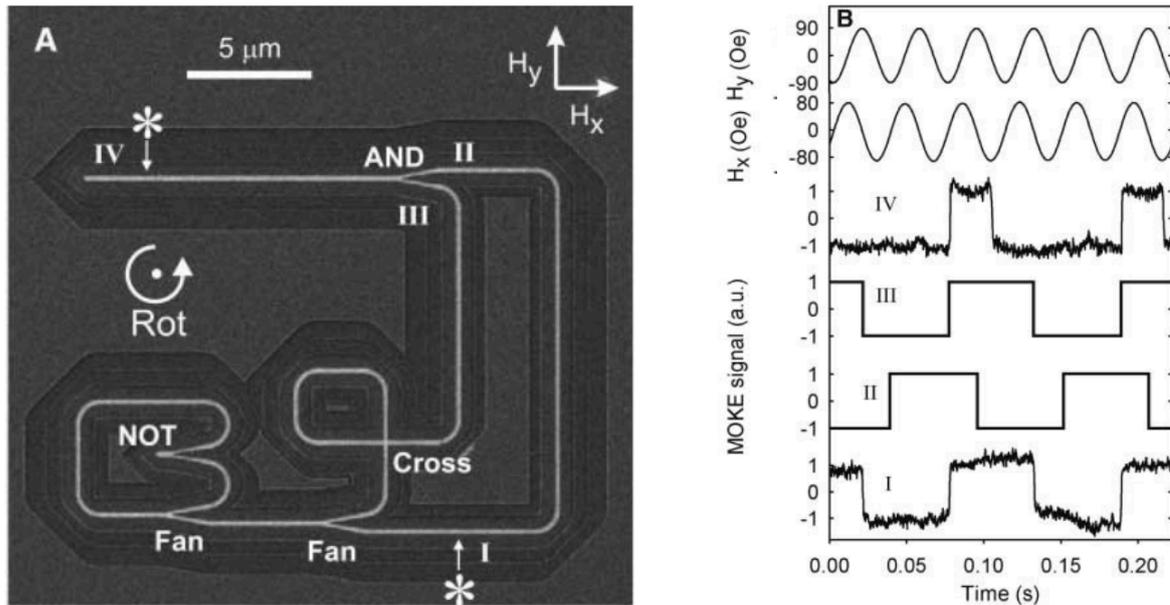
Figure 3.1. (a) Focussed ion beam image of a magnetic DW logic circuit comprising NOT gate, AND gate, fan-out and cross over elements. 'Rot' refers to the direction of externally applied field. Asterix mark where MOKE measurements were taken. Light areas denote ferromagnetic material (darkened regions are a by-product of fabrication). (b) Externally applied elliptical field traces and MOKE traces as-measured and as-inferred by MOKE. From [13].

Racetrack memory, in contrast, uses streams of DWs in single nanowires to represent digital information. First proposed by Stuart Parkin *et al.* in 2008 [14], magnetic nanowires also used regions of opposing magnetisation as bits that corresponded to logical "0" or "1." These would be propagated along nanowires (or the 'racetrack') by a spin-polarised current with bits read/written as they passed a magnetic tunnel junction [16]. The proposed design could enable ultra-high density storage by using a 3D, columnar series of racetracks. DWs are separated by geometrical constrictions, or notches, within the racetrack that prevent annihilation and loss of data and also define the bit length. Fundamentally, the device is a shift register with the train of bits moved back and forth to read/write the region of interest.

Both of these technologies suffered from the thermally driven stochasticity that will occur when a DW is de-pinned from the geometrical features used to control DW motion in the nanowire [17], [18]. If the de-pinning process cannot be reliably and repeatably controlled, the functionality of these devices is severely limited. The next section explores these pinning and de-pinning phenomena.

3.1.4 Domain wall pinning and de-pinning in nanostructures

In nanowires, DW propagation can be halted and controlled by local geometric defects that form an energy barrier to inhibit motion. Faulkner et al. [19] in 2004 used notches deliberately fabricated in the edge profiles of wires as defects to trap DWs and showed the field required to continue DW motion increased with depth of the notch (Fig. 3.2).
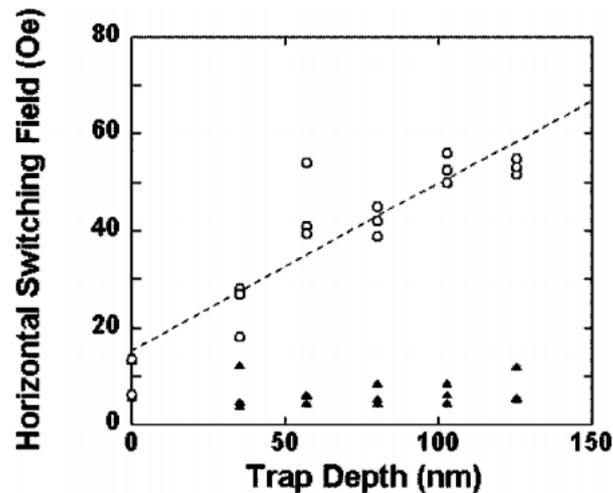
Figure 3.2. Plot of horizontal switching field before (black triangle) and after (open circle) DWs interact with notches in a Permalloy nanowire measured with MOKE microscopy. Line added as a guide for the eye. Taken from [19]

Micromagnetic modelling on constrictions in ferromagnetic nanorings was also carried out by Kläui [20] and then followed up experimentally with magnetoresistance measurements to show fields at which 'depinning' occurs (when motion resumes). Direct observation using magnetic transmission x-ray microscopy (MTXM) beamline based magnetic imaging [18] of DW depinning from notches showed it to occur over a range of de-pinning fields for any wire and notch geometry, which showed that the process is stochastic. Later studies found the complexity of DW motion, including the Walker breakdown process [21], [22] that changes the DW structure dynamically, and the de-pinning process induced multi-mode depinning distributions [17], [23], [24]. The stochasticity of DW depinning has been argued by Hayward to be intrinsic to DW motion in a nanowire [25], and the distribution of de-pinning fields or current densities required to propagate a DW past an energy barrier presents a significant challenge to their use in digital information devices. There have been many attempts to overcome the effects of stochastic depinning. These include: rectification using curved geometries

[26]–[28] that force a chirality based on the handedness of the curve; rare-earth doping to increase the magnetic damping of a material and so supress the complex Walker breakdown phenomenon that contributes to stochasticity (Fig. 3.3) [29]; or other lithographic based techniques such as a comb-like structure [30] that interrupts the Walker breakdown process part-way through and thus prevents transformation of the DW into a different structure.
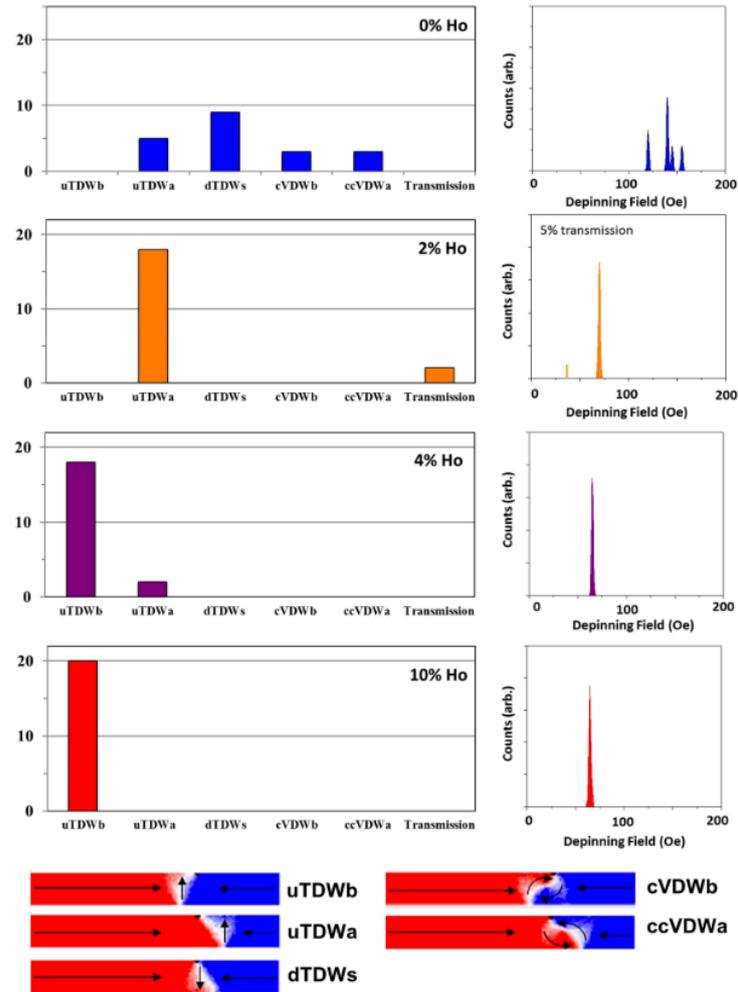
Figure 3.3. Plots of DW types pinned at an 18nm depth notch in Permalloy nanowires with length 1.5µm, width 100nm, thickness 20nm at various levels of Ho doping in 20 randomly seeded simulations (left). De-pinning field distributions of applied field required to continue DW propagation (right). Simulated structures of DW types reported. The stochasticity of de-pinning and multi-modal DW types found at 0% Ho are stabilised by RE doping. Taken from [29].

3.1.5 Ferromagnetic Nanorings

The ferromagnetic nanoring is a special case of a nanowire as it has no free wire ends. The lowest energy magnetic dipole configurations are the so-called 'onion' with two domains and two DWs separated by half of the ring length, and the 'vortex' state which is single domain and flux closed. These are shown schematically in Fig. 3.4.
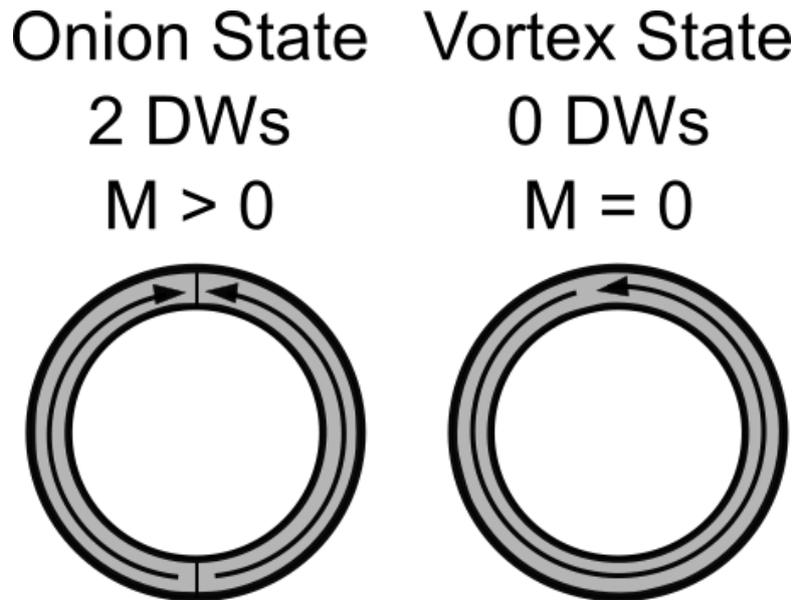
Figure 3.4 - Schematic of ferromagnetic nanorings in (left) onion state and (right) vortex state. An onion state ring has two walls separating domains whereas the vortex state has a single domain with dipole moments aligned with the geometry of the ring.

As the two domains in the onion state are not-flux closed, rings in this configuration will have an observable magnetisation. The vortex ring is flux closed, leading to no observable magnetisation and no sensitivity to imaging methods sensitive to out of plane magnetisation such as magnetic force microscopy (MFM). Compared to the vortex nanodisk, the vortex nanoring is much more stable from the lack of a vortex core [31].

Hysteresis loops of magnetic nanorings general are geometrically dependent, and examples are shown in Fig. 3.5. Single step switching is between onion and reverse onion as the internal magnetic dipole alignment switches with a reverse saturating field. Double switching transforms from onion to vortex to reverse vortex. The vortex state is accessed during reversal by displacement of one DW across half the ring, annihilating the other DW. Rings in the vortex state are switched to the reverse onion state by

nucleation of DWs in the half domain opposing the applied field [32]. Note the comparison to the vortex state minor loop obtained in Fig 2.6.
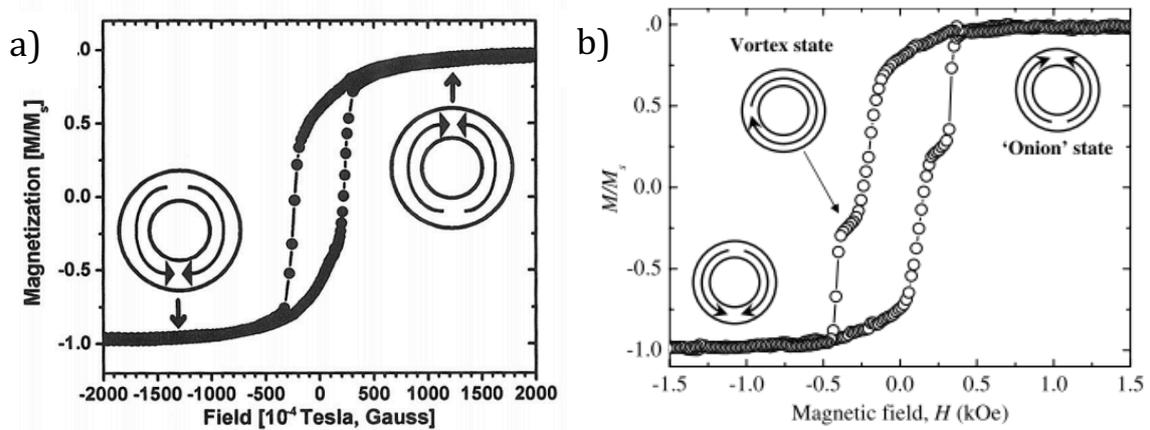
Figure 3.5. (a) Magnetic hysteresis loop obtained via MOKE showing single step switching in an array of Co nanorings 1.7μm in diameter, 225nm track width, 4nm thickness. Taken from [33]**. (b) Magnetic hysteresis loop taken from an array of Co nanorings 1.65μm in diameter, 350nm track width, 16nm thickness showing double switching as a reversal field is applied. Taken from** [34]**.**

The onion-to-vortex switching process can be visualised with micromagnetic modelling, such as performed by Lopez-Diaz *et al.* [35] (shown in Fig. 3.6). Here, an asymmetric ring was used to change the energetics of interaction with DWs in the onion state and confining one wall to one side of the ring. With one wall pinned, the other wall was driven around the perimeter by a reverse field until it came into close interaction and annihilated both walls.
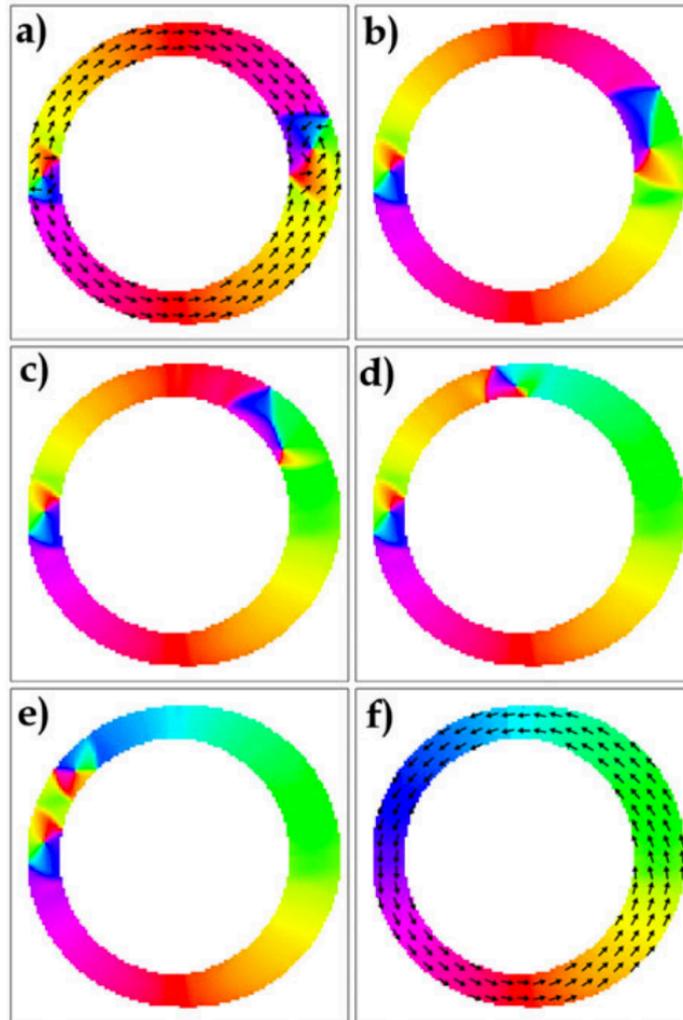
Figure 3.6. Micromagnetic simulation of onion-to-vortex switching in an asymmetric ferromagnetic Co nanoring. Ring diameter is 1.6μm with internal diameter of 1.3μm, thickness of 34nm.(a) and (f) are equilibrium states of onion and vortex respectively. (b)-(e) are stills taken during switching showing one DW pinned in the narrower constricted side of the nanoring. Taken from colour image in [36]**, originally reported in** [35]**.**

Vortex-to-onion switching was also micromagnetically simulated in another work by the same authors, where at a critical field, nucleation of a reverse domain occurred at the point of opposite magnetisation to the applied field [36]. Two DWs were created which propagated around the perimeter of the ring as the reverse domain grew. Once the reverse domain grew to consume the half of the vortex that was aligned opposite to the applied field, the ring became configured in an onion state as the two DWs formed an interface with the remaining half of the ring (that was already aligned with the applied field).

Scanning electron microscopy with polarisation analysis (SEMPA) [37] and photoemission electron microscopy magnetic imaging methods directly showed VDWs

in wider track width nanorings and TDWs in thinner tracks mirroring predictions earlier in straight nanowires [38].

DW motion in ferromagnetic nanorings has been studied for functionality in transporting ultra-cold atoms by the influence of stray field of a mobile DW [39] and by use of in-plane rotating fields [40], [41]. In the latter, DWs were pinned in rings at potential wells defined by the geometry of the ring and the direction of applied field. One relevant result from this work was the identification of DW motion in a nanoring as a progression of pinning/depinning or 'hopping' events, likely from fabrication defects. Significant defects are likely to impede DW motion, which was observed as a lag in the motion of DWs relative to the direction of an in-plane rotating magnetic field. DWs follow the sense of a rotating applied field provided the frequency is below some critical value and field strength sufficiently high.

Systems of interconnected nanorings have been studied previously [42], [43] observing magnetisation states and reversal processes with micromagnetic modelling as well as experimentally with focussed MOKE and magnetoresistance measurement.

3.2 Dynamics of Domain Walls

The constraints on magnetic energy terms imposed by nanostructure geometry add a level of complexity to the dynamics of domain movement compared with in bulk materials. For motion driven by external fields, as used in this thesis, the increase in Zeeman energy from the applied field increases the size of domains lying parallel to the field. The advancing interface of this domain is the domain wall, which as an entity in itself can be considered as the moving part.

Domain formation is a non-continuous process - a fine resolution view of a hysteresis loop would see steps arising from Barkhausen jumps [44]. The dynamics of magnetisation are therefore critical to understanding processes such as magnetisation reversal. Whilst this thesis does not concern itself with areas of nanoscale magnetics such as ferromagnetic resonance, it does lean heavily on micromagnetic modelling.

To minimise the Zeeman energy in a magnetic material, its moments attempt to align parallel to an applied field. The electron orbiting each moment has an angular momentum which acts against this change. There is therefore a torque acting upon the moment. To describe the response of magnetisation to these torques, the LLG equation was developed [45], [46].

A partial explanation follows, but reviews of the formulation provide greater detail [47], [48].

For a ferromagnet, the precession of the electron around the moment in a uniformly magnetised sample with an applied field, H, is described by the Landau-Lifshitz equation:

$$\frac{d\boldsymbol{M}}{dt} = -\gamma\boldsymbol{M} \times \boldsymbol{H}_{eff} \qquad\qquad Equation\ 3.1$$

Where $\boldsymbol{H}_{eff}$ is a combination of applied field, demagnetising field and other quantum mechanical considerations. γ is the electrons gyromagnetic ratio.

The Landau-Lifshitz description of dynamic equations for magnetisation and spin included a consideration of relativistic interactions as a damping term, such that equation 3.1 becomes:

$$\frac{d\boldsymbol{M}}{dt} = -\gamma\boldsymbol{M} \times \boldsymbol{H}_{eff} - \lambda\boldsymbol{M} \times (\boldsymbol{M} \times \boldsymbol{H}_{eff}) \qquad\qquad Equation\ 3.2$$

Where is λ is a damping term that is often rewritten as $\alpha\gamma M_s$ where α is a dimensionless constant, the damping constant. This is particularly relevant for micromagnetic simulation topics and the addition of extra terms accounts for relaxation to equilibrium.

A more useful form of this was proposed by Gilbert , which can be arranged in the following form as a function of α:

$$\frac{d\boldsymbol{M}}{dt} = -\gamma'\boldsymbol{M} \times \boldsymbol{H}_{eff} + \frac{\alpha}{M_s}(\boldsymbol{M} \times \frac{d\boldsymbol{M}}{dt}) \qquad\qquad Equation\ 3.3$$

where γ' is a transformation of γ to to describe precessional motion (as outlined in [47], [48]).

Micromagnetic modelling used in the thesis is based upon solving the LLG equation in discretised cells in order to predict magnetisation dynamics. The damping constant α

has a strong influence on the pathway to equilibrium and the computational processing time.

3.3 Artificial Spin Ices

Artificial Spin Ice (ASI) research is a topic of broad and current interest in magnetics [49]–[64], primarily driven by investigation into frustrated systems, which are found throughout nature. Frustration means that all interactions that move the system towards a ground state cannot be simultaneously satisfied, leading to degeneracy in energy states. Simple water ice is an example of such a system wherein the long-range ordering of oxygen forces disorder in the positioning of hydrogen atoms. Bernal-Fowler ice rules [65] mean that in the tetrahedra of oxygen ions, two hydrogen atoms will sit closer to the central oxygen ions than the other two. This difference in O-H bond lengths gives degeneracy of states in water ice (Fig. 3.7).
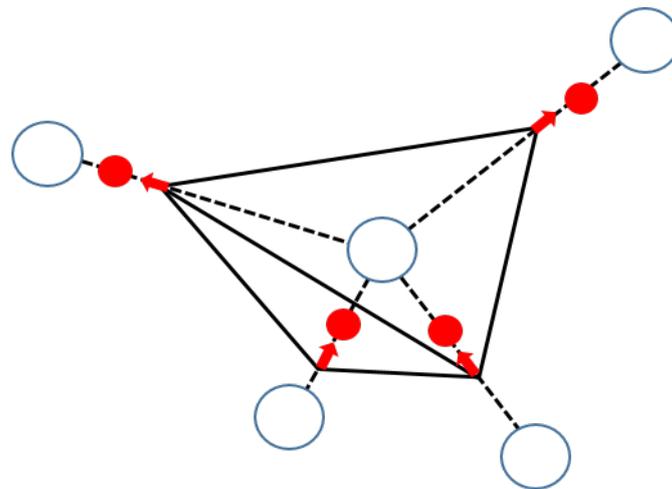
Figure 3.7. Arrangement of oxygen and hydrogen atoms in water ice showing inequivalence in O-H bond lengths as two H atoms are closer to the central oxygen atom and two are further away (red arrows).

This is an example of frustration by geometry, and a similar mechanism leads to disorder and frustration in magnetic materials such as holmium titanate ($Ho_2Ti_2O_7$) [66]. Here, antiferromagnetic ordering of spins at vertices of tetrahedra formed by the lattice of rare earth ions leads to the only possibility of a two in state A/two in state B formation at low temperatures. These two in, two out macroscopically degenerate states being so similar to water ice gives rise to the term 'spin ice' for materials of this

nature. Arrangements of dipoles in the superstructure of spin ice pyrochlores (of which $Ho_2Ti_2O_7$ is an example) gives a magnetic monopole-like behaviour as well as the appearance of Dirac strings (the idea of continuous 'strings' of magnetic flux between North and South monopoles) [67]–[69]. The idea of monopolar-like behaviour arises not from there being discrete, measurable particles with net magnetic charge but simply the treatment for convenience of either end of a magnetic dipole as a monopole. Castelnovo *et al.* [67] demonstrated that spin ice networks that have adjacent tetrahedra obeying the ice rule will have a net magnetic charge at the termini of the 'string' of dipoles in tetrahedra that are formed to obey the ice rule. The dipoles are inverted between tetrahedra at termini relative to those in the bulk of the string. These strings of inverted dipoles are termed 'Dirac strings' after the physicist who imagined monopoles as strings that carried magnetic flux [68].

Advances in lithographic techniques and the scales at which magnetic nanostructures can be created allow frustration to be forced. Ferromagnetic islands of a suitable aspect ratio are able to produce single domain Ising-like moments [49] by their shape anisotropy. These can then be fabricated into a regular lattice with vertices defined at the meeting point between adjacent islands [49]. Superstructures like these are termed 'artificial' spin ices (ASI) and can be visualised with magnetic imaging techniques.

Early ASI investigations took place on a square arrangement of islands (islands are oriented on orthogonal planes, see Fig. 3.8) made from thin films of $Ni_{81}Fe_{19}$. At any vertex of four islands the lowest energy is achieved when adjacent islands have two dipoles pointing in and two pointing out [49]. An external driving energy such as a magnetic field was applied to different square arrays of varying lattice parameters and the resulting distribution of dipoles investigated with MFM. Here, it was observed that a distribution of vertex types was obtained in a given area, not just the low-energy two-in, two-out. The full range of possible vertex types ($2^4 = 16$ variants) were categorised along with a basic overview of an ordered square lattice of aforementioned two-in, two-out or "type 2" vertices in Fig. 3.9.
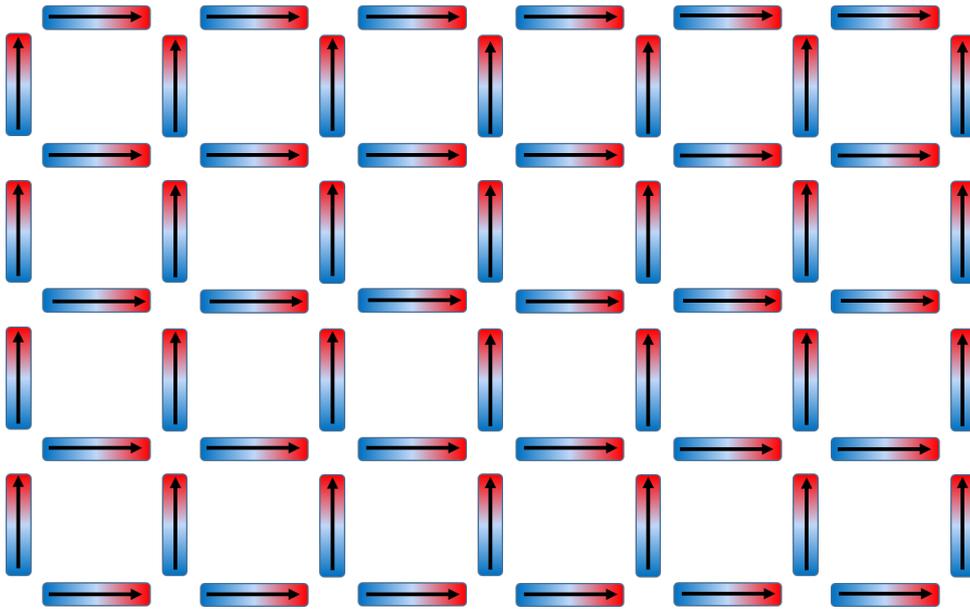
Figure 3.8 – A lithographically defined ASI of rectangular ferromagnetic islands. An ASI must have islands with aspect ratios that force only two discrete dipole directions. The arrangement of islands around vertices in this figure lead to a square artificial spin ice. Other ASI types include the honeycomb or Kagome lattie that have three islands arranged on 120° axes.
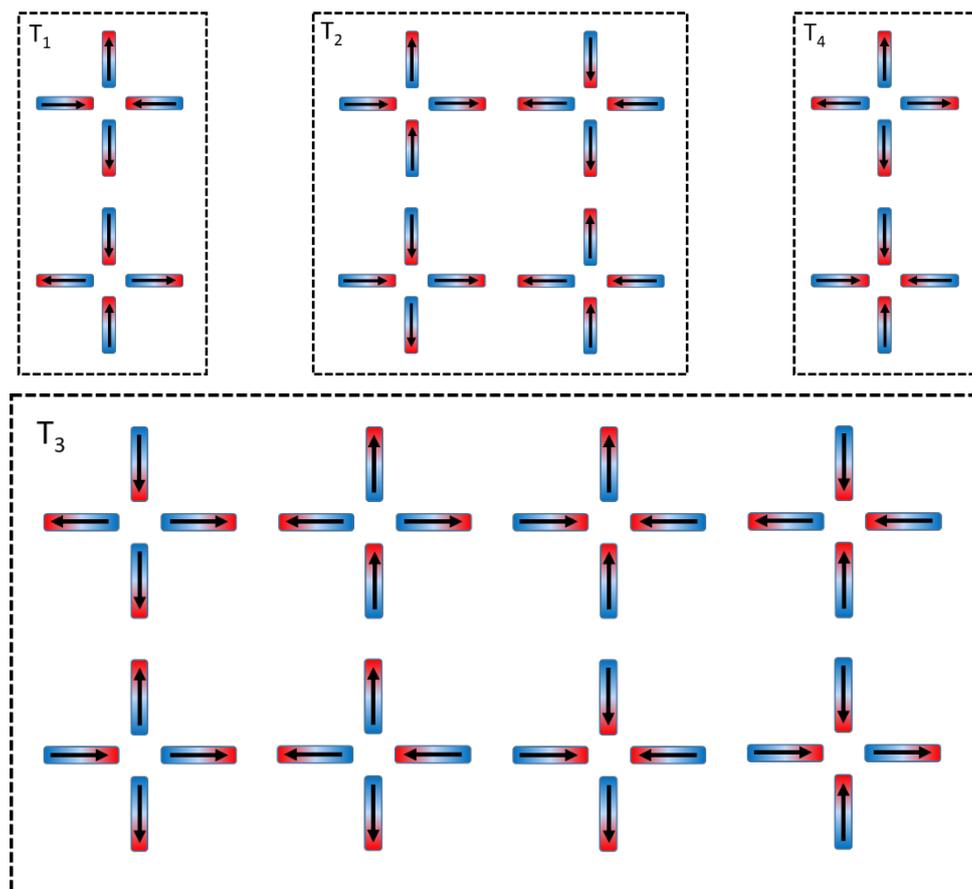
Figure 3.9 – Possible configurations of dipoles at vertices in a square ASI. These 16 configurations are grouped into four types - type 1 (T1), type 2 (T2)… etc.

Favourable alignments of spin pairs are head to tail along the same direction or head to tail on adjacent islands (e.g. top and right islands) and unfavourable pairs are tail to tail along the same directions (i.e. opposite poles next to one another). There are some vertex types that are therefore frustrated as they exhibit unfavourable pairings but are still in an ordered antiferromagnetic ground state from lack of degeneracy. Type 1 and 2 satisfy two-in, two-out rules though type 1 benefits from lower ground state energy from symmetry and there is no net 'magnetic charge.' Type 3 vertices have a net magnetic charge of +2 from three in, one out (or -2 from three out, one in) and type 4 vertices have a magnetic charge of +4 (or -4).

It should be noted that for square ice, the centre dipole-dipole spacing between opposite and adjacent islands is not constant, as depicted in Fig. 3.10. This difference

affects the energy of various states with the same number of in/out domains but in different configurations.
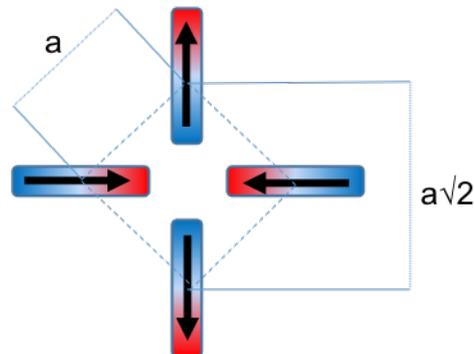
Figure 3.10 – Schematic of a type 1 vertex highlighting the asymmetry of dipole-dipole centerpoint spacing in different orthogonal axes.

Another commonly studied ASI structure is the Kagome ASI (or honeycomb of connected ferromagnetic wires following the same principles) which has three islands meeting at each vertex [70], [71]. Frustration in this configuration comes from 'pseudo-ice' rules where possible moment configurations are three in/out or two in, one out or two out, one in. The dipole-dipole spacing is constant, which means that all two-in/on-out (and two-out/one-in) configurations are degenerate.

An exciting avenue of study that ASIs has been in fundamental thermodynamics [54], [59], [60], [62], [72], [73]. The vast number of macrostates that a large array of vertices can fall into are time and temperature dependent functions that depend not only of interactions between islands but also on geometric parameters and external inputs [74]–[76]. For example, Gilbert et al. demonstrated through modelling a strong link between vertex type prevalence and island spacing in a square ASI [75] (Fig. 3.11). This showed that the lowest energy (Type 1) configurations were strongly preferred with low lattice spacing, i.e. when the coupling between islands was strong, but that this preference disappeared with more widely spaced (and weakly coupled) islands.

Figure 3.11. Figure from Gilbert et al [75] depicting vertex fractions dependence on lattice spacing in a square lattice. The system converges to ground state (type I) as lattice spacing decreases as island-island interactions begin to dominate.

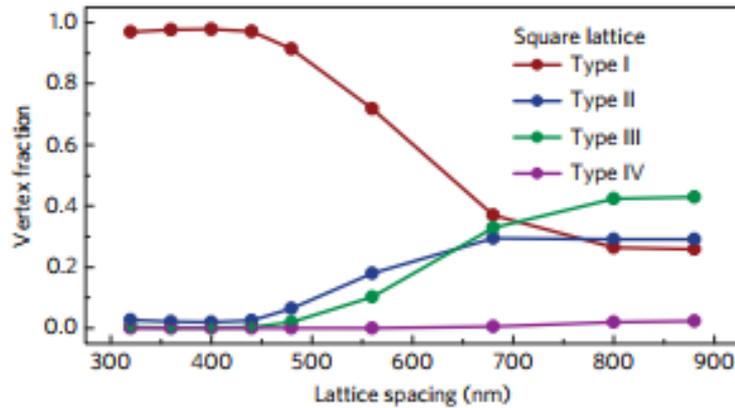Access to light source beamline techniques such as PEEM allows magnetic configurations such as island dipole configurations to be visualised. Mengotti *et al.* [57] were among the first to perform extensive studies of ASIs, in this case of Kagome type, using PEEM. Here, the degeneracy of available states in six island hexagons (six islands with two dipole directions gives $2^6 = 64$ possible states) were mapped and grouped according to energy levels. Experimentally, single Kagome rings demagnetised states are dictated by lattice parameters affecting coupling strength (i.e. island separation); when this coupling strength was high, 'vortex' rings (where dipoles formed a head-tail-head or tail-head-tail chain) were nearly always observed and when coupling strengths are low, vortices were almost always absent. Type 4-2 and 3-3 (the latter termed 'onion' with two chains of opposing head – tail chains) configurations were found in the latter case instead. At these low coupling strengths, the frequency of occurrence (which should be random) should be equal to the degree of degeneracy divided by total number of states. PEEM found that the occurrence of 4-2 and 3-3 states is significantly higher than random.

As additional six-island Kagome rings were added (introducing three-island vertices) the experimental observation of low energy states dropped from 94±2% to 48±8% to 31±6% after an experimental protocol of a rotation in an in-plane field followed by demagnetisation. The additional constraints introduced by neighbouring rings forming

three-island vertices restricted the ability of a Kagome ring to configure into a low energy state.

Whilst PEEM is an excellent tool for producing high resolution images of ASI structures, MFM is a more economical method to produce similar results [58], [73], [77], [78]. Schumann *et al* [58] is one such study on an extensive network of kagome rings (or honeycomb after its visual appearance), using the contrast to identify different orientations of dipoles. As previously mentioned, the kagome network has equal charge separation at vertices between three adjacent islands. Studying these images allows for categorisation of vertices much like for square ices in Fig. 3.9. Following Castelnova's [67] magnetic dipole charge as a concept to categorise vertices, a vertex satisfying the ice rule will have a charge of $\pm q$ whereas those that violate it will have charge of $\pm 3q$ (for vertices with three dipoles pointing in/out). In the honeycomb saturated parallel to a sublattice axis, dipoles are oriented in one direction with alternating $+q$ and $-q$ charges at adjacent vertices. If one dipole is flipped it will now have at its $+q$ vertex a $+3q$ charge and a $-3q$ charge at its $-q$ vertex. This can cause a domino-like cascade of dipole flipping along subsequent vertices to form a Dirac string between the effective monopole-antimonopole pair created from the ± 2 charge change at the ends of the chain. An example of directly imaged Dirac string formation in an ASI is shown in Fig. 3.12.

Observing honeycomb remanent states in this study found an abundance of type-2 ($\pm q$) vertices, with type-1 ($\pm 3q$) becoming more prevalent for larger island separations (showing an effect of coupling on vertex populations). Domains could be visually identified, with a clear change in the orientation axis of $+q$ and $-q$ vertices around the hexagon created by islands. As is common in various fields of materials science, for example atomic mismatch in metals, a defect can cause the misorientation that leads to a new grain/region/domain. Domain formation should be observed in other ASI systems when the symmetry of the ordered, saturated system is broken by defects such as a different vertex type. Indeed, domain formation is explored by Budrikis *et al*. [79] finding a domain boundary formed from a chain of type-2 vertices enabling growth and reduction of domains of type-I vertices (as calculated by Monte Carlo simulations).
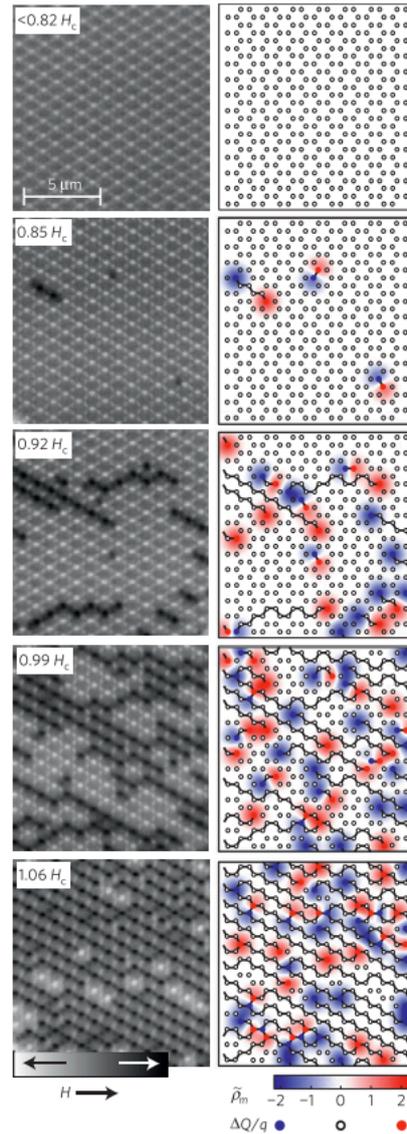
Figure 3.12. (Left) XMCD imaging of Dirac string formation as a reversal field is applied in steps to a Kagome ASI network. (Right) Associated charge map showing monopole-antimonopole creation and propagation in forming Dirac strings. Taken from [69]

Returning to Schumann *et al* [58], when observing the honeycomb at the coercive field, the more frustrated type-I vertex became more prevalent with the authors reasoning this being due to the difference in switching fields/mechanism between angled and horizontal dipoles at the coercive field. This was reinforced by a difference in abundance observed with field applied to coercivity along the hard axis. Visually, this abundance of type-I vertices produced alternating $\pm 3q$ charges leading, ironically, to a high degree of order from the most frustrated state. In fact, this charge ordering was observed to remain with the removal of the field, and also tended to form domains of

coupled type-I vertices. Monte Carlo simulations reproduced the observed abundance of type-I vertices at coercive fields and found good agreement with experimental results when looking at microscopic dipole interactions to identify a difference in switching between angled/horizontal bars.

Honeycomb systems with connected vertices (i.e. connected wires) have also been studied widely [61], [62], [80]. In these systems, DWs propagate during magnetisation reversal and act as effective 'charge carriers.' With sufficiently strong applied fields, a DW emitted from one vertex and across a link can trigger the emission of another DW/charge carrier from the receiving vertex. This makes possible avalanche-like behaviour of reversal until emission is terminated with an unbalanced magnetic charge or an emergent magnetic monopole (e.g. [78], [81]). These are Dirac strings as mentioned above in magnetostatic systems and are studied at length in the literature in natural and artificial spin ices [57], [68], [82], [83]. Whilst this Dirac-string behaviour is not exclusive to connected systems it is of note for this thesis that it is enabled through the interaction of domain walls/magnetic charge carriers moving through a connected lattice.

The thermalisation of ASIs is extensively studied to investigate statistical thermodynamics of these systems (e.g. [54], [55], [59], [64], [72], [84]–[86]). Whilst spin ices are effectively athermal in that thermal reversal at room temperature is many orders of magnitude lower than energy scales of each elements own shape anisotropy and also magnetostatic coupling between elements, they can still obey an effective thermodynamics – with effective temperature [86] and entropy [87], [88] definable. Morgan *et al.* [59] found ground state ordering could be induced from a frustrated state at room temperature and without explicit thermalisation or an applied magnetic field, leading to the conclusion through this and reinforced in subsequent studies [50] that thermal annealing in the fabrication of arrays can lead to observable ground state ordering.

It can be reasonably argued, as relevant to this thesis, that traditional systems of discrete ferromagnetic islands cannot change their macrostate without a thermal anneal or an applied magnetic field, and the true ground state cannot be obtained. The degree of ordering following this is dependent on geometrical factors such as size, shape, thickness, arrangement as well as inherent material properties.

Recent advances into forcing an ordered ground state include work by Gartside et al. [89], where the ferromagnetic tip of an MFM was used to flip the orientation of a single island within a sub unit of the Kagome lattice to produce a true ground state. This was previously extremely unlikely to be accessible by relaxation after thermalisation, given the competition across the entire array to minimise energy at every vertex.

3.4 Neuromorphic/Nonlinear Computing

With ever more impressive advances in computational power from innovations in hardware. One popular benchmark for supercomputers is their ability to learn to defeat the best humans at games with unfathomably large complexities in terms of possible moves – for example chess and Go.

The benchmark of beating a human, or rather the best humans, at these games is notable as it highlights the brain as an incredibly complex but effective processing unit. A unit that can be powered on Mars bars utilises a network of neurons to process data, motion, emotion, sensation and much more.

Gordon Moore's observed in 1965 that the number of transistors per given area on an integrated circuit had doubled every 18 months, and this trend continued since, albeit with a slight slowdown recently [90]–[92]. Impressive advances in miniaturisation have led to smaller and smaller transistors (on the order of 10^{-8} – 10^{-9} m) but increasingly architectural shifts in the approach to building computers was required and will be required to maintain the progress in processing power for computers (e.g hyperthreading, parallel processing on multiple cores, hyperscaling). This is primarily to overcome overheating and high-power consumption of CMOS component/transistors as they get smaller.

The brain is already an interconnected system capable of parallelism. Systems like this can have high processing speed for a minimal energy cost and are capable of easily tackling problems such as facial recognition or speech analysis that conventional computers struggle with (e.g. [93]–[95]).

A conventional computer has a central processor that reads instructions or data from a memory location. Instructions are used to perform a computation of data and then save the output to another memory location. This is a highly linear and sequential approach.

A conventional computer has a central processor that reads instructions or data from a memory location. Instructions are used to perform computation on the (digital) data and then save the (digital) output to another memory location [96]. This is a highly linear and sequential approach. This works well for many problems, particularly numerical calculations, but struggles to contend with more complex situations that the human brain performs with ease [97].

The state of the art in machine learning includes approaches such as artificial neural networks (ANN) [98]. These are a sequence of computational layers with weighted connections between nodes. These nodes are analogous to biological neurons and the weighted connection is similar to the strength of synapses. Adjusting the weight of each connection allows control of connectivity to be made, much as a synapse determines whether an inhibitory/excitatory neural contact is made [98]. The architecture of this is shown in Fig. 3.13.
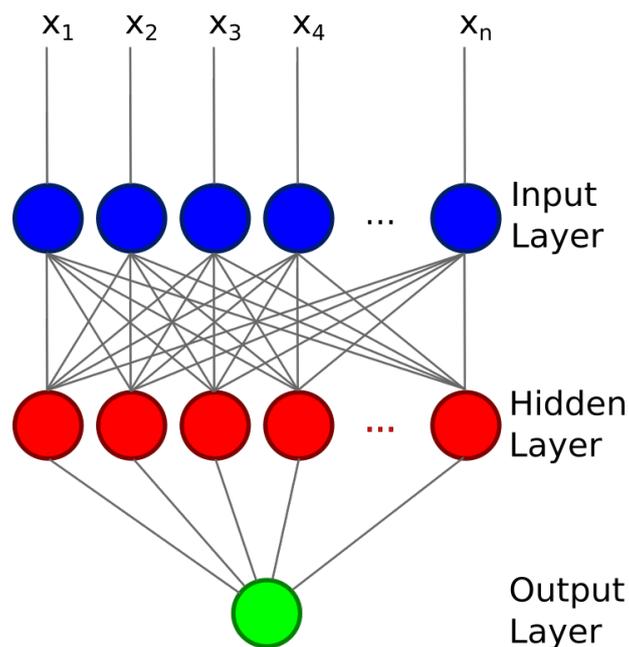
Figure 3.13. Diagram of an artificial neural network showing interconnectivity of hidden layer to the inputs, x_n. Connections can be weighted such that the function read out at the output layer is $\Sigma x_i . w_i$.

However, the sequential nature of these simple ANNs is still a bottleneck to performance compared to the parallelism of the brain.

One approach towards developing ANNs that is inspired by biological architectures is outsourcing computation to an interconnected, recurrent ANN with fixed weight connections. Data is fed in through an input later and classification of the computation

layer is performed with an adjustable output layer to read out a result. This approach is known as reservoir computing (RC) [99]–[102].
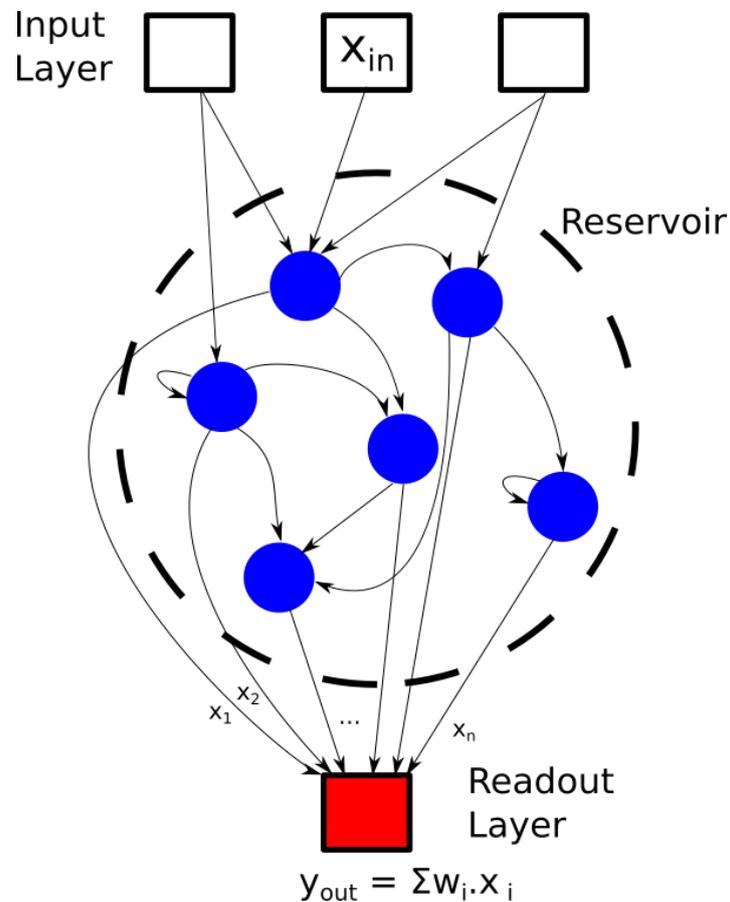
Figure 3.14. Diagram of a layout of a reservoir computer. This comprises an Input layer, a reservoir - with random fixed and weighted (wᵢ) connections between nodes, and one-dimensional output layer. Adapted from [99]**.**

An RC is not like a conventional computer in that there is no central processor and does not process linearly. Figure 3.14 shows the architecture of an RC. It consists of an input layer, the reservoir and an output layer. Information is fed in according to a (k x N) connectivity matrix, W_{in}, where k is the number of input connections and N the number of nodes. Nodes are internally connected in the reservoir by another (N x N) matrix W_{int}. W_{out} determines weighting between the reservoir and readout layer nodes. By randomly distributing connections, W_{in} and W_{int} both remain constant in time [103] and only the output weighting W_{out} will affect the readout – a linear transformation of the reservoir output. Randomly distributing inputs and connections creates multiple non-linear transformations of the same input. The linear transformation at the readout

can then approximate the functional relationship for the desired computational output [99], for example with a linear regression. This is also known as training the output.

Being randomly distributed, some connections in the reservoir are recurrent (hence RC is a type of recurrent neural network). Recurrence forms loops within the reservoir such that the current state depends on previous states. The significance of an input recedes over time, to create a feature of RC known as 'fading memory' [104].

Good reservoirs achieve high dimensionality by this response to both new and previous inputs. The form of the reservoir itself is unimportant so long as it is nonlinear and offers dynamic tuneability in response to external parameters [105]. Such requirements mean that a simple bucket of water can prove the principle of RC [106].

The simplicity of training the output in RC is a major advantage of RC compared to standard RNNs, drastically reducing computation time/cost and therefore power consumption.

There are several approaches that have been explored in the literature towards realising hardware implementations for RC. These include optoelectronic approaches for classification, prediction and system modelling such as nonlinear channel equalisation (removal of distortion in a signal) and speech recognition [103], [107] and radar signal error forecasting [108]. Memristor arrays have been used to great effect for image recognition by separating an input signal into segments and separately transforming outputs in each memristor. The array of memristors is behaving as a reservoir and the output current signals summed to give the state of the reservoir [109]. Similar memristor approaches have also been used for epileptic seizure detection [110]. These applications demonstrate the applicability of RC for machine learning based applications, so similar requirements such as cryptography, financial modelling, translation, bird call classification, rainfall and more [111] could benefit from using RC.

So far, however, the existing hardware approaches to RC do not meet all the requirements for its proliferation in application. These requirements include scalability, reproducibility from structure to structure, and low power consumption. Achieving a hardware platform that meets these requirements and is naturally suited to RC could see the technology's widespread uptake in a wide range of application areas.

68

3.5 References

[1]   B. Dieny *et al.*, "Spin-valve effect in soft ferromagnetic sandwiches," 1991.

[2]   M. Schneider, H. Hoffmann, and J. Zweck, "Magnetic switching of single vortex permalloy elements," *Appl. Phys. Lett*, vol. 79, p. 3113, 2001.

[3]   G. Hrkac, J. Dean, and D. A. Allwood, "Nanowire spintronics for storage class memories and logic," *Philos. Trans. R. Soc. A Math. Phys. Eng. Sci.*, vol. 369, no. 1948, pp. 3214–3228, 2011.

[4]   K. Yamada *et al.*, "Electrical switching of the vortex core in a magnetic disk.," *Nat. Mater.*, vol. 6, no. 4, pp. 269–3, 2007.

[5]   S. Bhatti, R. Sbiaa, A. Hirohata, H. Ohno, S. Fukami, and S. N. Piramanayagam, "Spintronics based random access memory: a review," *Materials Today*, vol. 20, no. 9. pp. 530–548, Nov-2017.

[6]   S. H. Chung, R. D. McMichael, D. T. Pierce, and J. Unguris, "Phase diagram of magnetic nanodisks measured by scanning electron microscopy with polarization analysis," *Phys. Rev. B - Condens. Matter Mater. Phys.*, vol. 81, no. 2, 2010.

[7]   D. Kumar, S. Barman, and a Barman, "Magnetic vortex based transistor operations.," *Sci. Rep.*, vol. 4, no. February, p. 4108, 2014.

[8]   V. Uhlíř *et al.*, "Dynamic switching of the spin circulation in tapered magnetic nanodisks," *Nat. Nanotechnol.*, vol. 8, no. 5, pp. 341–346, 2013.

[9]   V. Cambel and G. Karapetrov, "Control of vortex chirality and polarity in magnetic nanodots with broken rotational symmetry," *Phys. Rev. B*, vol. 84, no. 1, p. 014424, Jul. 2011.

[10]   V. Cambel *et al.*, "The influence of shape anisotropy on vortex nucleation in Pacman-like nanomagnets," *J. Magn. Magn. Mater.*, vol. 336, pp. 29–36, Jun. 2013.

[11]   S. K. Kim, K. S. Lee, Y. S. Yu, and Y. S. Choi, "Reliable low-power control of ultrafast vortex-core switching with the selectivity in an array of vortex states by in-plane circular-rotational magnetic fields and spin-polarized currents," *Appl. Phys. Lett.*, vol. 92, no. 2, 2008.

[12]   R. D. McMichael, J. Eicke, M. J. Donahue, and D. G. Porter, "Domain wall traps for low-field switching of submicron elements," *J. Appl. Phys.*, vol. 87, no. 9, pp. 7058–7060, 2000.

[13]   D. A. Allwood, G. Xiong, C. C. Faulkner, D. Atkinson, D. Petit, and R. P. Cowburn, "Magnetic domain-wall logic," *Science (80-.).*, vol. 309, no. 5741, pp. 1688–1692, 2005.

[14]   S. S. P. Parkin, M. Hayashi, and L. Thomas, "Magnetic Racetrack Memory," *Science (80-.).*, vol. 320, no. 5873, pp. 190–194, 2008.

[15]   D. A. Allwood, G. Xiong, M. D. Cooke, C. C. Faulkner, D. Atkinson, and R. P. Cowburn, "Characterization of submicrometer ferromagnetic NOT gates," *J. Appl. Phys.*, vol. 95, no. 12, pp. 8264–8270, 2004.

[16]   J.-G. Zhu and C. Park, "Magnetic tunnel junctions," *Mater. Today*, vol. 9, no. 11, pp. 36–45, 2006.

[17]   J. Akerman, M. Muñoz, M. Maicas, and J. L. Prieto, "Stochastic nature of the domain wall depinning in permalloy magnetic nanowires," *Phys. Rev. B - Condens. Matter Mater. Phys.*, vol. 82, no. 6, pp. 1–5, 2010.

[18]   M. Y. Im, L. Bocklage, P. Fischer, and G. Meier, "Direct observation of stochastic domain-wall depinning in magnetic nanowires," *Phys. Rev. Lett.*, vol. 102, no. 14, 2009.

[19]   C. C. Faulkner, M. D. Cooke, D. A. Allwood, D. Petit, D. Atkinson, and R. P. Cowburn, "Artificial domain wall nanotraps in Ni81Fe19 wires," *J. Appl. Phys.*, vol. 95, no. 11, pp. 6717–6719, 2004.

[20]   M. Kläui *et al.*, "Domain wall behaviour at constrictions in ferromagnetic ring structures," in *Physica B: Condensed Matter*, 2004, vol. 343, no. 1–4, pp. 343–349.

[21]   N. L. Schryer and L. R. Walker, "The motion of 180° domain walls in uniform dc magnetic fields," *J.*

Appl. Phys., vol. 45, no. 12, pp. 5406–5421, 1974.

[22]   S. Glathe, R. Mattheis, and D. V. Berkov, "Direct observation and control of the Walker breakdown process during a field driven domain wall motion," *Appl. Phys. Lett.*, vol. 93, no. 7, pp. 1–4, 2008.

[23]   U. H. Pi *et al.*, "Static and dynamic depinning processes of a magnetic domain wall from a pinning potential," *Phys. Rev. B - Condens. Matter Mater. Phys.*, vol. 84, no. 2, pp. 1–5, 2011.

[24]   J. Akerman, M. Muñoz, M. Maicas, and J. L. Prieto, "Selective injection of magnetic domain walls in Permalloy nanostripes," *J. Appl. Phys.*, vol. 115, no. 18, 2014.

[25]   T. J. Hayward, "Intrinsic Nature of Stochastic Domain Wall Pinning Phenomena in Magnetic Nanowire Devices," *Sci. Rep.*, vol. 5, 2015.

[26]   K. Omari *et al.*, "Ballistic rectification of vortex domain wall chirality at nanowire corners," *Appl. Phys. Lett.*, vol. 107, no. 22, p. 222403, Nov. 2015.

[27]   K. A. Omari and T. J. Hayward, "A Micromagnetic Protocol for Qualitatively Predicting Stochastic Domain Wall Pinning," *Sci. Rep.*, vol. 7, no. 1, p. 17862, 2017.

[28]   K. A. Omari *et al.*, "Toward Chirality-Encoded Domain Wall Logic," *Adv. Funct. Mater.*, vol. 0, no. 0, p. 1807282, Jan. 2019.

[29]   T. J. Broomhall and T. J. Hayward, "Suppression of Stochastic Domain Wall Pinning Through Control of Gilbert Damping," *Sci. Rep.*, vol. 7§, no. 1, 2017.

[30]   E. R. Lewis *et al.*, "Fast domain wall motion in magnetic comb structures," *Nat. Mater.*, vol. 9, no. 12, pp. 980–983, 2010.

[31]   L. Lopez-Diaz, J. Rothman, M. Kläui, and J. A. C. Bland, "Computational study of first magnetization curves in small rings," *IEEE Trans. Magn.*, vol. 36, no. 5 I, pp. 3155–3157, 2000.

[32]   J. Rothman *et al.*, "Observation of a Bi-domain state and nucleation free switching in mesoscopic ring magnets," *Phys. Rev. Lett.*, vol. 86, no. 6, pp. 1098–1101, 2001.

[33]   M. Kläui *et al.*, "Direct observation of spin configurations and classification of switching processes in mesoscopic ferromagnetic rings," *Phys. Rev. B - Condens. Matter Mater. Phys.*, vol. 68, no. 13, 2003.

[34]   C. A. F. Vaz *et al.*, "Ferromagnetic nanorings," *J. Phys. Condens. Matter*, vol. 19, no. 25, p. 255207, 2007.

[35]   L. Lopez-Diaz, J. Rothman, M. Kläui, and J. A. C. Bland, "Vortex formation in magnetic narrow rings: The role of magneto-crystalline anisotropy," *J. Appl. Phys.*, vol. 89, no. 11 II, pp. 7579–7581, 2001.

[36]   M. Kläui, C. A. F. Vaz, L. Lopez-Diaz, and J. A. C. Bland, "Vortex formation in narrow ferromagnetic rings," *Journal of Physics Condensed Matter*, vol. 15, no. 21. pp. 985–1023, 2003.

[37]   M. R. Scheinfein, J. Unguris, M. H. Kelley, D. T. Pierce, and R. J. Celotta, "Scanning electron microscopy with polarization analysis (SEMPA)," *Review of Scientific Instruments*, vol. 61, no. 10. pp. 2501–2527, 1990.

[38]   M. Kläui *et al.*, "Direct observation of spin configurations and classification of switching processes in mesoscopic ferromagnetic rings," *Phys. Rev. B - Condens. Matter Mater. Phys.*, vol. 68, no. 13, 2003.

[39]   D. A. Allwood, T. Schrefl, G. Hrkac, I. G. Hughes, and C. S. Adams, "Mobile atom traps using magnetic nanowires," *Appl. Phys. Lett.*, vol. 89, no. 1, pp. 1–4, 2006.

[40]   M. Negoita, T. J. Hayward, and D. A. Allwood, "Controlling domain walls velocities in ferromagnetic ring-shaped nanowires," *Appl. Phys. Lett.*, vol. 100, no. 7, p. 072405, 2012.

[41]   M. Negoita, T. J. Hayward, J. A. Miller, and D. A. Allwood, "Domain walls in ring-shaped nanowires under rotating applied fields," *J. Appl. Phys.*, vol. 114, no. 1, p. 013904, 2013.

[42]   G. Bordignon *et al.*, "Analysis of magnetoresistance in arrays of connected nano-rings," *IEEE Trans.*

Magn., vol. 43, no. 6, pp. 2881–2883, 2007.

[43]   Y. Ren, S. Jain, A. O. Adeyeye, and C. A. Ross, "Magnetization states in coupled Ni80Fe20 bi-ring nanostructures," *New J. Phys.*, vol. 12, no. 11pp, p. 93003, 2010.

[44]   K. J. Sixtus and L. Tonks, "Propagation of Large Barkhausen Discontinuities," *Phys. Rev.*, vol. 37, no. 8, pp. 930–958, Apr. 1931.

[45]   L. Landau and E. Lifshits, "On the Theory of the Dispersion of Magnetic Permeability in Ferromagnetic Bodies," in *Collected Papers of L.D. Landau*, vol. 8, 1965, pp. 101–114.

[46]   T. L. Gilbert, "Classics in Magnetics A Phenomenological Theory of Damping in Ferromagnetic Materials," *IEEE Trans. Magn.*, vol. 40, no. 6, pp. 3443–3449, 2004.

[47]   M. Lakshmanan, "The fascinating world of the Landau-Lifshitz-Gilbert equation: An overview," *Philosophical Transactions of the Royal Society A: Mathematical, Physical and Engineering Sciences*, vol. 369, no. 1939. pp. 1280–1300, 2011.

[48]   G. V Skrotskii, "The Landau-Lifshitz equation revisited," *Sov. Phys. Uspekhi*, vol. 27, no. 977, 1984.

[49]   R. F. Wang *et al.*, "Artificial 'spin ice' in a geometrically frustrated lattice of nanoscale ferromagnetic islands," *Nature*, vol. 439, no. 7074, pp. 303–306, 2006.

[50]   C. Nisoli, "On thermalization of magnetic nano-arrays at fabrication," *New J. Phys.*, vol. 14, no. 15pp, p. 35017, 2012.

[51]   S. A. Morley *et al.*, "Thermally and field-driven mobility of emergent magnetic charges in square artificial spin ice," vol. 1, pp. 1–10, 2018.

[52]   J. C. Gartside, D. M. Burn, L. F. Cohen, and W. R. Branford, "A novel method for the injection and manipulation of magnetic charge states in nanostructures," *Sci. Rep.*, vol. 6, 2016.

[53]   Y.-L. Wang *et al.*, "Rewritable artificial magnetic charge ice," *Science (80-.).*, vol. 352, no. 6288, pp. 962 LP – 966, May 2016.

[54]   A. Farhan *et al.*, "Direct observation of thermal relaxation in artificial spin ice," *Phys. Rev. Lett.*, vol. 111, no. 5, 2013.

[55]   A. Farhan *et al.*, "Thermally induced magnetic relaxation in building blocks of artificial kagome spin ice," *Phys. Rev. B*, vol. 89, no. 21, p. 214405, 2014.

[56]   A. Farhan *et al.*, "Emergent magnetic monopole dynamics in macroscopically degenerate artificial spin ice," *Sci. Adv.*, vol. 5, no. 2, 2019.

[57]   E. Mengotti *et al.*, "Building blocks of an artificial kagome spin ice: Photoemission electron microscopy of arrays of ferromagnetic islands," *Phys. Rev. B - Condens. Matter Mater. Phys.*, vol. 78, no. 14, 2008.

[58]   A. Schumann, P. Szary, E. Y. Vedmedenko, and H. Zabel, "Magnetic dipole configurations in honeycomb lattices: Order and disorder," *New J. Phys.*, vol. 14, 2012.

[59]   J. P. Morgan, A. Stein, S. Langridge, and C. H. Marrows, "Thermal ground-state ordering and elementary excitations in artificial magnetic square ice," *Nat. Phys.*, vol. 7, no. 1, pp. 75–79, 2011.

[60]   Z. Budrikis *et al.*, "Disorder strength and field-driven ground state domain formation in artificial spin ice: Experiment, simulation, and theory," *Phys. Rev. Lett.*, vol. 109, no. 3, 2012.

[61]   S. Ladak, D. E. Read, W. R. Branford, and L. F. Cohen, "Direct observation and control of magnetic monopole defects in an artificial spin-ice material," *New J. Phys.*, vol. 13, 2011.

[62]   W. R. Branford, S. Ladak, D. E. Read, K. Zeissler, and L. F. Cohen, "Emerging Chirality in Artificial Spin Ice," *Science (80-.).*, vol. 335, no. 6076, pp. 1597 LP – 1600, Mar. 2012.

[63]   J. P. Morgan, A. Stein, S. Langridge, and C. H. Marrows, "Magnetic reversal of an artificial square ice: Dipolar correlation and charge ordering," *New J. Phys.*, vol. 13, 2011.

[64] S. A. Morley *et al.*, "Temperature and magnetic-field driven dynamics in artificial magnetic square ice," *Proc. SPIE*, vol. 9551. 2015.

[65] J. D. Bernal and R. H. Fowler, "A Theory of Water and Ionic Solution, with Particular Reference to Hydrogen and Hydroxyl Ions," *J. Chem. Phys.*, vol. 1, no. 8, pp. 515–548, 1933.

[66] M. J. Harris, S. T. Bramwell, D. F. McMorrow, T. Zeiske, and K. W. Godfrey, "Geometrical Frustration in the Ferromagnetic Pyrochlore Ho2Ti2O7," *Phys. Rev. Lett.*, vol. 79, no. 13, pp. 2554–2557, 1997.

[67] C. Castelnovo, R. Moessner, and S. L. Sondhi, "Magnetic Monopoles in Spin Ice," *Nature*, vol. 451, no. 7174, p. 6, 2008.

[68] D. J. P. Morris *et al.*, "Dirac Strings and Magnetic Monopoles in the Spin Ice Dy2Ti2O7," *Science (80-.).*, vol. 326, no. 5951, pp. 411–414, 2009.

[69] E. Mengotti, L. J. Heyderman, A. F. Rodríguez, F. Nolting, R. V Hügli, and H.-B. Braun, "Real-space observation of emergent magnetic monopoles and associated Dirac strings in artificial kagome spin ice," *Nat. Phys.*, vol. 7, no. 1, pp. 68–74, 2011.

[70] M. Tanaka, E. Saitoh, H. Miyajima, T. Yamaoka, and Y. Iye, "Domain structures and magnetic ice-order in NiFe nano-network with honeycomb structure," in *Journal of Applied Physics*, 2005, vol. 97, no. 10, pp. 10–710.

[71] M. Tanaka, E. Saitoh, H. Miyajima, and T. Yamaoka, "Asymmetric field variation of magnetoresistance in Permalloy honeycomb nanonetwork," *Cit. J. Appl. Phys.*, vol. 99, pp. 10–710, 2006.

[72] C. Nisoli *et al.*, "Ground state lost but degeneracy found: The effective thermodynamics of artificial spin ice," *Phys. Rev. Lett.*, vol. 98, no. 21, 2007.

[73] Y. Qi, T. Brintlinger, and J. Cumings, "Direct observation of the ice rule in an artificial kagome spin ice," *Phys. Rev. B - Condens. Matter Mater. Phys.*, vol. 77, no. 9, 2008.

[74] I. Gilbert *et al.*, "Emergent ice rule and magnetic charge screening from vertex frustration in artificial spin ice," *Nature Physics*, vol. 10, no. 9, pp. 670–675, 2014.

[75] I. Gilbert *et al.*, "Emergent reduced dimensionality by vertex frustration in artificial spin ice," *Nat. Phys.*, vol. 12, no. 2, pp. 162–165, 2016.

[76] T. Schrefl, J. Fidler, K. J. Kirk, and J. N. Chapman, "Domain structures and switching mechanisms in patterned magnetic elements," *J. Magn. Magn. Mater.*, vol. 175, no. 1, pp. 193–204, 1997.

[77] M. Tanaka, E. Saitoh, H. Miyajima, T. Yamaoka, and Y. Iye, "Magnetic interactions in a ferromagnetic honeycomb nanoscale network," *Phys. Rev. B*, vol. 73, no. 5, p. 52411, Feb. 2006.

[78] S. Ladak, D. E. Read, W. R. Branford, and L. F. Cohen, "Direct observation and control of magnetic monopole defects in an artificial spin-ice material," *New J. Phys.*, vol. 13, 2011.

[79] Z. Budrikis *et al.*, "Domain dynamics and fluctuations in artificial square ice at finite temperatures," *New J. Phys.*, vol. 14, no. 14, 2012.

[80] P. Mellado, O. Petrova, Y. Shen, and O. Tchernyshyov, "Dynamics of magnetic charges in artificial spin ice," *Phys. Rev. Lett.*, vol. 105, no. 18, 2010.

[81] R. V Hügli *et al.*, "Artificial kagome spin ice: Dimensional reduction, avalanche control and emergent magnetic monopoles," *Philos. Trans. R. Soc. A Math. Phys. Eng. Sci.*, vol. 370, no. 1981, pp. 5767–5782, 2012.

[82] L. D. C. Jaubert and P. C. W. Holdsworth, "Signature of magnetic monopole and Dirac string dynamics in spin ice," *Nat. Phys.*, vol. 5, no. 4, pp. 258–261, 2009.

[83] A. Pushp *et al.*, "Domain wall trajectory determined by its fractional topological edge defects," *Nat. Phys.*, vol. 9, no. 8, pp. 505–511, 2013.

[84] J. P. Morgan *et al.*, "Real and effective thermal equilibrium in artificial square spin ices," *Phys. Rev.*

B - Condens. Matter Mater. Phys., vol. 87, no. 2, 2013.

[85]   D. Shi *et al.*, "Frustration and thermalization in an artificial magnetic quasicrystal," *Nat. Phys.*, vol. 14, no. 3, pp. 309–314, 2018.

[86]   C. Nisoli, J. Li, X. Ke, D. Garand, P. Schiffer, and V. H. Crespi, "Effective temperature in an interacting vertex system: Theory and experiment on artificial spin ice," *Phys. Rev. Lett.*, vol. 105, no. 4, 2010.

[87]   A. P. Ramirez, A. Hayashi, R. J. Cava, R. Siddharthan, and B. S. Shastry, "Zero-point entropy in 'spin ice,'" *Nature*, vol. 399, no. 110, pp. 333–335, 1999.

[88]   P. E. Lammert *et al.*, "Direct entropy determination and application to artificial spin ice," *Nat. Phys.*, vol. 6, no. 10, pp. 786–789, 2010.

[89]   J. C. Gartside *et al.*, "Realization of ground state in artificial kagome spin ice via topological defect-driven magnetic writing," *Nat. Nanotechnol.*, vol. 13, no. 1, pp. 53–58, 2018.

[90]   G. E. Moore, "Cramming more components onto integrated circuits," *Electronics*, vol. 38, no. 8, 1965.

[91]   G. E. Moore, "Progress in Digital Integrated Electronics," in *International Electron Devices Meeting, IEEE*, 1975.

[92]   G. E. Moore, "Moore's Law at 40," in *Understanding Moore's Law*, 2006.

[93]   P. J. Phillips and A. J. O'Toole, "Comparison of human and computer performance across face recognition experiments," *Image and Vision Computing*, vol. 32, no. 1. pp. 74–85, 2014.

[94]   P. J. Phillips *et al.*, "Face recognition accuracy of forensic examiners, superrecognizers, and face recognition algorithms," *Proc. Natl. Acad. Sci.*, vol. 115, no. 24, pp. 6171–6176, Jun. 2018.

[95]   Y. LeCun, Y. Bengio, and G. Hinton, "Deep learning," *Nature*, vol. 521, p. 436, May 2015.

[96]   J. von Neumann, "First draft of a report on the EDVAC," *IEEE Ann. Hist. Comput.*, vol. 15, no. 4, pp. 27–75, 1993.

[97]   N. K. Upadhyay, H. Jiang, Z. Wang, S. Asapu, Q. Xia, and J. Joshua Yang, "Emerging Memory Devices for Neuromorphic Computing," *Adv. Mater. Technol.*, vol. 4, no. 4, pp. 1–13, 2019.

[98]   A. Krogh, "What are artificial neural networks?," *Nat. Biotechnol.*, vol. 26, no. 2, pp. 195–197, 2008.

[99]   G. Van Der Sande, D. Brunner, and M. C. Soriano, "Advances in photonic reservoir computing," *Nanophotonics*, vol. 6, no. 3, pp. 561–576, 2017.

[100]   J. H. Jensen and G. Tufte, "Reservoir Computing with a Chaotic Circuit."

[101]   G. Tanaka *et al.*, "Recent advances in physical reservoir computing: A review," *Neural Networks*, vol. 115, pp. 100–123, 2019.

[102]   D. Prychynenko *et al.*, "Magnetic Skyrmion as a Nonlinear Resistive Element: A Potential Building Block for Reservoir Computing," 2018.

[103]   H. Jaeger and H. Haas, "Harnessing Nonlinearity: Predicting Chaotic Systems and Saving Energy in Wireless Communication," *Science (80-.).*, vol. 304, no. 5667, pp. 78 LP – 80, Apr. 2004.

[104]   J. Torrejon *et al.*, "Neuromorphic computing with nanoscale spintronic oscillators," *Nature*, vol. 547, no. 7664, pp. 428–431, Jul. 2017.

[105]   Y. Paquot *et al.*, "Optoelectronic reservoir computing," *Sci. Rep.*, vol. 2, 2012.

[106]   F. Chrisantha and S. Sampsa, "Pattern Recognition in a Bucket," in *European Conference on Artificial Life*, 2003, pp. 588–597.

[107]   C. Lee, V. Spirin, H. Song, and K. No, "Drying temperature effects on microstructure, electrical properties and electro-optic coefficients of sol-gel derived PZT thin films," *Thin Solid Films*, vol. 340, no. 1–2, pp. 242–249, 1999.

[108] F. Duport, A. Smerieri, A. Akrout, M. Haelterman, and S. Massar, "Fully analogue photonic reservoir computer," *Sci. Rep.*, vol. 6, 2016.

[109] C. Du, F. Cai, M. A. Zidan, W. Ma, S. H. Lee, and W. D. Lu, "Reservoir computing using dynamic memristors for temporal information processing," *Nat. Commun.*, vol. 8, no. 1, p. 2204, 2017.

[110] D. Kudithipudi, Q. Saleh, C. Merkel, J. Thesing, and B. Wysocki, "Design and Analysis of a Neuromemristive Reservoir Computing Architecture for Biosignal Processing," *Front. Neurosci.*, vol. 9, no. February, p. 502, 2015.

[111] G. Tanaka *et al.*, "Recent advances in physical reservoir computing: A review," *Neural Networks*, vol. 115, pp. 100–123, 2019.

Chapter 4 -Experimental Techniques

4.0 Introduction

This chapter describes experimental techniques and methods used within this study for processing, characterisation and imaging of magnetic nanostructured materials and devices.

These are well established techniques, the description here of which will cover literature where relevant as well as a focus on background and some parameters and procedures, though some experimental procedures accompany results obtained using them in relevant chapters.

Generally, permalloy ($Ni_{81}Fe_{19}$) nanostructures are patterned onto Si wafers by electron beam lithography and thermal evaporation to realise metallisation. Sample designs were chosen following micromagnetic modelling to simulate magnetic phenomena. Polarised Neutron Reflectometry (PNR) and magneto-optic Kerr effect (MOKE) magnetometry were used to experimentally characterise magnetic properties. Magnetic circular dichroism (MCD) techniques of magnetic transmission x-ray microscopy (MTXM) and photoemission electron microscopy (PEEM), and magnetic force microscopy (MFM) were used to directly image domain configurations in nanostructures.

4.1 Electron Beam Lithography

Electron Beam Lithography (EBL) [1]–[3] is the only technique used to pattern nanostructures used in this thesis. It is a method of fabricating nanostructures by use of an electron beam, which offers the benefits of high spatial resolution (as small as <3nm [4]) and computer generated patterns without the need for a separate mask.

EBL uses an electron beam to expose a photoresist layer to a designed pattern such that a mask can select which areas are developed. A solvent (developer) then dissolves either the developed or undeveloped photoresist (the solvent is specifically selected depending on which is required to be removed) leaving behind a pattern on a substrate with channels for material to be deposited into. A 'positive' photoresist is one that is inert, but exposure to the electron beam breaks long polymer chains into soluble, monomer fragments in the examples of long chain polymers such as polymethylmethacrylate (PMMA) or ZEP-520 [5]. Alternatively, negative photoresists such as hydrogen silsesquioxane (HSQ) [4]) have crosslinks created by electron beam exposure, reducing its solubility.

A technique such as thermal evaporation or sputtering deposits the coating of metal onto the resist/channels. After deposition of metal, another solvent is used to remove the remaining photoresist, leaving metal on the surface of the substrate (e.g. acetone in the case of a PMMA resist), leaving behind just the newly deposited material that adhered to the substrate. This is shown in Fig. 4.1.
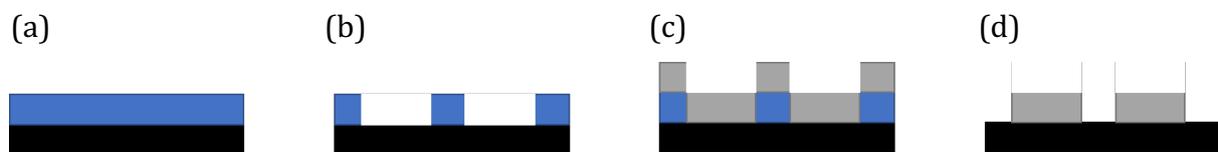
(a)   (b)   (c)   (d)

Figure 4.1. Schematic of photolithography. (a) Photoresist is spin coated onto a substrate. (b) An electron beam is used to expose areas of the photoresist that are then developed to create a mask or to directly create channels on the substrate. (c) A deposition technique such as thermal evaporation deposits metal on the whole of the substrate. Metal deposited into channels/not on the mask adhere to the substrate. (d) the photoresist is removed with a solvent, leaving behind metal in the desired pattern.

Photolithography using short wavelength (e.g. extreme ultraviolet [6]) and positive resist fixed photomasks are used elsewhere to create intricate micro- and nanoscale. This technique is widespread in the patterning transistors onto computer components on an industrial scale. However, an advantage of EBL is the ability to 'direct write', such that the beam can selectively pattern areas on a resist at extremely high resolutions.

In this work, structures were designed and patterned using a RAITH Voyager EBL system, capable of fabricating approximately 10nm sized features is used in conjunction

with RAITH150 software to create required patterns. This was carried out by Dr Paul Fry at The University of Sheffield's Nanoscience Centre.

An example of a sample map is presented in Fig 4.2. This shows the use of arrow markers and patterned annotations to navigate to desired structures when viewing samples through magnifying optics.
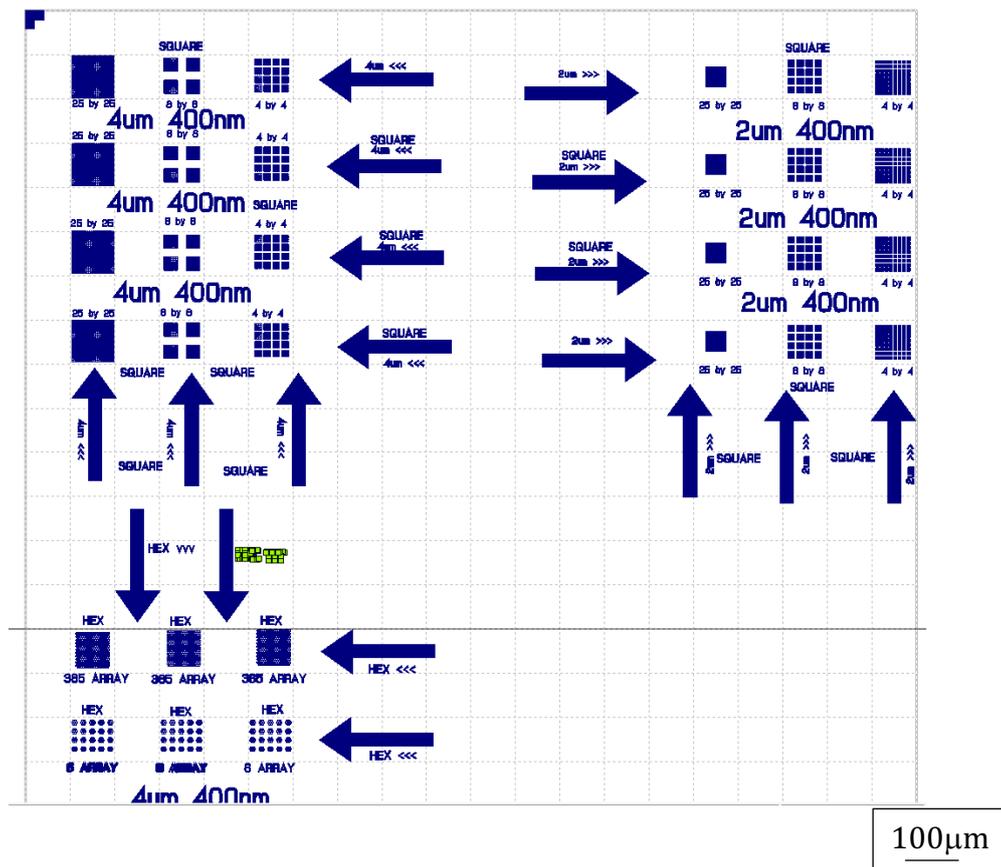

Figure 4.2. Sample map created in RAITH for PEEM experimentation (as used in §7.3). Annotations and arrow markers are patterned and metallised such that an operator viewing an electron beam (or other microscopy technique) image would be able to orient themselves and navigate to relevant structures.

The resist, developer and lift off chemicals were chosen following iterations of optimisation to obtain the best features at small scales. As an electron beam enters the resist, elastic scattering will occur with the effect of slightly broadening the beam. This is particularly pronounced for low beam energies. The proximity effect, wherein backscattered electrons re-merge in the resist away from the primary beam causing overexposure and pattern distortion in nearby features.

Temperature of and immersion time in the developer are also key parameters to optimise, leading to under- and over-development.

Feature resolution is therefore dependent on, but not limited to, the following features:

- Electron beam energy
- Resist material
- Resist thickness
- Developer
- Development temperature
- Development time

The pattern quality is also dependent on the exposure dose (or time of exposure). This affects the distribution of fragments of soluble monomers in the resist [7].

Throughout this project, patterning was performed using a 130nm thick layer of CSAR-62 (primarily poly(α-methylstyrene-co-methyl chloroacrylate)) positive e-beam resist spin coated onto a Si(001) wafer substrate. The resist was developed in xylene (dimethylbenzene). After metallisation via thermal evaporation (see §4.2) lift off was performed in warm 1165 remover (1-methyl-2pyroolidinone based). Experimental applications that required transmission of light, such as magnetic transmission x-ray microscopy (see §4.6), used a silicon nitride (Si_3N_4) membrane as a substrate material.

4.2 Thermal Evaporation

Deposition of metals for use in experiments reported in this thesis was carried out via thermal evaporation – a type of physical vapour deposition (PVD). Thermal evaporation produces deposits coatings onto substrates from a few angstroms to micrometre thickness. Solid powder is heated under a high vacuum, melting in the process, until vapour pressure is reached. Particles can then escape from the liquid phase, moving through a vacuum chamber and depositing a coating when contacting a surface such as a substrate placed inside the chamber. The technique is compatible with both metals and non-metals (though some metals have too high a melting temperature to be compatible) and is commonly used for deposition of electrical contacts using Ag or Al [8] or for thin film devices such as organic light emitting diodes (OLED) [9].
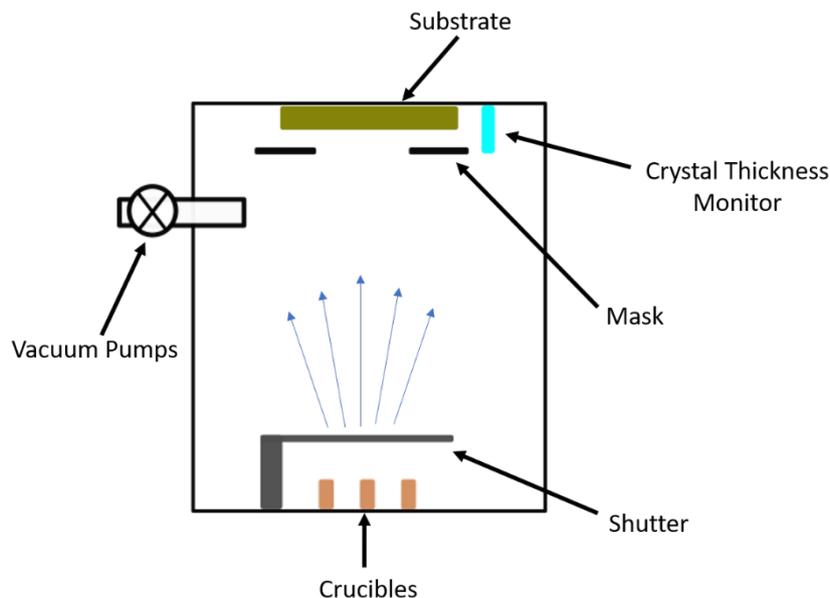
Figure 4.3. Schematic of the Functional Materials – Magnetics group at the University of Sheffield's Wordentec thermal evaporator. Substrates are mounted on a rotating carousel that can move different samples over the hole in the mask, allowing selective deposition.

The thermal evaporator used in this work was custom built by Wordentec Ltd. Alumina-coated tungsten crucibles were used for holding and melting metal powders, with up to three being available during each growth run (i.e. no need to evacuate the chamber to change metal type in between depositions). A compressed air powered shutter can be moved between an open and closed position, where the former allows sample deposition and the latter screens the sample, depositing metal on the underside of the shutter instead. A rotating sample carousel and sample mask are used to selectively expose up to five samples in turn. A quartz crystal oscillator was used to monitor the thickness of deposited films to angstrom resolution via changes in the resonant frequency of oscillation due to growth. Required tooling factors for materials used here were calibrated using previous deposition and atomic force microscopy (AFM).

Evaporation was typically carried out at a base pressure of 1×10^{-7} mbar with growth pressure. A bake out of the sample crucible was performed prior to sample growth for each required material. This heats the chamber without exposing the sample substrate. Growth pressure was between 1×10^{-6} mbar and 5×10^{-5} mbar. Powdered $Ni_{81}Fe_{19}$ with a maximum particle size of 45μm (purchased from Goodfellow [10])was used to metallise all ferromagnetic nanostructures in this thesis. Growth rates were between 0.3 and 0.6 Å/s.

Samples were held in place on a sample holder (cleaned prior to use with acetone and IPA) using small droplets of PMMA solution applied to the back surface. The holder was then inserted into the carousel facedown such that the samples were presented to the tungsten crucibles. The carousel was masked such that only one sample will be exposed to evaporated material at a given time. There were six slots per holder, with one left empty for bake out. Therefore, in the same deposition run, up to five samples could be metallised.

Crucibles were loaded with powder and the chamber was evacuated to base pressure. Heating was carried out by gradually increasing the power supplied to a crucible. Two-minute steps between increments were used to allow the crucible to equilibrate with the increased power and avoid failure by thermal shock. The power was increased until desired growth rate was achieved.

A bake-out step was carried out where the metal was heated to growth temperature and approximately 20nm (for Ni-Fe) was grown on a blank area of the sample holder. This reduced the presence of impurities, especially from oxide formation after the chamber had been exposed to atmosphere during loading. The sample shutter was used to block evaporated material from reaching the substrate when growth was not desired.

After bake-out, the power was ramped down over 15 minutes and the evaporator left to pump down to base pressure again. Growth was performed in the same manner as bake-out, but the carousel being rotated to the relevant sample location.

After growth the evaporator was left to cool before venting to remove samples. Cooling prevents oxidation of samples and powder which occurs at elevated temperatures.

4.3 Scanning Electron Microscopy

Scanning electron microscopy (SEM) was used to image at nanometre and micrometre length scales. Compared to ordinary light microscopy, that has a resolution of approximately 200nm with optimised conditions, electrons can have wavelengths multiple orders smaller than photons such that smaller structures can be resolved using electron microscopy than using optical light, as different features can be distinguished.

This gives an SEM a resolution limit of approximately 1nm. Different types of measurements can be performed with the SEM depending on the mode of imaging chosen which themselves depend on which electrons interactions with the sample are tracked.

A typical SEM has an electron source (usually an electron gun); a column that electrons travel in with scanning coils to deflect the beam in x and y axes and a series of condenser lenses for focussing the beam; various detectors for electrons once they have interacted with the sample; a vacuum chamber for the sample; and a computer that will control the beam and display a digitised image made from detected electrons. The schematic in Fig. 4.4 shows the arrangement of such an SEM.
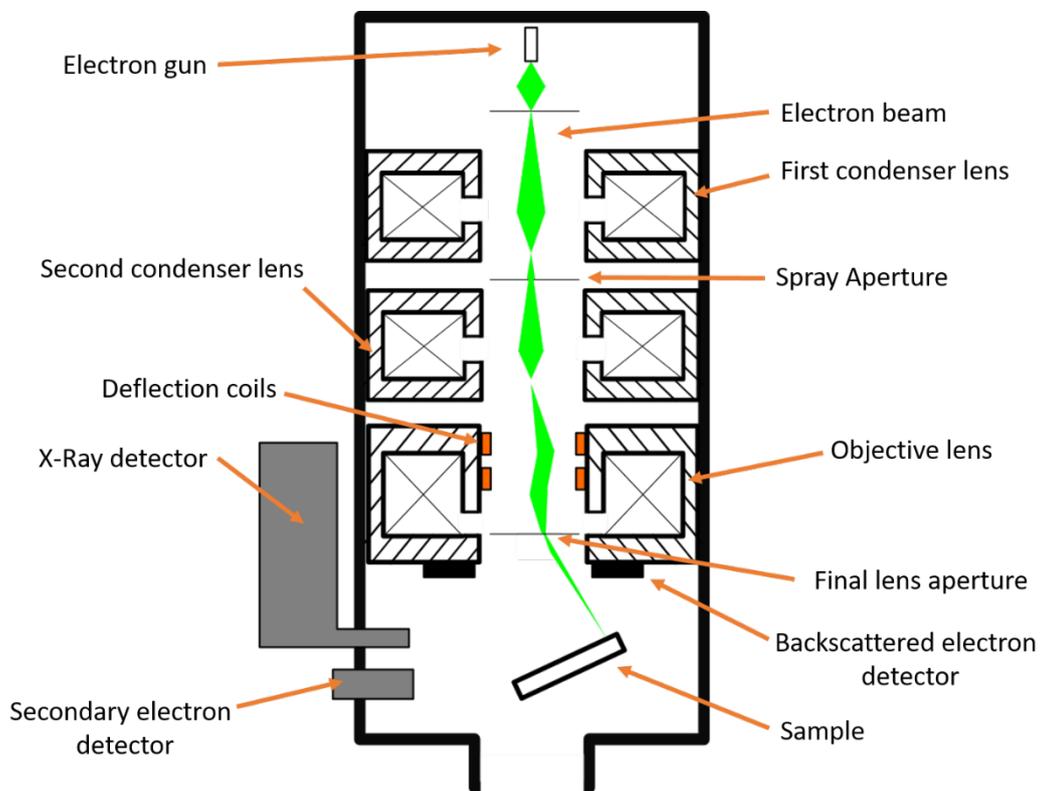

Figure 4.4. Schematic of an SEM demonstrating the principles of electron microscopy. Adapted from [11]**.**

The energy of the electron beam will affect the volume of interaction beneath the sample surface [12]. This is the teardrop shaped volume caused by scattering and absorption of electrons from 100nm-5μm beneath the surface. The depth of penetration of the interaction volume depends on the energy of the incident beam and

different depths are ideal for imaging each of the above three signals. Thus the beam parameters are modified depending on which type of image is desired. As electrons interact with the sample, they produce secondary electrons, backscattered electrons, and x-rays characteristic of the elements in the sample. Detectors are placed to observe each of these signals and a digital image can be created as the incident beam is scanned across the sample.

Secondary electrons (SE) are low energy electrons that are emitted from the k-orbitals of sample elements following a collision (inelastic scattering) from the incident beam. These are most commonly detected by an Everhart-Thornley detector [13], which is a Faraday cage that accelerates SEs towards a scintillator-photomultiplier system. This produces a current that can be amplified and processed to produce an image. Imaging via secondary electrons is the most common type of imagine with an SEM.

Backscattered electrons (BSEs) originate from the incident beam and are elastically scattered by electrostatic interactions with sample nuclei. Those that are scattered back towards the incoming beam are available for detection. Elements with larger nuclei cause stronger electron scattering and thus BSE imaging is very effective at discriminating between sample regions of different elemental compositions.

4.4 Polarised Neutron Reflectometry
4.4.1 General Principles

Polarised Neutron Reflectometry (PNR) was used to quantitatively measure the magnetisation of arrays of magnetic structures that had been subject to a particular field sequence (see §6.1). PNR was carried out in collaboration with Dr Joshaniel Cooper and Dr Nina-Juliane Steinke at the OFFSPEC Beamline, ISIS Neutron Source at the Rutherford Appleton Laboratory.

At a simple level, neutron reflectometry (NR) directs a collimated beam of neutrons onto a sample surface and measures the intensity of reflected radiation as a function of the scattering vector q_z ($q_z = 4\pi\lambda.\sin(\theta)$) where λ is the wavelength of incident radiation and θ is the scattering angle. The shape of reflectivity profile of scattering vector against scattered beam intensity can be used to extract information on sample

structures, thickness and roughness. NR is a specular reflection technique in that the angle of the incident beam is the same as the angle of the reflected beam.

The OFFSPEC beamline used in this thesis allows information in the directions parallel and perpendicular to the sample surface to be inspected. This is useful for thin films and nanostructures where interactions in the plane of the surface are of interest.

PNR measures the interaction of a polarised neutron beam with a magnetised sample surface. The scalar polarisation of the beam is related to the number of neutrons that have spin-angular momentum in either positive or negative (referred to as 'up' or 'down') directions (with respect to an external magnetic field). This spin gives neutrons an inherent magnetic moment that interacts with a magnetic sample. The reflectivities of oppositely polarised neutrons as a function of angle of incidence is measured.

In a magnetised sample such as a ferromagnetic thin film, neutron spins can be flipped when interacting with in-plane magnetisations. The number of neutrons that have their spin flipped can be directly measured by reference to a beam of polarised neutrons with no reflection from a magnetic sample. There were therefore 4 measurements taken – the number of spin flipped (SF) and non-spin flipped (NSF) up neutrons and SF and NSF down neutrons. The axis of neutron quantisation was perpendicular to the applied field direction.

Information about magnetic structure and locations (including domain structure) can be extracted by measuring the proportions of flipped and non-flipped neutrons reflected from a sample. In this work, neutrons scattered from magnetised nanorings, exposed Si from the surrounding wafer and intra-ring Si. The coherence scale of PNR is larger than the 4µm diameter of discrete rings, therefore each contribution to reflectivity of spin flipped neutrons is equivalent to the net magnetisation projected onto the neutron quantisation axis. For a ring in vortex state, this magnetisation contribution is 0 and for an onion state aligned parallel to the applied field this normalised magnetisation will be a maximum.

Preceding beamline scientists have automated much of data collection and plotting of PNR results. Reflectivity plots were automatically produced, though additional data, such as sample magnetisation, which was pertinent for this thesis, were obtained through secondary data analysis by curve fitting in the small angle region of reflectivity

data (low q_z). GenX [14] open source software was used to fit these data utilising a differential evolution algorithm. A sample plot showing differences in curves arising from a difference in contributions to magnetisation can be found in Fig 6.1.

A greater explanation of PNR can be found in literature [15]–[18] , with particular attention paid to ISIS/OFFSPEC specific publications such as [19], [20].

4.4.2 Array preparation

PNR required immense arrays of ferromagnetic nanorings to be created to gather enough reflected neutrons at the detector - on the order of 10^{-2} m. Arrays fabricated for experiments presented in this section had 25 million rings in the largest square arrays, pushing the limits of EBL software and requiring 17 hours write time.

Electron microscopy was used to investigate the quality of fabrication. Structures created to produce these dose testing images are made with Au rather than Ni-Fe for its superior deposition qualities following thermal evaporation. Dose test images were produced by Dr Paul Fry at the Nanoscience Centre, University of Sheffield.
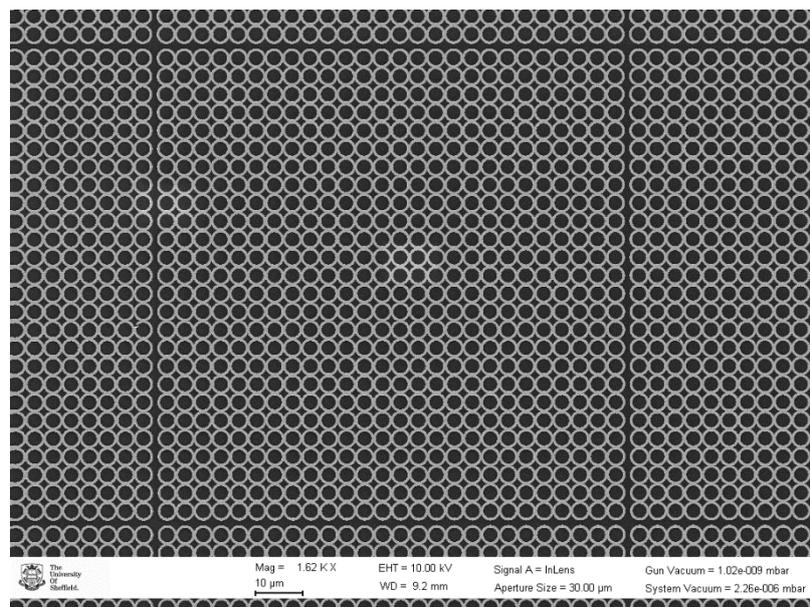

Figure 4.5. An SEM image of a subset of the ultra large arrays investigated with PNR. 1620X magnification

Figure 4.5 shows part of an ultra large square array. The write field of the EBL system limits arrays to 100μm², hence the channels separating a true ultra large array into an 'array of arrays.'

The fill factor of rings is a measure of how much of the array was Ni-Fe and how much was Si. Fill factors were calculated with ImageJ on a screenshot of the original RAITH file to pixel count black/white areas. For a large square array, the fill factor was calculated as 42%.

For PNR experiments, rings were designed that were 4μm in diameter, 400nm track width (500nm for later experiments), 20nm thickness.
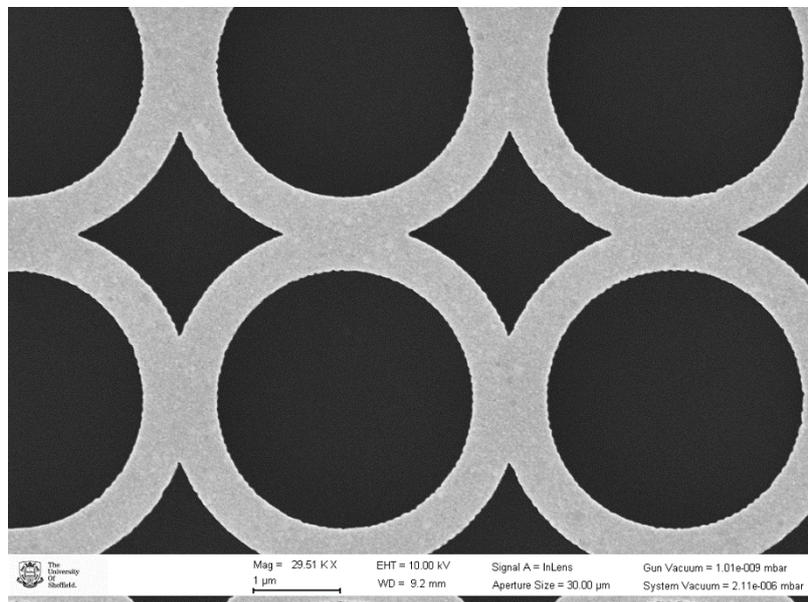

Figure 4.6. Higher magnification (26,500X) SEM image of a square array, highlighting defects in the writing process. ~30000x magnification.

Figure 4.6 shows a magnified image of the square array, and with it the splining of a curved path for the inner ring can be observed. This is normal for such a process, especially as RAITH does not actually draw circles but polygons. The quality of roundness is determined by the capability of the fabrication machine and size of desired features. Domain wall motion can be affected by this, and other defects that occur during the EBL/metallisation process, as seen in various examples in the literature [21], [22]. Vortex stability is also affected by edge roughness [23] though rings fabricated in this study are large enough to negate any detrimental effects on exchange energy

contributions. Indeed, the presence of notches in nanowire investigations is widespread [24]–[28].
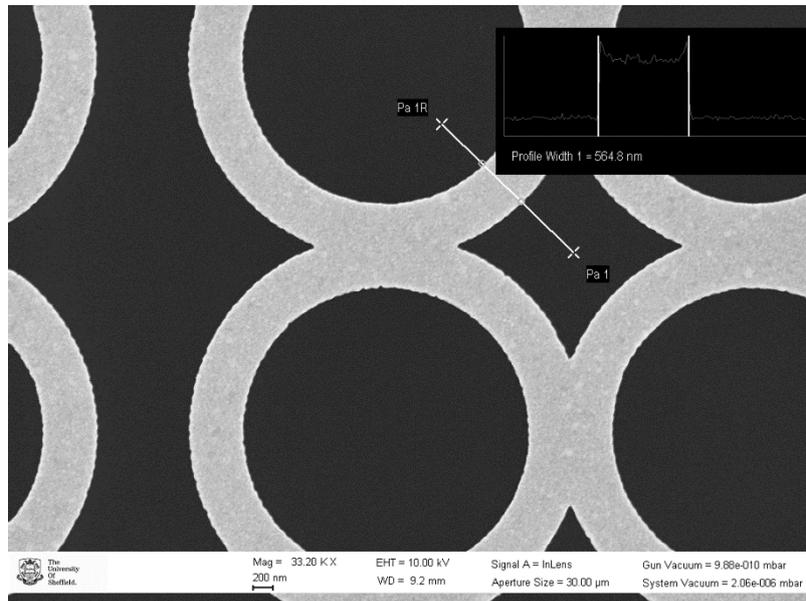

Figure 4.7. Measured track width of an ultra large square array nanoring comparing experimental result to design. 39000x magnification.

Figure 4.7 annotates a higher magnification (39,000x) image with the track width. The designs in RAITH for this file specified a 500nm track width, though experimentally 565m, was produced. This error induced by optimising beam dosage has some bearing on the results obtained but is not deemed critical.
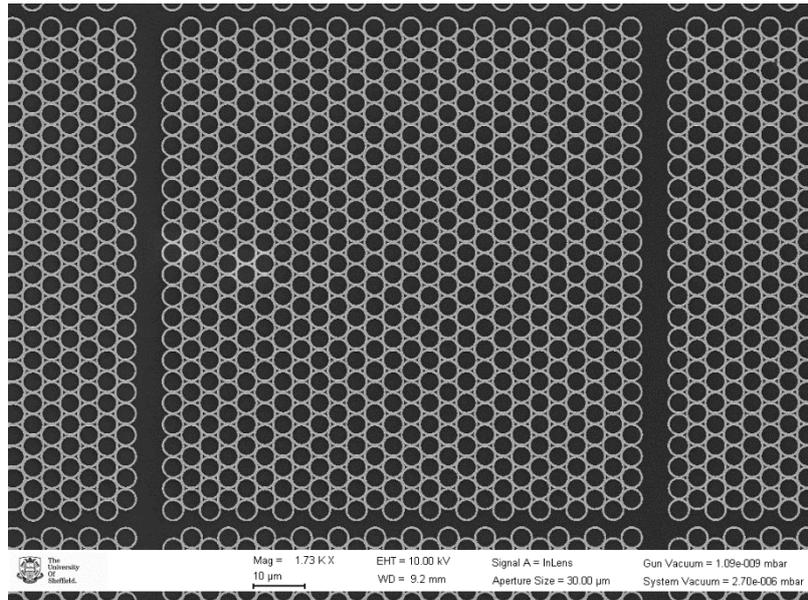
Figure 4.8. A single write field from an ultra large array of interconnected nanorings in a trigonal arrangement. Note the increased proportion of Si in the write field channels. 1730x magnification

Figure 4.8 shows the write field for an ultra large trigonal array of 598 interconnected nanorings, the maximum number of rings that could be fit into a single write field. The fill factor of this arrangement is 35%.
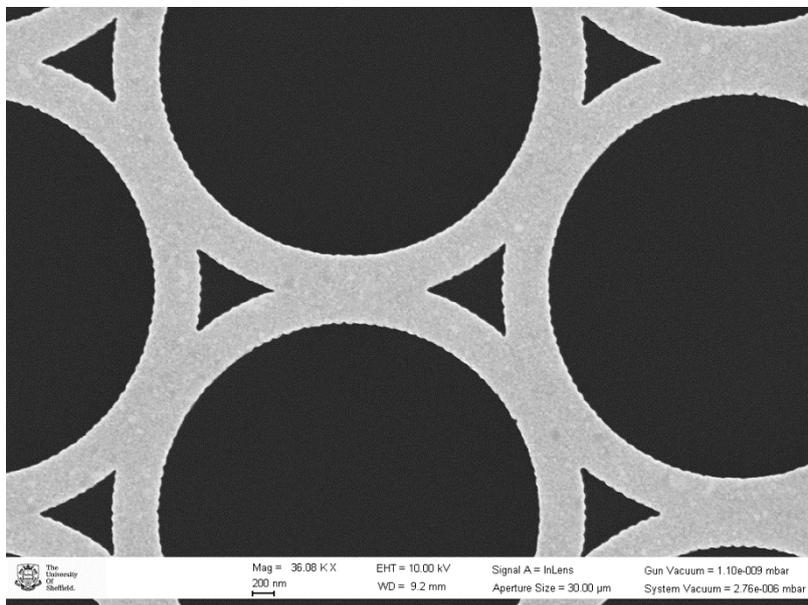

Figure 4.9. Higher magnification (36,000x) SEM image of a trigonal array

Figure 4.9 shows part of the array at approximately 36,000x magnification. Of note here and in Fig. 4.8 is that the ratio of wire that comprises a junction to normal wire is heavily biased towards junctions. Trigonal investigations for imaging preferred thinner

wires or those with less of an overlap to avoid potentially unintended magnetostatic interactions from adjacent nanowires ([29] and [30] highlight the changes in coercive field during magnetisation reversal that result from these interactions).
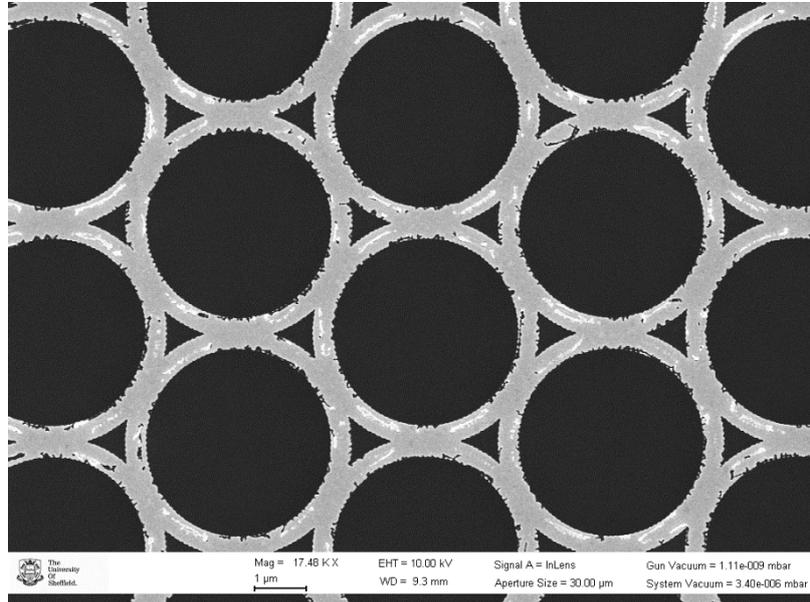

Figure 4.10. SEM image of part of a trigonal array showing damage from incorrect exposure

Figure 4.10 is from an EBL attempt that was underexposed, demonstrating the importance of dose optimisation, leading to breakage within nanowires. These arrays were of too poor quality for experimentation. Potential future experiments may investigate intentional notching within rings, perhaps randomly selected, to exert some measure of influence on the array response.
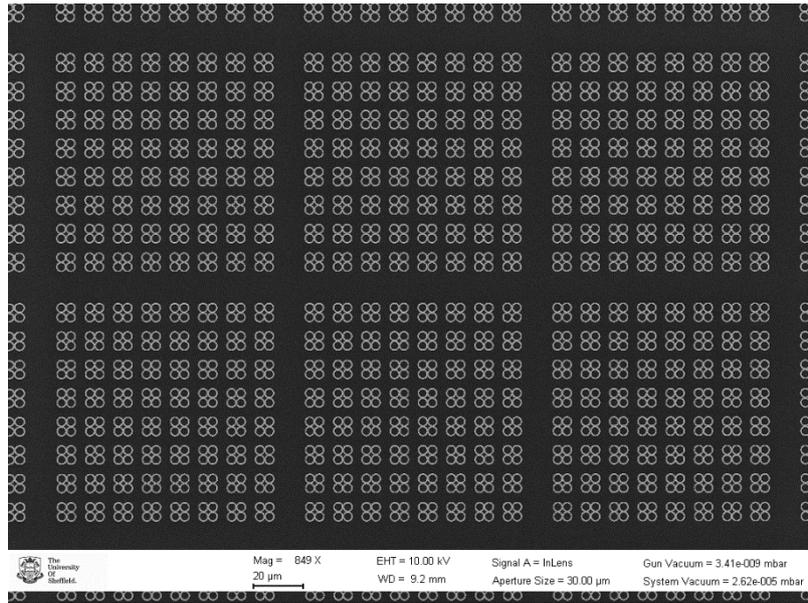
Figure 4.11. SEM image of subsets of two write fields of 2x2 square arrays. 850x magnification.

Figure 4.11 is an SEM image of subsets of a write field of 2 by 2 arrays – four arrays of 64 2 by 2 arrays form a single write field. In retrospect, optimisation of spacing and array distribution within a write field could have been carried out. Lead times for producing arrays and the constraints of beamline timetables prevented this inconvenience from being rectified. Additionally, as arrays got smaller, the percentage of Si increased further. The fill factor for a 2 by 2 write field is 21%.
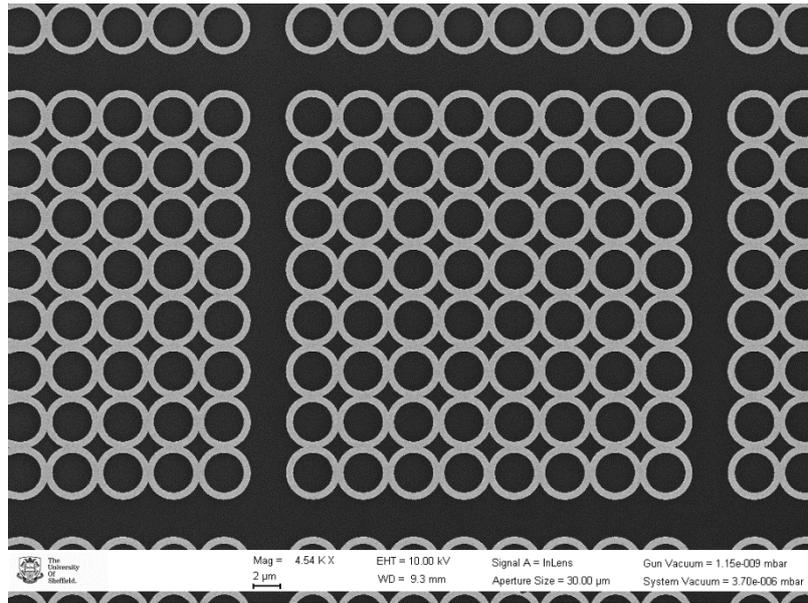
Figure 4.12. A subset of a write field of 8x8 square arrays. 4540x magnification.

Figure 4.12 shows 8 by 8 square arrays that were also split the write field into subsets. Similar Si/Ni-Fe ratio issues from poor array spacing selection were present in this array type, though to less of an extent than the 2x2 array. Fill factor for the array itself including channels is 36%.

4.4.3 Experimental arrangement

The experimental requirement, as detailed in §6, was to measure magnetisation of an array following application of an external rotating field. An electromagnet was installed around the sample holder such that fields could be applied in situ, and such that beam polarisation could be achieved. Depolarised beams cannot be used to measure reflectivities of 'up' and 'down' polarised neutrons following interaction with a magnetised sample. The minimum field that was needed to polarise the beam was 1Oe which was therefore used as a field to relax to following application of a rotating field.
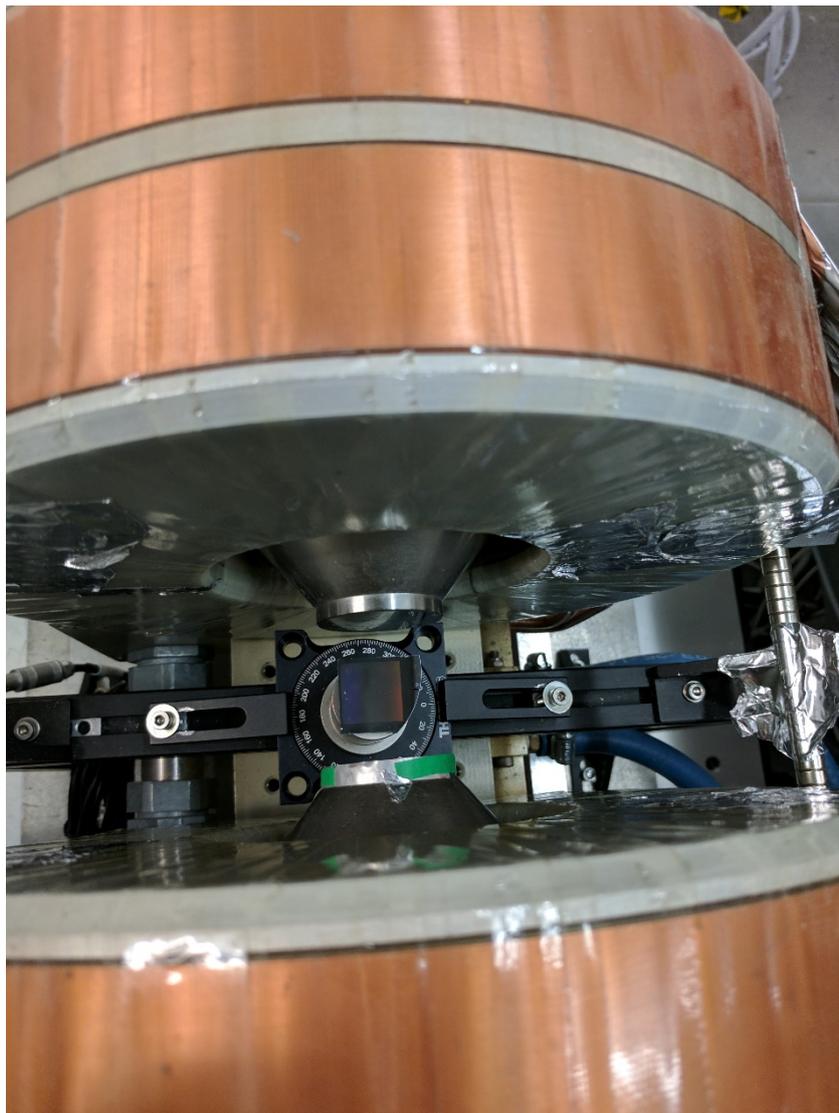
Figure 4.13. Photograph from the OFFSPEC beamline at ISIS showing the positioning of an ultra-large square array within an electromagnet on a rotating stage. Screws are M6 for size reference.

Samples were placed on a rotating stage in the centre of the electromagnet and loosely aligned with a laser. This loose alignment is then fine-tuned by exposing the sample to the beam and optimising alignment via actuation to micrometre/hundreds of nanometre resolution to maximise the intensity of the reflected beam. Figure 4.13 shows a photograph of a sample mounted on stage. Later experiments used a small amount of vac grease to give a degree of adhesion between sample and stage. Rotation was manual, with approximately seven steps per rotation and a short dwell between each step to reset finger position. Frequency of rotation was on the order of 10^{-1}Hz. 50 rotations were applied, unless specified otherwise, with the aim of equilibration of the sample.

4.5 Magneto-Optic Kerr Effect Magnetometry

The majority of MOKE measurements performed in this thesis use a system with a moderately focussed laser spot, henceforth referred to as the focussed MOKE system. The system is shown schematically in Fig. 4.14.
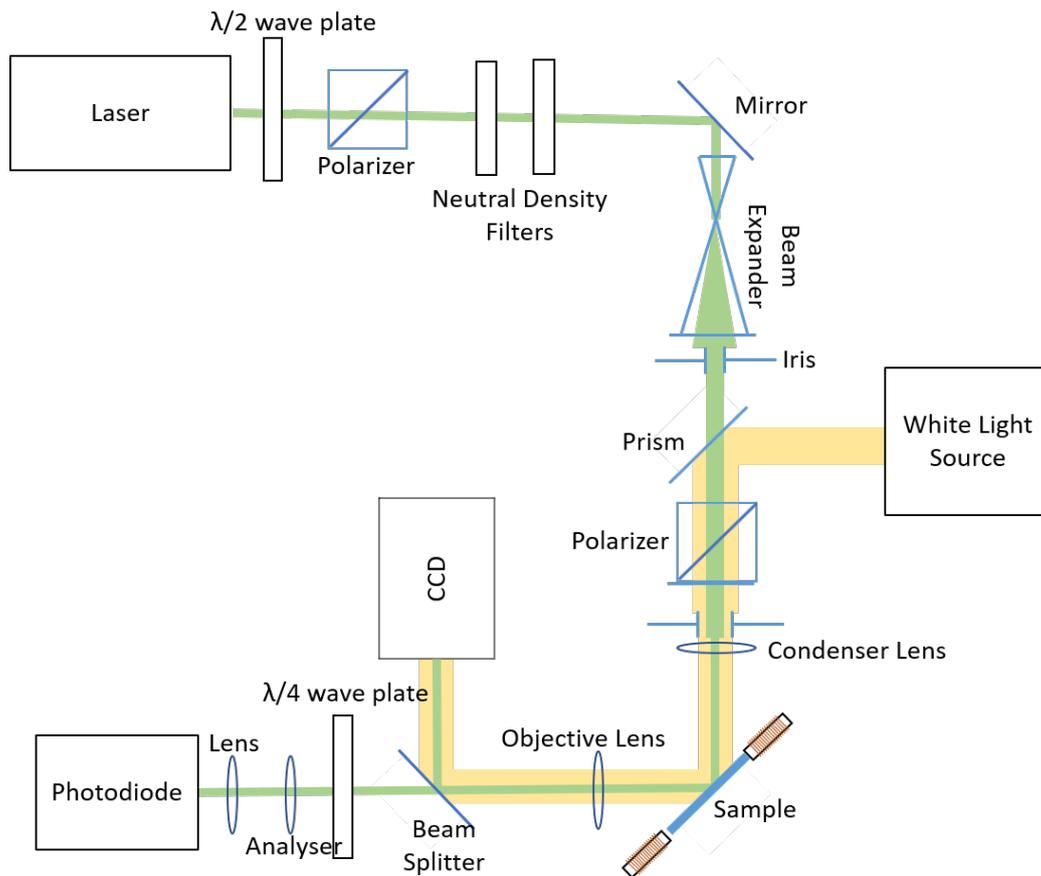

Figure 4.14. Schematic of f-MOKE equipment used experimentally for characterisation of magnetic nanostructures (shown during alignment as white light is shown but not used during measurement). CCD – charge coupled device (camera).

The laser used for results in this thesis was a Vortran Stradus® 532-40 with 532nm wavelength and 40mW power output. A half wave plate is rotated to an angle that determines transmitted laser power (8% for f-MOKE). The polariser is used to select the mode of polarised light for switching between polar and longitudinal MOKE. In this work, longitudinal MOKE was used. A white light source is used during alignment for illuminating the sample surface such that nanostructures can be viewed optically with

the CCD. The sample is held in a quadrupolar electromagnet, the magnetic field emitted from which is controlled from a PC script for bespoke software that is fed into a National Instruments BNC-2110. This converts the PC input into a current that is amplified with a pair (one for each magnetisation axis on the quadrupole) of Kepco Bipolar Op-Amp power supplies/amplifiers. Figure 4.15 shows the quadropolar electro magnet and sample mounting arrangement.
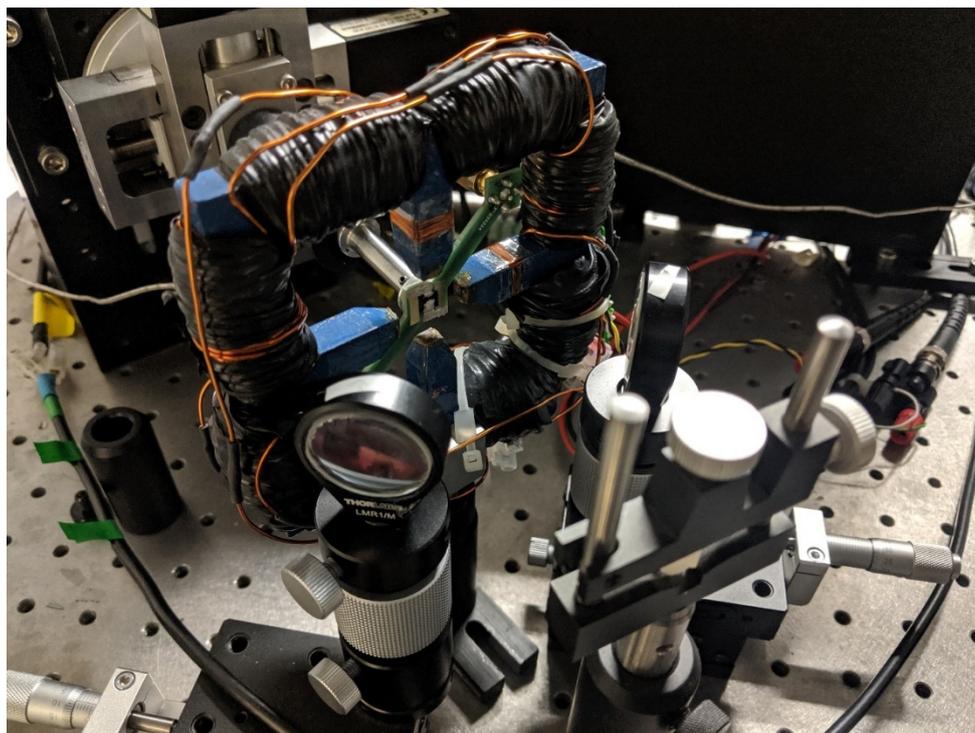

Figure 4.15. The Functional Materials - Magnetics quadrupole electromagnet demonstrating sample positioning. Condenser (foreground) and objective lenses can be seen.

The procedure for aligning the f-MOKE system first positions the sample to bring the reflected beam onto the photodiode (an ET-2030 from Electro-Optics Technology Inc.). The objective lens was then adjusted to image the sample surface using white light. The condenser lens position was then adjusted to bring the laser to a focus, as seen on the CCD camera image. The reflected beam could be positioned using by moving the condenser and the sampled moved laterally or by rotation. The white light was then removed, and the analyser and quarter wave plate are used to minimise the intensity of laser light reaching the photodiode. This is the 'extinction' condition. The analyser angle was then offset to optimise fractional MOKE signal response. An external magnetic field

could then be applied using the electromagnet to change the magnetisation of the sample. The changes to reflected amplitude from Kerr rotation will then be picked up by the photodetector. These are linked to an Agilent infiniium 54832D MSO oscilloscope that was used to average field and MOKE data over multiple waveforms, each of which could have multiple field cycles. These data were then sent to the PC, where the bespoke software was used to further reduce the noise by folding the multiple cycle data down to that for a single field cycle, and by binning neighbouring data points by a user-defined extent. This typically resulted in just over 1000 points per field cycle. The software integrated the electromagnet signals (as they were produced by inductance) to recover the original field profiles and calibrated using a Gaussmeter against measurements of the field produced by the electromagnet. Parametric plotting of the magnetic field and MOKE data allowed hysteresis loops to be obtained.

Note that an additional square wave signal was used to define the data stream length that represented one cycle. For some experiments here, this would contain several rotations of magnetic field (see Chapter 6) but allowed the required data stream to be obtained multiple times to assist with improving the signal-to-noise ratio

4.6 X-Ray Magnetic Circular Dichroism

X-ray magnetic circular dichroism (XMCD) is a standard image contrast technique, built from the x-ray spectroscopic measurements were made in 1987 by Schutz et al. [31] followed in 1993 by imaging of ferromagnetic domains by Stohr et al. [32]. In the decades since, advances in the technique have developed XMCD as a key tool for investigation and imaging of magnetism in solids, thin films and nanoparticles and nanostructures [33]–[36].

Circularly polarised x-ray light is absorbed in differing quantities dependent on the vectors of atomic magnetic moment that each chirality of light interacts with. As each of the x-ray absorption spectra for left- and right-circularly polarised light are therefore different, the difference spectrum will have intensity peaks where absorption of each mode of light differs. This can be used to produce a contrast image, which is used in this thesis for producing magnetically sensitive images of ferromagnetic domains.

4.6.1 Photoemission electron microscopy

Photoemission electron microscopy (PEEM) is a technique that utilises the photo-electrons emitted by excitation of a sample by absorption of X-ray or ultraviolet light. These electrons are accelerated and then magnified by a series of lenses and recorded at an electron-sensitive detector.

Magnetic contrast PEEM imaging is enabled by measuring the electron yield from magnetised samples as they are excited by circularly polarised X-ray light.

XMCD-PEEM (henceforth referred to as PEEM) was carried out at beamline I06 at the Diamond Light Source with the assistance of beamline scientist Dr Francesco Maccherozzi. An advantage of PEEM over MFM for looking at DW topology in this thesis is the non-invasive nature of a light-based instrument. Some concerns over tip-DW interaction arose in MFM experiments which would not be a problem in PEEM. In this regard, PEEM offered the best way to experimentally match micromagnetic modelling. PEEM was carried out over 18 shifts. The speed at which PEEM could be used to produce an magnetic circular dichroism image over MFM was useful – 4 minutes compared to an hour and a half for MFM. A specifically fabricated sample holding cartridge was imported from the LEEM (low energy electron microscope)-PEEM beamline group at the ALBA Synchrotron in Spain [37], [38]. This allowed a rotating field to be applied in-situ, which, given the PEEM is vented to the order of 1×10^{-9} $mbar$ vacuum after sample change, is extremely convenient. Foerster et al. [38] provide a calibration for the electromagnet in this cartridge, with 100Oe fields able to be applied without excessive heating incurring damage to the coils or excessive physical drift from heating of the sample holder. Figure 4.16 shows the calibration plot for this cartridge sample holder.
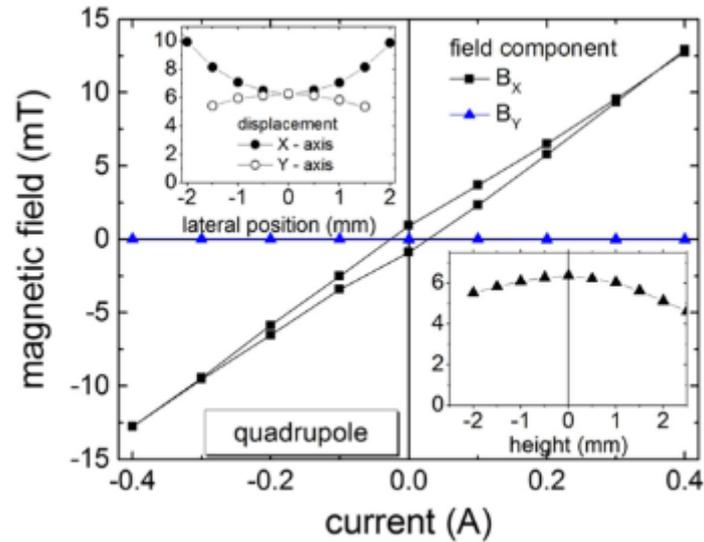
Figure 4.16. Magnetic field as measured for the sample holder cartridge as a function of current. Squares and triangles indicate field measured along orthogonal directions as current is applied along the x-direction. The main plot is for measurement at 0.5mm from the sample surface, with the right inset showing the Hall probe measurement difference with height from the plane of the yoke holding the sample. The left inset shows field change as it laterally displaced from the centre. Taken from [38]**.**

A reduced field range meant that a 5nm thick sample was used for experimentation. This would achieve saturation sooner and reduce field ranges that were observed in previous experiments on similar arrays. This sample was capped with a 2nm thick layer of Al to prevent oxidation of Ni-Fe and to fulfil the sample specification of having a conductive surface (this prevents surface charge formation that affects the obtained electron yield and image quality [39]).

4.7 Atomic and Magnetic Force Microscopy

Atomic force microscopy (AFM) is part of the scanning probe microscopy range of methods which includes magnetic force microscopy (MFM), piezoresponse force microscopy, scanning tunnelling microscopy and a wealth of other bespoke applications. It is an incredibly versatile and valuable technique that can be applied to a variety of areas, from simple surface investigations[40] to biological/medical [41], [42] to artificial micro/nanostructures such as with this thesis. A Nobel prize in physics was

awarded to the inventor of the scanning tunnelling microscopy (STM) technique, Gert Binning [40]. AFM is advantageous over STM, however, in that the sample does not need to be conductive.

AFM tracks the deflection of a specially fabricated cantilever with a very sharp tip as it is scanned close to the surface of a material. It can be used to image structures down to tens of nanometres laterally.

Coulombic and Van der Waals interactions from the surface of the material with the cantilever tip cause deflections in the cantilever. As the former is repulsive and the latter attractive, there is an interplay between these effects and an optimum separation between surface and tip must be selected to balance these. At a distance too close to the surface, Coulombic repulsion will cause the tip to excessively deflect and break.

'Tapping mode' AFM is used wherein the tip is oscillated slightly below resonance. As the tip reached the bottom of its swing, the oscillation was damped. The change in amplitude (or phase) was used to measure the instantaneous separation between tip and surface, and a feedback circuit adjusted the height of the probe to maintain a constant amplitude of oscillation.

Deflection tracking was achieved by reflecting a laser from the back face of the cantilever to a quadrant photodetector. Shifts in the reflected beam were measured by the relative changes in voltage at each quadrant of the photodetector and converted to a change in height. As the beam was rastered along a surface, a topographical map was produced.

The feedback circuit controlling the probe height is critical to avoid the tip contacting the sample surface and being damaged. A feedback circuit adjusts the height of the tip depending on the detected surface height. Nanoscope software includes a feature to monitor the detected stage voltage of the trace of each scanline. AFM take a forward trace of a sample but also measures the retrace as the scanner moves backwards on the same line before it drops down a row to measure the next line. The difference between forward and reverse traces is used to assess the quality of the feedback loop and adjust parameters such as scan speed to obtain a useable image.

MFM operates on similar principles except tip deflection/attraction from interaction between magnetised tips and out-of-plane magnetic fields from a magnetised sample.

The system used here is Digital Instruments Veeco Multimode AFM/MFM with Nanoscope 3.1 software. For AFM, Bruker OTESPA-R3 Si tips with a resistivity of 0.01-0.02 Ω.cm and a resonant frequency of approximately 300kHz were used. For MFM, Bruker MESP-LM-V2 tips with resonant frequency of approximately 75kHz were used. A magnetic CoCr coating was applied to the tip face to provide the MFM interaction. Figure 4.17 shows the University of Sheffield's Veeco Multimode AFM/MFM and noise minimisation hood.
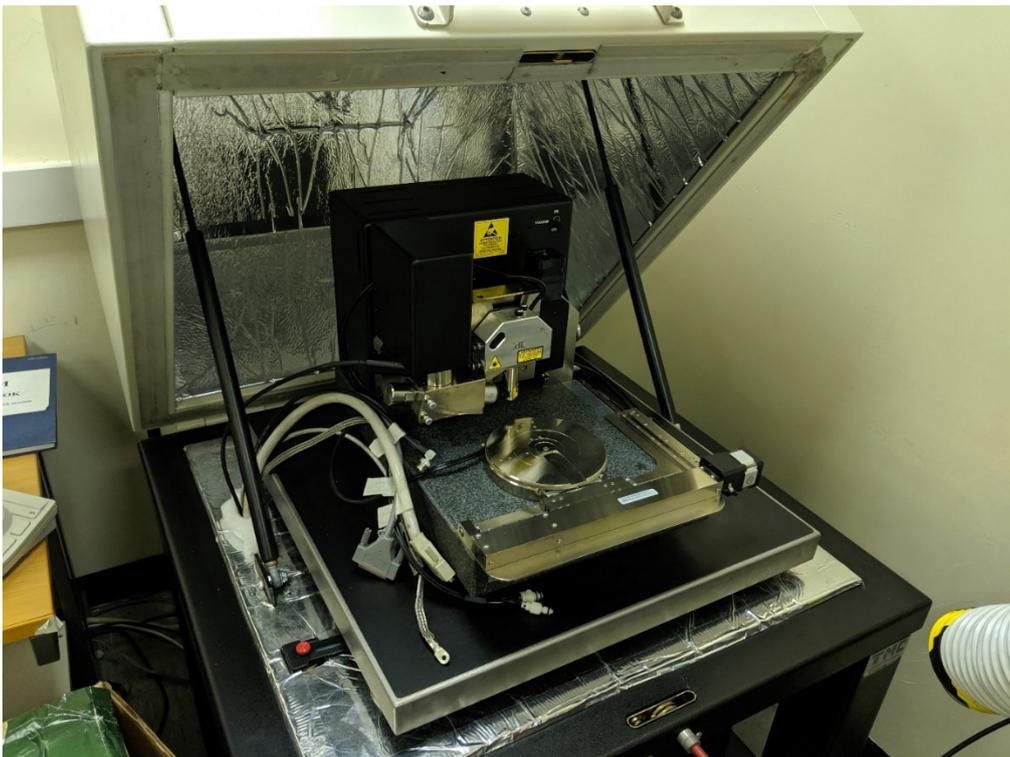

Figure 4.17. Veeco Multimode AFM with noise minimisation hood (shown in the up position). Samples are mounted on a vibration resistant plate to isolate the sample from noise such as cooling equipment vibrations or movement on the floor above.

In this thesis, whilst MFM is preferred as an economical method of producing images of magnetic states, the tip could directly interact with the ferromagnetic nanostructures being imaged. This could lead to movement of free domain walls or switching of magnetisation directions within the ring [43]. However, as seen in literature review, in certain artificial spin ice applications, this can be harnessed for functionality [44].

4.8 Micromagnetic Modelling

Micromagnetic modelling is a powerful numerical simulation tool in the field of nanomagnetism, allowing researchers to explore magnetisation dynamics and interpret or predict experimental results. The term micromagnetics follows from Brown's approach in 1959 [45] to describing magnetisation as a continuum. Here, magnetism is thought of as a continuous vector rather than singular atomic spins. This allows for modelling of large structures in a short scale of time relative to atomistic methods.

Micromagnetic modelling works by using a mesh to define sample geometry and solving the Landau-Lifshitz-Gilbert (LLG) equation within each mesh cell. Each cell is subject to an effective field consisting of magnetic energy terms. Exchange and demagnetisation interactions with every other cell in the simulation also contribute to this effective field. The result of this sum is then applied forwards to other cells such that an iteration of the LLG is carried out. Small cell sizes are useful for capturing a fuller extent of the behaviour of a magnetic nanostructure. Close to the exchange length will include individual contributions from more magnetic dipoles than a larger cell. However larger cells require less computational resources and time to solve. For example, simulating a $1\mu m^2$ square structure requires 100 square cells of $100nm^2$ or 400 square cells of $50nm^2$, quadrupling time taken to simulate.

There are multiple open source packages available [46]–[48] to simulate a wide variety of structures, materials, magnetisation states and external conditions.

In this thesis, micromagnetic modelling via the MuMax3[48] finite difference package is predominately used. This is an open-source simulation program using GPU acceleration. This differs to the other finite difference package OOMMF (Object Orientated Micromagnetic Framework) used in this research programme which uses CPU acceleration. CPU based packages are limited by the number of available cores whereas GPUs offer massive parallelisation at low cost [49].

Though finite element packages are better at replicating geometric intricacies, the systems simulated in this study are geometrically simple enough that finite difference will suffice and be able to do so with better speed.

Cells could be assigned properties such as material parameters that will affect their output after discretisation. MuMax3 allowed for cells to be assigned to regions that had different material parameters. Different operations could also be performed on a region-by-region basis, such as externally applied fields in two different directions in two regions.

In this thesis, cell sizes were fixed to be 4nm x 4nm x 20nm – a 4µm x 4µm x 20nm simulation space subdivides into a mesh grid of 1000 x 1000 x 1 cells. Grid sizes were varied to achieve desired dimensions of simulated space, with cell sizes kept constant.

These simulations were run for a sufficient period of time to allow minimisation to occur. Most simulations in this thesis use rotational fields, which are modelled by fields being applied in 15° angle steps of a larger 360° rotation. Each step is run for 12ns – 15ns to allow minimisation to occur.

Other parameters used are saturation magnetisation of 715×10^3 A/m , exchange stiffness of 13×10^{-12} J/m and a damping constant of 1. This high damping constant 'turns off' changes in magnetisation vector from Gilbert damping to obtain a highly simplified model of DW motion in simulations. As this thesis is not concerned with gyroscopic dependent effects such as Walker breakdown, this is considered acceptable for reducing simulation timescales. The value of M_{Sat} of Py used was chosen based on ferromagnetic resonance measurements of Py thin films grown using the same equipment as experimental samples. The quality of Py powder used is suspected to have given this lower value than often quoted for Py (usually around 800×10^3 A/m). Zero temperature simulations are also carried out to produce deterministic models.

4.9 References

[1]   M. Stepanova and S. Dew, *Nanofabrication: Techniques and principles*. Springer Vienna, 2014.

[2]   M. A. McCord and M. J. Rooks, "Electron Beam Lithography," in *Handbook of Microlithography, Micromachining, and Microfabrication. Volume 1: Microlithography*, SPIE PRESS, 1997, pp. 80–115.

[3]   M. A. Mohammad, M. Muhammad, S. K. Dew, and M. Stepanova, "Fundamentals of electron beam exposure and development," in *Nanofabrication: Techniques and Principles*, Vienna: Springer Vienna, 2012, pp. 11–41.

[4]   D. S. Macintyre and S. Thoms, "Comparison of hydrogen silsesquioxane development methods for sub-10 nm electron beam lithography using accurate linewidth inspection," *J. Vac. Sci. Technol. B, Nanotechnol. Microelectron. Mater. Process. Meas. Phenom.*, vol. 29, no. 6, p. 06F307, Nov. 2011.

[5]   T. Nishida, M. Notomi, R. Iga, and T. Tamamura, "Quantum wire fabrication by e‐beam elithography using high-resolution and high-sensitivity e‐beam resist zep-520," *Jpn. J. Appl. Phys.*, vol. 31, no. 12 S, pp. 4508–4514, 1992.

[6]   C. W. Gwyn, R. Stulen, D. Sweeney, and D. Attwood, "Extreme ultraviolet lithography," *J. Vac. Sci. Technol. B Microelectron. Nanom. Struct. Process. Meas. Phenom.*, vol. 16, no. 6, pp. 3142–3149, 1998.

[7]   M. Aktary, M. Stepanova, and S. K. Dew, "Simulation of the spatial distribution and molecular weight of polymethylmethacrylate fragments in electron beam lithography exposures," *J. Vac. Sci. Technol. B Microelectron. Nanom. Struct.*, vol. 24, no. 2, p. 768, Mar. 2006.

[8]   D. Natali and M. Caironi, "Organic photodetectors," in *Photodetectors: Materials, Devices and Applications*, B. B. T.-P. Nabet, Ed. Woodhead Publishing, 2016, pp. 195–254.

[9]   J. Shinar, R. Shinar, and R. Groarke, "An Overview of Organic Light-Emitting Diodes and their Applications," in *Reference Module in Materials Science and Materials Engineering*, Elsevier, 2016.

[10]   "Goodfellow Ni81/Fe19 powder: http://www.goodfellow.com/E/NJ01-Nickel-Iron-Powder.html." .

[11]   U. Steff, "Diagram of an SEM with English captions." [Online]. Available: https://commons.wikimedia.org/wiki/File:Schema_MEB_(en).svg. [Accessed: 11-Aug-2019].

[12]   J. Goldstein *et al.*, *Scanning Electron Microscopy and x-Ray Microanalysis*, 3rd ed. Springer US, 2003.

[13]   T. E. Everhart and R. F. M. Thornley, "Wide-band detector for micro-microampere low-energy electron currents," *J. Sci. Instrum.*, vol. 37, no. 7, pp. 246–248, 1960.

[14]   M. Björck and G. Andersson, "GenX: an extensible X-ray reflectivity refinement program utilizing differential evolution," *J. Appl. Crystallogr.*, vol. 40, no. 6, pp. 1174–1178, Nov. 2007.

[15]   J. Daillant and A. Gibaud, *X-ray and Neuron Reflectivity: Principles and Applications*, vol. 58. 1999.

[16]   G. P. Felcher, "Neutron reflectometry as a tool to study magnetism (invited)," *Cit. J. Appl. Phys.*, vol. 87, p. 5443, 2000.

[17]   F. Ott and A. Bataille, "Neutron Scattering on Magnetic Thin Films," *Neutron News*, vol. 22, no. 4, pp. 28–31, 2011.

[18]   J. F. Ankner and G. P. Felcher, "Polarized-neutron reflectometry," *J. Magn. Magn. Mater.*, vol. 200, no. 1, pp. 741–754, 1999.

[19]   R. M. Dalgliesh, S. Langridge, J. Plomp, V. O. De Haan, and A. A. Van Well, "Offspec, the ISIS spin-echo reflectometer," *Phys. B Phys. Condens. Matter*, vol. 406, pp. 2346–2349, 2011.

[20]   J. R. P. Webster, S. Langridge, R. M. Dalgliesh, and T. R. Charlton, "Reflectometry techniques on the Second Target Station at ISIS: Methods and science," *Eur. Phys. J. Plus*, vol. 126, 2011.

[21]   D. Atkinson, D. A. Allwood, G. Xiong, M. D. Cooke, C. C. Faulkner, and R. P. Cowburn, "Magnetic domain-wall dynamics in a submicrometre ferromagnetic structure," *Nat. Mater.*, vol. 2, no. 2, pp. 85–87, 2003.

[22]   C. A. F. Vaz *et al.*, "Ferromagnetic nanorings," *J. Phys. Condens. Matter*, vol. 19, no. 25, p. 255207, 2007.

[23]   C. A. F. Vaz, C. Athanasiou, J. A. C. Bland, and G. Rowlands, "Energetics of magnetic ring and disk elements: Uniform versus vortex state," *Phys. Rev. B - Condens. Matter Mater. Phys.*, vol. 73, no. 5, 2006.

[24]   K. A. Omari and T. J. Hayward, "Chirality-based vortex domain-wall logic gates," *Phys. Rev. Appl.*, vol. 2, no. 4, 2014.

[25]   T. J. Broomhall and T. J. Hayward, "Suppression of Stochastic Domain Wall Pinning Through Control of Gilbert Damping," *Sci. Rep.*, vol. 7§, no. 1, 2017.

[26]   M. Kläui *et al.*, "Domain Wall Pinning in Narrow Ferromagnetic Ring Structures Probed by Magnetoresistance Measurements," *Phys. Rev. Lett.*, vol. 90, no. 9, p. 4, 2003.

[27]   M. Kläui, C. A. F. Vaz, A. Lapicki, T. Suzuki, Z. Cui, and J. A. C. Bland, "Domain wall pinning in ferromagnetic structures fabricated by focused ion beam," in *Microelectronic Engineering*, 2004, vol. 73–74, pp. 785–789.

[28]   K. A. Omari and T. J. Hayward, "A Micromagnetic Protocol for Qualitatively Predicting Stochastic Domain Wall Pinning," *Sci. Rep.*, vol. 7, no. 1, p. 17862, 2017.

[29]   A. O. Adeyeye, J. A. C. Bland, C. Daboo, and D. G. Hasko, "Magnetostatic interactions and magnetization reversal in ferromagnetic wires," *Phys. Rev. B*, vol. 56, no. 6, pp. 3265–3270, Aug. 1997.

[30]   A. O. Adeyeye, J. A. C. Bland, and C. Daboo, "Magnetic properties of arrays of 'holes' in Ni80Fe20films," *Appl. Phys. Lett.*, vol. 70, no. 23, pp. 3164–3166, 1997.

[31]   G. Schutz *et al.*, "Absorption of Circularly Polarized X Rays in Iron," 1987.

[32]   J. Stohr *et al.*, "Element-Specific Magnetic Microscopy with Circularly Polarized X-Rays," *Science (80-.).*, vol. 259, pp. 658–661, 1993.

[33]   C. T. Chen, F. Sette, Y. Ma, and S. Modesti, "Soft-x-ray magnetic circular dichroism at the L2,3 edges of nickel," *Phys. Rev. B*, vol. 42, no. 11, pp. 7262–7265, 1990.

[34]   G. Schtz *et al.*, "Absorption of circularly polarized x rays in iron," *Phys. Rev. Lett.*, vol. 58, no. 7, pp. 737–740, 1987.

[35]   Y. Oba *et al.*, "X-ray magnetic circular dichroism study on ferromagnetic Pd nanoparticles," *J. Phys. D. Appl. Phys.*, vol. 41, no. 13, p. 5, 2008.

[36]   K. Ito *et al.*, "X-ray magnetic circular dichroism of ferromagnetic Co4N epitaxial films on SrTiO3(001) substrates grown by molecular beam epitaxy," *Appl. Phys. Lett.*, vol. 99, no. 25, p. 252501, 2011.

[37]   L. Aballe, M. Foerster, E. Pellegrin, J. Nicolas, and S. Ferrer, "The ALBA spectroscopic LEEM-PEEM experimental station: Layout and performance," *J. Synchrotron Radiat.*, vol. 22, pp. 745–752, 2015.

[38]   M. Foerster *et al.*, "Custom sample environments at the ALBA XPEEM," *Ultramicroscopy*, vol. 171, pp. 63–69, 2016.

[39]   B. Gilbert, R. Andres, P. Perfetti, G. Margaritondo, G. Rempfer, and G. De Stasio, "Charging phenomena in PEEM imaging and spectroscopy," *Ultramicroscopy*, vol. 83, no. 1–2, pp. 129–139, 2000.

[40]   G. Binnig, C. F. Quate, and C. Gerber, "Atomic Force Microscope," *Phys. Rev. Lett.*, vol. 56, no. 9, pp. 930–933, Mar. 1986.

[41]   D. Passeri *et al.*, "Magnetic force microscopy: quantitative issues in biomaterials," *Biomatter*, vol. 4, p. e29507, 2014.

[42]   K. D. Jandt, "Atomic force microscopy of biomaterials surfaces and interfaces," *Surf. Sci.*, vol. 491, no. 3, pp. 303–332, Oct. 2001.

[43]   S. P. Li *et al.*, "Flux closure structures in cobalt rings," *Phys. Rev. Lett.*, vol. 86, no. 6, pp. 1102–1105, 2001.

[44]   J. C. Gartside *et al.*, "Realization of ground state in artificial kagome spin ice via topological defect-driven magnetic writing," *Nat. Nanotechnol.*, vol. 13, no. 1, pp. 53–58, 2018.

[45]   W. Fuller Brown, "Micromagnetics : Successor to domain theory ?," *J. Phys. Radium*, vol. 20, no. 3, pp. 101–104, 1959.

[46]   "Magpar. http://www.magpar.net/." .

[47]   U. of Southampton, "Nmag. http://nmag.soton.ac.uk/nmag/." .

[48]   A. Vansteenkiste, J. Leliaert, M. Dvornik, M. Helsen, F. Garcia-Sanchez, and B. Van Waeyenberge, "The design and verification of MuMax3," *AIP Adv.*, vol. 4, no. 10, pp. 1–32, 2014.

[49]   J. Nickolls and W. J. Dally, "The GPU Computing Era," *IEEE Micro*, vol. 30, no. 2, pp. 56–69, 2010.

Chapter 5 - Modelling of Nanoring Arrays

5.0 Introduction

This first research chapter presents modelling used to define and explore an artificially created emergent system of magnetic nanostructures. As emergence is complex behaviour manifesting from simpler interactions between elements, §5.1 defines these constituent elements as a simple system of interconnected nanorings, i.e. arrays of nanowire rings that overlap their neighbours to create wire junctions.

In §5.2, micromagnetic modelling is presented to investigate the validity of assumptions made about ring behaviour in light of previous literature and planned experiments and how emergence in multi-ring systems may manifest.

§5.3 presents an analytical model created to predict behaviour of increasing numbers of interconnected rings in large arrays. This approach uses domain wall (DW) population as the state variable of the array in order to predict the steady-state magnetic behaviour of ring arrays subject to rotating magnetic fields. In this section, the analytical model created prior to this work is interrogated in a linear chain of interconnected rings and updated to account for missing terms.

§5.4, §5.5 and §5.6 cover the update to analytical models of square, trigonal and 'defect' interconnected nanoring array types by applying the same method for updating the linear chain. New analytical models are presented in each section.

All micromagnetic simulations reported as figures in this thesis are provided in original .gif format on the electronic copy that this thesis is submitted with.

5.1 The Interconnected Magnetic Nanoring System

Emergence describes characteristic complex large-scale phenomena that manifest as the result of many simpler but varied interactions occurring between smaller, component units. A magnetic nanoring array is potentially one such simple system, with individual soft ferromagnetic rings able to support magnetic configurations of a 'vortex' with no DWs or an 'onion' state with two DWs [1]. As discussed in §3, the particular magnetic state of a nanoring depends on the history of applied magnetic field, temperature, and ring geometry [2].

By applying a rotating magnetic field to an onion state nanoring, the DW positions in the ring generally follow the sense of the field [3]. If one wall could be trapped, for example by the introduction of a defect in the ring [4], the other wall will continue to rotate into the trapped wall and cause annihilation of both [5].The loss of the DWs will see the onion state configuration becoming a vortex state, and the overall magnetisation of the ring would also fall to zero.

It is well known (e.g. [6], [7]) that pinned DWs can overcome the pinning defect by the addition of energy into the system to overcome the energy barrier induced by the change in geometry in the magnetic medium. Commonly, this is achieved through increasing the probability of de-pinning by increasing the temperature of the system (reducing the mean waiting time [8] for de-pinning) or the strength of the applied field.

Whilst notched nanowires/nanorings are commonly experimented on [4], [6], [9] wire junctions also create potential barriers that pin DWs due to the local change in geometry [10]. Overlapping nanorings have been investigated relatively little [11], [12]but are of interest here as the junction between rings presents a pinning potential for DWs to overcome.

The other important principle relevant here is of adjacent DWs meeting and 'annihilating', resulting in the loss of both DWs and a continuous magnetic domain instead. This effect is also well known and observed in nanostructures [5], [13].
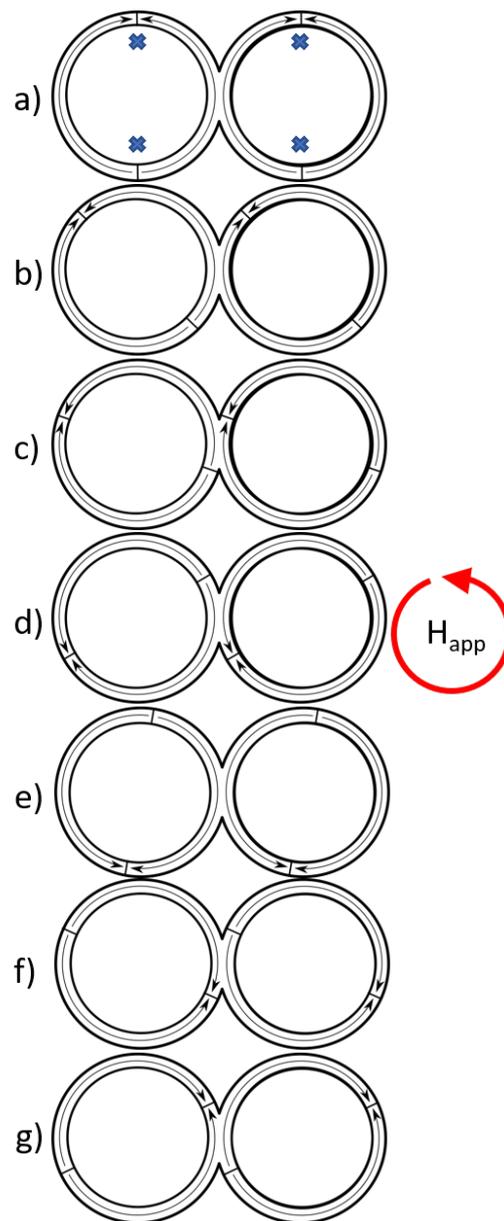
Figure 5.1. Schematic of two connected soft ferromagnetic nanowire rings (a) initially in the magnetic 'onion' state with two domain walls per ring. Arrows show magnetic domain orientation and black lines across the rings show the position of domain walls. As a rotating magnetic field of infinite strength is applied to the two ring system in a), DWs (marked with blue crosses in (a)) are free to progress around each ring (b-g).

Consider the system of two nanorings presented in Fig. 5.1 as strong applied magnetic field, H_{app}, sufficient to cause DWs to overcome any pinning potentials, is rotated anti-clockwise in the sample plane. There are four DWs in this system, located on opposite sides of each ring (marked with blue crosses); Fig. 5.1a) shows their initial configuration. The DWs will follow the sense of the field rotation and Fig. 5.1b)-g) show

the progression of DW position. In this regime of reliably overcoming pinning, DWs propagate much as they would in unconnected rings.

Figure 5.2 shows the dynamic principle of two joined rings initially in onion states (Fig. 5.2a) when the applied rotating field is strong enough to move walls through nanowires but not to overcome the pinning potential of the junction.
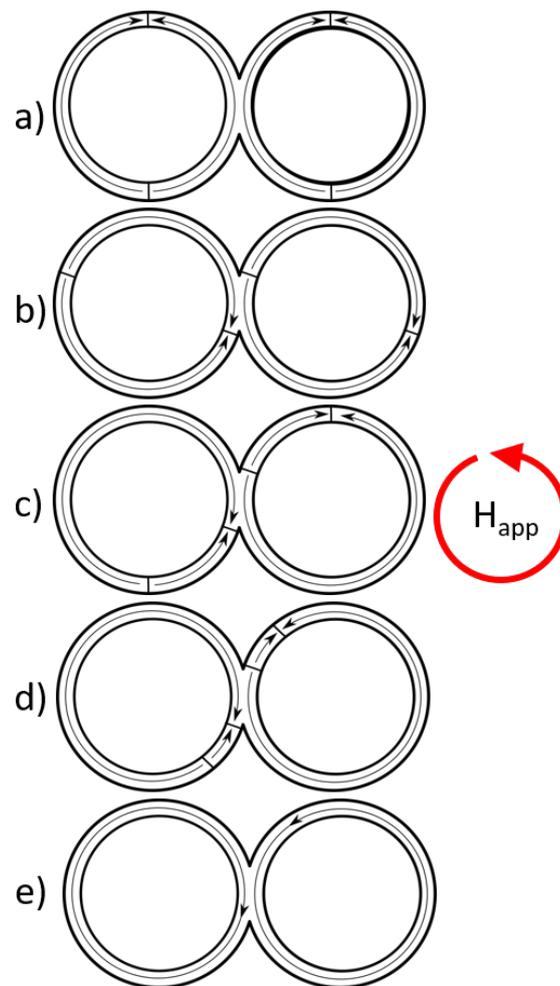

Figure 5.2. A system of two interconnected nanorings with a relatively small applied field, H_{app}, that is insufficient to overcome the energy barrier presented by the junction. As the sense of the applied field progresses, the DW pair in each ring is brought closer to the junction and eventually each pair annihilates. Two vortex state nanorings are left in e).

This means that the first DWs to reach the wire junction become trapped there (Fig. 5.2b) and c)); they can no longer follow the sense of the applied field, although this also prevents it from moving backwards away from the junction. The other DWs continue to rotate with the sense of the applied field (Fig. 5.2c) until they reach the pinned DWs (Fig. 5.2d). They will then annihilate the pinned DWs. This will convert the system's

magnetisation configuration from four DWs to zero, and from two onion state rings to two vortex states.

These principles can then be extended to systems with more rings. For example, Fig. 5.3 shows a schematic of magnetisation evolution in a chain of three nanowire rings. Here, the rings initially have 'onion' magnetic configurations with DWs aligned along the vertical axis (Fig. 5.3a). The rotating field strength causes DWs to become pinned at junctions (Fig. 5.3b), although each of the outer rings still have a free DW that continues to follow the sense of the applied field (Fig. 5.3c&d). The free DWs contact the pinned ones, causing DW annihilation and converting the edge rings from onion to vortex states (Fig. 5.3e). The central ring is unchanged, as both its walls have been trapped by the junction and are unable to switch between states. The total DW population in the three-ring system has changed from six to two.
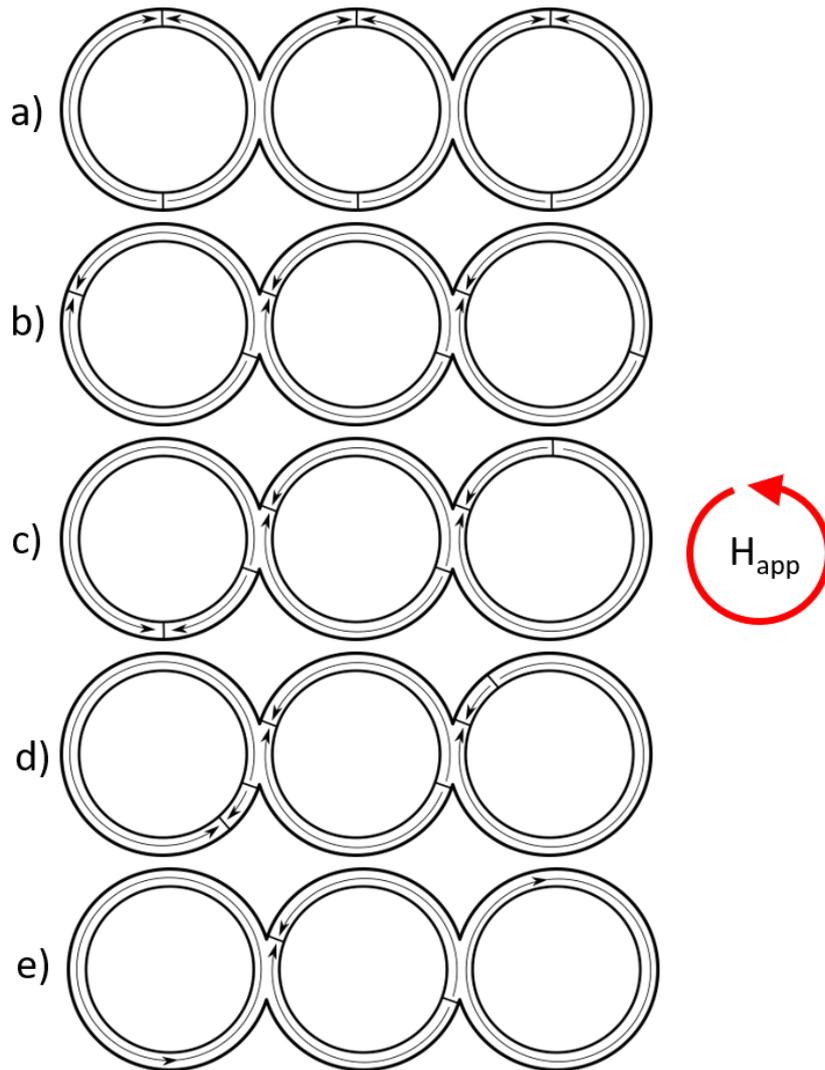
Figure 5.3. A system of three interconnected nanorings with a low rotating field applied, H_{app}, that is insufficient for DWs to overcome the energy barrier at the junction. As the wall pair in the outer ring is still free to follow the sense of the field, conversion from onion to vortex occurs in the outer rings. Two DWs remain in the central ring and thus it stays as in the onion state.

.

Using larger arrays operated at intermediate rotating magnetic field strengths to give probabilistic DW pinning at junctions promises to yield complex magnetic behaviour, yet the interconnected nature of the structures means that this might lead to repeatable, large-scale ('emergent') behaviour.

5.2 Micromagnetic Modelling of Interconnected Nanorings

Micromagnetic modelling was used to simulate the two and three ring cases presented schematically in Figs. 5.1 – 5.3. Mumax3 [14] simulations were run on a cluster of GPU-based computation nodes. The parameter values of $Ni_{80}Fe_{20}$ were used, i.e. M_S = 715 $\times 10^3$ A/m (refer to §4.8), α = 1, K_1 = 0, A_{ex} = 13pJ/m. Cell sizes were $4nm^2$, grid sizes were scaled to give 1000 cells per ring diameter, while a single cell was used through the thin structures' thickness. A simulation temperature of 0K was used throughout, which means that all simulations were deterministic and no probabilistic pinning would be seen.

The rings were initialised into onion states by applying a large (1000 Oe) external field in the y-direction (see Fig. 5.4) and then allowed to relax. The magnetic rotating field of fixed magnitude was updated by 15° every 12 ns, which allowed time for DWs to equilibrate into new positions. Unless otherwise stated, each ring was simulated to have tracks 400 nm wide and 20 nm thick, forming rings of 4 μm diameter that overlap by 50%, i.e. 200nm from each ring overlaps with its neighbour. Figure 5.4 shows the colour designation of magnetisation direction used throughout this thesis in images of micromagnetic simulations.
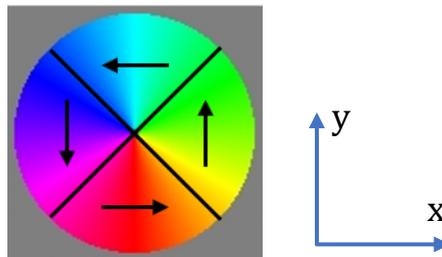

Figure 5.4 - Colour wheel and direction conventions for micromagnetic images in this thesis, with arrows showing the magnetisation direction represented by the colour. Z-direction is in the plane of the page.

5.2.1 Two connected nanorings – pin and propagate

Figure 5.5 shows micromagnetic simulations of two connected nanorings in onion state with two VDWs per ring. Figure 5.5a shows the case of a field strength insufficiently strong to allow DWs to overcome the wire junction's pinning potential (here, 50 Oe). DW pinning and subsequent annihilation with the DWs arriving later are seen here, as shown schematically in Fig. 5.2. This results in the initial onion state ring configurations being converted to vortex states, as suggested in Fig. 5.2. The point at which the first two DWs arriving at the junction become pinned (Fig. 5.5a, panel 3) shows that they merge to adopt a diamond-like configuration through the wire junction region.
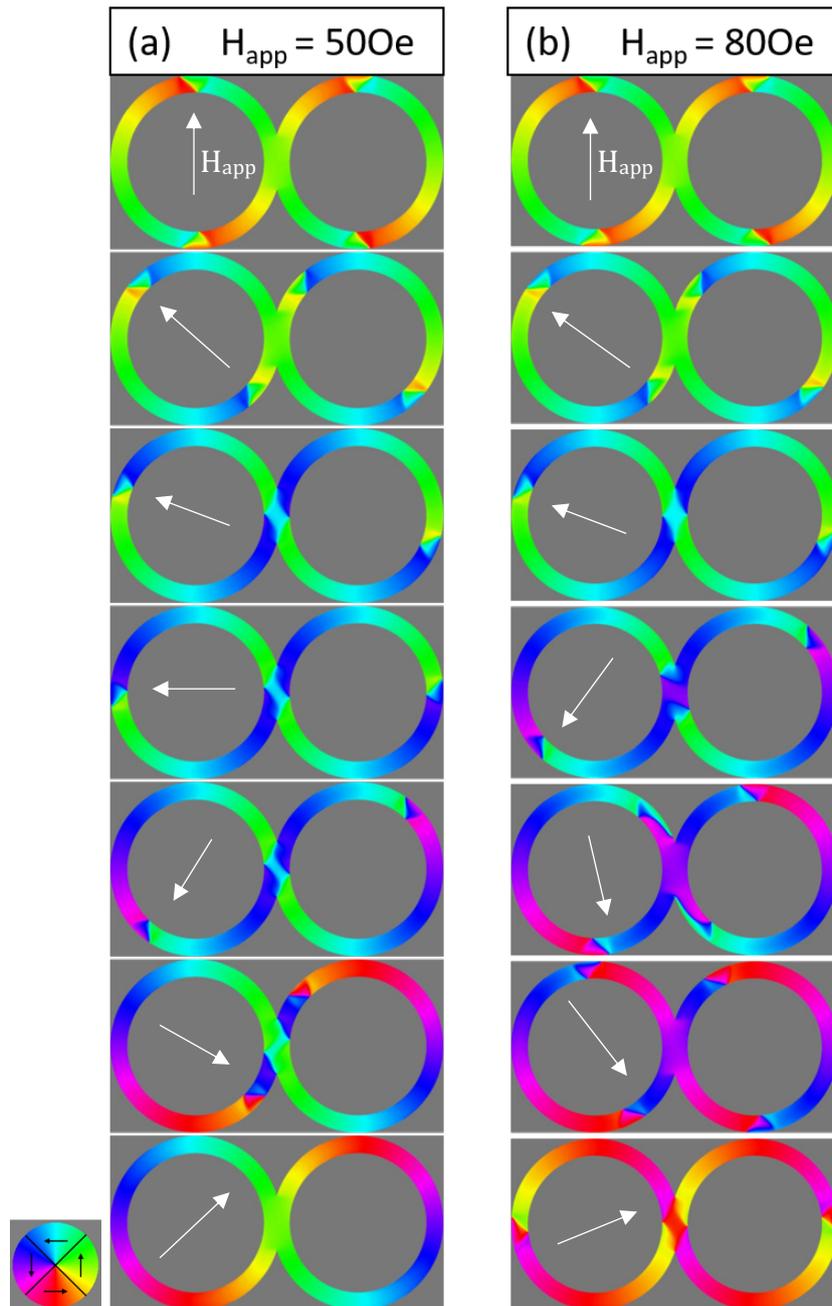
Figure 5.5. Micromagnetic simulation of a two interconnected nanoring system as a rotating field is applied (anti-clockwise). Ring dimensions are 4μm diameter, 400nm track width, 20nm thickness and 50% overlap. Timestep between images is irregular - frames are selected to show magnetisation states at points of interest. As DWs are rotated with the sense of the applied field, two walls from opposing rings will meet in the junction. These orientation of walls in the junction whilst they are here gives the visual impression of a diamond. (a) 50Oe applied rotating field strength is insufficient for depinning from the junction leading to annilhation of DWs. (B) 80Oe is a sufficient field strength to allow DWs to de-pin from the junction and continue to propagate around the system. White arrows denote the direction of the external field (H_{app}). Note a slight lag in DW position (consistent with [3])

Increasing the applied field strength allowed DWs to pass through the junction region, as shown in Fig. 5.5b for 80Oe field amplitude. The walls again form a diamond-like structure after entering the junction region (Fig. 5.5b panel 3); however, in this higher-

field case, the diamond shape distorts until two walls separate from it and return to their path around the ring. The $H_{app} = 50Oe$ case showed this distortion too (Fig. 5.5a panels 4&5), but not enough to separate. The field direction was almost parallel to the junction when the walls de-pinned under an 80Oe field amplitude (Fig. 5.5b panel 6), i.e. parallel to the magnetic domain left in the junction after depinning and almost 90° to the field required to introduce the walls to the junction. Increasing the field strength further caused DW depinning to occur sooner, and before the applied field vector became parallel to the wire junction.

Previous work on connected magnetic nanorings using techniques such as MFM has highlighted the junction as a region of magnetic complexity in a ground state ring [12] but offered insufficient spatial resolution to determine the detailed configuration, such as the diamond seen here.

5.2.2 Two interconnected nanorings – investigating other geometries

Figure 5.6 shows a simulation of two coupled rings with narrower (200nm wide) track width but still with 50% (100nm) wire overlap at the junction. The rings were again initialised into onion states and VDWs were obtained again. An anti-clockwise rotating magnetic field of amplitude 50Oe was applied. This resulted in identical behaviour to the wider wires at 50Oe (Fig. 5.5a), with junction pinning of DWs, annihilation with the arrival of subsequent DWs, and conversion of the rings from onion to vortex state. This time, however, the pinned DWs do not form a diamond structure within the junction but instead pin at the entrance to the junction in their respective wires, demonstrating a criticality to junction geometry for the formation of the diamond arrangement.
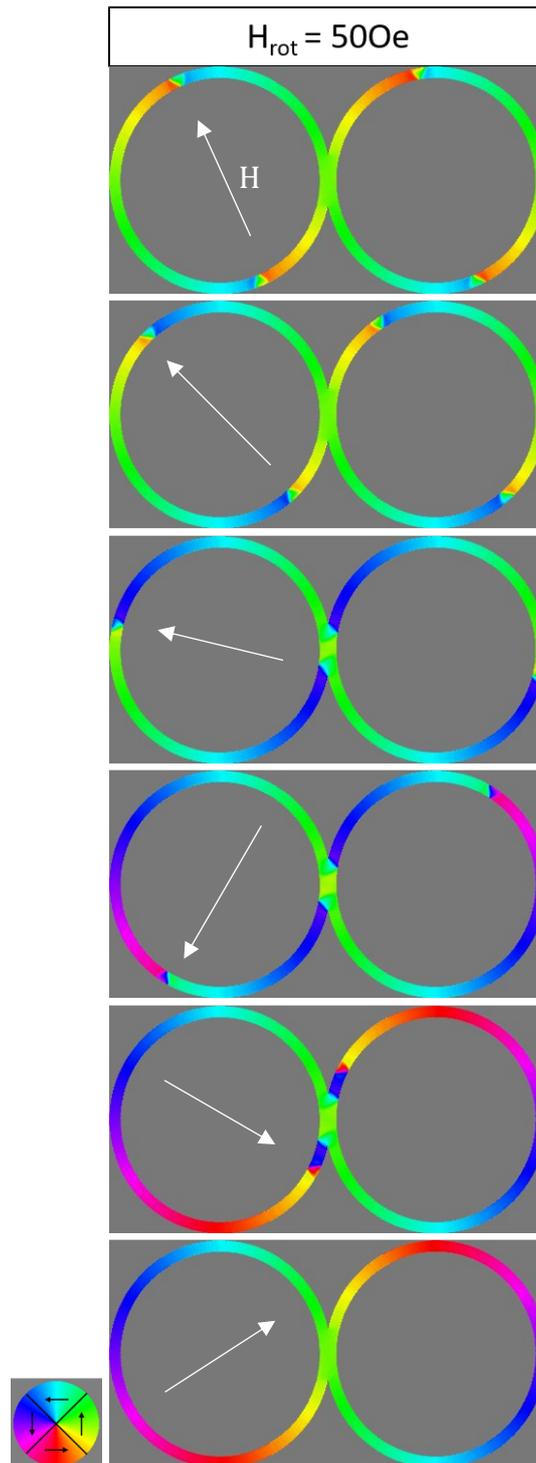
Figure 5.6 - Two joined narrow (200nm track width) rings showing the effect of an anti-clockwise rotating field of 50Oe on magnetic configurations with an initial onion state configuration. Ring dimensions are 4μm diameter, 200nm track width, 20nm thickness and 50% overlap. Applied field annotated with white arrows.
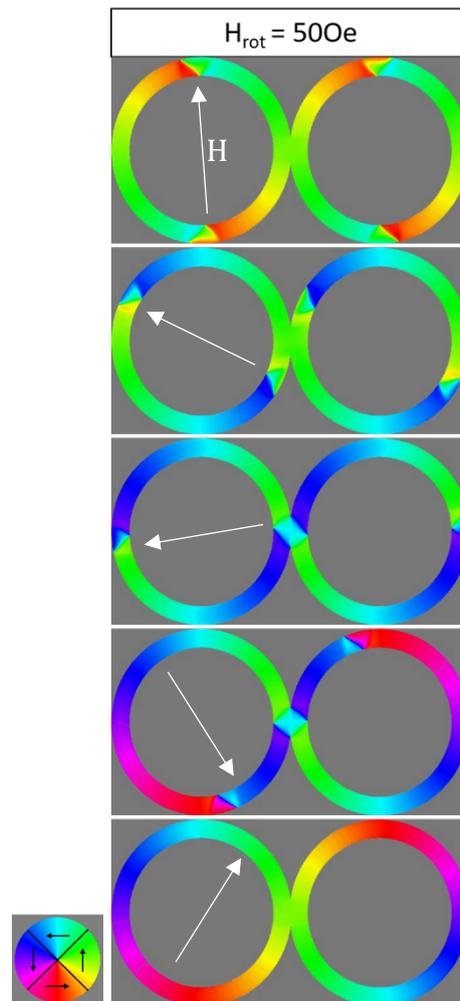
Figure 5.7 - Two interconnected nanorings with a reduced overlap of 10% of wire width. Other ring dimensions are 4μm diameter, 400nm track width, 5nm thickness. Applied rotating field (anti-clockwise) strength is 50Oe and annotated with white arrows.

Figure 5.7 shows 400nm wide wires but now overlapping by just 40nm (10 % of wire width). The rotating field strength is again 50Oe. The DWs again pin and are annihilated. The diamond configuration appears once more but is more resilient to the changing direction of applied field and does not appear to change noticeably.

Figure 5.8 shows the result of simulating a 5nm thick two-ring system with 200nm track widths and 50% overlap (as in Fig. 5.6) subject to a 50Oe rotating magnetic field. In these thinner structures DWs were able to pass through the wire junction at a field where they would previously pin. The differences in wire width and DW type are likely to have caused this. This is similar to differences in switching and DW pinning characteristics types observed in isolated, straight magnetic nanowires dependent on different DW types [15] and wire width [16] reported elsewhere. Micromagnetic modelling in this group has already investigated the transverse DW dynamics

dependence on nanowire thickness and width [17] and empirically derived a relationship between the two showing mobility is proportional to $\frac{width^{0.5}}{thickness^{0.25}}$. In interconnected nanorings, this appears to reduce the field at which depinning in a junction can occur. Later work with X-ray photoemission electron microscopy uses rings with these dimensions (§7.3).
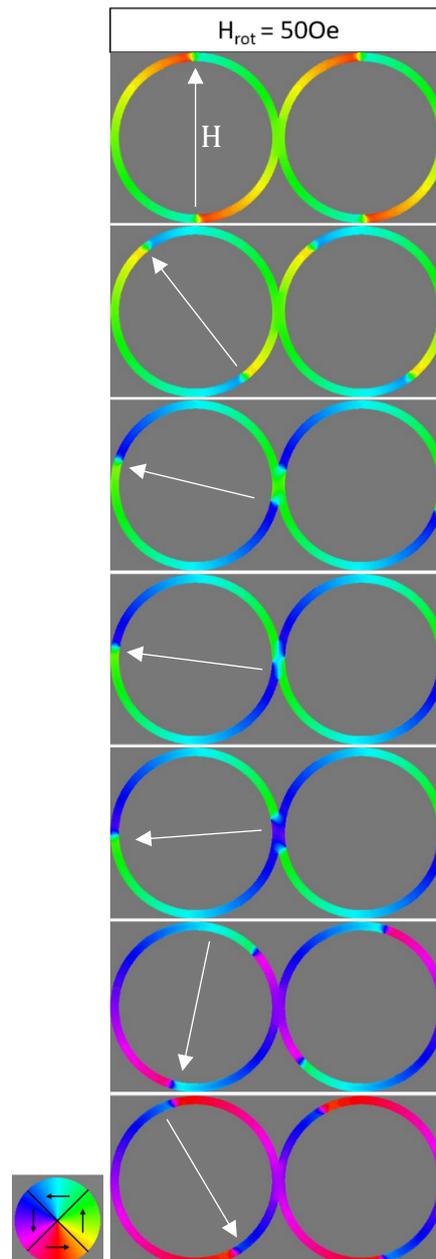

Figure 5.8. Micromagnetic simulation of DW propagation in two interconnected nanorings with diameter of 4μm, track width 200nm, 50% overlap and thickness 5nm and applied rotating field of 50Oe. Whereas this field has DW pinning in thicker (track and structure) simulations, propagation is achieved here. However a significant lag is seen in the sixth frame as one wall de-pins from the junction. By the last frame, this wall has nearly caught up again with the applied field direction. Applied field annotated with white arrows.

5.2.3 Three interconnected nanorings

Figure 5.3 presented a schematic of how the magnetic configuration of a linear three-ring system might evolve when DWs would pin at junctions. Micromagnetic simulations as presented in Fig. 5.9 shows that the population change in DWs (from six to two) is consistent with behaviour demonstrated in Fig. 5.3.
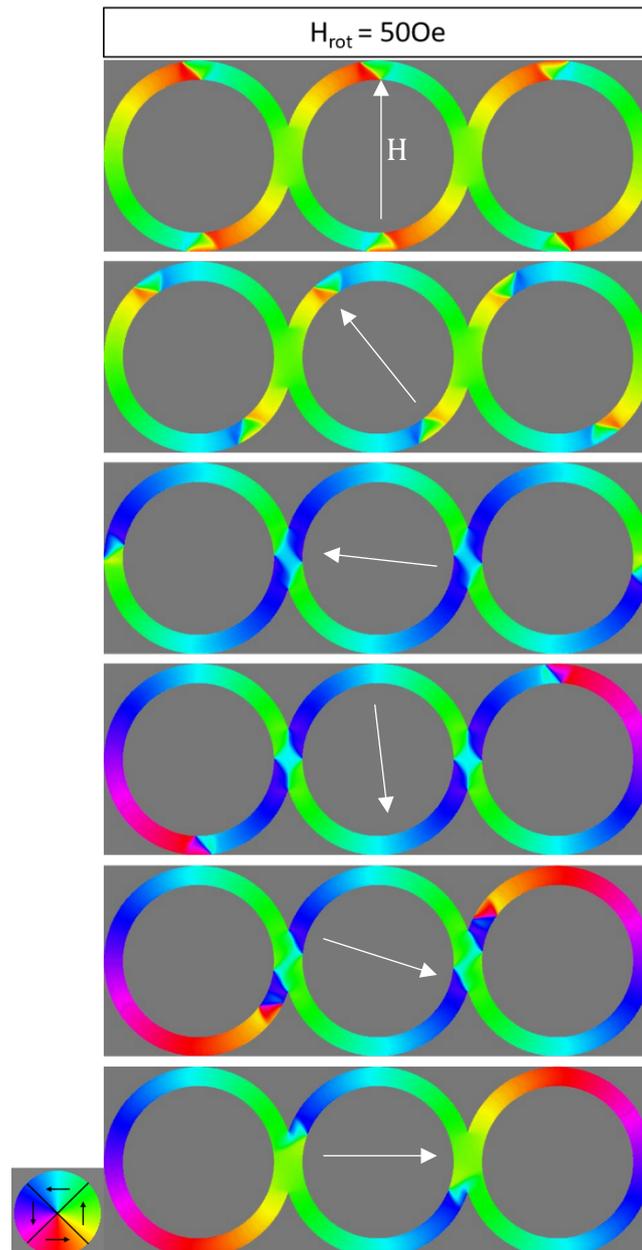

Figure 5.9 – Micromagnetic simulation of three interconnected nanorings with a 'low' applied rotating field (anti-clockwise) that is insufficient for DWs to de-pin from junctions (50 Oe). Edge rings have DWs annihilated converting from onion to vortex and the central ring is trapped in onion state. Ring dimensions are 4μm diameter, 400nm track width, 20nm thickness, 50% overlap. Applied field annotated with white arrows.

5.2.4 Population gain in interconnected nanorings

The previous simulations were of rings all initialised into 'onion' configurations, i.e. two DWs in each ring. Here, an initialised state is considered of two joined nanorings, one in an onion state, as before, and one in a vortex state, with no DWs (Fig. 5.10 panel 1). The script to obtain this is given in Appendix A1.2.

Figure 5.10 shows the micromagnetic simulation of how the ring system's magnetic configuration evolves from this initial state when a rotating magnetic field of 100Oe magnitude was applied. This field was large enough to drive a DW through the junction (Fig. 5.10 panels 2 and 3), resulting in two DWs being maintained in the original 'onion' state ring. An additional consequence, however, was that the DW passing through the junction created two further DWs that passed into the previously vortex-state ring, converting it to the onion state (Fig. 5.10 panels 4 and 5). As the applied field continued to rotate, the new DWs followed the sense of the field (Fig. 5.10 panels 6 and 7) and passed through the junction, as seen previously in Fig. 5.5 b). The newly created walls consist of two different types of TDW, one standard that has the same form as the TDWs in the adjacent ring (red circle) and the other compressed as a result of the configuration of moments in the adjacent domains (blue cross) (Fig. 5.10 panels 4 and 5). After passing through the junction again as the field continued to rotate, the compressed TDW was converted into a standard structure (Fig. 5.10 panel 7) as the orientation of moments in the adjacent domain equalises with the applied field.

These simulations of population gain used a smaller step size of 10° rather than 15° to better observe nucleation behaviour.
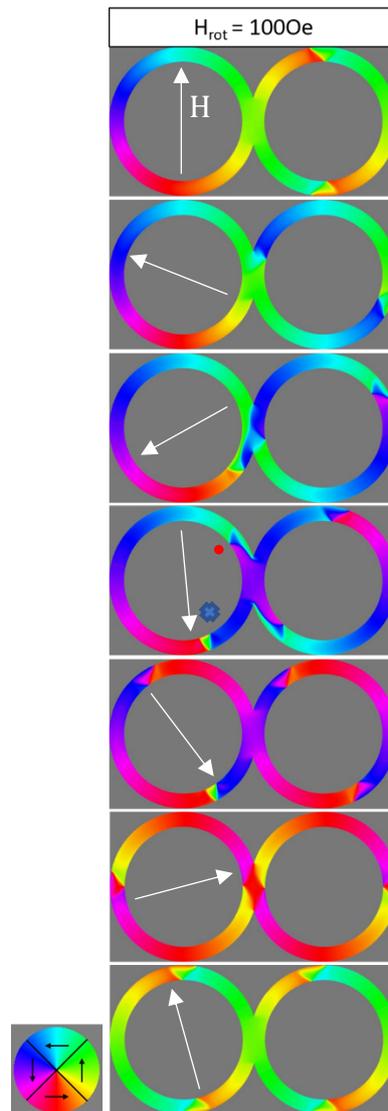
Figure 5.10. Results of micromagnetic simulations of an applied rotating field (anti-clockwise) of 100Oe applied to a two-ring system initialised such that one ring is onion and the other is vortex (panel 1). As a domain wall from the onion state ring moves across the junction a DW is nucleated in the lower arm of the vortex state ring. With continued rotation another DW is nucleated in the upper arm and these are free to rotate with the sense of the field. Applied field annotated with white arrows. The red circle denotes a 'standard' TDW similar to those in the adjacent ring. The blue cross shows a 'compressed' TDW forced into this state by the configuration of the domain it nucleates into.

The field amplitude needed in this model to pass a single DW through the wire junction was 100Oe but was 80Oe when two DWs arrived at a junction and continued to propagate. This difference is likely to be due to each DW having to expand less when two are present at a junction compared to when just one is present

The behaviour observed in Fig. 5.10 can be considered in straightforward terms as single DW propagation through a four-wire junction. It may also be described as

conversion of a ring in a magnetic vortex state to an onion state, or as DW repopulation of a previously 'empty' ring. These higher level descriptions will prove invaluable in later experiments dealing with arrays of larger numbers of rings.

DW repopulation is also observed in nanowire rings of different geometries. For example, Fig. 5.11 shows the same phenomenon in a two-ring system, again of 400 nm wide, 20 nm thick wires, but with a smaller overlap (10%) than in Fig. 5.10. The minimum magnetic field amplitude to achieve single DW passage through the wire junction increased to 150Oe here. The change in junction geometry to a shorter, wider region resulted in both new DWs immediately having a vortex structure (Fig. 5.11 panel 6).
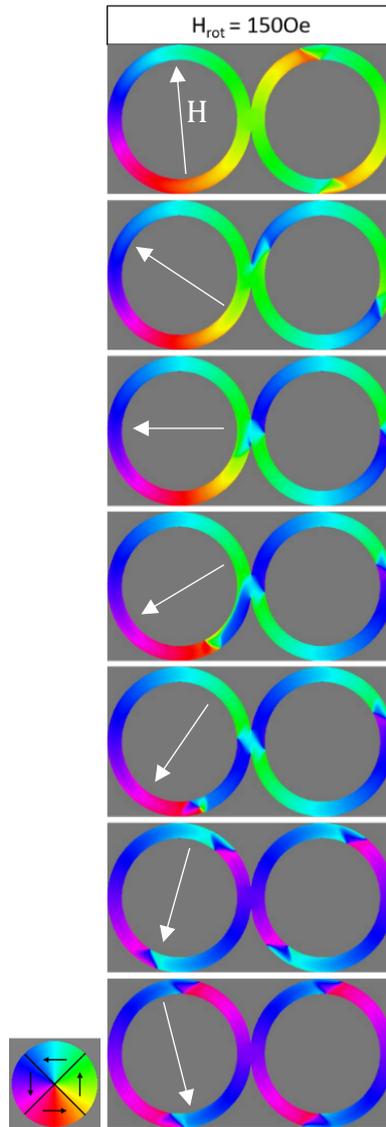
Figure 5.11. Two ring interconnected nanoring system with a 10% overlap initialised into one onion/one vortex configuration. Ring dimensions are 4μm diameter, 400nm track width and 20nm thickness. Image progression shows an applied rotating field (anti-clockwise) of 150Oe.

5.3 Analytical modelling of DW population

DW gain mechanisms have been shown at sufficiently high fields under certain conditions (adjacent onion/vortex states). It has also been demonstrated that pinning at sufficiently low fields will preserve the DW population in non-edge ring systems and annihilate when a free domain wall comes around the ring.

What happens when the applied field lies somewhere between 'sufficiently high' and 'sufficiently' low boundaries? Depinning in nanowires is probabilistic (e.g. [18]), dependent on temperature and field strength as well as ring and junction geometry. Assuming this probabilistic regime of depinning occurs at an intermediate field between sufficiently high/sufficiently low, there will exist a probability that sometimes a wall will depin and can go on to cause population/depopulation events and sometimes it will not, leading to similar possibilities of being involved in those events.

Here, an analytical model is introduced to express the equilibrium between loss and gain mechanisms in a system of interconnected nanorings based on the probability of a domain wall passing a junction. This is initially presented for the case that walls are free-standing within the tracks rather than combined into diamond as seen in micromagnetic modelling, based on previous work by Mohaned Mahmoori [19]. Updates in this work consider the effect of diamond arrangement in junctions as well as include omissions to the original model to provide a more robust estimation based on observations in micromagnetic modelling.

The original model assumed a homogeneous DW population in an array of an arbitrary number of connected magnetic nanowire rings. The proportion (or population) of rings in onion states is W, with a maximum value of 1 (for all rings in onion states). Assuming that all rings are either in onion or vortex states means that the proportion of vortex states is $1 - W$.

The probability of a DW passing a junction, P_{pass}, was simplified as a single value and did not distinguish between one or two DWs arriving at a junction.

Different rings have different number of junctions, n, depending on the array design and a ring's position in the array, e.g. the centre, edge or corner rings in a square array have 4, 3, and 2 junctions, respectively. An array of R rings consists of f_n rings with n junctions, meaning that the proportion of rings with n junctions in the Mahmoori model was $C_n = \frac{f_n}{R}$.

For any set of rings with n junctions, the probability of a DW passing through all junctions without pinning in one cycle of rotating magnetic field was P_{pass}^n. This meant that the probability of a DW becoming pinned at some point in a field cycle was $\left(1 - P_{pass}^n\right)$.

DW annihilation occurs when one DW in an onion state is pinned and its partner DW was able to overcome all junctions between the pair's original positions opposite each other in the ring. For certain starting positions of DWs, the number of junctions that the mobile DW overcomes to achieve annihilation depended exactly on which junction the pinned DW was located. Therefore there must be a term to account for the relative proportions of rings that have different numbers of junctions to overcome for each ring type. For example, in a three junction ring, what proportions have one junction to overcome to cause annihilation and what proportion have two? In the Mahmoori model, these proportions were P_m where m is the number of junctions overcome to cause annihilation. This thesis retains elements of Mahmoori's original model that schematically outline starting positions, e.g. Fig. 5.12. From this, relative proportions can be calculated.

These parameters are summarised in Table 5.1, together with others used in the following model development.

Table 5.1 – Summary of parameters used for analytical modelling. Terminology follows from Mahmoori's original model.

Parameter	Definition
W	Proportion of onion states
$1 - W$	Proportion of vortex states
n	Number of junctions
$(P_{Pass})^n$	Probability of passing n junctions (assumes uniform probability) during a full cycle
$1 - P_{pass}^n$	Probability of pinning during a full cycle
W^+	Increasing component of DW population from repopulating vortex rings
W^-	Decreasing component of DW population from pinning and annihilation events
$P_1, P_2, P_3, P_4, \ldots, P_m$	Proportion of domain walls in the system that pass m junctions to reach its pair that is pinned
$C_n = \dfrac{f_n}{R}$	The ratio of total rings in a system with n junctions, f_n, to total rings, R. $C_1 + C_2 + \cdots C_n = 1$

The DW repopulation of a vortex state seen in Fig. 5.10 and of DW annihilation seen in Fig. 5.5 represent DW population gain and loss mechanisms, respectively. The increase in onion state (containing DWs) population per field cycle, W^+, can be calculated as:

$$W^+ = 2W(1 - W) \sum_1^n C_n (P_{pass})^n \qquad Equation \ 5.1$$

Here, the factor 2 is due to two DWs being in each onion state, W shows the number of available onion states (i.e. with DWs) to perform repopulation, 1-W shows the number of vortex states available to be repopulated (and so approximately the probability of a neighbouring ring to an onion ring being in a vortex state), and the summation shows the probability of DWs propagating completely around a ring, averaged for the different types and proportions of rings present.

The loss of ring states per cycle, W^-, is then given by:

$$W^- = 2W \sum_1^n C_n (1 - P_{pass}^n)(P_1 P_{pass} + P_2 P_{pass}^2 + \cdots P_m P_{pass}^n) \qquad Equation \ 5.2$$

where the factor 2 shows that either DW in an onion state may pin, W shows the number of onion state rings available, and the final term in parentheses gives the probability of the unpinned DW reaching the pinned DW, based on it having to overcome P_m junctions between them, where m = 1,2,3….

However, an update to the model considers the micromagnetically modelled ring systems and that there exist states where no junctions must be overcome before annihilation (refer to Fig. 5.5). The former is a consequence of DWs depinning from junctions rather than overcoming or "passing" them. For the latter, there must be an update such that the lowest value of m is zero and when this is the case it is invariant of P_{pass}. Equation 5.3. uses an updated form of W^- to show this , though Appendix 2.1 contains the original form of the analytical model).

At equilibrium, $W^+ = W^-$, therefore

$$2W(1-W)\sum_1^n C_n(P_{pass})^n =$$

$$2W\sum_1^n C_n(1-P_{pass}^n)(P_0 + P_1 P_{pass} + P_2 P_{pass}^2 + \cdots P_n P_{pass}^n) \qquad Equation\ 5.3$$

Simplifying and rearranging gives:

$$(1-W) = \frac{\sum_1^n C_n(1-P_{pass}^n)(P_0 + P_1 P_{pass} + P_2 P_{pass}^2 + \cdots P_n P_{pass}^n)}{\sum_1^n C_n(P_{pass})^n} \qquad Equation\ 5.4$$

$$W_{equilbrium} = 1 - \frac{\sum_1^n C_n(1-P_{pass}^n)(P_0 + P_1 P_{pass} + P_2 P_{pass}^2 + \cdots P_n P_{pass}^n)}{\sum_1^m C_n(P_{pass})^n} \qquad Equation\ 5.5$$

or

$$W_{eq} = 1 - \frac{B}{A} \qquad Equation\ 5.6$$

where B = $\sum_1^n C_n(1-P_{pass}^n)(P_0 + P_1 P_{pass} + P_2 P_{pass}^2 + \cdots P_m P_{pass}^n)$ and A = $\sum_1^n C_n(P_{pass})^n$

Equation 5.5 can be used to calculate DW population based on the geometric factors (C_n, P_0, P_1, P_2, P_3…P_m) and the probability of any DW passing any junction (P_{pass}). Thus, it can be applied to a huge range of arrays, geometries and systems after ascertaining the number of rings, R, and the number of rings with n junctions, f_n.

5.3.1 Chains of nanorings with an updated model

Consider the possible start positions for the different ring types in the chain system, i.e. where the number of junctions, n, can be 1 or 2. Figure 5.12 shows a schematic devised by Mahmoori to analyse start positions:
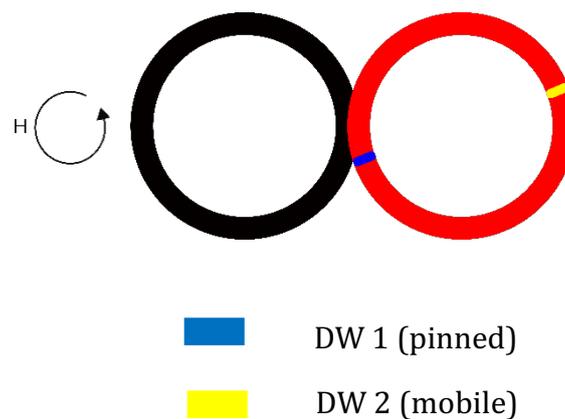
$n = 1$ (end rings)

Figure 5.12. Potential DW start position in a chain system ring with one junction as defined by Mahmoori With anti-clockwise applied field, there is one junction that must be overcome.

It is now known that DWs in a diamond arrangement within a junction will annihilate when they have not de-pinned and the critical parameter is not probability of passing a junction but probability of de-pinning. For the above case of two rings with one junction, where one DW is mobile and one is pinned, there will always be annihilation. This can be visualised by reversing the sense of the applied field in Fig. 5.12 to show the mobile DW is unimpeded (i.e. this is what will happen in the black ring).

Mahmoori counted these rings as contributing to the proportion of states that must overcome one junction, P_1, however this new analysis shows that for $n = 1$ the model is only dependent on P_0. This has already been reflected in the update to equation 5.3.

There are two possible start positions for the mobile DW (left ring or, as in Fig. 5.12, the right ring) and the pinned DW is always in the junction. For both possible start positions, there are zero junctions that need to be de-pinned from, thus $P_0 = 100\% = 1$. All higher P_m terms are zero.

Using equation 5.5, equilibrium wall population in end rings is:

$$W_{end} = 1 - \frac{C_1(1 - P_{de-pin})(1)}{C_1(P_{de-pin})^0} \qquad \text{Equation 5.7}$$

Equilibrium wall population here has been renamed W_{end} for this specific case as these represent the rings on the end of a linear chain. This general term can then be used in longer chains as they will also have two end rings.

P_{pass} has been renamed P_{de-pin} to reflect the change in behaviour of DWs in interconnected nanorings. Equation 5.6 has been altered in this updated model so that A is $\sum_1^n C_n(P_{de-pin})^{n-1}$ and B is $\sum_1^n C_n(1 - P_{de-pin}^n)(P_0 + P_1 P_{de-pin} + P_2 P_{de-pin}^2 + \cdots P_{n-1}P_{de-pin}^{n-1})$. This is justified by the general change that is one less junction to 'overcome' than previously modelled.
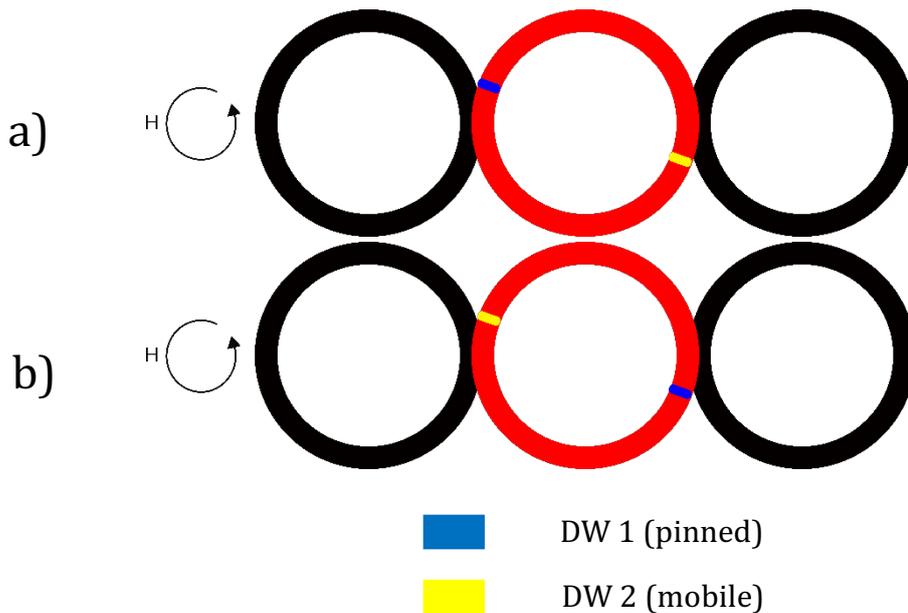
$n = 2$ (centre rings)

Figure 5.13. Potential DW start positions in a chain ring system with two junctions as defined by Mahmoori

Figures 5.13 a) and b) show Mahmoori's assumptions of DW start position two different pinning positions for DWs. In this configuration, there would be two junctions to overcome and $n = 2$. Based on new assumptions, with one mobile DW and one pinned DW, there only has to be de-pinning event from one junction for the newly mobile DW to reach the pinned partner DW, though there are still two possible cases depending on which of the walls is mobile. The proportion of possible cases that must de-pin from one

junction for a ring with two junctions to cause annihilation is therefore, 100%, so $P_0 = 0, \; P_1 = 1, P_2 = 0, P_3 = 0$, etc.

Equation 5.5 for a centre ring, with updates applied as per equation 5.7 becomes:

$$W_{centre} = 1 - \frac{C_2 \left(1 - P_{de-pin}^2\right)\left((1)P_{de-pin}\right)}{C_2 \left(\left(P_{de-pin}\right)^0 + \left(P_{de-pin}\right)^1\right)} \qquad Equation\ 5.9$$

where W_{centre} is the equilibrium wall population in the centre rings of a linear chain.

The equilibrium DW population of a linear chain is a sum of centre and end effects weighted to their proportion of the total chain size, $W_{eq} = C_{end} * W_{end} + C_{centre} * W_{centre}$.

At this point it is noted that the changes made to the Mahmoori model mean terms in $C_1, C_2 \dots C_n$ are present in both numerator and denominator and will cancel. They are no longer included in analytical model forms from this point. Introduction of weighted terms such as C_{end} maintains this dependence of model behaviour on relative proportions of ring types.

The equilibrium wall population in the whole system is therefore:

$$W_{eq} = C_{end} * W_{end} + C_{centre} * W_{centre}$$

$$= C_{end} * \left(1 - \frac{\left(1 - P_{de-pin}\right)}{\left(P_{de-pin}\right)^0}\right) + C_{centre} * \left(1 - \frac{\left(1 - P_{de-pin}^1\right)\left(P_{de-pin}\right)}{\left(1 + P_{de-pin}\right)}\right) \quad Equation\ 5.10$$

Tables 5.2 and 5.3 give example values of f and R, and in this example are used to calculate C_{end} and C_{centre}, for four and 10 ring chains. Care must be taken in future examples such as for a regular square that have rings with the same number of junctions but different types of behaviour and thus different weighting terms.

Table 5.2 – Analytical model parameters for a four ring linear chain properties

4 ring linear chain	
Parameter	Value
Junctions	3
R	4
f_1	2
f_2	2
f_3	0
f_4	0
f_5	0
f_6	0
C_{end}	$\dfrac{1}{2}$
C_{centre}	$\dfrac{1}{2}$

Table 5.3 – Analytical model parameters for a 10 ring linear chain properties

10 ring linear chain	
Parameter	Value
Junctions	9
R	10
f_1	2
f_2	8
f_3	0
f_4	0
f_5	0
f_6	0
C_{end}	$\dfrac{1}{5}$
C_{centre}	$\dfrac{4}{5}$

Equation 5.10 is then adjusted to describe a four-ring chain to become:

$$\frac{1}{2} * \left(1 - \frac{(1 - P_{de-pin})(1)}{(P_{de-pin})^0}\right) + \frac{1}{2} * \left(1 - \frac{(1 - P_{de-pin}^2)(P_{de-pin})}{(1 + P_{de-pin})}\right) \qquad Equation\ 5.11$$

and for an 10-ring chain as:

$$\frac{1}{5} * \left(1 - \frac{(1 - P_{de-pin})(1)}{(P_{de-pin})^0}\right) + \frac{4}{5} * \left(1 - \frac{(1 - P_{de-pin}^2)(P_{de-pin})}{(1 + P_{de-pin})}\right) \qquad Equation\ 5.12$$

5.3.2 Analytical chain model

Mahmoori's original plot was invariant on the number of rings in the chain, as shown in Fig. 5.14. This is clearly incorrect, such as is evident by analysis of a three ring chain in Fig. 5.9.
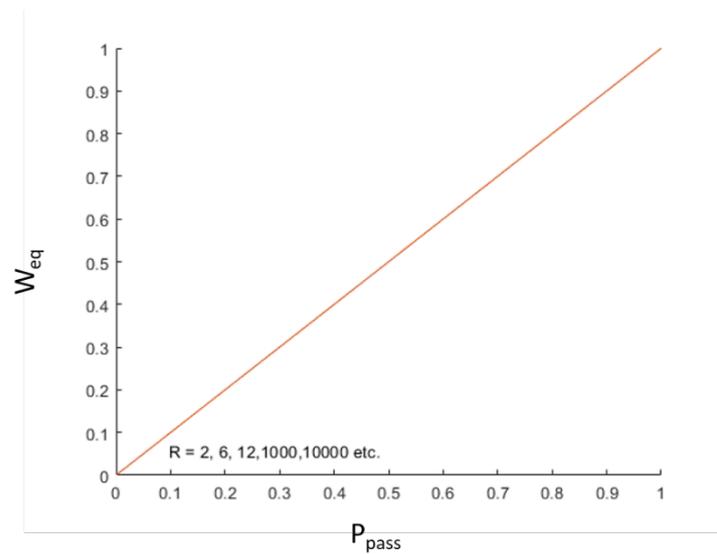

Figure 5.14 - Mahmoori's original analytical model for linear chain of interconnected rings.

With the adapted analytical model described by equation 5.10, the new modelled behaviour for a linear chain is shown in Fig. 5.15.
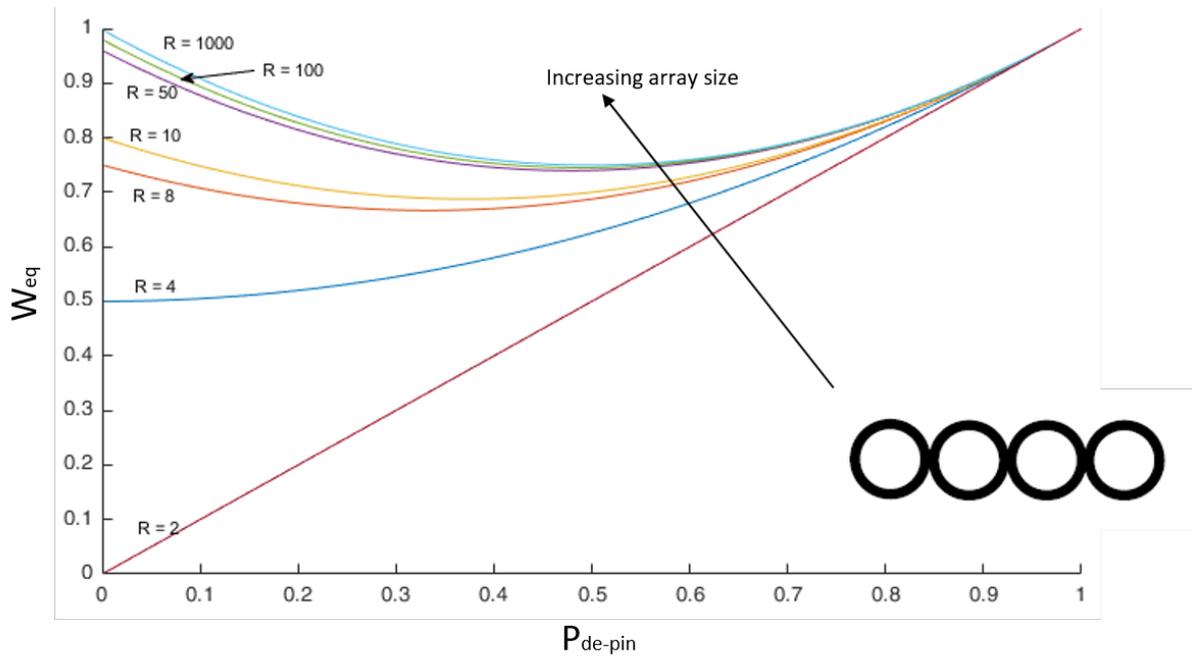
Figure 5.15 – Updated analytical model for a linear chain. Note the change to P_{de-pin} to reflect the change in known wall behaviour in an interconnected nanoring system.

Immediate differences are obvious; the four-ring chain no longer has zero equilibrium wall population, which reflects the micromagnetic model. Two ring chains now show full annihilation at $P_{de-pin} = 0$ and fully propagate with no change in DW population ($W_{eq} = 1$) when $P_{de-pin} = 1$. Towards the infinite chain, minimum wall population approaches 0.75 at $P_{de-pin} = 0.5$. There is a symmetric response either side of this minimum, non-monotonic response.

5.4 Regular square systems

5.4.1 Micromagnetic modelling of regular square systems

Micromagnetic modelling was used to simulate structures larger than the two and three ring chains studied earlier, to find behaviour at $P_{de-pin} = 0$ and $P_{de-pin} = 1$. The change in probability was achieved when the simulated field was above the threshold level for DW depinning from junctions. This approach does not investigate the effects of stochastic depinning as all junctions will either have DWs de-pin or none shall.
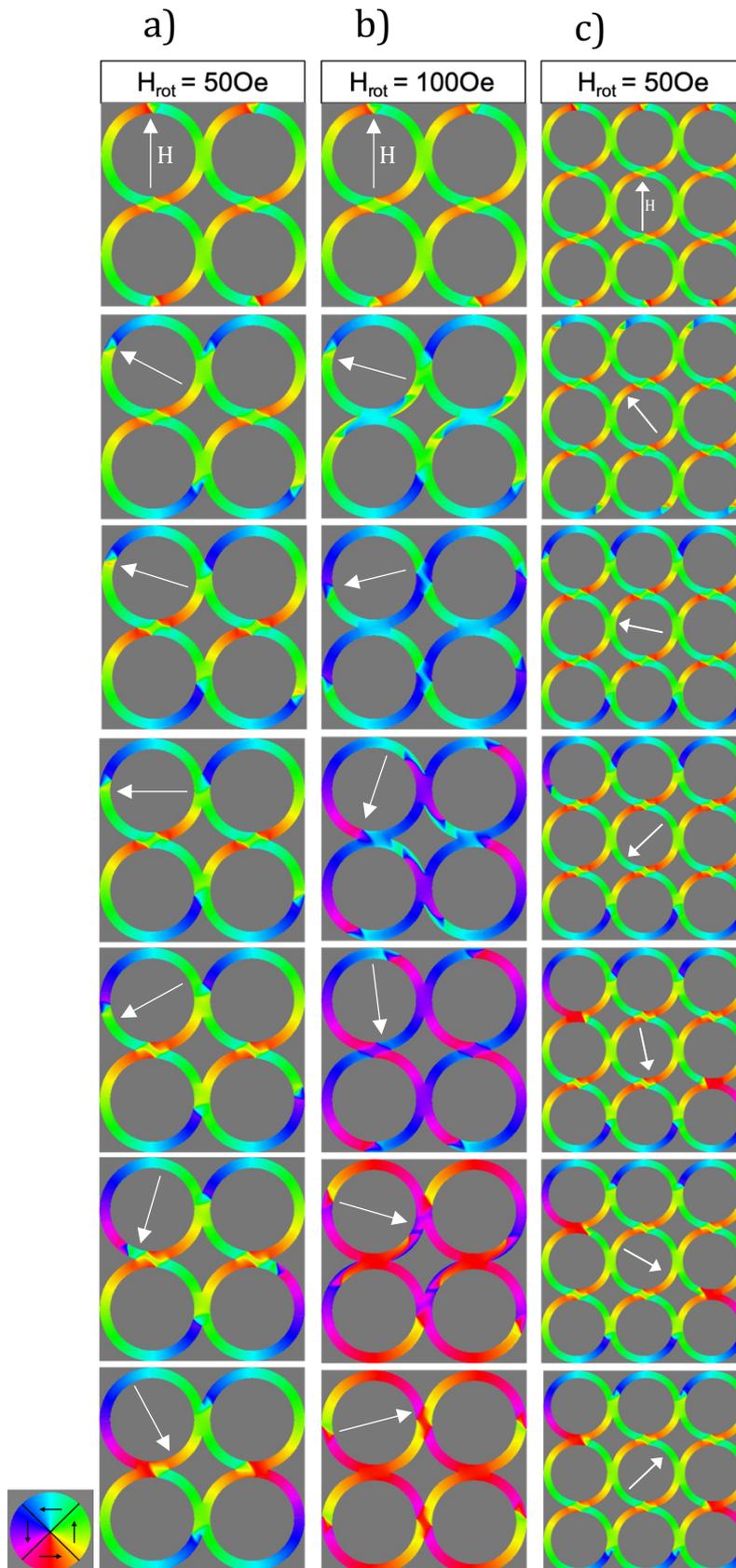
Figure 5.16. Micromagnetic simulations of standard (4µm diameter, 400nm track width, 20nm thickness, 50% overlap) interconnected nanorings in n=4 square arrays for a) 50Oe and b) 100Oe applied rotating fields and c) in an n = 9 square array with a 50Oe applied rotating field. Field rotation is anti-clockwise. At low fields that do not enable DW propagation, two corner rings annihilate as the free wall encounters no junctions to pin at. White arrows denote applied field direction.

Figure 5.16 shows three cases of interconnected square arrays. When $H_{app} = 50Oe$ in Fig. 5.16 a), walls are unable to overcome the potential barrier to de-pin from junctions. For the top right and bottom left rings this means their free DW becomes pinned at the next junction it encounters (on the vertical centre line). For the other two rings, their free DW rotates around the ring into the next junction it encounters which is already populated with trapped DWs. This causes annihilation and these two rings convert to vortex.

Simple analysis predicts that reversal of applied field rotation direction could be used to annihilate remaining walls in the micromagnetic model, but analytical models are built with an assumption of a single applied field rotation direction. Instead, two configurational considerations will be needed for corner rings.

In Fig. 5.16 b), coherent rotation with the externally applied field was possible at 100Oe applied field strength. This is the behaviour at $P_{de-pin} = 1$ and therefore equilibrium wall population will also be 1 at this point.

In addition to two junction corner rings being configurationally dependent, a micromagnetic simulation on a nine-ring array highlights a similar dependence in three junction edge rings Fig. 5.16 c). In this array, edge rings also retain initial DW population.

Limits on computational time prevented simulations of square arrays of 16 or more rings, although it is noted that this structure, the DWs in two of the corner rings will always annihilate at low fields, with the 'non-pinned' DWs not having any junctions to overcome, and the rest of the array will be locked in onion states. This scales up as the number of rings in the regular array increases.

The key to updating Mahmoori's model lies in calculating equilibrium population as a weighted sum of corner, edge and bulk ring states with the addition of configurational assumptions for corner rings and including previous changes given the diamond arrangement that reduces the number of junctions that must de-pinned from for annihilation to occur.

As the analytical model is homogeneous in that the overall population is a state variable, it is not well suited to these configurational issues that are dominant in small arrays. For

larger arrays, where bulk ring behaviour dominates, the model will become much more rigid. Experimentally this can be reflected by selection of a large array size to test modelled behaviour.

5.4.1 Analytical modelling of regular square systems

In a regular square system, the ring types will include those with two junctions at the corners of the square (f_2 in number) those with three junctions along the edges (f_3 in number), and those with four junctions constituting the bulk of the array (f_4 in number).

$n = 2$ (corner rings)

For the corner rings with two junctions there are two situations dependent on starting position of walls relative to the applied field (c.f. Fig. 5.16). Given that a four-ring square behaves like a four-ring chain (two annihilate and two don't), the general form of edge and centre rings are used to represent two configurations of corners. As the number of junctions has increased, the behaviour of the fixed corner ring is dependent on $\left(1 - P_{de-pin}^2\right)$. This represents that there are two junctions where de-pinning events can occur from to avoid annihilation.

$$W_{annihilating\ corner} = 1 - \frac{\left(1 - P_{de-pin}\right)(1)}{\left(P_{de-pin}\right)^0} \qquad \text{Equation 5.13}$$

$$W_{fixed\ corner} = 1 - \frac{\left(1 - P_{de-pin}^2\right)\left(P_{de-pin}\right)}{\left(1 + P_{de-pin}\right)^1} \qquad \text{Equation 5.14}$$

For both starting positions in $W_{fixed\ corner}$ there is a junction that must be overcome for annihilation to occur (which can be seen in Fig. 5.16). Hence the proportion of starting states of these corner rings are dependent only P_1 instead of P_0, and its value is 1.

For $n = 3$ (edge rings) and $n = 4$ (bulk rings), new forms of equation 5.5 are created as follows:

$n = 3$ (edge rings)

For n = 3 , the general equation of the system describing wall populations is dependent only on terms multiplied by C_3. Mahmoori's diagrams are used again as they are functionally similar – the pinned wall simply moves into the nearest junction when the field is applied to form a diamond. In case a) must de-pin from the left-hand junction and the top junction, so counts towards the proportion of P_2. This is the same for case b) which must de-pin from the right-hand junction and the top junction. For case c), only one junction needs to be de-pinned from to enable annihilation. Thus, the proportion of starting cases are distributed such that $P_2 = \frac{2}{3}$ and $P_1 = \frac{1}{3}$.

c)
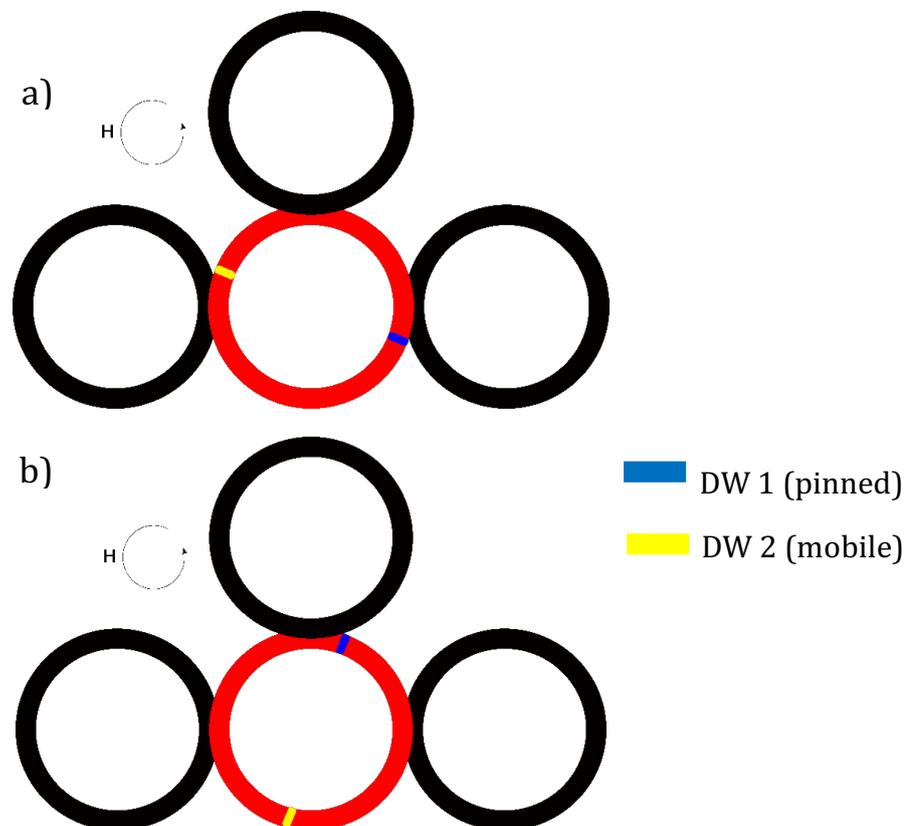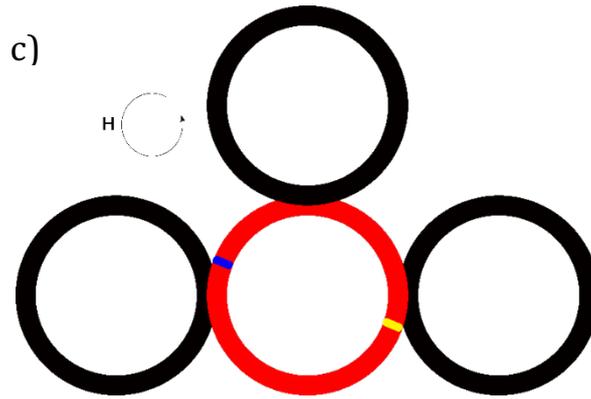
Figure 5.17. Potential starting positions of domain walls in rings with three junctions, as modelled by Mahmoori.

Thus, using n = 3 in equation 5.5 and adapted with similar changes as in equation 5.7, the wall population in an edge ring can be created

$$W_{edge} = 1 - \frac{\left(1 - P_{de-pin}^3\right)\left(\frac{1}{3}P_{de-pin} + \frac{2}{3}P_{de-pin}^2\right)}{\left(1 + P_{de-pin} + \left(P_{de-pin}\right)^2\right)} \qquad Equation\ 5.15$$

$n = 4$ (bulk rings)

Mahmoori's potential start positions of domain walls are straightforward, with each DW having two junctions to overcome before annihilation can occur (Fig. 5.17). This is still the same case when diamond arrangement considerations are made. For example, in Fig. 5.17 a), the mobile DW must de-pin from the right hand junction and the top junction for annihilation.
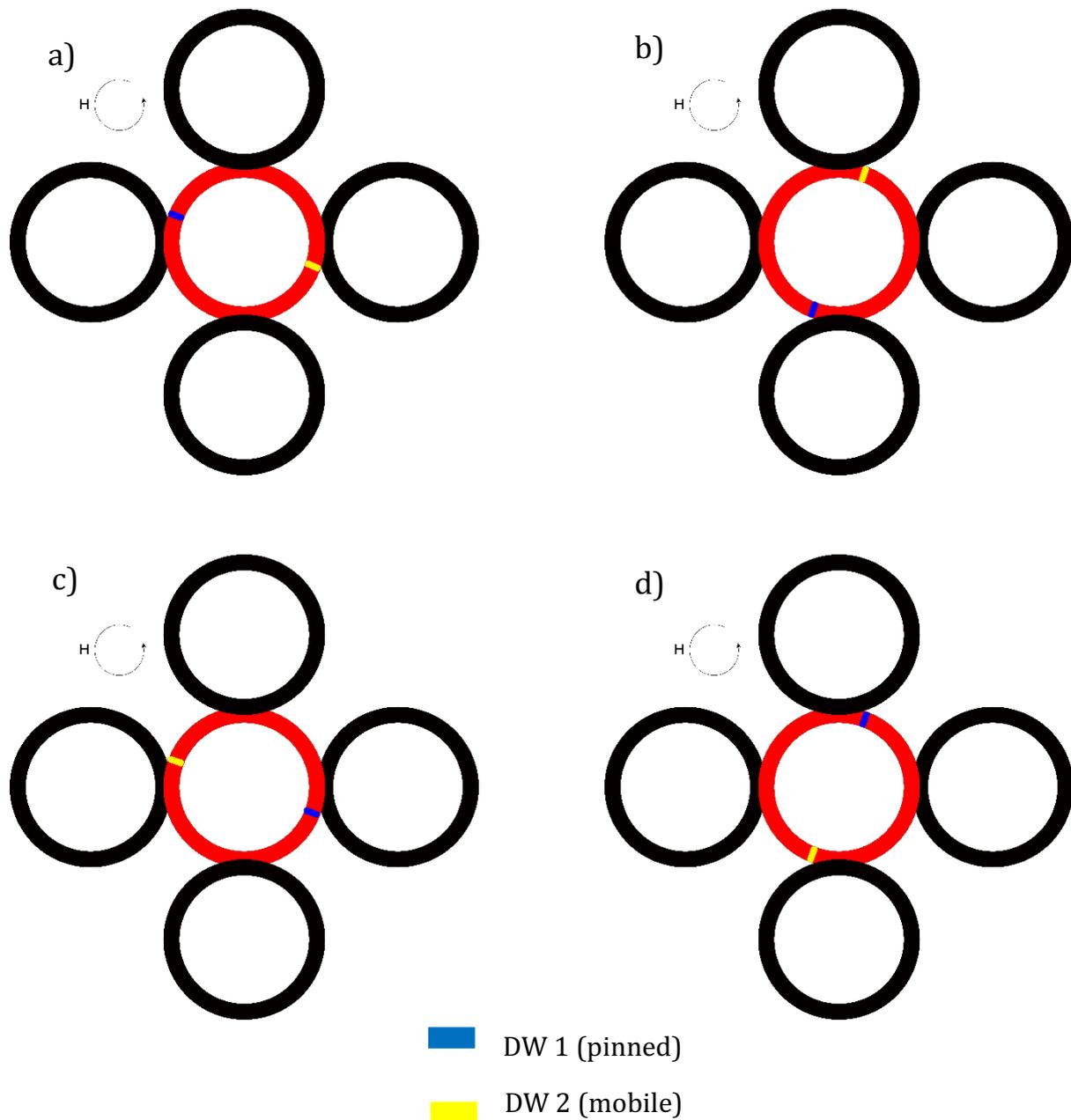
Figure 5.18 – Potential DW start positions for a bulk ring with four junctions following Mahmoori's notation. When accounting for the change to diamond arrangement within junctions there are still two depinning events for annihilation but one less junction for repopulation.

Therefore, $P_2 = 1$ and all other P_n coefficients are zero.

For bulk rings, applying updates as in equations 5.7, 5.9 and 5.15 the equilibrium DW population is.

$$W_{bulk} = 1 - \frac{\left(1 - P_{pass}^4\right)\left(P_{pass}^2\right)}{\left(1 + (P_{Pass}) + (P_{Pass})^2 + (P_{Pass})^3\right)} \qquad Equation \ 5.16$$

Mahmoori's original plot is presented for square systems in Fig. 5.19.
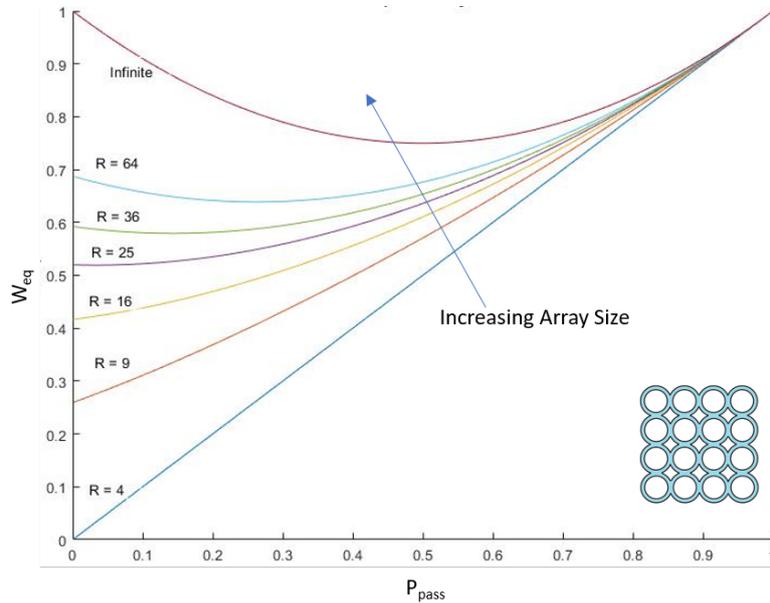
Figure 5.19 - Mahmoori's original analytical model for regular square arrays with increasing number of rings.

Figure. 5.19 is demonstrably erroneous when compared to Fig. 5.16 for R = 4; wall population is $\frac{1}{2}$ and not 0. By taking equilibrium wall population in the entire array as the weighted sum of corner, edge and bulk rings, equation 5.17 is created as the updated analytical model for regular square arrays.

$$W_{eq} = C_{fixed\ corner} * W_{fixed\ corner} + C_{annihilating\ corner} * W_{annihilating\ corner}$$
$$+ C_{edge} * W_{edge} + C_{bulk} * W_{bulk}$$

$$W_{eq=}\ C_{fixed\ corner} * \left(\left(1 - \frac{(1 - P_{de-pin})(1)}{(P_{de-pin})^0} \right) + \left(1 - \frac{(1 - P_{de-pin}^2)(P_{de-pin})}{(1 + P_{de-pin})} \right) \right)$$

$$+ C_{edge} * \left(\frac{(1 - P_{de-pin}^3)\left(\frac{1}{3} P_{de-pin} + \frac{2}{3} P_{de-pin}^2\right)}{((1 + P_{de-pin} + (P_{de-pin})^2)} \right)$$

$$+ C_{bulk} * \left(1 - \frac{(1 - P_{pass}^4)(P_{pass}^2)}{(1 + (P_{Pass}) + (P_{Pass})^2 + (P_{Pass})^3)} \right) \qquad Equation\ 5.17$$

Note the simplification of $C_{fixed\ corner}$ as this is equal to $C_{annihilating\ corner} = 2$

This is plotted in Fig. 5.20 for similar array sizes to Fig. 5.19.
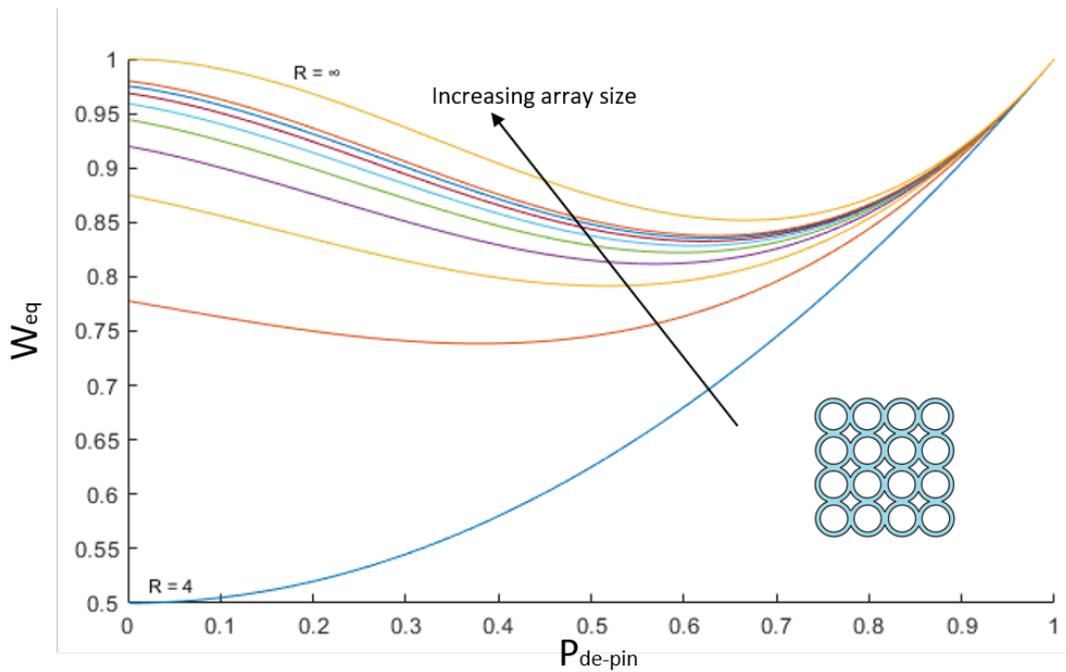

Figure 5.20 - Updated analytical model for regular square systems. Array size increases in square numbers from 4 to 100 with the infinite case shown (top-most line)

This model is more rigid for smaller arrays given the minimum equilibrium wall population at $P_{de-pin} = 0$ is equal to full population less the population of two rings, or $\frac{R-2}{R}$.

As the number of bulk rings dominates, $W_{eq} = W_{bulk}$ and equation 5.16 can be used to model DW population (yellow line in Fig. 5.20). This plot tends to an equilibrium wall population of 1 at $P_{de-pin} = 0$, which is consistent with bulk rings being locked in place, unable to change state. There is a minimum population at $P_{de-pin} \approx 0.67$ of 0.852. There is a difference in gradient either side of the minimum population reflecting a difference between the changes in rate of population gain and loss mechanisms. This is interesting to note given the difference in onset of propagation of DWs in Fig. 5.5 at 80Oe and the onset of repopulation at 100Oe in Fig. 5.10.

5.5 Regular trigonal system

5.5.1 Micromagnetic modelling of trigonal arrays

Micromagnetic modelling was also performed on a seven-ring trigonal array (Fig. 5.21). These had identical ring and junction geometries to those used in square arrays, with 4µm ring diameter, 400nm track width, 20nm thickness and 50% junction overlap. As with most other simulations, the structure was first initialised into a configuration in which all rings were in the onion state, with DWs aligned to a single axis. Anti-clockwise rotating fields of different amplitudes were then applied.

Under low fields where DWs pin always at junctions (5Oe; Fig. 5.21 a), two rings again underwent DW annihilation and became vortex states. Other rings all maintained two DWs, although the position of the DWs depended on the local ring arrangement relative to the initialised DW position.

The trigonal structures required higher fields to propagate DWs than was seen in the square arrays (10Oe is used in Fig. 5.21b, compared to 7.5Oe in square arrays above). This was surprising given the similarity of the rings geometries but must be a consequence of the different array geometry. The reduced distance between successive junctions in the trigonal arrangement reduces the aspect ratio of the track between junctions, which will have an influence on the magnetic behaviour in the soft magnetic materials investigated here. Micromagnetic images in Fig. 5.21 shows that some complex magnetic configurations emerge in and around the centre ring, which is likely to be representative of 'bulk' rings in larger arrays.

Establishing the simpler behaviour described by the analytical model may require thinner wire widths, in order to reduce the size of tracks and increase the shape anisotropy of regions between junctions. Figure 5.22 shows an identical trigonal array to Fig. 5.21 but with narrower wires, now 200nm. The low field (5Oe) behaviour with DWs becoming pinned at junctions (Fig. 5.22a) was very similar to that seen with the wider wires (Fig. 5.21a). In contrast, the narrower track width resulted in the applied field for propagation type behaviour increased to 15Oe (Fig. 5.22b). The DWs also now track the applied field direction more closely and the complex configurations at junctions seen with wider wires (Fig. 5.21b) did not appear with the narrower tracks.

The narrower wires, therefore, appear to recover wire-like behaviour between junctions and separate the junctions. Where this isn't the case (e.g. with wider wires), configurational dependencies may cause experiments to deviate from the simple analytical model. These might be described though simply by adjusting the pass probabilities in the analytical equations to represent DW passage through junctions specifically in the trigonal arrangement, rather than simply a DW passing through an isolated but otherwise identical junction.
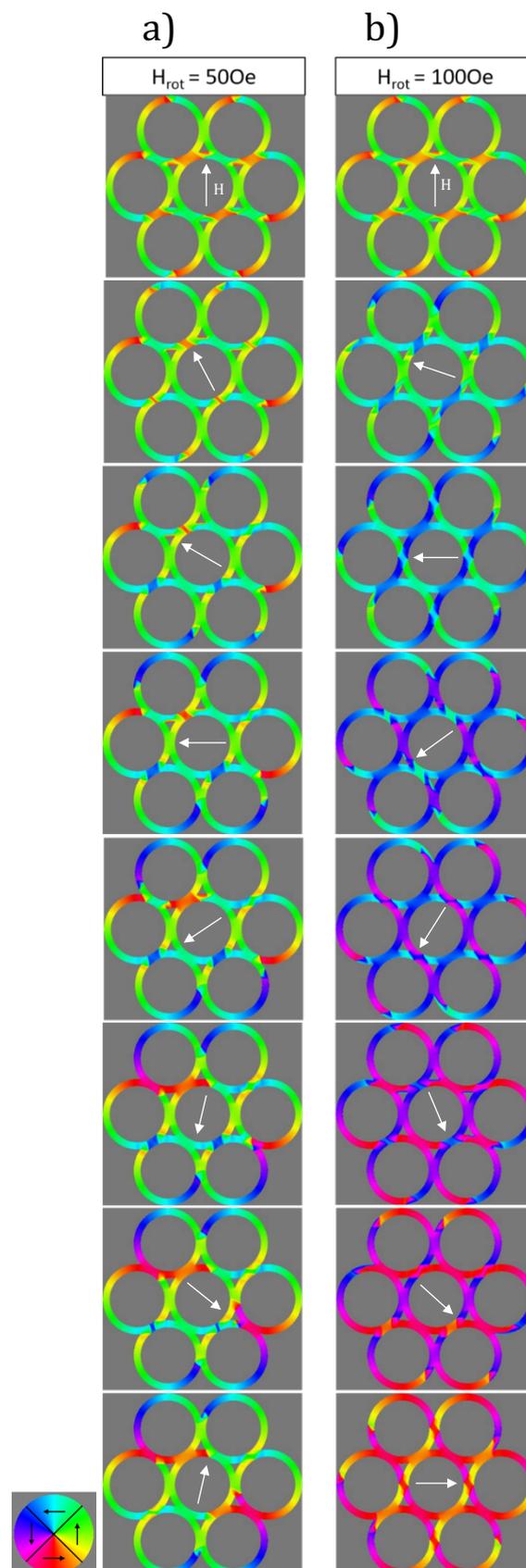
Figure 5.21. Mumax3 simulations of standard interconnected nanorings in n = 7 trigonal array for a) 50Oe and b) 100Oe applied rotating fields. Ring dimensions are 4μm diameter, 400nm track width, 20nm thickness, 50% overlap. Magnetic field rotation is anti-clockwise. At low fields that do not enable DW propagation, two rings in the outer layer of edge rings have DWs annihilated, changing the ring to vortex state. White arrows denote applied field direction.
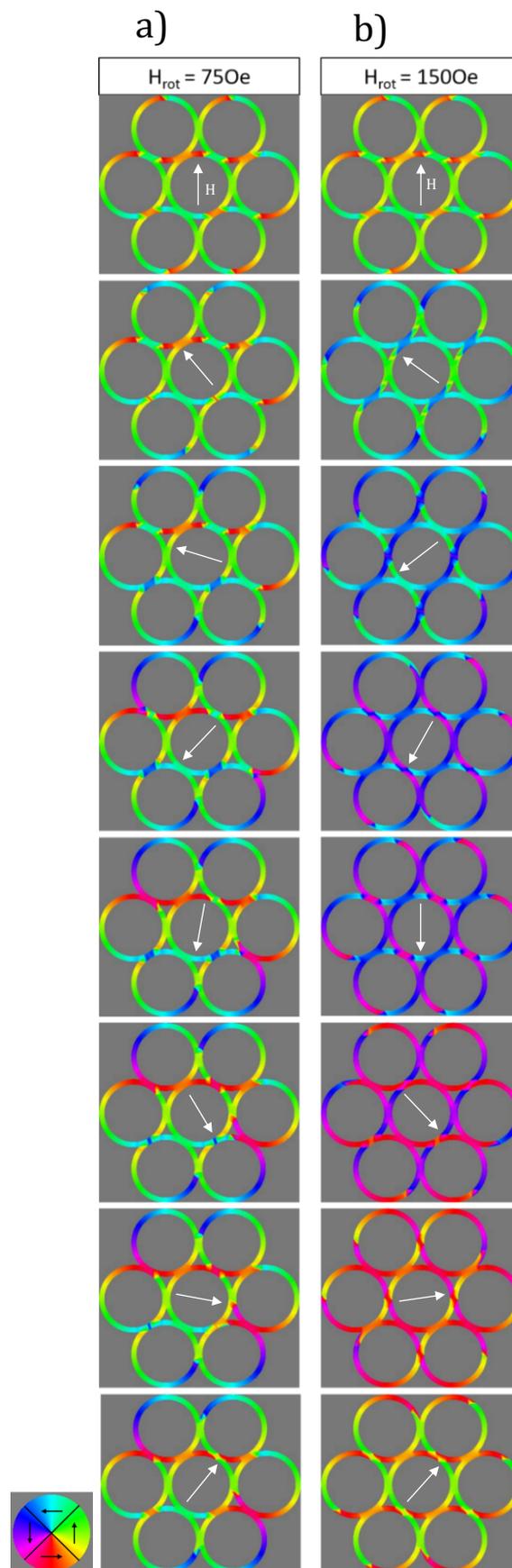
Figure 5.22. Mumax3 simulations of standard interconnected nanorings with simulated track widths of 200nm in n = 7 trigonal arrays for a) 75Oe and b) 150Oe applied rotating fields. Ring dimensions are 4μm diameter, 400nm track width, 20nm thickness, 50% overlap. Fields rotation is anti-clockwise, with white arrows showing applied field direction in each frame.

5.5.2 Analytical modelling of trigonal arrays

For a regular trigonal system, the types of rings that are found are f_3 on the 'corners' (the outmost ring on 60° axes from the centre of the ring), f_4 on the edges and f_6 in the bulk of the array. Fig. 5.23 shows a schematic of a 19-ring trigonal array to display all types of ring (as Fig. 5.22 only shows f_3 and f_6).
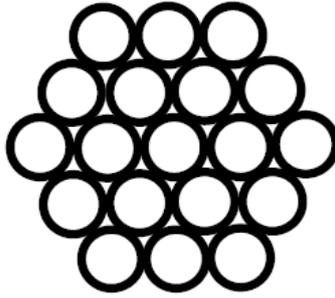

Figure 5.23 – Schematic of a 19-ring trigonal array, displaying all possible ring types in this arrangement.

Rings with three junctions generally have the same forms as derived in §5.4.2 but micromagnetic modelling showed two of these six are configurationally dependent and will always annihilate. Thus two forms of model must be created as with corner rings in square arrays. Edge rings have the same number of junctions as bulk rings in a square array but start position analysis shows a difference in values of P_n. It remains to derive an expression for systems with six junctions as is the case with the bulk of the trigonal array.

$n = 3$ (corner rings)

Using the general form of an edge ring in a square array will describe a fixed corner and the general form of an end ring in a chain will describe an annihilating corner. This is the same logic that was applied in equations 5.13 and 5.14.

$$W_{annihilating\ corner} = 1 - \frac{\left(1 - P_{de-pin}^1\right)}{\left(P_{de-pin}\right)^0} \qquad Equation\ 5.18$$

$$W_{fixed\ corner} = 1 - \frac{\left(1 - P_{de-pin}^3\right)\left(\frac{1}{3}P_{de-pin} + \frac{2}{3}P_{de-pin}^2\right)}{\left(1 + P_{de-pin} + \left(P_{de-pin}\right)^2\right)} \qquad Equation\ 5.19$$

$n = 4$ (edge rings)

The general form of a ring with four junctions was already found in equation 5.16. Fig. 5.24 applies analysis to start positions as previously to determine values for P_n.
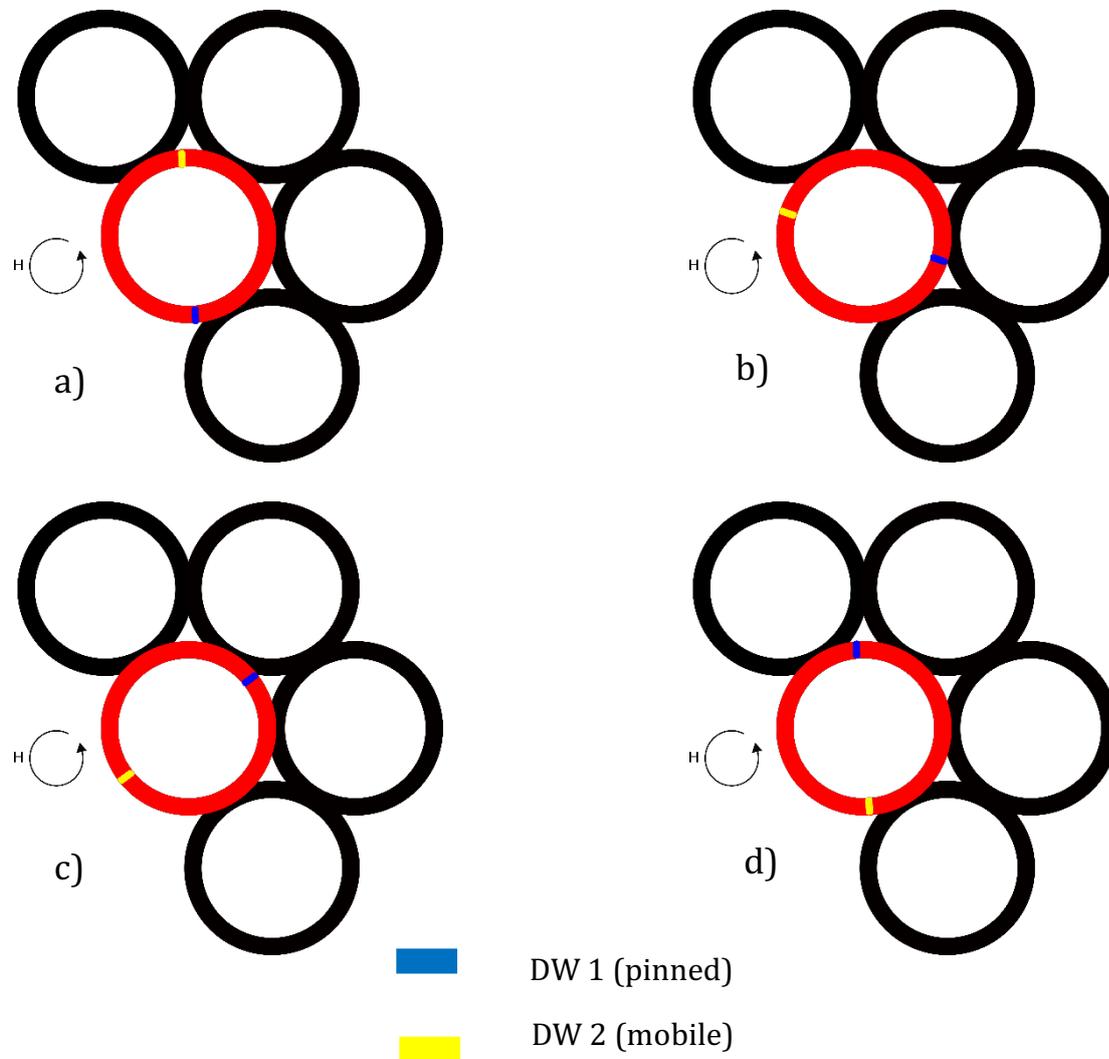

Figure 5.24 - Potential DW start positions for a ring with 4 junctions (trigonal arrangement) as originally described by Mahmoori.

Of the four starting positions; a) and b) have one junction to de-pin from, c) has two junctions and d) has three junctions. As such, $P_1 = \frac{2}{4}$, $P_2 = \frac{1}{4}$ and $P_3 = \frac{1}{4}$.

Putting this into the general equation for f_4 rings, as used for bulk centre rings in a square array:

$$W_{trigonal\;edge} = 1 - \frac{\left(1 - P_{pass}^4\right)\left(\frac{1}{2}P_{pass} + \frac{1}{4}P_{pass}^2 + \frac{1}{4}P_{pass}^3\right)}{\left(1 + P_{Pass} + P_{pass}^2 + P_{pass}^3\right)} \qquad \text{Equation 5.20}$$

$n = 6$ (trigonal bulk rings)

The general equation for a six-junction ring takes the form of:

$$W_{trigonal\;bulk} = 1 -$$
$$\frac{\left(1 - P_{pass}^6\right)\left(P_0 + P_1 P_{pass} + P_2 P_{pass}^2 + P_3 P_{pass}^3 + P_4 P_{pass}^4 + P_5 P_{pass}^5 + P_6 P_{pass}^6\right)}{\left(1 + P_{Pass} + P_{pass}^2 + P_{pass}^3 + P_{pass}^4 + P_{pass}^5\right)} \quad \text{Equation 5.21}$$

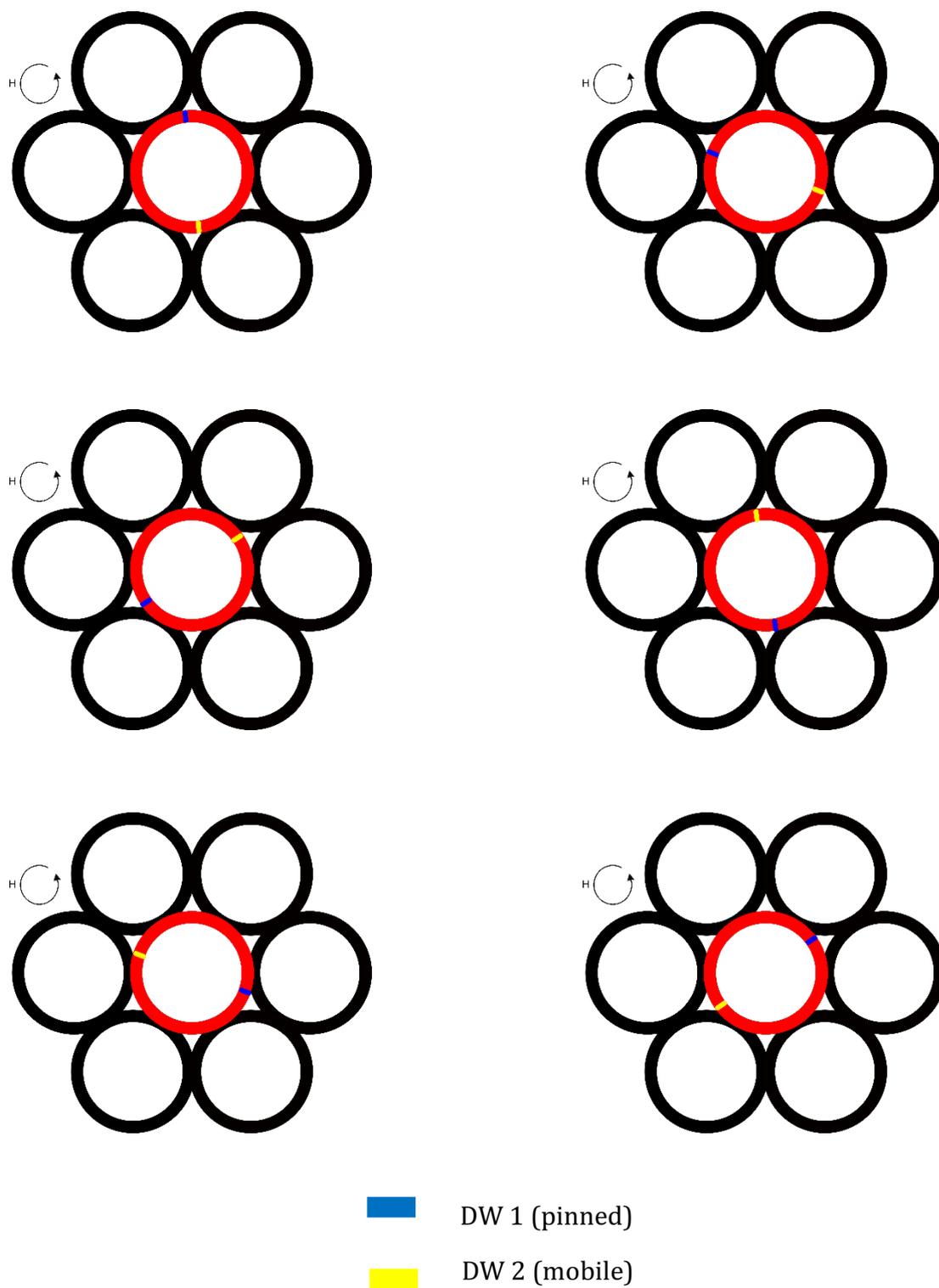As with previous sections, analysing start positions allows determination of P_n.

Figure 5.25. Potential DW start positions for a ring that has 6 junctions (trigonal arrangement) as originally described by Mahmoori.

Figure 5.25 shows that for each potential start position, there are three junctions to overcome. Therefore $P_3 = 1$ and other coefficients are zero.

Putting this into equation 5.19 obtains:

$$W_{trigonal\ bulk} = 1 - \frac{(1 - P_{pass}^6)(P_{pass}^3)}{\left(1 + P_{Pass} + P_{pass}^2 + P_{pass}^3 + P_{pass}^4 + P_{pass}^5\right)} \qquad Equation\ 5.22$$

The equilibrium population for the trigonal array is, as with chains and square arrays, the weighted sum of equations 5.18, 5.19, 5.21 and 5.22.

$$W_{eq} = C_{fixed\ corner} * W_{fixed\ corner} + C_{annihilating\ corner} * W_{annihilating\ corner}$$

$$+C_{trigonal\ edge} * W_{trigonal\ edge} + C_{trigonal\ bulk} * W_{trigonal\ bulk} \qquad Equation\ 5.23$$

The weighting of $C_{fixed\ corner}$ and $C_{annihilating\ corner}$ are $\frac{2}{3}$ and $\frac{1}{3}$ respectively, which can be seen in Fig. 5.22.

Again, Mahmoori's original plot is shown in Fig. 5.26 with the updated model in Fig. 5.27.
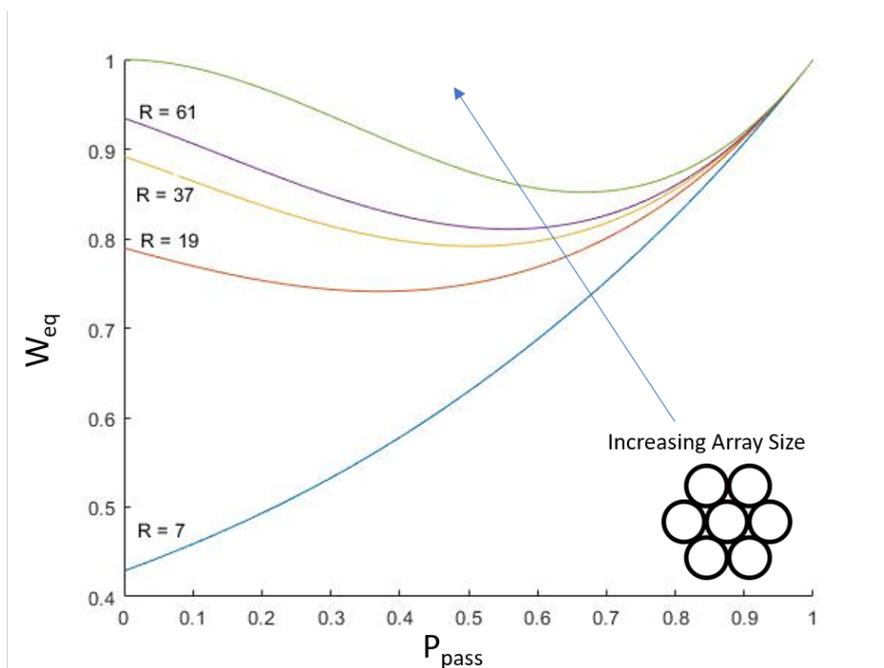

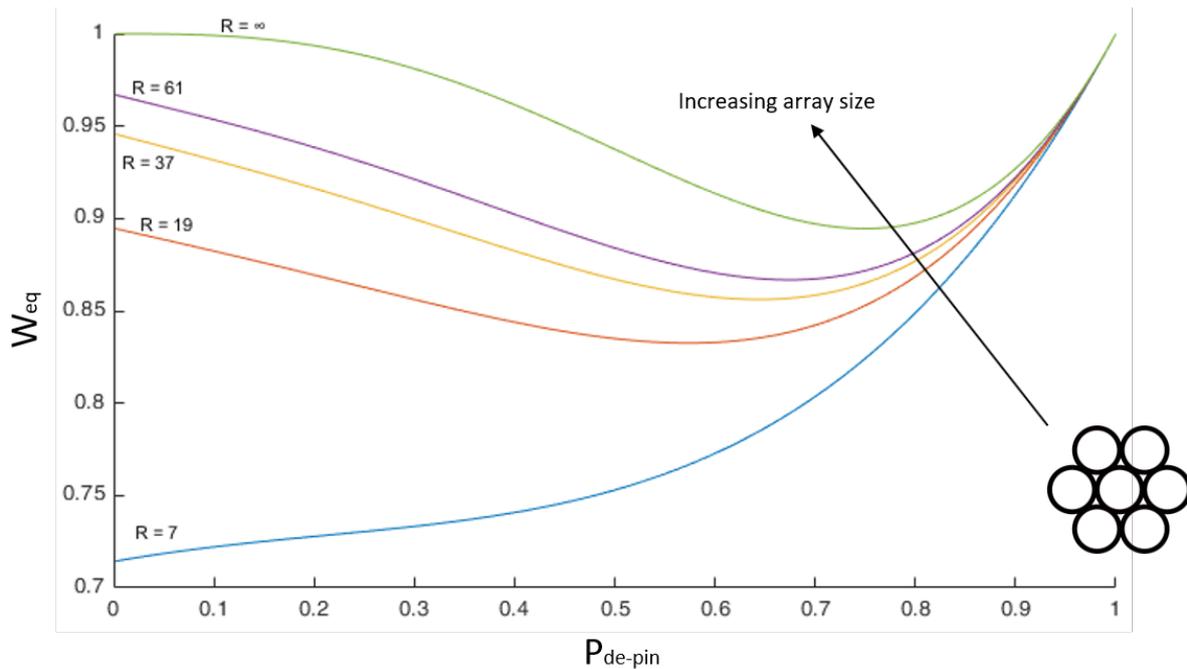**Figure 5.26. Mahmoori's original analytical model for regular trigonal arrays with increasing number of rings.**

Figure 5.27 - Updated analytical model for regular trigonal systems. The infinite case, where bulk trigonal rings dominates is the top, green line.

None of the finite cases were predicted to depopulate completely. For the minimum size trigonal array (R = 7), the central and $\frac{2}{3}$ of the edge rings are 'locked' as an onion much giving a minimum equilibrium wall population of 0.716.

For the infinite array, shown by the green line in Fig. 5.27, the minimum population occurs at P_{de-pin} = 0.75, a higher value than for regular square array. The population itself is slightly higher at 0.895, compared to 0.852 for the square array.

5.6 Defect system

5.6.1 Micromagnetic modelling of defect arrays

Square, eight-ring 'frame' structures were also modelled (Fig. 5.28). These were effectively a 3 x 3 ring array with the central ring missing. This is potentially interesting as the absence of a ring could be considered a 'defect' in an otherwise continuous array and here forms what is effectively a closed chain of rings with two junctions.

The modelling showed that at low magnetic field amplitude (50Oe), despite the numbers of junctions changing, DW annihilation will still only occur in two corner rings (Fig. 5.28a). The original position of DWs in the other corners and the edge rings mean they all become pinned at junctions. Increasing applied rotating field to 75Oe (Fig. 5.28 b) to allow DWs to overcome junctions sees them fill all rings, as above. Removal of rings from larger square arrays may affect the dependence of array DW population on the applied field magnitude, compared to a continuous array.
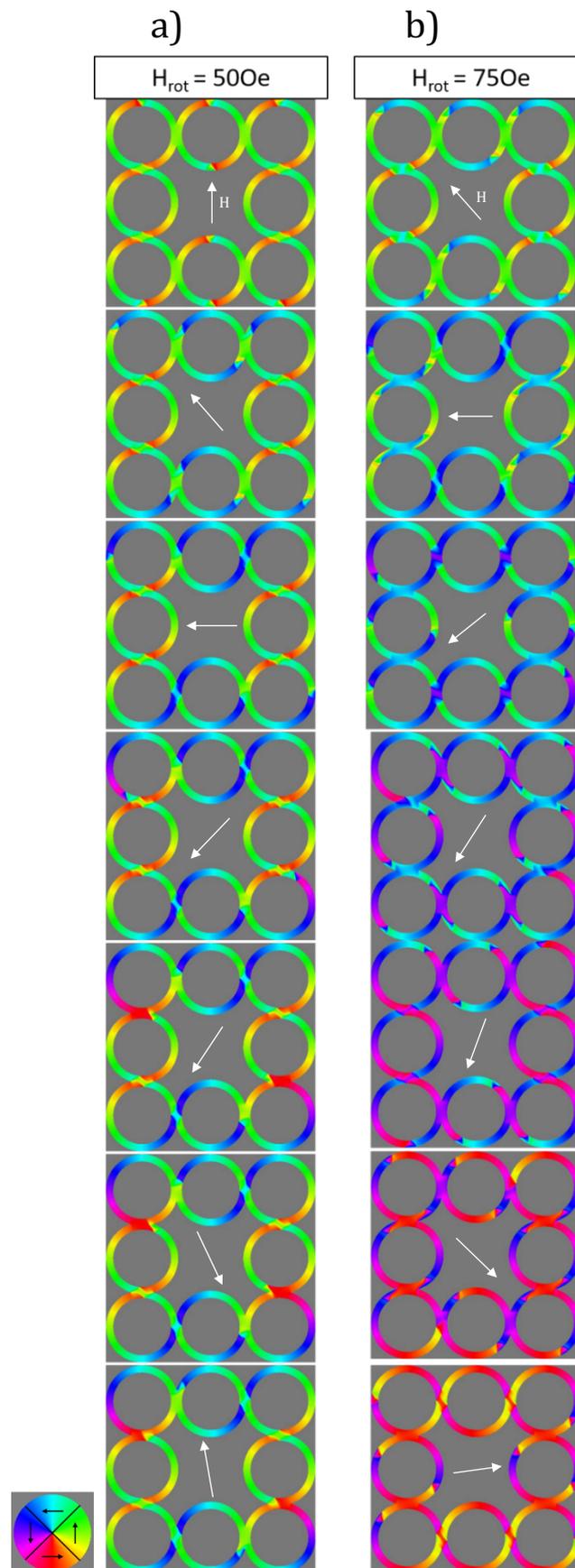
Figure 5.28. Mumax3 simulations of standard interconnected nanorings in n = 8 square defect array for a) 50Oe and b) 75Oe applied rotating fields. Magnetic field rotation is anti-clockwise. Ring dimensions are 4µm diameter, 400nm track width, 20nm thickness, 50% overlap. At a pinning field of 50Oe, only corner rings annihilate to form vortex as with the full square array.

Finally, a Kagome or trigonal six-ring arrangement was also simulated, with 400nm wide rings and all other geometric features identical to those used in Fig. 5.22, but now with the central ring missing (Fig. 5.29). These are also closed loop chains of interconnected rings.

At low fields, DW pinning causes annihilation in two edge rings and DW propagation through junctions only becomes possible at 100Oe. The rings that see DW annihilation again depends on the initialised position of DWs. The removal here of the central ring in trigonal structures simplifies the magnetic configuration close to junctions again. The extended DWs seen at high field amplitudes (Fig. 5.29b) as the walls approach de-pinning from junctions also explains the complex magnetic configurations seen in the trigonal structure (Fig. 5.28) where the junctions were in closer proximity and DWs from nearby junctions would be more likely to overlap.

One of the potential advantages of the Kagome arrangement of rings is that all rings may exist in vortex states without magnetic frustration. This compares with work in artificial spin ices searching for a true ground state that is inaccessible without external influence on the system [20].
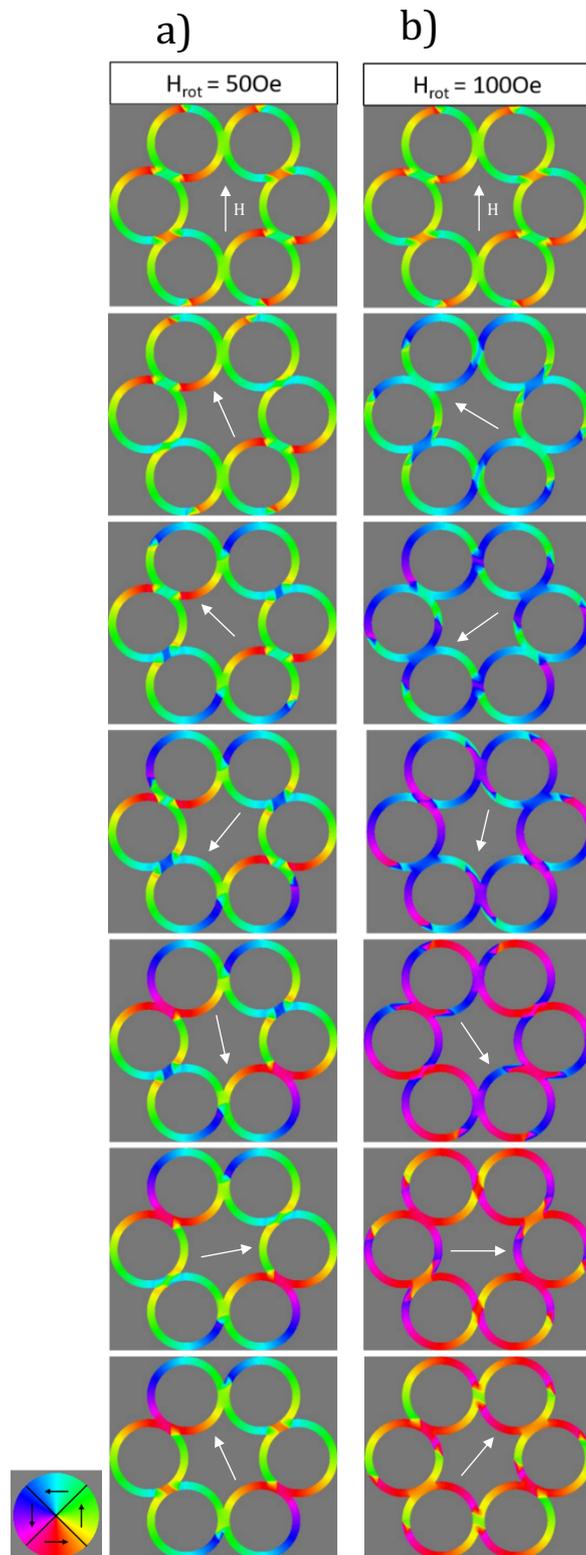
Figure 5.29. Mumax3 simulations of interconnected nanorings with simulated track widths of 400nm in a Kagome array for a) 50Oe and b) 100Oe applied rotating fields. Ring diameter is 4µm, thickness is 20nm, overlap is 50%. Field rotation is anti-clockwise. At a pinning field, two of the six corner rings will annihilate to vortex. White arrows denote applied field direction.

The analytical model for defect arrays the same as for a linear chain with different weightings for rings that always annihilate, $C_{annihilating\ corner}$.

$$W_{eq} =$$

$$C_{annihilating\ corner} * \left(1 - \frac{\left(1 - P_{de-pin}\right)}{\left(P_{de-pin}\right)^0}\right) + C_{rest} * \left(1 - \frac{\left(1 - P_{de-pin}^1\right)\left(P_{de-pin}\right)}{\left(1 + P_{de-pin}\right)}\right) \qquad Equation\ 5.24$$

where C_{rest} is the proportion of rings that are standard, two junction that form the rest of the array. For the Kagome in Fig 5.29, these proportions are $\frac{1}{3}$ and $\frac{2}{3}$ for $C_{annihilating\ corner}$ and C_{rest} respectively.

Mahmoori's original model took the same form as the linear chain for each form of the defect structure (i.e. Fig. 5.14). Figures 5.30 and 5.31 show updated analytical model for square and trigonal defect arrays. These generally show similar behaviour to linear chains (note the difference in scale for equilibrium wall population) with slight differences in the value of P_{de-pin} at minimum wall populations. In general, there is non-monotonic variation as with other array types.
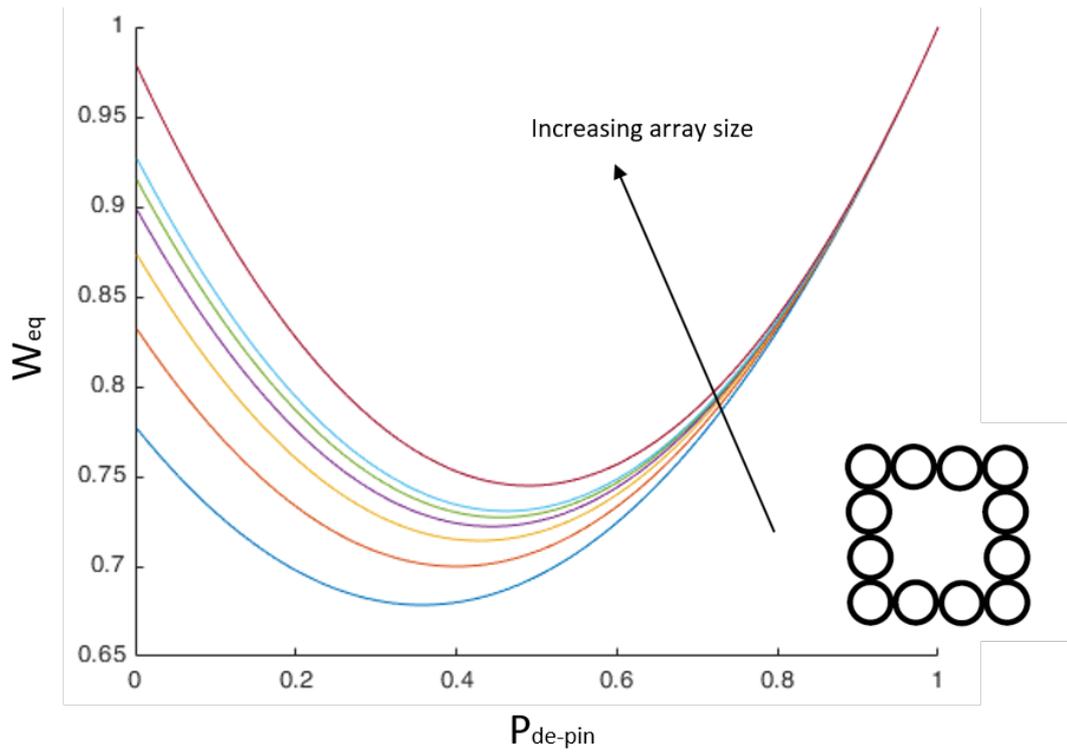
Figure 5.30. Updated analytical model for square defect arrays. This plot shows R = 8 (3 by 3) as the darker blue line to R = 28 (8 by 8) as the lighter blue line, with R = 100 (26 by 26) as the dark red line.
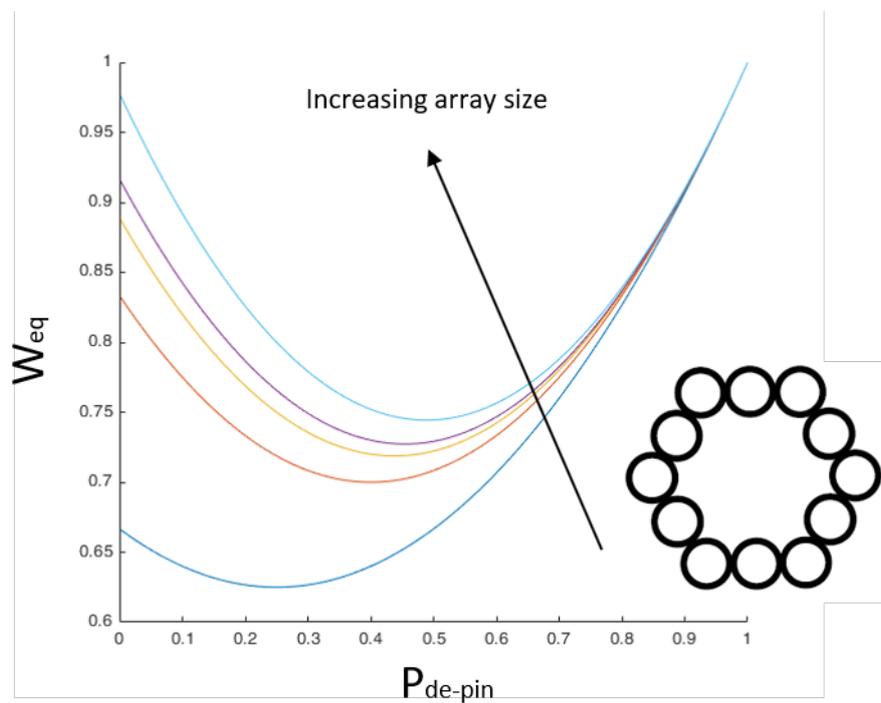

Figure 5.31. Updated analytical model for trigonal defect arrays. This plot shows R = 6 as the darker blue line to R = 30 as the lighter blue line.

5.6 Summary

This chapter has focussed on modelling interconnected ring systems. The key step taken here is showing predictions of how DW population in these systems when driven by a rotating magnetic field could be an emergent property of the ring ensemble.

Micromagnetic simulations showed the possibility of mechanisms for DW population loss and gain when the rings are subject to an in-plane rotating magnetic field. An analytical model of homogeneous equilibrium DW population based on these mechanisms was presented. This model predicts that infinite interconnected nanoring arrays have a very powerful output – the wall population of the array. At low field amplitudes, DWs are unable to overcome the pinning potentials of junctions. At high field amplitudes, DWs pass through any junction encountered and the model predicts that the array becomes 'saturated' with two DWs per ring, with each ring in the so-called 'onion' state configuration. The analytical model assumed that in the intermediate field region, DWs will have a probability per field cycle of de-pinning from any junction encountered. The model used this probability to together with information from the array geometry to predict the extent of DW loss and gain mechanisms to predict an equilibrium DW population W_{eq}. The output can be altered by modification of P_{de-pin}, which is dependent on: fixed variables such as ring and junction geometry, and material properties; and tuneable parameters such as temperature, frequency of applied field rotations and rotating field magnitude. This latter parameter is important as it will be the one most easily investigated experimentally. The chapter also presented further micromagnetic and analytical models that investigated the configurational dependencies likely to be seen in different array symmetries, array edges, at 'defects' due to missing rings, and where junctions are at different levels of proximity.

The form of the analytical model for infinite interconnected nanoring array populations suggests the ensemble behaviour of the array is dependent on interactions between individual nanorings. Experimental systems will, of course, have a distribution of DW de-pin probabilities as no two fabricated junctions will be identical. It would be interesting to incorporate these into future spatially-dependent models but the basis of the system in locally probabilistic behaviour resulting in whole-ensemble, emergent behaviour being seen should be robust still.

5.7 References

[1]   L. Lopez-Diaz, J. Rothman, M. Kläui, and J. A. C. Bland, "Computational study of first magnetization curves in small rings," *IEEE Trans. Magn.*, vol. 36, no. 5 I, pp. 3155–3157, 2000.

[2]   C. A. F. Vaz *et al.*, "Ferromagnetic nanorings," *J. Phys. Condens. Matter*, vol. 19, no. 25, p. 255207, 2007.

[3]   M. Negoita, T. J. Hayward, J. A. Miller, and D. A. Allwood, "Domain walls in ring-shaped nanowires under rotating applied fields," *J. Appl. Phys.*, vol. 114, no. 1, p. 013904, 2013.

[4]   M. Kläui *et al.*, "Domain Wall Pinning in Narrow Ferromagnetic Ring Structures Probed by Magnetoresistance Measurements," *Phys. Rev. Lett.*, vol. 90, no. 9, p. 4, 2003.

[5]   M. Kläui, C. A. F. Vaz, L. Lopez-Diaz, and J. A. C. Bland, "Vortex formation in narrow ferromagnetic rings," *Journal of Physics Condensed Matter*, vol. 15, no. 21. pp. 985–1023, 2003.

[6]   M. Y. Im, L. Bocklage, P. Fischer, and G. Meier, "Direct observation of stochastic domain-wall depinning in magnetic nanowires," *Phys. Rev. Lett.*, vol. 102, no. 14, 2009.

[7]   V. D. Nguyen *et al.*, "Elementary depinning processes of magnetic domain walls under fields and currents," *Sci. Rep.*, vol. 4, 2014.

[8]   W. Wernsdorfer *et al.*, "Nucleation of magnetization reversal in individual nanosized nickel wires," *Phys. Rev. Lett.*, vol. 77, no. 9, pp. 1873–1876, 1996.

[9]   M. Kläui *et al.*, "Domain wall behaviour at constrictions in ferromagnetic ring structures," in *Physica B: Condensed Matter*, 2004, vol. 343, no. 1–4, pp. 343–349.

[10]   D. A. Allwood, G. Xiong, C. C. Faulkner, D. Atkinson, D. Petit, and R. P. Cowburn, "Magnetic domain-wall logic," *Science (80-.).*, vol. 309, no. 5741, pp. 1688–1692, 2005.

[11]   G. Bordignon *et al.*, "Analysis of magnetoresistance in arrays of connected nano-rings," *IEEE Trans. Magn.*, vol. 43, no. 6, pp. 2881–2883, 2007.

[12]   Y. Ren, S. Jain, A. O. Adeyeye, and C. A. Ross, "Magnetization states in coupled Ni80Fe20 bi-ring nanostructures," *New J. Phys.*, vol. 12, no. 11pp, p. 93003, 2010.

[13]   J. Zhang *et al.*, "360° Domain walls: Stability, magnetic field and electric current effects," *New J. Phys.*, vol. 18, no. 5, 2016.

[14]   B. Van Waeyenberge, "Mumax3." .

[15]   M. Hayashi, L. Thomas, C. Rettner, R. Moriya, X. Jiang, and S. S. P. Parkin, "Dependence of current and field driven depinning of domain walls on their structure and chirality in permalloy nanowires," *Phys. Rev. Lett.*, vol. 97, no. 20, 2006.

[16]   H. Y. Yuan and X. R. Wang, "Domain wall pinning in notched nanowires," *Phys. Rev. B*, vol. 89, p. 54423, 2014.

[17]   M. T. Bryan, T. Schrefl, and D. A. Allwood, "Dependence of transverse domain wall dynamics on permalloy nanowire dimensions," *IEEE Trans. Magn.*, vol. 46, no. 5, pp. 1135–1138, 2010.

[18]   V. D. Nguyen *et al.*, "Elementary depinning processes of magnetic domain walls under fields and currents.," *Sci. Rep.*, vol. 4, p. 6509, 2014.

[19]   M. Mahmoori, "MSc Thesis - Domain Walls in Magnetic Multi-Nanorings Structures," 2014.

[20]   J. C. Gartside *et al.*, "Realization of ground state in artificial kagome spin ice via topological defect-driven magnetic writing," *Nat. Nanotechnol.*, vol. 13, no. 1, pp. 53–58, 2018.

Chapter 6 – Interconnected Nanoring Arrays

"We are all now connected…like neurons in a giant brain" – Stephen Hawking

6.0 Background

The previous chapter (§5) presented modelling that showed how DW population of a nanowire ring array might be used as an ensemble output. This chapter demonstrates the form of the DW population dependence on applied magnetic field.

§6.1 presents investigations with polarised neutron reflectometry (PNR) on ultra-large arrays of nanorings performed at the ISIS neutron source.

§6.2 shows results of magneto-optic Kerr effect (MOKE) magnetometry performed on some of the ultra-large arrays used at ISIS and other, smaller array geometries. The analysis over multiple cycles of magnetic field required careful normalisation in order to allow quantitative values of various ring configurations to be obtained.

§6.3 summarises the results of these experiments, the different types of sensitivity of the two approaches and compares the results to the analytical model in §5.

6.1 Polarised Neutron Reflectometry

An overview of the PNR technique is given in §4. Here, the OFFSPEC beam line at the ISIS Neutron Source was used. Scanning electron microscopy images of the samples used are shown in §4.3. Briefly described, these were arrays of permalloy nanowire rings of thickness 20nm, 400nm wire width and 4µm diameter, arranged in a square pattern with rings overlapping either by 50% of their wire width. The arrays were in

blocks of 26 x 26 rings, with the block pattern repeated to extend over an area approximately 2 cm x 2 cm to obtain a large signal from the PNR instrument.

A 26 x 26 array can be described using the nomenclature developed in §5 by f_2 = 4, f_3 = 96 and f_4 = 576. This sized block was used due to write field limitations within the electron beam writing system. However, given the relevant f_n values, we assume that the blocks approximate the behaviour of an infinite square array pattern.

The experimental set-up is explained in detail in §4 and, briefly, the protocol for measurement consisted of:

1) Application of a large, saturating magnetic field (1900Oe) along one direction to leave the nanoring array filled with two DWs in each ring upon removal of the field;
2) Reduction of the field to the test magnetic field;
3) Rotation of the sample in the test field, usually by 50 rotations;
4) Reduction of the field to 18Oe, chosen to be small enough not to perturb the magnetic configuration significantly while being large enough to allow neutrons to maintain their polarisation;
5) PNR measurement.

6.1.1 Field-dependent PNR response

The method outlined above was used on the ultra-large arrays with different test fields, i.e. the saturating field was applied before applying each test field.

Figure 6.1 shows an example PNR plot, showing the normalised neutron reflectivity as a function of the neutron wave vector component normal to the sample, q_z (i.e. as angle of incidence changes, see §4.4) When carried out on a magnetised sample, up and down polarised neutron intensities differ and a split emerges between them. GenX [1] software allows analysis of this split and here was used to provide a value of magnetisation, based on the layer properties and proportion of surface coverage of the Ni-Fe magnetic arrays on the Si substrate. It is useful to note that larger magnetisation results in larger splitting of oppositely polarised neutrons.

Figure 6.1 shows reference measurements taken from the ultra-large square array. The plots for 1900Oe were obtained during application of this field. The 18Oe data in Fig. 6.1 were obtained using the full procedure, with 18Oe used as the test field during 50 sample rotations. The reduced difference between the 'up' and 'down' polarised neutron reflectivities compared with the 1900Oe case indicates a reduction in magnetisation. The inset plot in Fig. 6.1 shows the difference in reflected intensity between up and down polarised traces for each field case and allows the change in difference to be seen directly.
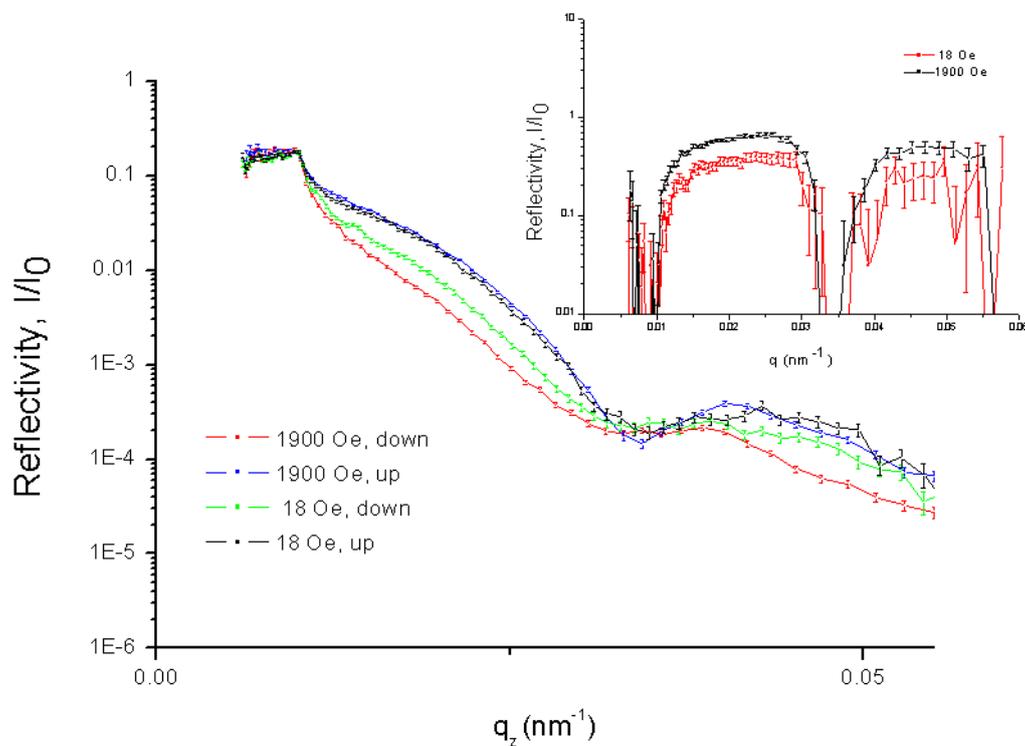

Figure 6.1. PNR plot of intensity of measured up- and down-polarised neutrons taken on an ultra large square array with the annotated fields applied. The inset graph plots the difference in reflectivity between up/down data ($\frac{\Delta I}{I_0}$). Error decreases with increasing number of detected neutrons, hence at high angles (high q_z) error increases.
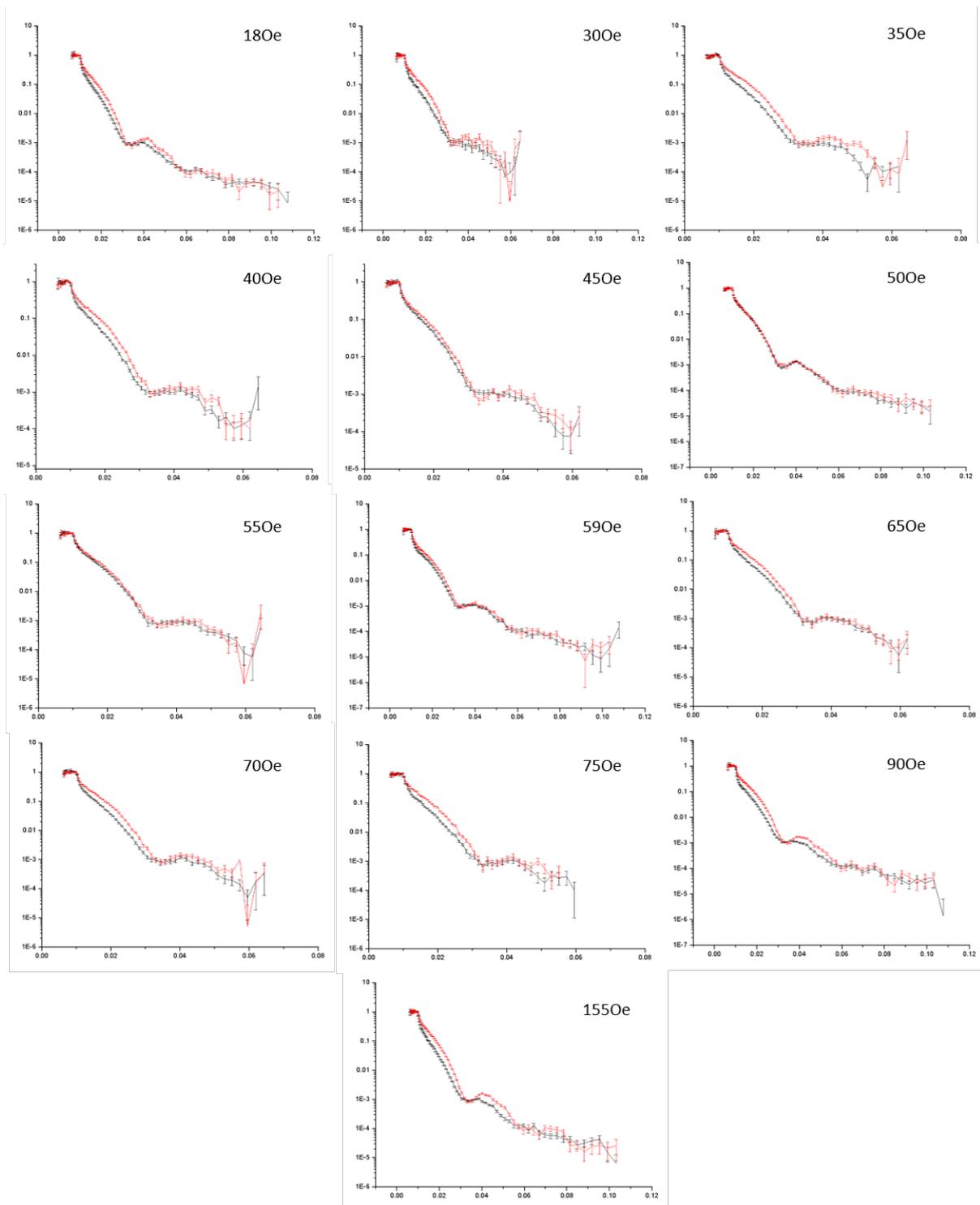
Figure 6.2. Individual PNR data for a field sweep as measured after 50 rotations in a field at the indicated values. X-axes are scattering vector, q_z (i.e. angle of measurement) and y-axes are reflectivity I/I_0. Red lines are measured intensities using a beam of 'up' polarised neutrons and black lines are the corresponding measurement with 'down' polarised neutrons.

All the PNR data for the different fields with 50 applied rotations are shown in Fig. 6.2. Interestingly, these show that the reflectivity splitting is present at low and high fields but disappears for an intermediate test field of 50Oe.
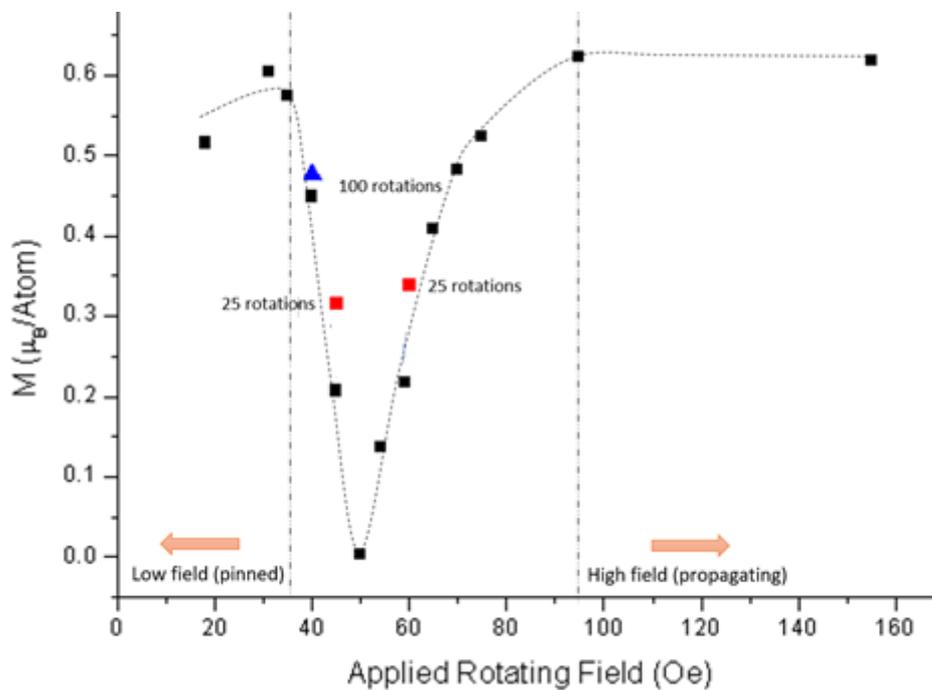

Figure 6.3. PNR-derived magnetisation as a function of applied rotating field magnitude response for an ultra-large square array of Ni-Fe nanorings. Black squares are from 50 rotations at indicated field, red squares are from 25 rotations and the blue triangle is from 100 rotations. Dashed lines highlight suggested low field and high field behaviours as defined in §5. Dotted line is a guide for the eye.

The GenX-fitted magnetisation extracted from PNR measurements are plotted against magnetic field in Fig. 6.3. These results are striking for several reasons. The first is the observation of non-monotonic variation in the magnetisation of the array is similar to the intermediate field regime behaviour predicted by the analytical model (see §5.4). Noting that 'onion' states (rings with two DWs) will have a net magnetisation whereas vortex states (rings with no DWs) have zero net magnetisation (see §3), the PNR magnetisation data in Fig. 6.3 may be interpreted as showing a change in the total number of DWs in the ring array. This allows a link to wall population and rotating field strength to be made experimentally.

The intermediate field regime is clearly definable in Fig. 6.3. and it is remarkable that the magnetisation should go even go close to zero here. Interpreting this using the naïve approach of onion-state or vortex-state rings only would suggest an array configuration made up of vortex states with an equal number (possibly none) of oppositely magnetised onion state rings. A perfect balance between oppositely magnetised onion states within a system with a constantly varying bias field is unlikely to appear though, since the rotating field will be constantly biasing the system one way or the other. The detailed magnetic configurations are relevant to the MOKE measurements later (§6.2) and investigated further in the microscopy experiments in the following chapter.

Micromagnetic modelling in §5.4 predicted that walls should be in states where they will all pin or all propagate. However, this modelling was conducted at a simulation temperature of 0K and temperature-dependent stochastic behaviour was excluded. Nonetheless, the lack of significant change in magnetisation at fields that are sufficiently low or sufficiently high suggests that these regimes are characteristic of DWs being completely pinned (low fields) and always passing through junctions (high fields). It is consistent that the intermediate field region develops due to probabilistic de-pinning from wire junctions, but this is not fully demonstrated here.

There are, however, two distinct ways in which the analytical model for an infinite case array does not describe the PNR experiment. As Fig. 6.3 shows, at 50Oe the array appeared to completely depopulate of DWs, yet this was not predicted by the analytical model – approximately 80% of DWs would be retained if the model were completely accurate (Fig. 5.20). There is also a difference in the gradient either side of 50Oe towards the low/high fields, i.e. the experimentally determined magnetisation increases more rapidly at smaller fields than 50Oe than in going to higher fields, which was obtained with updated analytical modelling. Differences in the onset of propagating and repopulation applied field values were noted as a possible contribution to the difference in gradient, but the relationship (and degree of non-linearity) between applied field and P_{pass} will need to be determined to better understand this difference. The probabilistic nature of de-pinning from a junction compares with literature describing Arrhenius-Néel behaviour describing magnetisation reversal probability at a given field [2].

Given the first-order approximations that underpin the analytical model, the PNR result in Fig. 6.3 is important in demonstrating a clear, non-linear magnetisation response of

the ring ensemble to applied field strength that is broadly consistent with predictions based on stochastic DW pinning in the ring array.

Experiments using 25 rotations (red points) and 100 rotations (blue triangles) of applied field are also shown in Fig. 6.3. These were performed to investigate the extent to which magnetic configurations were equilibrated at different cycle numbers. The 100-rotation magnetisation at 4Oe is 6.4% larger than that for 50 rotations at the same field. However, the 25-rotation magnetisation values are 52.6% (45Oe) and 55.7% (60Oe) larger than the values for 50 rotations at identical fields. This suggests that the magnetisation configurations are still equilibrating at 25 cycles but are relatively equilibrated, although subject to cycle-to-cycle variations, by 50 rotations. However, there is a lack of evidence here, which was hampered by the long time required to obtain each data point. This also means the degree of error is unknown, requiring further experimentation to test repeatability. It would also be valuable in future experiments to look at how magnetisation progresses after each cycle (or after a certain number of repeated cycles) at a field value to understand equilibration and the variations in magnetisation thereafter more clearly.

6.1.2. Investigations without saturation

The non-monotonic variation of array magnetisation as a function of applied rotating field strength with the array reinitialised in between steps raised the question of whether similar behaviour would be seen without the initialisation step, i.e. purely from changed probability of DWs passing junctions? The removal of the condition of initial array saturation would make future implementation of the arrays as functional devices far simpler.

6.1.2.1 Double field sweep

The experimental protocol was modified to achieve a field sweep with no saturation field between test values, as follows:

a) Apply saturating field (2kOe);

b) Apply desired field;

c) Rotate sample 50 full turns;

d) Apply polarisation field (18Oe);

e) Align sample relative to neutron beam;

f) Run PNR measurement;

g) Apply next desired field;

h) Rotate sample 50 full turns;

i) Apply polarisation field (18Oe);

j) Align sample relative to neutron beam;

k) Run PNR measurement;

l) Apply next desired field;

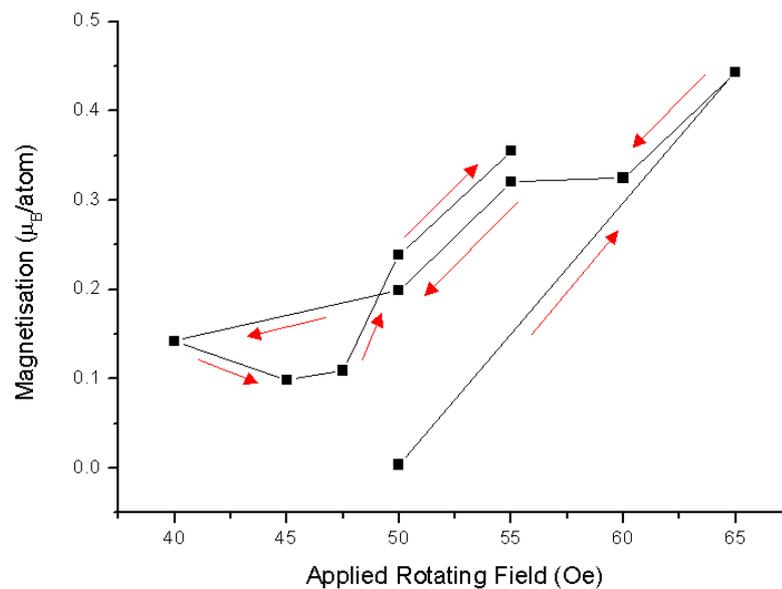m) Repeat from step g) as many times as needed.

Figure 6.4. PNR-derived magnetisation of an ultra-large square array of Ni-Fe nanorings array as a function of applied rotating field following 50 rotations and no intermediate saturation step. Arrows show the chronological order of field strengths that were tested.

Figure 6.4 presents the PNR-derived magnetisation for a series of field values using the above protocol, starting with a post-initialisation test field of 50Oe and without any further initialisation for subsequent fields. The first data point taken at 50Oe was significant in that in this independent test, the array magnetisation once again reached zero, as in Fig. 6.3. This suggests that this phenomenon is repeatable and characteristic following saturation.

The second data point, obtained at an applied rotating field of 65Oe, showed an increase in magnetisation to $\sim 0.45 \mu_B$/atom. This is difficult to justify if the previously near-zero magnetisation was indeed associated with an array full of vortex state rings since there is no explanation for the subsequent increase in DW numbers (at 65Oe), since this later test field is too low for DW nucleation. The possibility remains that a minute DW population repopulated the array over the 50 cycles of 65Oe field to an equilibrium level, but this would be surprising over all the individual arrays that make up the 2cm x 2cm super-array.

Decreasing field amplitude from 65Oe saw the magnetisation decrease again until the lowest field of 40Oe was applied. No minimum in magnetisation was seen in this field sweep, although this was possibly due to a large field spacing. However, it was noticed that at 50Oe during this field sweep, the magnetisation did not return to zero. This suggests that the reduced number of domain walls that the array starts with leads to a lower equilibrated population, although this appears counter to the previous observation of repopulation. Nonetheless, these differences provide the first information on the tolerance in magnetisation to applied field strength.

Increasing the field strength from 40Oe again, though, did yield an identifiable minimum in magnetisation at 45Oe. At higher fields of 50Oe and 55Oe the magnetisation was similar to the values on the reducing field sweep, becoming 10.8% and 19.9% larger, respectively. Zero magnetisation was again not observed at 50Oe, reinforcing the likelihood that this does not occur without prior saturation. This possible dependence upon previous state configurations suggests that the ring array system may have a memory (or hysteretic) effect, which can be desirable for reservoir computing applications.

6.1.2.2 Increased field rotations

A simple investigation was performed into the influence of the number of field rotations on array magnetisation. Following relaxation from saturation, a magnetic field strength of 60Oe was chosen. The sample was rotated ten times between PNR measurements (with no further saturation).
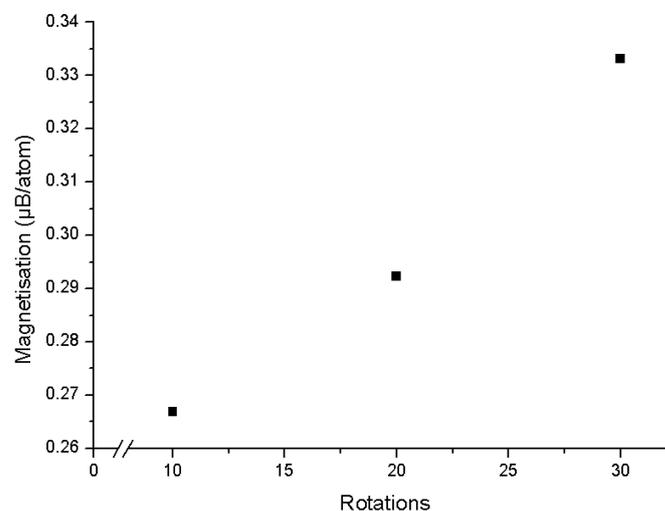

Figure 6.5. PNR-derived magnetisation of an ultra-large square array of Ni-Fe nanorings array as a function of the number of rotations in a 60Oe applied magnetic field.

Fig. 6.5 shows the PNR-measured array magnetisation for 10, 20 and 30 rotations at 60Oe. The magnetisation at 10 cycles was larger than that previously found at 50Oe (Fig. 6.3). Subsequent measurements after 20 and 30 cycles increased the magnetisation further, to give a maximum difference (between 10 and 30 cycles) of 24.8%. The magnetisation is highly sensitive to field changes in this region (Fig. 6.3) and the differences in the two experiments may be due to remanence differences in the electromagnet. Otherwise, the data show a degree of natural variation in the magnetisation with successive field cycles.

6.2 MOKE Investigation into Dynamic Array Behaviour

MOKE magnetometry was carried out as a faster and local method of probing array behaviour. It also has the advantage of being able to dynamically observe arrays, whereas PNR gave information on a final magnetic state following application of fields. This section describes how MOKE was used to observe the path arrays take to reach equilibrated DW populations.

6.2.1 MOKE Experimental Methods

The general principles of MOKE and the key features of the magnetometer used here are given in §2.4 and §4.5. Here, the particular approach of how the system was used to characterise the magnetic nanoring arrays is described. The system allows electromagnet current (and therefore magnetic field) to be defined from a text file that is interpreted by the MOKE control software and sent to an analog-output board, with the horizontal (x) and vertical (y) axes addressed by data in neighbouring text file columns. The current is updated by the data in successive rows at a rate defined by the user via the MOKE control software. This was typically an update frequency of 9,400 with 1,000 rows. When operated continuously, this provided a rotating field of 9.4Hz frequency (except for the first result in §6.2.2 which used a 27.4Hz rotating field). The MOKE system laser was operated at 40mW and the analyser angle was 4°.

An Excel macro template (Fig. 6.6) was created to output field file formatted columns with a single cycle of a 'priming' field that saturates the array (shown in Fig. 6.7 as the 2V amplitude voltage cycle), followed by 25 cycles at specified voltages in the x and y directions. The phase difference in the two field channels visible in Fig. 6.7 resulted in a field amplitude rotating in a circular profile in the plane of the sample. More details on the software can be found in Appendix §A3.1. Voltages were selected from calibration of the system's electromagnet (AC peak-to-peak voltage) with a Gaussmeter.

A 25-cycle field protocol was selected to allow data to be obtained with reasonable signal-to-noise. Rotation frequencies in the range 9.4Hz – 27Hz were investigated to avoid unphysical comparisons given when using the slow rotation frequencies used in PNR experiments, and more than 25 cycles in usually resulted in a detrimental drift in MOKE signal. Kerr signal was recorded in the time domain along with the orthogonal applied fields. Signals from 32 field sequences (initialisation + 25 field cycles) were acquired and averaged to reduce the noise of each measurement.
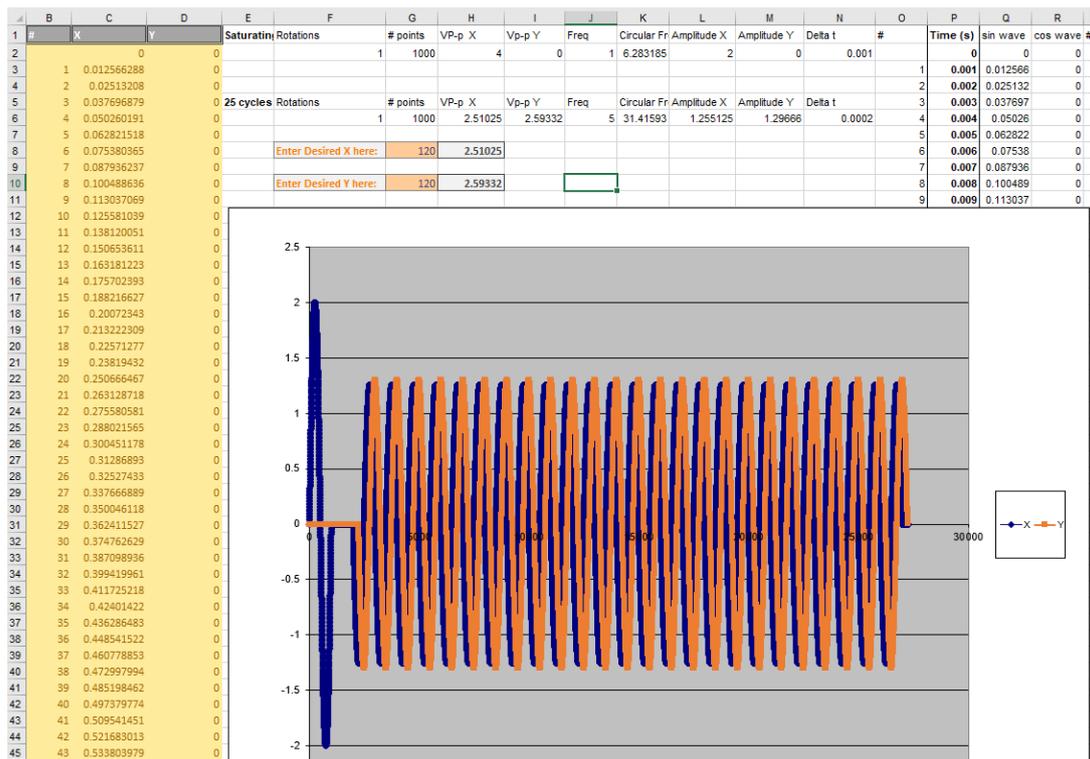

Figure 6.6. Screenshot of a Microsoft Excel macro used to create field files. Plotted is the general voltage protocol sent to the analog-output board.
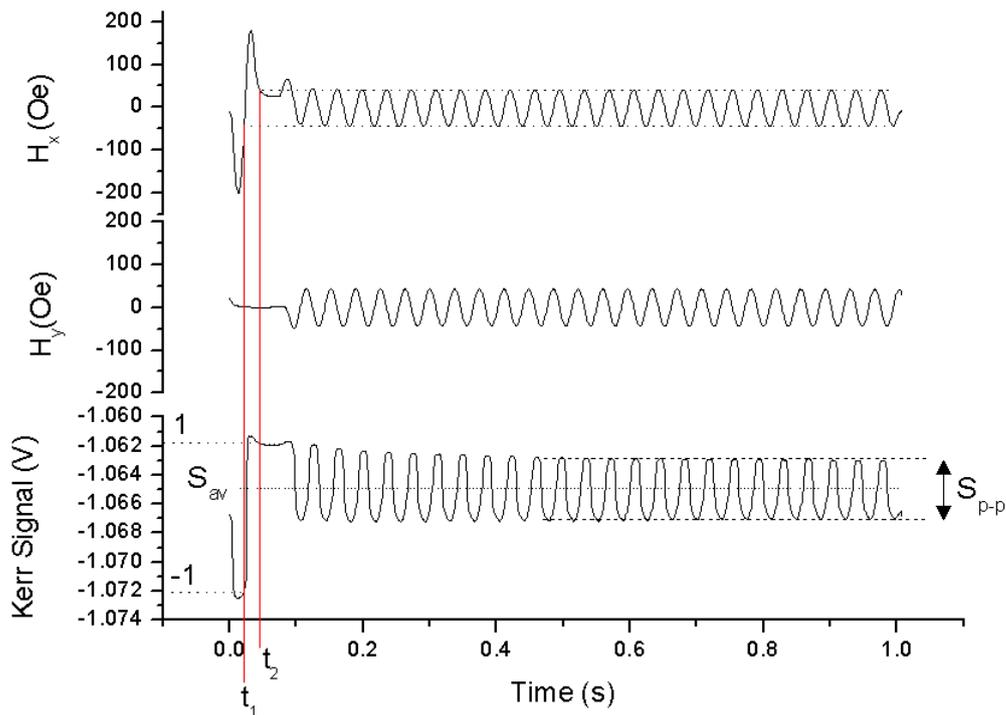
Figure 6.7. Annotated horizontal magnetic field, H_x, vertical magnetic field, H_y, Kerr voltage vs time plot for a standard MOKE on interconnected nanoring arrays experiment. The 25-cycle field maximum/minimum are noted and the times, t_1 and t_2 at which the falling edge of the saturating field is at this field value are noted. These are then used to take the Kerr voltages at t_1 and t_2 to find the minimum and maximum (respectively) for normalisation. Also annotated on this graph are the signal amplitude and signal average of the Kerr voltage during the 25-field cycle protocol.

Figure 6.7 shows an example set of field and Kerr data obtained from a subset of the 2cm x 2cm ultra-large square array sample used in §6.1. In this case the rotating magnetic field had an amplitude of 47.5Oe. The field data show the initial saturating cycle in the horizontal (H_x) direction before settling into the 25-cycle field rotation pattern. The Kerr data shows a corresponding saturation response followed by a dwell period and then the corresponding Kerr response from the 25-cycle field rotations.

It was important to be able to normalise the Kerr data effectively in order to obtain a quantitative understanding of the magnetic configurations. The largest changes in Kerr signals from relaxed magnetic states could be expected for arrays filled with oppositely oriented onion state (i.e. two DWs each) magnetic arrangements. The challenge here was that, even when DWs were stationary, magnetic domains in the rings will naturally rotate into the applied field direction. This creates a field-dependence to the Kerr signal,

even when no DWs move, and is seen in Fig. 6.8 throughout the initial saturation cycle. Normalising to the maximum and minimum values of the Kerr signal will not be the maximum and minimum Kerr signal in the 25-cycle field regime. This was resolved by identifying the times within the saturation cycle where the positive and negative field strength was equal to that of the field amplitude in the subsequent train of 25 cycles (labelled as t_1 and t_2 in Fig. 6.8). The Kerr signals at these positions then provide normalisation values of +1 and -1 for the remainder of that particular signal trace (since the longitudinal Kerr configuration was used, which gave sensitivity along the direction of H_x). The quantities of Kerr peak to peak signal amplitude $S_{peak-peak}$ and average Kerr signal $S_{average}$ for each cycle (where n is the cycle number) could then be measured from the normalised data; these values are indicated in Fig. 6.8 for the final cycle.

Analysis of the data then involved assuming that each ring was in one of three states:

1. No DWs (vortex state), with relative population P_{vortex}
2. Two mobile DWs (onion state), with relative population P_{mobile}
3. Two pinned DWs (onion state), with relative population P_{pinned}

and that $P_{vortex} + P_{mobile} + P_{pinned} = 1$.

Mobile DWs will be the only configuration that contributes to dynamic changes in Kerr signal (or peak to peak signal, S_{p-p} in Fig. 6.8), which means that:

$$S_{p-p} = P_{mobile} \qquad\qquad Equation\ 6.1$$

Pinned DWs with domains along one direction contribute a net, stable magnetisation and hence are responsible for offsetting the average signal, $S_{average}$ (or S_{av} in Fig. 6.8), from zero. This gives:

$$S_{average} = P_{pinned} \qquad\qquad Equation\ 6.2$$

The remaining states must be vortices, hence:

$$P_{vortex} = 1 - \left(P_{pinned} + P_{mobile}\right) \qquad\qquad Equation\ 6.3$$

With normalisation voltages recorded, a MATLAB .m file protocol was created to measure the peak and trough of each cycle and output results and allow the pinned, propagating and vortex populations to be calculated.

Looking at sample MOKE traces at high and low fields (as defined in PNR experimentation) gives a general idea of differences in S_{p-p} and $S_{average}$ in different regimes.
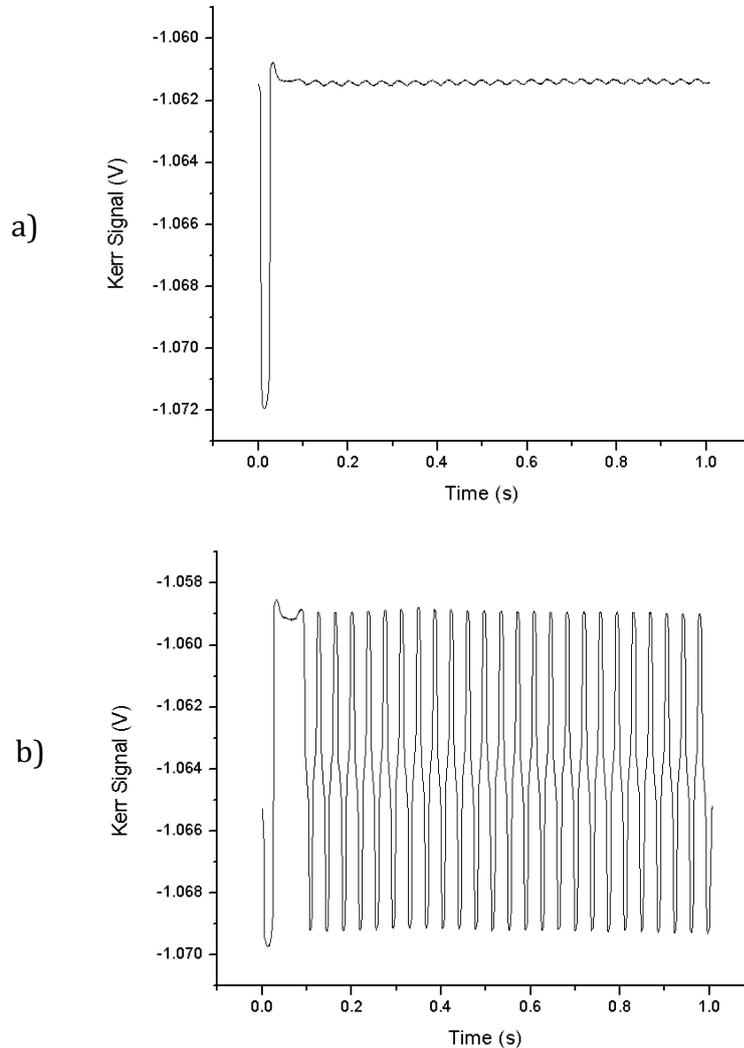

Figure 6.8. Time-dependent Kerr signal against elapsed measurement time at rotating field amplitudes of (a) 1Oe and (b) 57.5Oe taken on a large array of interconnected nanorings in a square arrangement. 25 cycles are applied following initialisation.

Figure 6.8 shows example MOKE traces of 25 cycles at 1Oe and 57.5Oe applied rotating field strengths. Immediately noticeable is the difference in the obtained signal amplitude, which, as equation 6.1 indicates, is representative of an increased proportion of propagating DWs. The signal average of the 1Oe trace is very offset, which indicates the presence of a high number of pinned DWs, whereas the 57.5Oe trace has an average somewhere close to the middle of the plot, indicating little DW pinning.

Two plots are typically including here from MOKE data analysis. The first shows state populations as a function of field amplitude. This is usually based on data from the 25th cycle but occasionally may use data from earlier cycles where significant drift occurred (i.e. the 23rd or 24th point). The second plot shows the evolution of the state populations by cycle number (e.g. Fig 6.10).

6.2.2 Ultra Large Arrays with Collimated Beam

A collimated beam of light was used by removing condenser and objective lenses from the focussed MOKE set up described in §4.5. This created a beam of size approximately 1mm^2 at the sample to allow sampling of a large number of rings, as was performed with PNR measurements.
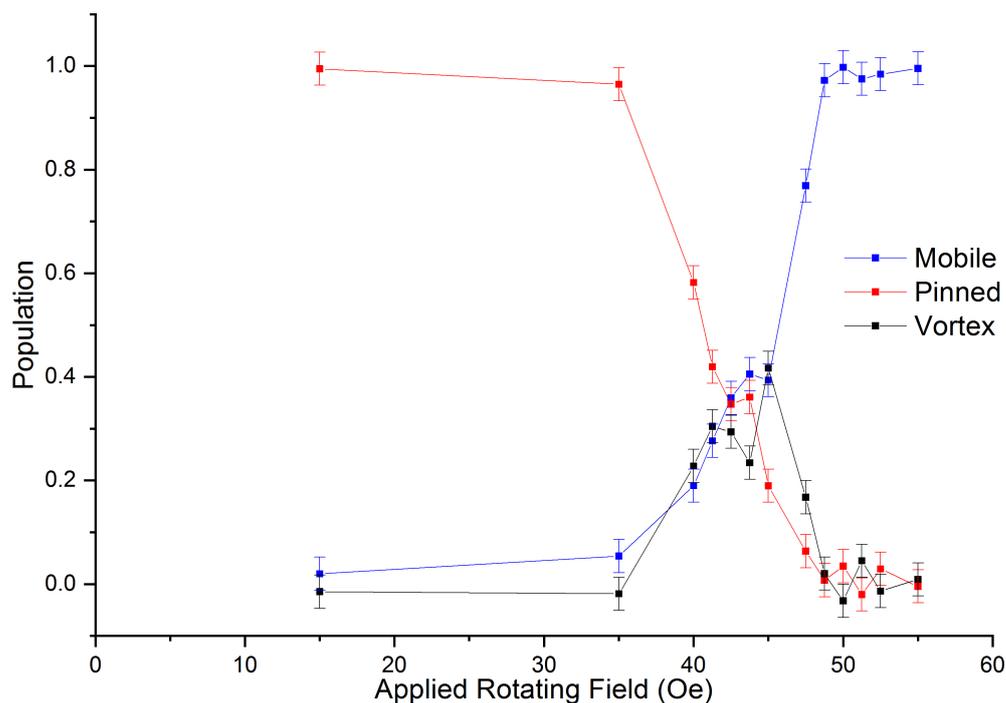

Figure 6.9. Plot of relative populations of propagating and pinned onion states and vortex states in an ultra large square array after 25 cycles of rotating magnetic field obtained via MOKE magnetometry. Lines are included as guides for the eye. Error bars represent maximum error from operator analysis and normalisation. Error analysis is expanded in §6.2.3.

Figure 6.9 shows the derived relative populations for an ultra large square array of the same geometry as in §6.1.2 and §6.1.3. The overall DW population is found from the sum of the pinned and mobile DW populations as per equation 6.3. From Fig. 6.9 it is clear that the general form of non-monotonic variation in wall population as predicted by the analytical model is again present. The minimum DW population appears to be close to 43Oe field amplitude, with an increased proportion of pinned DWs present at lower fields and of mobile DWs at higher fields. This field is close to that which gave zero magnetisation in PNR measurements (Fig. 6.3). It is noteable, however, that the minimum DW population measured by MOKE of ~0.55 is non-zero, unlike the PNR-measured minimum magnetisation. This differs from the analytical model (§5.4.1) that predicted a minimum population of 0.852. Error bars represent the range of possible values a point could be when accounting for the error by the operator in selecting values to normalise at.
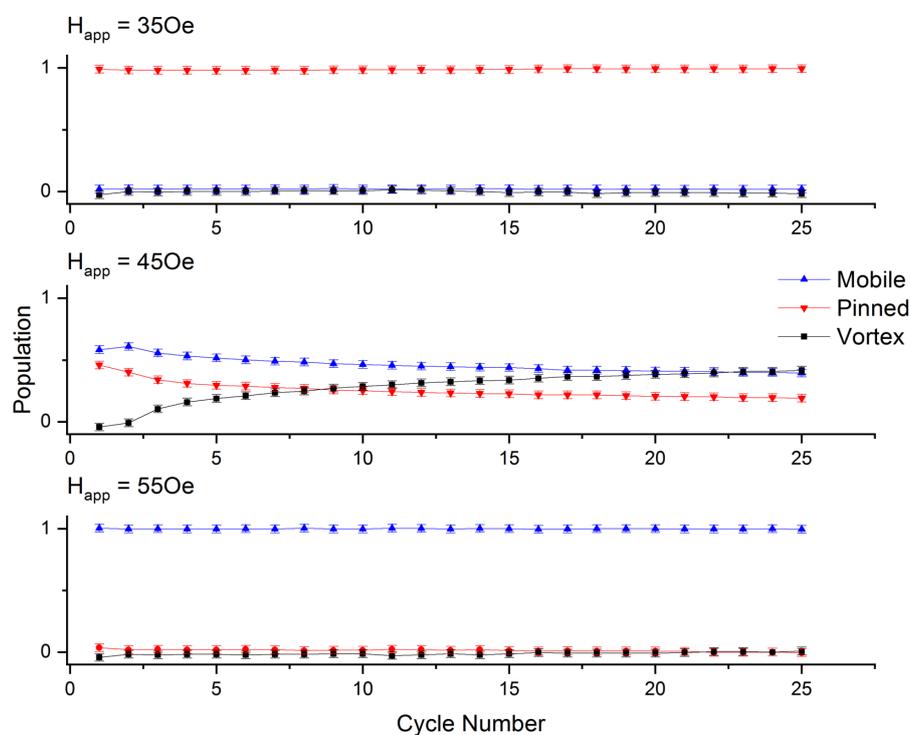

Figure 6.10. Ring state population changes in an ultra large square array at low, intermediate and high field regime values as increasing cycles of rotating field are applied at indicated values. 25th cycle values are those shown in figure 6.9 at these fields. Lines are included as guides for the eye. Error bars represent maximum error from operator analysis and normalisation.

Figure 6.10 shows the cycle-by-cycle changes in ring state populations at fields in the low (35Oe), intermediate (45Oe) and high (55Oe) field regimes. Comparing 35Oe and 55Oe, propagating and pinned lines switch positions between ~0 and ~1 and as a result vortex population is ~0 in both cases.

For 45Oe, equilibration of vortex population can be seen. With increasing cycles, vortex population increases until approximately 20 cycles. Looking at propagating and pinned states, it appears stabilisation occurs as the number of pinned states decreases. This is consistent with the predicted behaviour of the array; each cycle is another attempt for a wall to pass the required number of junctions and annihilation to occur.

Important differences between this initial MOKE investigation and PNR experiments are that there are 25 fewer cycles that are carried out at a higher frequency (27.4Hz in MOKE measurements, manual rotation of the sample stage in PNR measurements). Depinning is frequency dependent [3] as mean pinning time is dependent on attempt frequency such that

$$\frac{1}{\tau} = f_0 \exp\left(-\frac{E(B)}{k_B T}\right) \qquad\qquad Equation\ 6.7$$

where τ is mean pinning time, f_0 is attempt frequency, $E(B)$ is the height of the energy barrier to be overcome, k_B is the Boltzmann constant and T is temperature.

A reduced frequency for MOKE measurements was investigated to bring conditions closer to that used in PNR. Manual stage rotation for PNR measurements meant rotation was on the order of 10^{-1}Hz. The stability of MOKE measurements restricted the lowest frequency to 9.4Hz. The ring state populations as a function of field rotation strength for this frequency are shown in Fig. 6.11. The peak vortex population appears now to have shifted to close to 50Oe, which is in keeping with PNR on that same array.
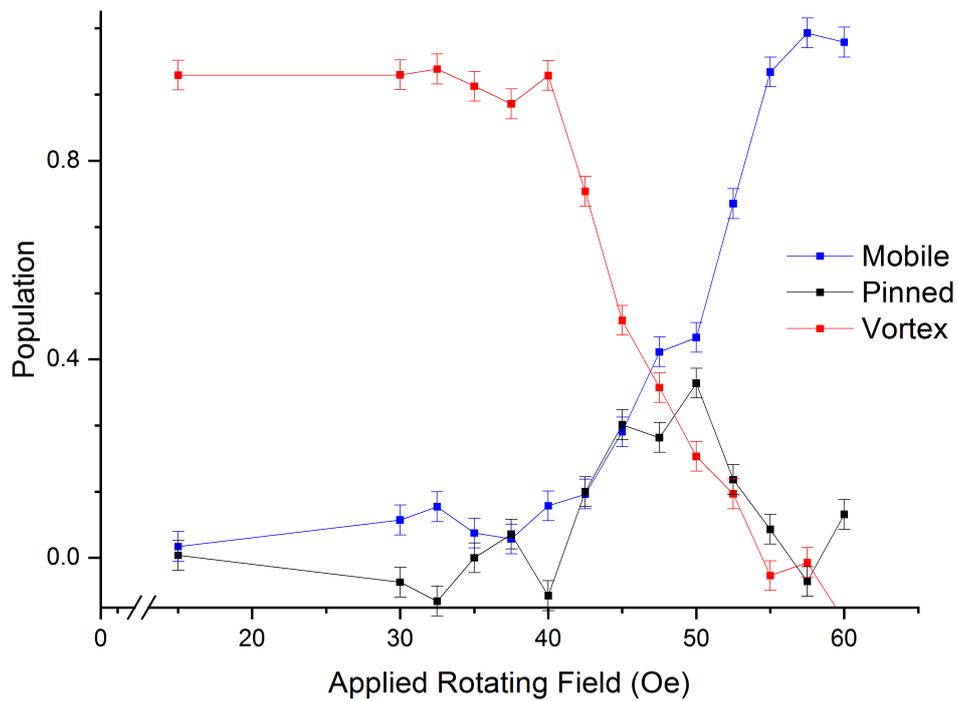
Figure 6.11. Plot of relative calculated populations of propagating and pinned onion states and vortex states in an ultra large square array following the application of 25 rotations at the indicated field. This is obtained via MOKE magnetometry at 9.4Hz frequency of applied field rotation. Lines are included as guides for the eye. Error bars represent maximum error from operator analysis and normalisation.

Figure 6.12 shows cycle-by-cycle population change at this reduced frequency. Again, low field and high field behaviour are clearly caused by predominance of either pinned or mobile DWs. 47.5Oe is chosen for an intermediate field to highlight the reduction in population decline of propagating and pinned states compared to Fig. 6.10. This has produced a vortex population that is lower than that obtained at fields either side of it (45Oe and 50Oe).
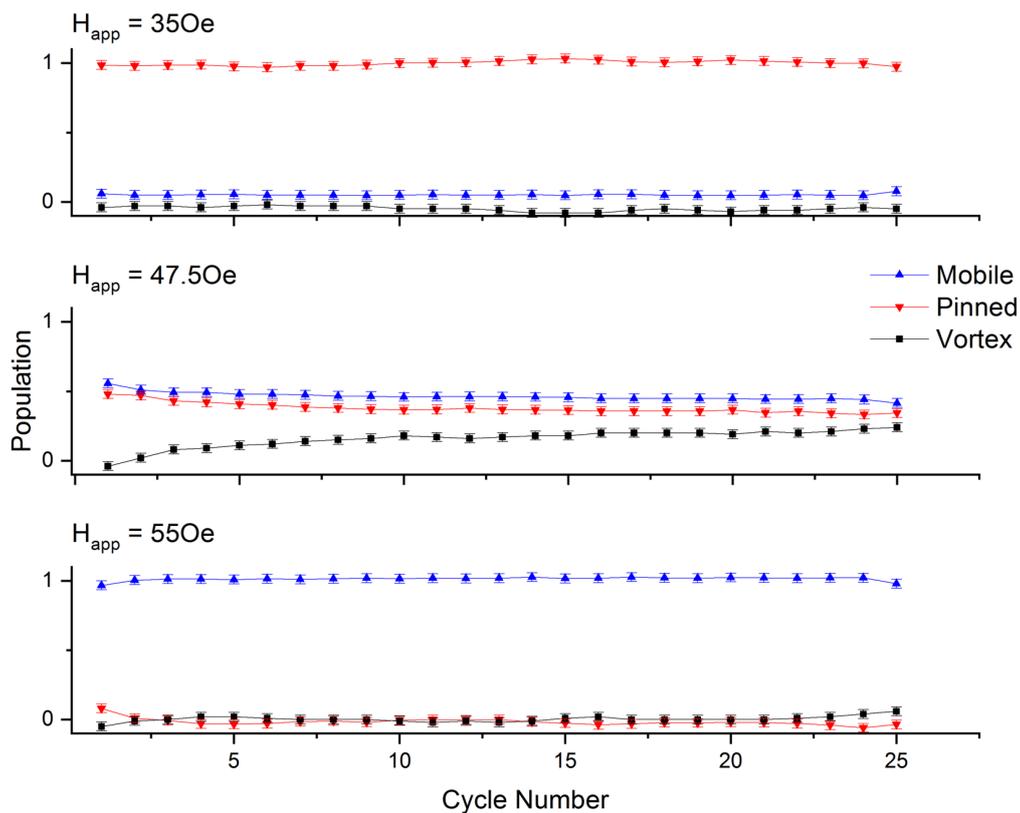
Figure 6.12. Population changes in an ultra large square array as increasing cycles of rotating field are applied at indicated values at 9.4Hz. 25th cycle values correspond to values in Fig. 6.11. Lines are included as guides for the eye Error bars represent maximum error from operator analysis and normalisation.

These population change plots in Figs. 6.10 and 6.12 show the dynamics of equilibration in interconnected nanoring arrays. Vortex state creation in the intermediate field regime is a result of the monotonic decrease in populations of nanorings containing pinned and mobile DWs. Both show that this decay towards equilibrium takes place over at least 20 cycles.

MOKE results have independently obtained similar results to the analytical model and PNR experiment, utilising a different mode of measurement to the latter. There is a strong argument that these two experimental results verify general analytical model behaviour and are indicative of the interconnected array's emergent properties. However, questions remain about why there was a discrepancy between the apparent populations of vortex states and DWs obtained from PNR and MOKE, about whether the depopulation of DWs from the array can be complete, and the validity of the assumption of rings being in one of three states. These are addressed through imaging experiments in §7.

6.2.3. Changing array size

2µm rings with 200nm track widths and 20nm thicknesses (50% overlap) were used for investigating varying array sizes. Prior to experimentation, micromagnetic modelling was carried out on these new dimensions, and suggested for depinning to occur a higher field would be needed than 4µm diameter, 400nm track width rings. Table 6.1 summarises the results of this modelling:

Table 6.1. Comparison of micromagnetic modelling behaviours for 2µm diameter, 200nm track width, 20nm thickness, 50% overlap rings and 4µm diameter, 400nm track width, 20nm thickness, 50% overlap rings

Field	4µm behaviour	2µm behaviour
50Oe	Pin + Annihilate	Pin + Annihilate
80Oe	De-pins and propagates	Pin + Annihilate
100Oe	De-pins and propagates	Pin + Annihilate
120Oe	De-pins and propagates	De-pins but doesn't escape and propagate. Falls back to diamond then annihilates
150Oe	De-pins and propagates	De-pins (some difficulty escaping junction, but de-pinned wall then catches up)

For this experiment, the MOKE system condenser lens was included but defocussed to obtain a laser spot size on the sample of approximately 50µm^2. This allowed the individual arrays here to be measured in isolation.

2 x 2 arrays were first investigated given they contain no rings with four junctions, which analytical modelling showed to dominate bulk behaviour and lead to non-monotonic variation in large arrays. Results are plotted in Fig. 6.13.
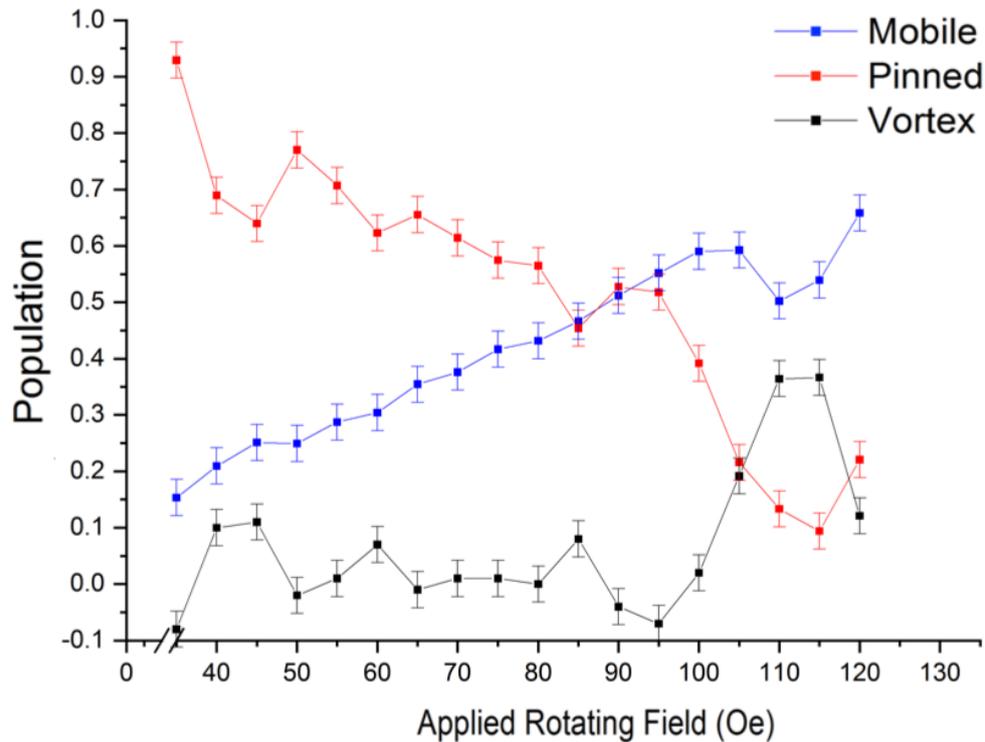
Figure 6.13 - Plot of relative calculated populations of propagating and pinned onion states and vortex states in an array of 2 x 2 interconnected nanoring arrays following the application of 25 rotations at the indicated field. Lines are included as guides for the eye. Error bars represent maximum error from operator analysis and normalisation.

Most notable is the predicted increase in field to cause onset of vortex formation – fields used did not fully define a high field regime. 150Oe was the field as predicted by micromagnetic modelling (table 6.2) to ensure propagating (and even then it was hindered by the process of depinning). This field sweep only reaches 120Oe and as propagating states are increasing towards but not yet reaching ~1 is indicative that this field still needs probing to fully cover array behaviour.

The gradient of population of onion state rings with mobile DWs is shallower than as seen in 4μm rings. Onset of de-pinning appears to be much harder, steadily decreasing until >95Oe where a change in the rate of walls that are pinned occurs. This increases the vortex state population as mobile DW population is increasing relatively linearly.

The non-monotonic change in mobile DW population at 110Oe and 115Oe away from this linear trend contributes further to an increase in vortex state population. The off-trend nature of this dip (given that 120Oe appears to return to the linear projection of

population) necessitates an analysis of error and limitations of this analysis. Identified sources of error are:

- Drift in signal average by the 25th cycle.
- Selection of Kerr signal and time values during normalisation.
- Multi-sequence averaging.

The erroneous nature of drift can be controlled by analysis of population change in the equilibrated region, taken as 20-25 cycles. A better plot of relative populations would sample upwards of 25 cycles and take the average value of cycles 20-n, where n is the number of the last field cycle, as well as plotting the standard error of this data set. This would greatly reduce the effect of outliers on population plots. On a point to point basis, the 20 averages taken before data transfer from oscilloscope to MOKE control software help to control the detrimental effects of drift. Operator discretion is employed to discard data gathered for a point when drift appears to significant.

Error in normalisation can lead to unphysical reported populations such as negative populations in Fig. 6.13. This error is compounded when two normalisations are performed to obtain both pinned and mobile populations. Normalisation is a manual process that involves selecting four values (two values of time and then two Kerr signals) further compounding potential slight deviations from actual values that should be taken. To account for this, error bars have been included on MOKE plots to show the range that a human error during value selection carried through to normalisation. This is approximately 3% of the normalised Kerr signal.

Another technical source of multi-sequence averaging error in finite arrays can be visualised in a 2 x 2 array that has an intermediate field applied once following saturation, five times. If three instances were all vortex and two were all onion (pinned or mobile) then the reported vortex population would be 0.6, which is impossible with a four-ring array. In the context of an array of arrays this is not a detrimental source of error, as it is likely indicative that 60% of arrays, or indeed 60% of total rings in the ensemble are in vortex state.

Figure 6.14 shows 25th cycle populations for a 5 x 5 array. The majority of rings in this array have four junctions, meaning array behaviour is closer to the ultra-large square than that in Fig. 6.13.
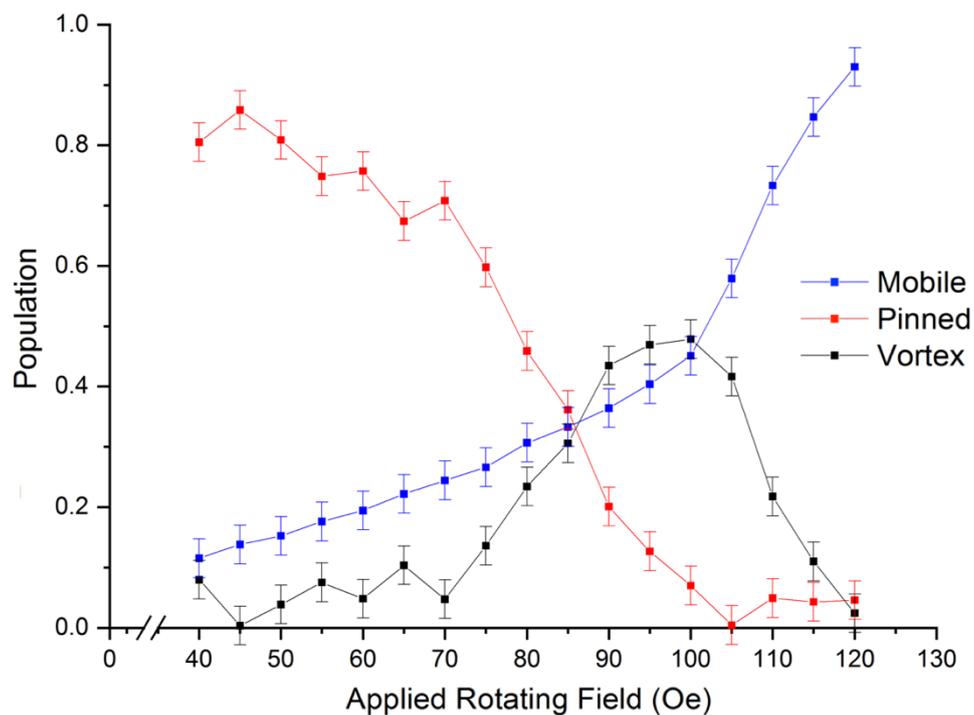

Figure 6.14. Plot of relative calculated populations of propagating and pinned onion states and vortex states in an array of 5 x 5 interconnected nanoring arrays following the application of 25 rotations at the indicated field. Lines are included as guides for the eye. Error bars represent maximum error from operator analysis and normalisation.

The predicted increase in field at which depinning occurs for smaller rings is noted, with a peak in vortex formation around 100Oe. Using guides for the eye, propagating wall population appears to be a much smoother and regular process, with two notable gradients. Pinned states appear to be 'noisier' in that though there does seem to be an underlying trend (negative gradient), it is susceptible to aberrations such as at 60Oe/70Oe (or indeed 55Oe and 65Oe may be 'off trend').
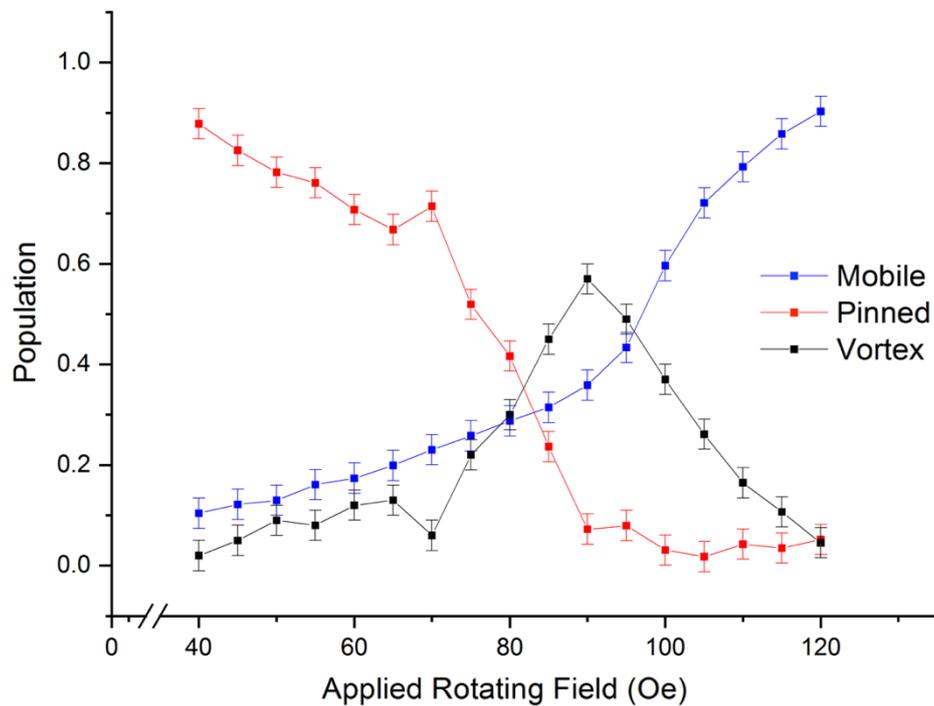
Figure 6.15. Plot of relative calculated populations of propagating and pinned onion states and vortex states in an array of 8 x 8 interconnected nanoring arrays following the application of 25 rotations at the indicated field. Lines are included as guides for the eye. Error bars represent maximum error from operator analysis and normalisation.

Figure 6.15 for 8 x 8 arrays showed similar profiles to the non-monotonic PNR results and MOKE on ultra-large and 5 x 5 square arrays. A narrower peak at 90Oe was observed, though this could be from the pinned population being 'off-trend' giving a higher vortex population.

Once again, mobile DW population appears much more consistent with a gradient change at 95Oe. This is interesting in the context of micromagnetic modelling showing repopulation having a later onset than de-pinning. If repopulation is statistically more likely to occur at >95Oe applied rotating fields, then there is a greater population of DWs that can be mobilised.

Compared to analytical models of DW population in square arrays (§5.4.1), these finite arrays show minimum DW populations (maximum vortex populations) at higher field values than infinite arrays. The total population of DWs (not vortex states) is lower than for an infinite array, which is consistent with analytical models.
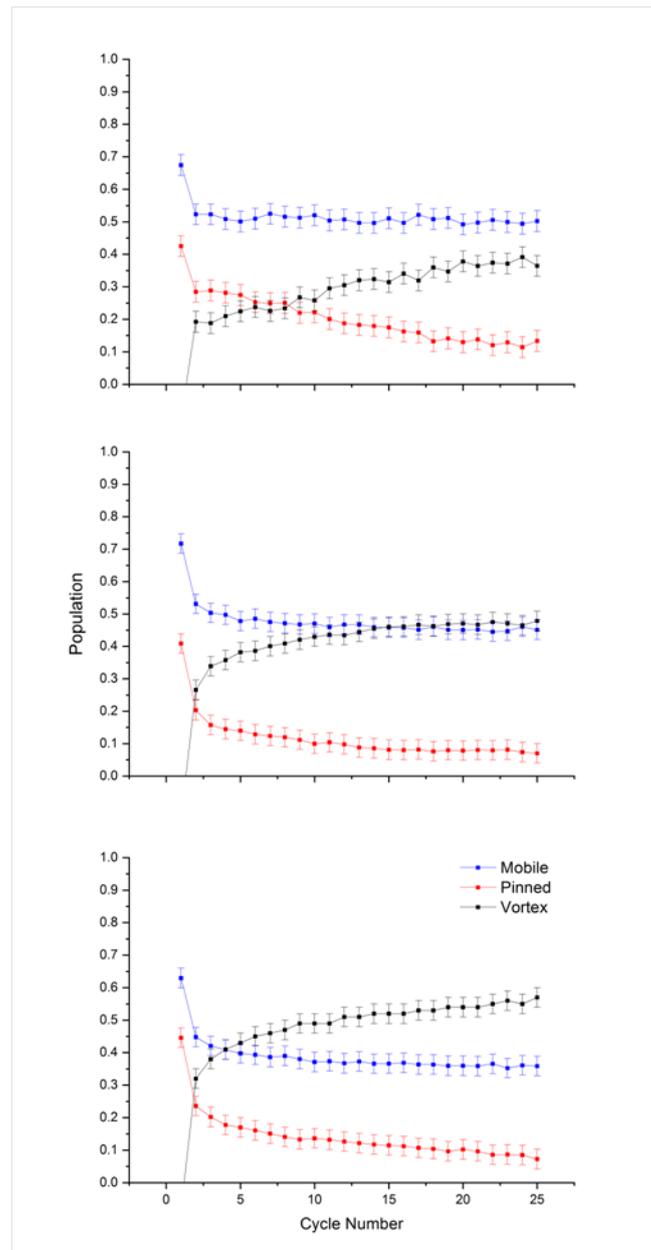
Figure 6.16. Intermediate field population changes for 2μm diameter, 200nm track width, 20nm thickness and 50% overlap interconnected nanorings in (a) 2 x 2 at 110Oe applied rotating field strength (b) 5 x 5 at 100Oe applied rotating field and (c) 8 x 8 arrays at 90Oe applied rotating field. Error bars represent maximum error from operator analysis and normalisation.

Figure 6.16 shows intermediate field cycle-to-cycle population changes with enlarged y-axis for these finite arrays at maximum vortex population to highlight the equilibration behaviour of these arrays. These plots show that vortex conversion is mostly enabled by conversion from pinned to vortex as these drop towards zero population whereas mobile rings appear to hit a limit to the proportion they can drop to. As repopulation is

dependent on mobility of DWs through a junction, newly nucleated DWs into a formerly vortex ring could lead to this observed equilibrated minimum in mobile rings.

These population graphs suggest that equilibrium has not quite been achieved by the 25th cycle, and analysis of point-point change in population of vortex states finds while ΔPopulation approaches zero, it is still increasing (Fig. 6.17).
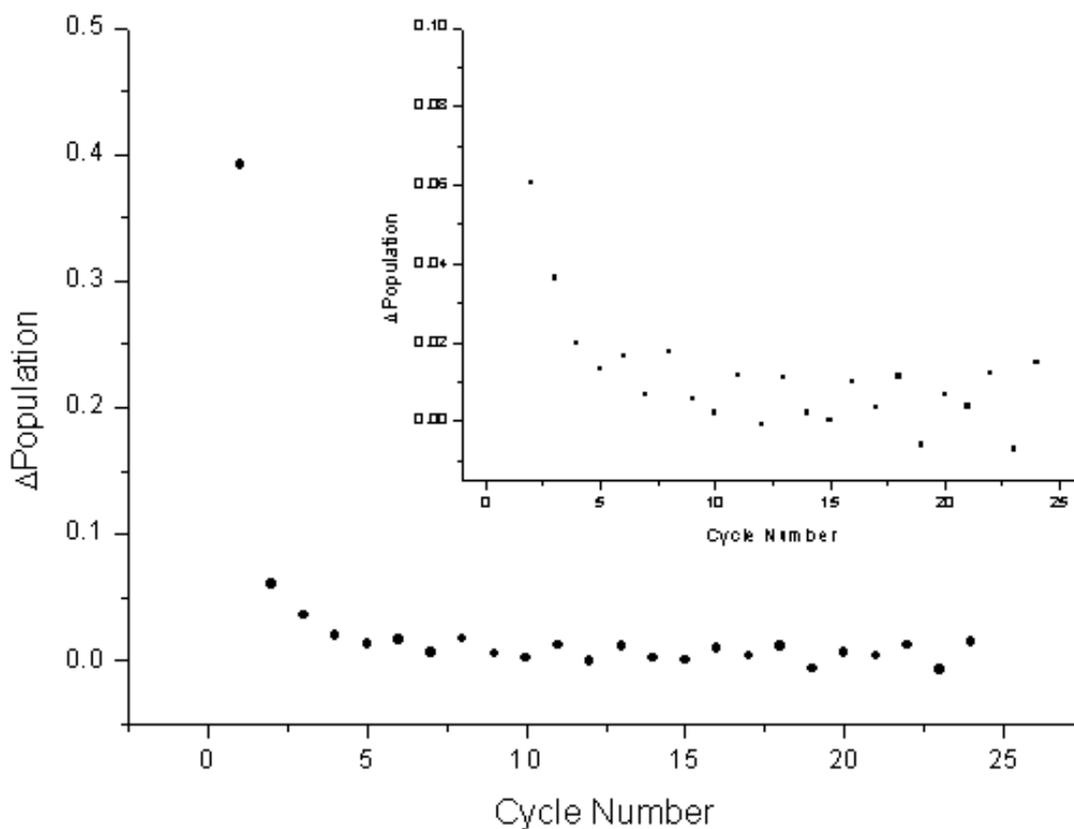

Figure 6.17. Point to point variation of vortex population for H$_{app}$ = 90Oe applied to an 8 x 8 ring array. The inset shows the 2nd and 24th intervals at a higher resolution to show whilst variation is small it is still present.

6.2.4. Sample-to-sample repeatability

As described above, the ultra-large square array sample consisted of many smaller arrays of 26 x 26. PNR measurements in §6.1 and MOKE measurements in §6.2.2 combined signals from many such small arrays, so any differences in individual small-array response could not be distinguished. In addition, the spatial position of array blocks within the electromagnet field may lead to differences in array behaviours that are averaged in the ensemble.

Here, several individual 26 x 26 arrays within the ultra-large array were characterised by MOKE by including the condenser lens in the system and adjusting the laser spot size as viewed on the CCD display to be approximately 100µm x 100µm (i.e. one array block). The spot was then placed centrally over one of the arrays to ensure the Kerr signal would be dominated by the magnetic behaviour of that array.

The field protocol outlined in §6.2.1 above was used (initialisation followed by 25 in-plane rotations at the desired measurement magnetic field amplitude).

Figure 6.18 presents the ring state populations from four individual arrays that were measured by MOKE (no other arrays were measured as part of this experiment). The larger fields to obtain population changes compared with §6.2.1 and §6.2.2 are most likely due to the changes in ring dimensions. The most striking feature of these plots, however, is their similarity. This is further accentuated in Fig. 6.19, which shows on one plot the 'vortex state' data for each of the arrays. These all show maxima in the vortex population between 75Oe and 80Oe, and very similar maximum vortex population value, with an average of 0.38 and 0.44, respectively, and a standard deviation of 0.18 and 0.05. Figure 6.19 shows that two arrays yielded an increase in vortex state population at lower fields than the others, leading to higher deviation at 75Oe (as shown in Fig. 6.20). However, the overall consistency in behaviour between nominally identical arrays lends confidence to the data from ultra-large arrays presented earlier in this chapter being representative of individual arrays, and that structure-to-structure repeatability is likely to be reasonably good. In fact, no discrete ring array structures failed to show the types of behaviour described in this chapter.
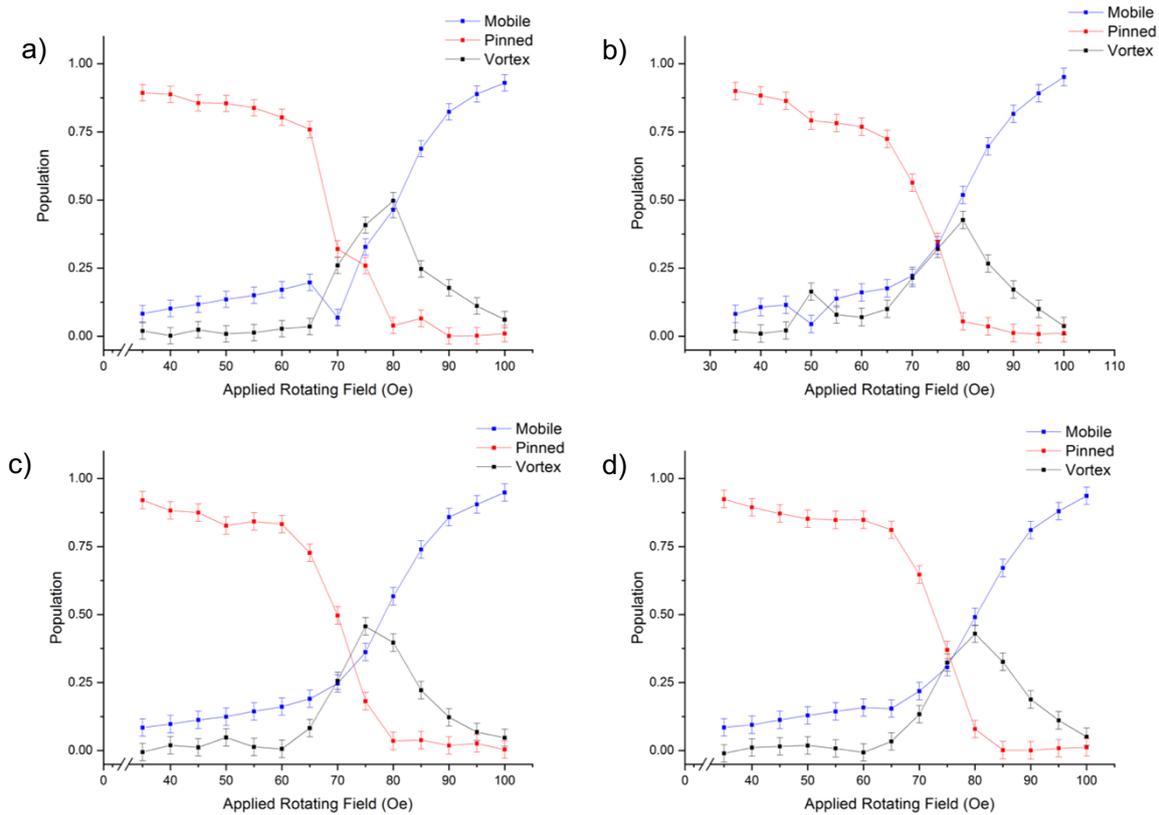
Figure 6.18. Population plots of mobile and pinned onion and vortex states at varying applied rotating fields (25 cycles, 9.4Hz). All lines are guides to the eye. Dimensions are 26 x 26 arrays of 4µm rings, 400nm track width, 20nm thickness and 50% overlap. Each array block is at millimetres away from others from distinctly different parts of the ultra large array. Error bars represent maximum error from operator analysis and normalisation.
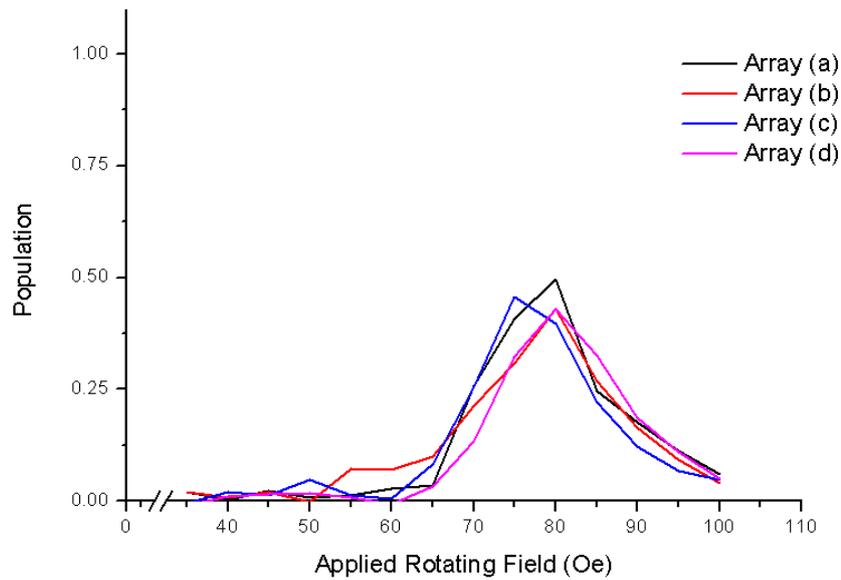
Figure 6.19. Collated vortex state population plots for four individual 26x26 interconnected nanoring arrays. Guides to the eye from Fig. 6.23 are plotted rather than individual data points for ease of visualisation.
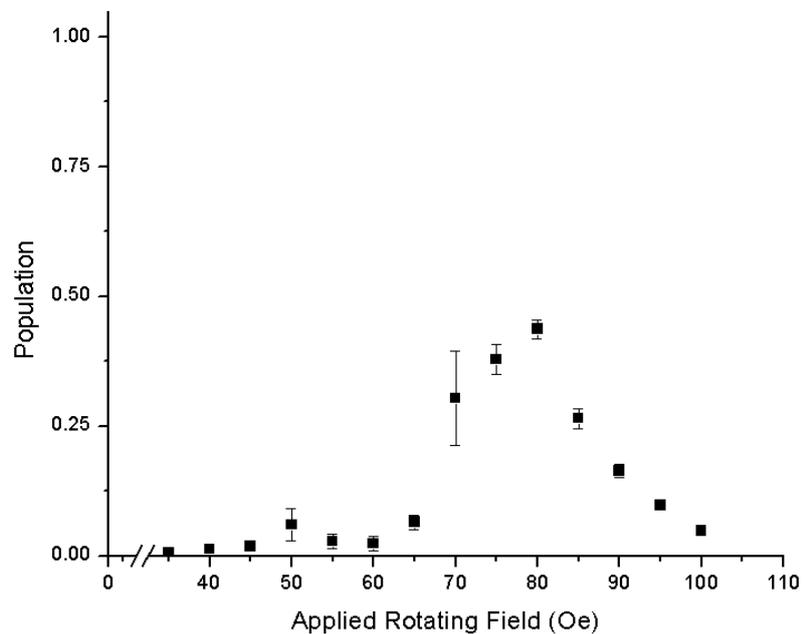

Figure 6.20. Plot of mean and standard error of Fig. 6.20 for vortex population of 26 x 26 interconnected nanoring arrays. This error analysis also shows that phantom peaks, such as seen at 50Oe, could be captured by single array measurements.

6.3 Discussion

The work in this chapter has demonstrated whole ensemble, emergent behaviour in interacting magnetic nanoring arrays experimentally. An in-plane rotating magnetic field is shown to result in a consistent magnetisation or DW population response from the arrays. The quantitative nature of PNR creates significant confidence in the existence of an emergent response, while the MOKE data show that the equilibrium is dynamic. This substantiates the main assumptions behind the analytical model in §5, of DW loss (through stochastic pinning and annihilation) and gain (through stochastic de-pinning of DWs at junctions with empty rings) results in an equilibrium DW population.

There is, however, an apparent conflict in the observed minimum in magnetisation from PNR measurements going to zero and the minimum calculated DW population from MOKE measurements being approximately 0.5. This suggests that the simple framework of three allowable magnetic ring configurations (vortex state, onion state with pinned DWs, onion state with mobile DWs) for characterising the MOKE measurements of arrays may be somewhat naïve. However, this approach does give significant insight into the arrays' behaviour and may be a reasonable analogue to signals that might be obtained with future magnetoresistance measurements of the arrays. This is very appealing as the basis of reservoir computing (RC) in providing a 'fading memory' of the previous magnetic state. Other array behaviour demonstrated here in that the systems appears to have a non-linear response, a quantifiable output and be repeatable and scalable also lend credit to the selection of the interconnected array for realising RC hardware.

It has been demonstrated in this chapter that the interactions between neighbouring magnetic rings transform stochastic behaviour of DW pinning at individual ring junctions into a reliable, measurable ensemble behaviour. To understand the structure and ground state position, there are methods that allow magnetisation and domain observation. Artificial spin ice structures, as discussed in the literature, are often viewed with magnetic force microscopy and synchrotron based magnetic circular dichroism methods.

6.4 References

[1] M. Björck and G. Andersson, "GenX: an extensible X-ray reflectivity refinement program utilizing differential evolution," *J. Appl. Crystallogr.*, vol. 40, no. 6, pp. 1174–1178, Nov. 2007.

[2] W. Wernsdorfer *et al.*, "Nucleation of magnetization reversal in individual nanosized nickel wires," *Phys. Rev. Lett.*, vol. 77, no. 9, pp. 1873–1876, 1996.

[3] V. D. Nguyen *et al.*, "Elementary depinning processes of magnetic domain walls under fields and currents.," *Sci. Rep.*, vol. 4, p. 6509, 2014.

Chapter 7 – Imaging of Nanoring Arrays

"I can see clearly now" – Johnny Nash

7.0 Background

Chapter 6 highlighted generally good agreement between PNR and MOKE results with analytical modelling of the magnetic behaviour of large arrays of soft ferromagnetic interconnected rings driven by an in-plane rotating magnetic field. These approaches all produced results that average behaviour over the ensemble of arrays. Direct imaging of local configurations promises a greater understanding of the processes taking place under the applied field.

Direct imaging of DWs has long been possible through a variety of experimental methods such as magnetic force microscopy (MFM), magnetic transmission X-ray microscopy (MTXM), scanning electron microscopy with polarisation analysis (SEMPA), and photoemission electron microscopy (PEEM). Most of these approaches tend to have slow temporal resolution; even when MTXM and PEEM are used with ultra-fast X-ray pulses available at many synchrotron sources, the sample must be re-initialised after each exposure. As domain wall motion occurs at high velocities, especially compared to their size (i.e. movement in mm/s for a region a few nanometres wide), these techniques often look at the state of a system after external parameters have been applied.

Experiments in Chapter 6 showed the DW population of a ring array initialised into a saturating state remains at or close to a maximum at low and high rotating field strengths but went through a minimum at an intermediate field. This agreed with predictions made with analytical modelling in Chapter 5. This shows that the DW population of nanoring arrays can be regarded as a characteristic emergent property. However, much detail of how the DWs interact is unknown. The assumptions made in creation of the analytical

model regarding DW behaviour may lie behind some of the surprising results obtained in magnetometry. A greater understanding of the details of local DW behaviour in the arrays may inform our understanding of a range of ring arrays.

This chapter presents MFM and PEEM images used to study the magnetic configurations in arrays of interacting permalloy nanowire rings. MFM offered a higher resolution, which helped visualise the details of DW configurations, but PEEM offered a wider field of view, which enabled a greater understanding of the magnetic behaviour of the array as a whole.

7.1 Magnetic Force Microscopy

Magnetic force microscopy (MFM) was used to image the magnetic states of ring arrays after the application of magnetic fields – usually either a saturating field of 250Oe or 25 cycles of a known intermediate field (verified with MOKE magnetometry). The field was applied while samples were outside the MFM, and then the samples placed in the MFM system for imaging.

MFM has the advantage of being carried out in-house on equipment (further detailed in §4.8) relatively cheaply compared to other imaging techniques. Its drawback is the time taken to produce an image (∼90 minutes) and the extent of noise that is produced. Post-processing on images was carried out to rectify this through a series of filters and line suppression macros. Often, repeating noise motifs would appear on images that lowered the quality and value of otherwise good data, but post-processing was able to recover reasonable images. However, some images retain this noise when further filtering would compromise data interpretation.

For images here, tip to sample separation varied but was between 40nm and 60nm. Samples were placed at a 45° angle to the direction of tip travel to minimise travel time across a junction. This was to avoid perturbation of domain walls within junctions by the tip as much as possible, which is because of the magnetically soft nature of $Ni_{81}Fe_{19}$. Previous work has shown tip interactions on NiFe islands in artificial spin ices can reverse the direction of magnetisation in a ferromagnetic island [1], [2].

7.1.1 Saturated Array

The ultra large square array used at ISIS for PNR experimentation in §6.1 was sectioned to a 5mm x 5mm sample and a saturating field of 250Oe applied.

Micromagnetic modelling in §5.1 showed that DWs in interconnected ring arrays can combine in junctions to form a 'diamond' configuration. These diamond states were seen in the modelling in opposing junctions of rings in a square array, whereas the orthogonal junctions simply had a slight canting of dipole moments.

Figure 7.1 shows a 40μm x 40μm MFM image of the large array of rings that had been saturated. As can be expected and as predicted by micromagnetic modelling (§5.1), the rings shown were in the onion state configuration, although some distortions in the centre of the image make this less obvious. The reliability of finding DWs in this configuration was very high, e.g. Fig. 7.1 shows over 100 rings from an array of millions. More widely, imaging of approximately 3,000 rings in saturated states from random locations of the larger array showed just one case where a ring was not in the regular onion state. This suggests that the onion state arrangement is strongly favoured following the application of a saturating magnetic field. The single anomaly was likely to have been defect induced, presumably due to an error in the fabrication process at some point.
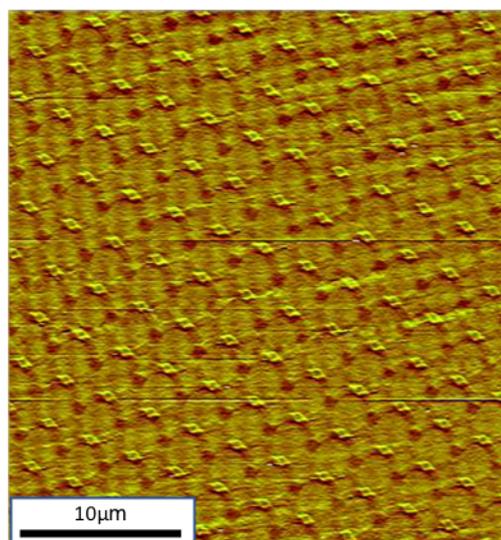

Figure 7.1. MFM image of an interconnected nanoring array taken after application and removal of a saturation field.
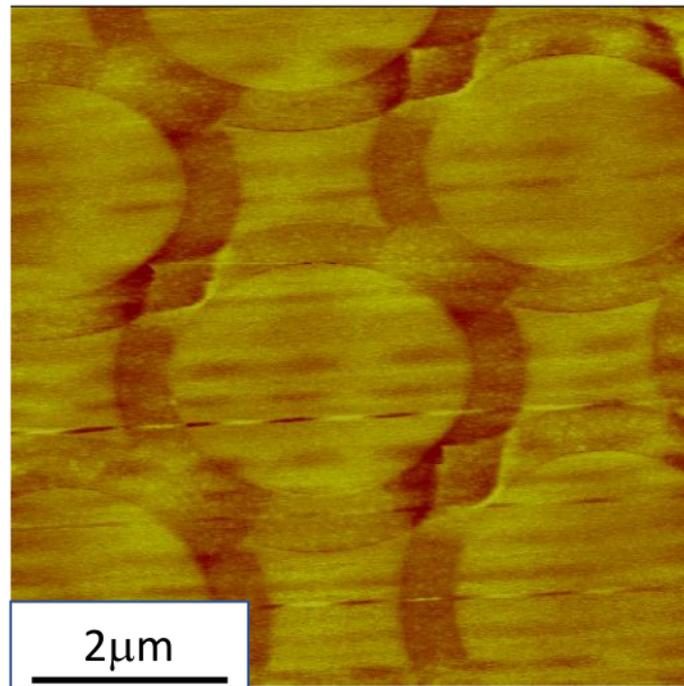
Figure 7.2. 7μm x 7μm MFM image from rings in the saturated array as used in Fig. 7.1. This highlights the appearance in MFM of diamond magnetic configurations of DWs at junctions. The horizontal line in the centre is a noise artefact.

Fig. 7.2 shows a higher resolution MFM image of a region of the ring array shown in Fig. 7.1. This magnified image shows diamond configurations at wire junctions where DWs from neighbouring rings have combined. This is similar to the structure predicted through micromagnetic modelling earlier (e.g. Fig. 5.5). The junctions at 90° ring positions to the DWs also show light and dark contrast in the MFM image due to the presence of divergence of magnetic flux in this region.

To confirm the origin of the appearance of the MFM images, a micromagnetic model was adapted to simulate the MFM response from onion state rings. Figure 7.3 shows a cross of five 4 μm diameter rings with 50% overlap, i.e. those imaged experimentally. Fig. 7.3a shows the magnetic configuration of an equilibrated simulation, including the formation of diamond-like DW configurations at two of the junctions. MFM images magnetic field gradient, which can be calculated as the divergence in magnetic flux. Mumax3 has an inbuilt 'MFM' function to calculate this, and results for the magnetic configuration in Fig. 7.3a are shown in Fig. 7.3b, for a simulated tip lift height of 40nm chosen to match experimental conditions. This image shows that the diamond shape of combined DWs is

replicated in the MFM simulation, while individual vortex DWs appear as a triangular region in MFM.
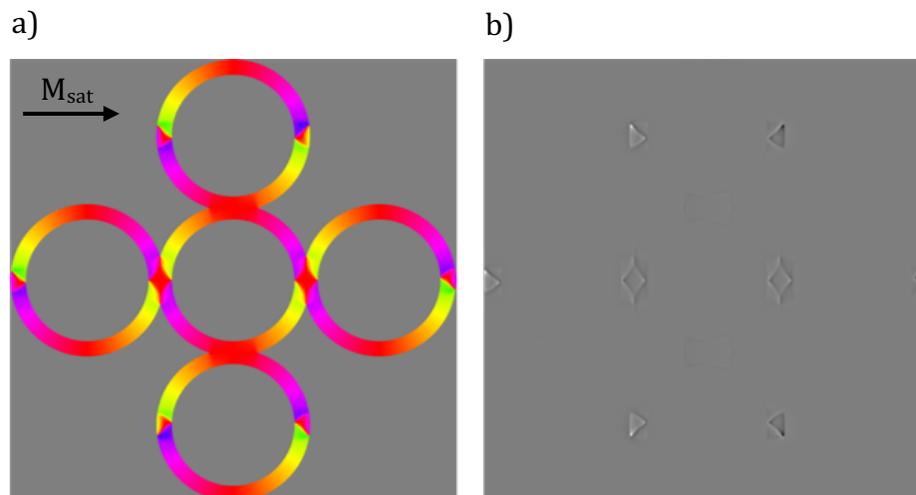

Figure 7.3. a) A Mumax3 simulation of five 4μm diameter, 400nm track width, 20nm thickness, 50% overlap rings relaxed following saturation. B) Simulated MFM of (a) using in-built MFM function using a lift height of 40nm.

7.1.2 Intermediate Strength Field Rotation

This section presents results from MFM imaging on an interconnected array of 4μm diameter, 400nm track width, 20nm thickness and 50% overlap nanorings in square arrangement following application of a saturating field then 25 rotations at 47.5Oe. MOKE magnetometry performed with this protocol on this array showed this to be an intermediate field (§6.2.2) at which the number of DWs should have reduced and vortex ring states created. This is designated in this section as the intermediate array in contrast to the saturated array from §7.1.1.
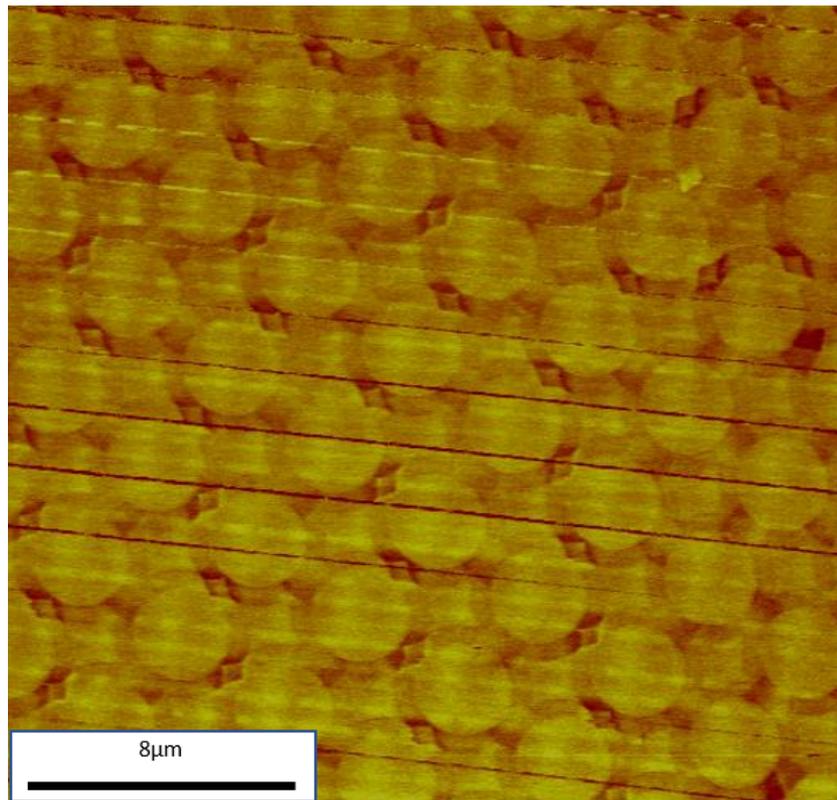
Figure 7.4. 25μm x 25μm MFM scan from an ultra large interconnected nanoring array that had been subject to 25 rotations of 47.5Oe in-plane magnetic field. Diamond states and contrast from junctions free of DWs are again visible but there is also evidence of new behaviour in some junctions. Furthermore, the diamond configurations are no longer in a regular arrangement and can be found in adjacent junctions.

As with the saturated array, many separate areas of the array of arrays were imaged. One of these is presented in Fig. 7.4. The regular arrangement of diamond arranged DWs in opposing junctions were no longer present following the application of this intermediate field. Diamond configurations were often found in an adjacent junctions, breaking the symmetry of the onion state into two unequally sized domains.

Following a convention of assigning light and dark edges of domain walls to head and tail of domains respectively allowed the image in Fig. 7.4 to be annotated with magnetic domain directions, shown in Fig. 7.5. Arrows are colour coded according to different configurations, to highlight rings that had similar magnetic arrangements. Black arrows are used when the state cannot be fully defined. It is also used when three arrow heads or three tails enter a single junction.
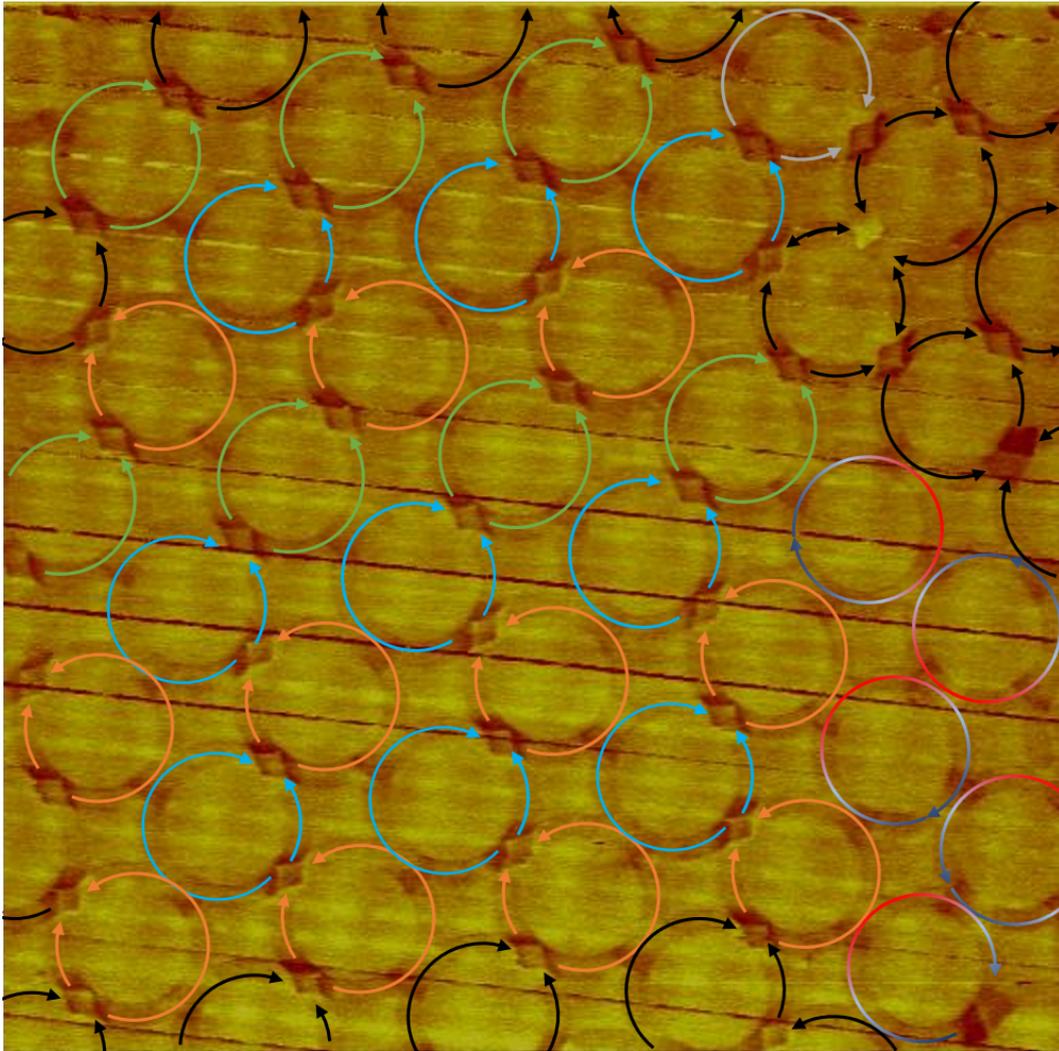
Figure 7.5. Annotated 25 μm x 25 μm MFM scan shown in Fig. 7.4. Each different magnetic configuration of a ring is assigned a different colour. Black arrows are used when a ring structure cannot be confirmed.

Fig. 7.5 reveals several distinct patterns. To start, the bottom right corner reveals that vortex states are present. MFM contrast is visible from junctions in these rings but there were no DWs present. The vortex in the bottom right corner contains some form of distorted domain wall or dipole arrangement within the junction, leading to its irregular appearance. Neighbouring vortex state rings appear to have opposite chiralities.

Most rings were in a configuration where one domain occupied three-quarters of the ring and the other domain occupied the remaining quarter. These are highlighted in Fig. 7.5 using light blue and orange arrays, with the different colours showing two different orientations of the DWs (there is also another of these 'three-quarter' states in the top right of Fig. 7.5, shown using white arrows). It is striking that identical configurations of the 'three-quarter' states shown by light blue and orange arrows and onion states (shown

by green arrows) appeared in lines, which suggests some sort of collective mechanism of DW motion occurred in the array.

Most of the junctions in Fig. 7.5 are made up of two arrow heads and two arrow tails, i.e. they have zero magnetic charge locally. Junctions were observed with three arrows or tails too, however, and with four identically charged domains, both in the top-right corner of Fig. 7.5. These indicate a degree of frustration in the array. The proximity of these junctions to vortex states may mean the change in local DW population has forced the creation of a 'three-in-one-out' junction, which in turn may have led to a long-range ordering of diamonds and pairing of chirality to create these patterns. The intermediate array may exist in a frustrated quasi-static state as a result of the creation of vortex states, however the sample size from this image is too limited to assert this confidently. Later, PEEM experimentation will look for further evidence of frustration and long-range ordering.

Fig 7.6 shows a magnified view of a three-in junction (highlighted with an orange spot) and an example of a 360° DW (highlighted with a blue spot) that appeared as a 'double diamond' configuration.
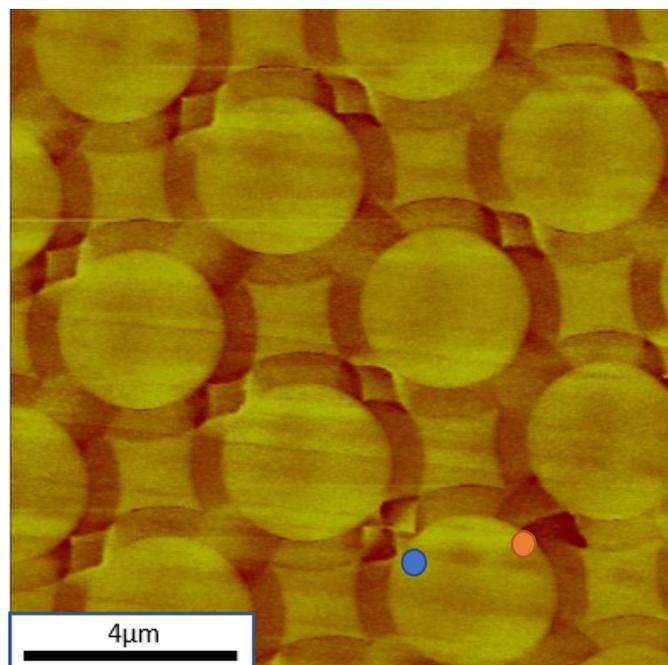

Figure 7.6. 11.7μm x 11.7μm MFM image of a region of the ultra large interconnected nanoring array following application of an intermediate rotating field.
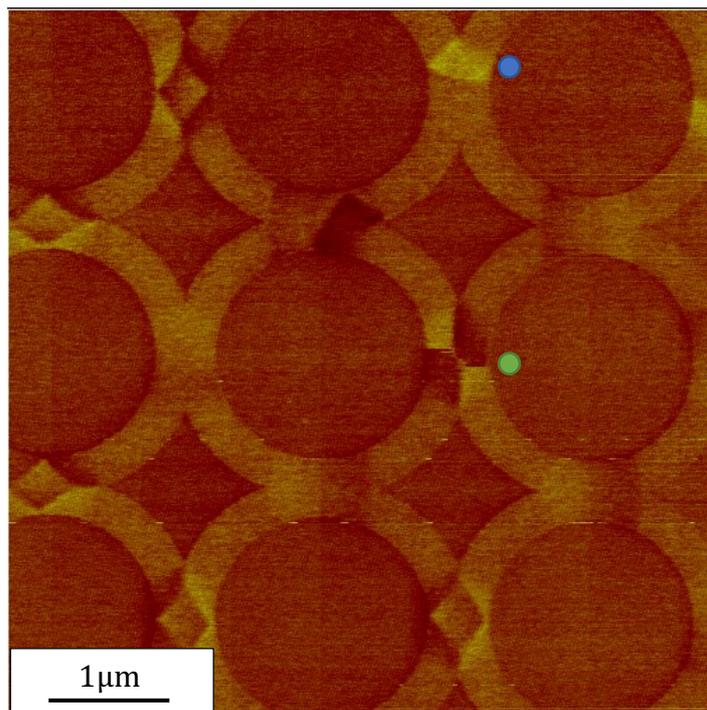
Figure 7.7. 10µm x 10µm MFM image of a region of the ultra large interconnected nanoring array following application of an intermediate rotating field, highlighting the 'chequered' junction type.

Other examples of different junction types that can be found with MFM are shown in another image in Fig. 7.7. This includes an unusual 'chequered' junction (green dot); this is an example of a two-in, two-out domain arrangement that does not take the form of a diamond. The orientations of which of the ring arms that are 'in' and which that are 'out' have changed from being in the same ring with diamonds to across the diagonal of the junction. The relative scarcity of this junction compared to the abundance of diamond states that can be found in MFM images suggests that the chequered junction is not as energetically favourable as the diamond; this is further explored in §7.3.

Figure 7.7 also contains examples in the top centre ring of the three-in-one-out junction arrangement seen in Fig. 7.6 (blue dot).

7.2 Similarity to artificial spin ices

A square ASI with four moments to consider at each vertex can take on a total number of configurations = 2^4 = 16. These can be separated into four topologies or types, described as type I, II, III and IV. The nature of junctions in interconnected ring arrays have an

identical multiplicity of domain directions in the wires making up the junction. The three-in, one-out ring junction configurations here are similar to Type III vertices in ASI and two-in, two-out junction configurations are similar to Type I and Type II ASI vertices [3]. The available configurations in the ring system are shown schematically in Fig. 7.8 and follow the Type I-IV definitions used in ASI.
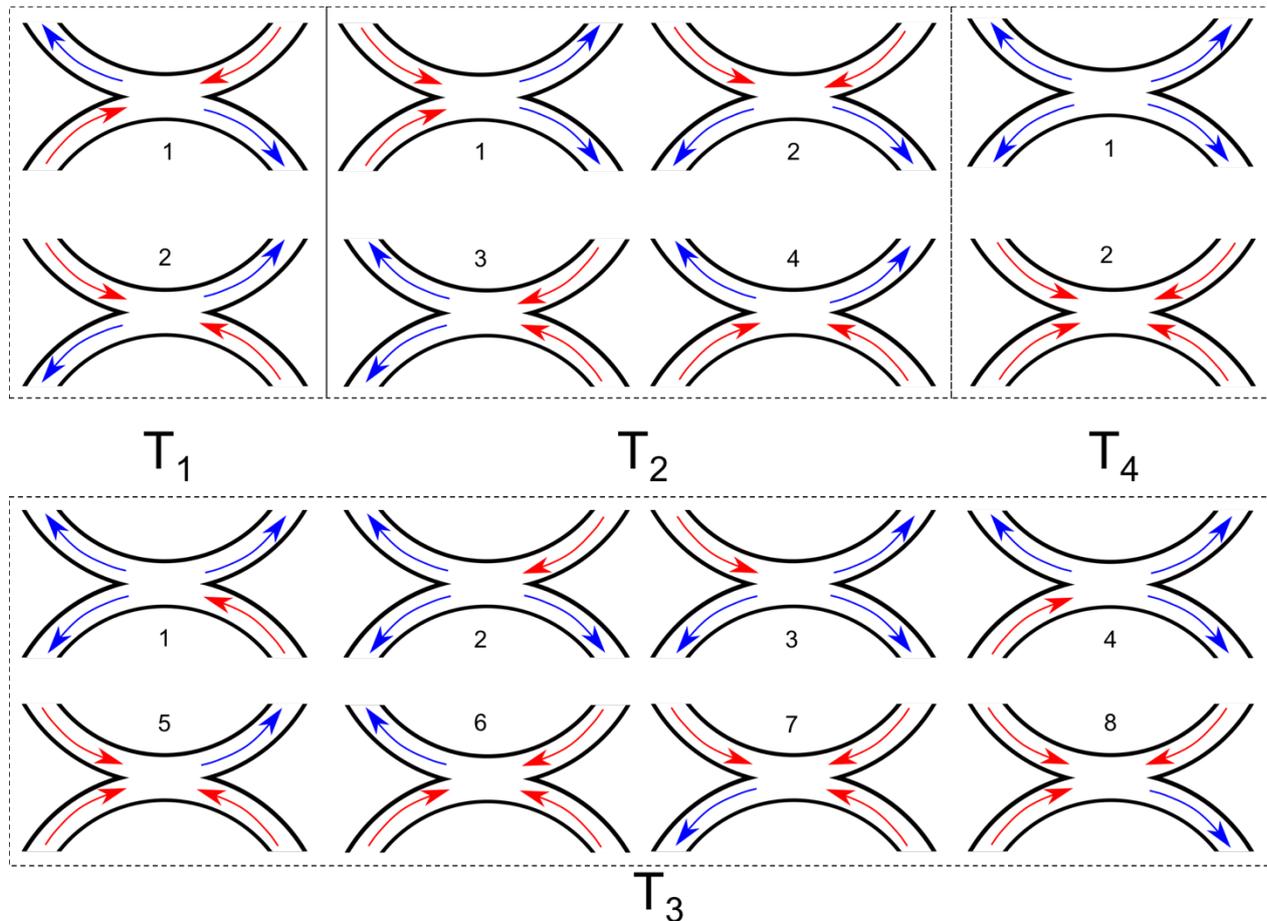

Figure 7.8. The possible magnetisation configuration in the arms around a nanowire ring junction grouped into four types (T1-4) of arrangements based on similarity to established conventions in artificial spin ices. Arrows show the direction of magnetisation in each arm.

In Fig. 7.8, colour coding has been used to differentiate between dipoles pointing into and out of junctions but should not be confused with red-blue contrast in images that will follow in §7.3 (Fig. 7.10). Also established here, to differentiate between ASIs and this system is the use of T1-4 to describe interconnected nanoring junctions compared to Roman numerals I-IV for an ASI.

The energetic difference between type I and III vertices in an ASI is more than twice that for I and II as modelled by Wang et al [3] using OOMMF on arrays with a lattice constant of 320nm. Mumax3 was used here to simulate an interconnected nanoring junction to calculate the total energy of the magnetic configurations shown in Fig. 7.8. A junction region of two 4μm diameter, 400nm track width, 20nm thickness rings overlapped by 50% was used, with materials parameters being identical to those listed in §4.9. Appendix A1.3 contains a sample Mumax script for this.

To model junctions, a PNG format image of the junction was created (at a ratio of 1px = 1nm in simulation space) and filled in to give a black/white image that was used with the ImageShape function (refer to §5). The simulation space was divided into quadrants, as defined in Fig. 7.9, and each was given a positive or negative M_x according to the desired direction of magnetisation. Arrow colours carries over from Fig. 7.8 to separate domains entering and leaving a junction and should not be confused with MuMax's colour coding of magnetisation as assigned in the colour wheel of Fig. 7.10.
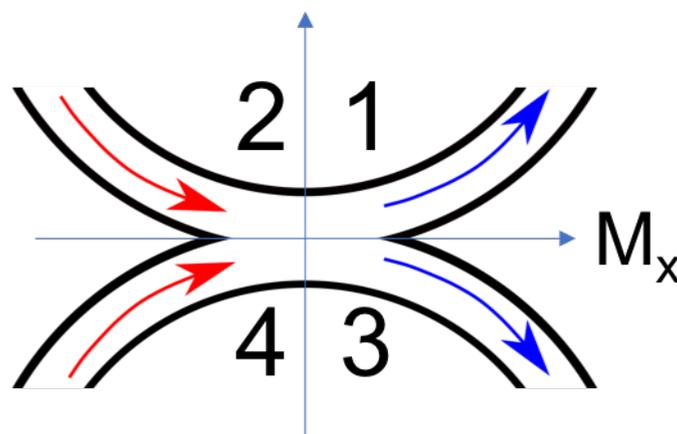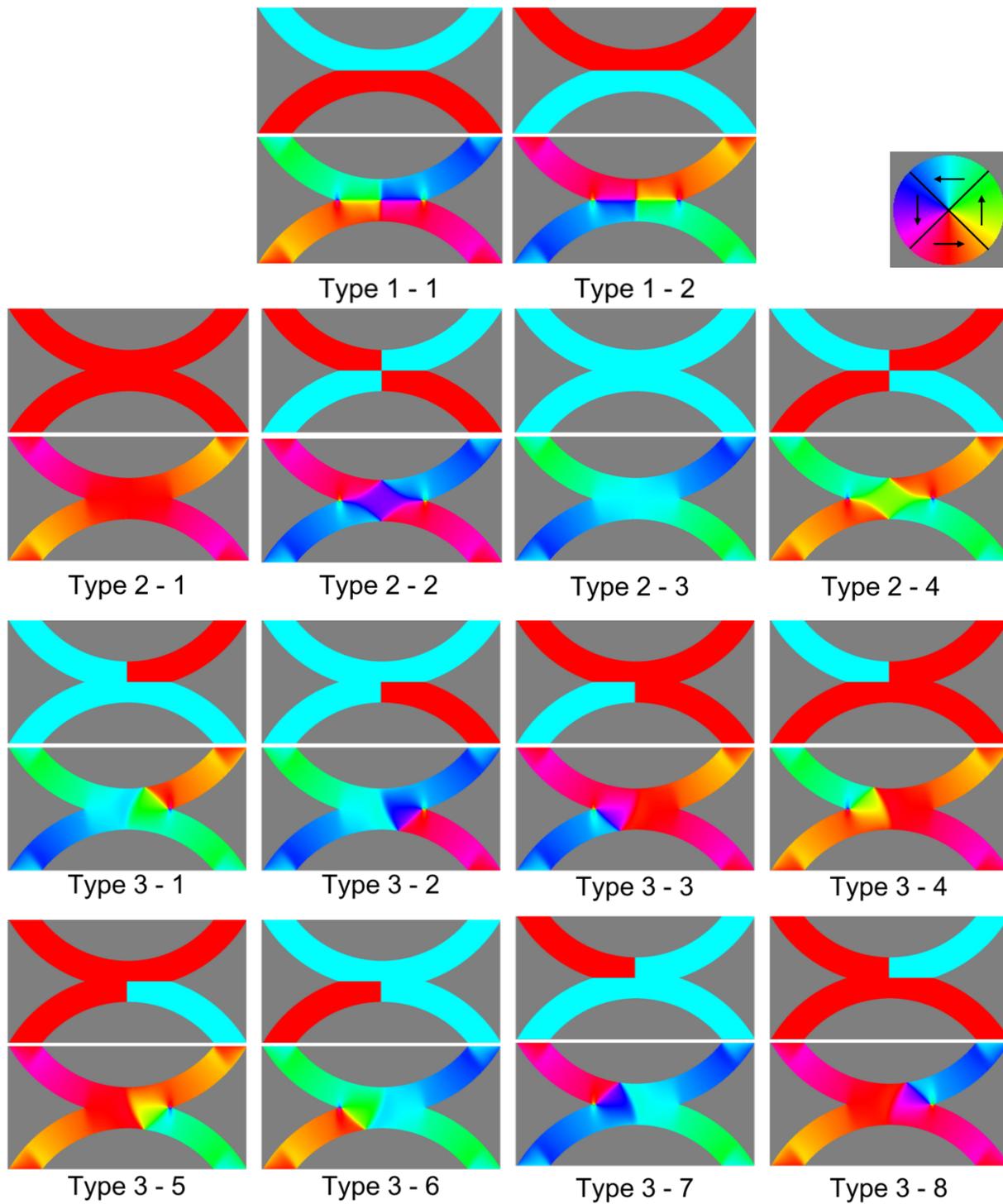

Figure 7.9. Schematic of quadrant assignment for micromagnetic modelling of ground states for different junction types as outlined in figure 7.8. For this example of Type 2, all quadrants are +1. Colour coding follows the same convention as Fig. 7.8 rather than the Mumax colour contrast from Fig. 7.10.

Fig. 7.10 shows simulations of initial state (top) and relaxed magnetic configuration (bottom) for each of the 16 arrangements possible at a junction. They are organised as configurations of Type 1-4, by analogy to the Type I-IV configurations seen in square ASI arrays. Some simulated configurations in Fig. 7.10 are similar to those seen in MFM imaging above (Figs. 7.2– 7.7).

Type 1 - 1　　Type 1 - 2

Type 2 - 1　　Type 2 - 2　　Type 2 - 3　　Type 2 - 4

Type 3 - 1　　Type 3 - 2　　Type 3 - 3　　Type 3 - 4

Type 3 - 5　　Type 3 - 6　　Type 3 - 7　　Type 3 - 8
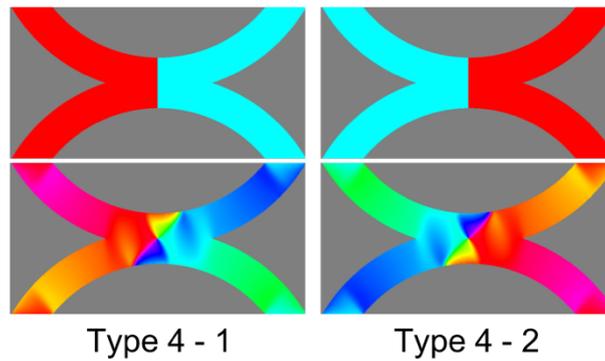
Type 4 - 1   Type 4 - 2

Figure 7.10. Micromagnetic models of nanoring junctions for the various possible arrangements of magnetisation in the wires making the junction. These arrangements are separated by type as assigned in Fig 7.8 relative to standard artificial spin ice comparisons. The top image in each set is the initial state and the lower image the magnetic configuration following relaxation.

Table 7.4 – Calculated mangnetostatic and exchange energy for relaxed junctions for each type as assigned in figure 7.16.

	Magnetostatic Energy (J/m³)	Exchange Energy (J/m³)	Total Energy (J/m³)
Type 1			
1	914.7	277.2	**1192**
2	914.7	277.2	**1192**
Type 2			
1	719.8	21.72	**741.5**
2	853.3	216.8	**1070**
3	719.8	21.72	**741.5**
4	853.3	216.8	**1070**
Type 3			
1	949.2	124.2	**1073**
2	950.0	124.1	**1074**
3	950.2	124.2	**1074**
4	950.0	124.3	**1073**
5	950.0	124.1	**1074**

6	950.0	124.2	**1074**
7	950.0	124.	**1073**
8	949.2	124.2	**1073**
Type 4			
1	1818	204.2	**2023**
2	1818	204.2	**2023**

The magnetostatic and exchange energies as well as total energy for each junction type from micromagnetic modelling are listed in table 7.2. Type 2-1 and 2-3 junctions have no DW (and hence a very low exchange energy contribution) and are the lowest energy states of the various configurations available. A vortex state ring has all its junctions in these configurations and so will be the lowest energy configuration. The other Type 2 configurations, Type 2-2 and 2-4 are the configurations seen in junctions that contain DWs following an initialisation field. These have an increased exchange contribution compared with the Type 2-1 and 2-3 junctions, and exhibit the characteristic 'diamond' shape commonly seen in MFM images of these DWs (e.g. Fig. 7.2). The onion state rings following initialisation will have two of the Type 2-1 and 2-3 junctions on opposite sides, with Type 2-2 and 2-4 configurations on the other two sides (in a square array).

The Type 3 configurations all have a similar overall energy, which is very similar indeed to that of the Type 2-2 and 2-4 arrangements. This helps to explain how a Type 3 junction was seen in a ring following initialisation earlier (Fig 7.1).

Type 1 junctions have the next largest total energy and feature the crosstie DW structure and chequered magnetic configuration that was also seen experimentally in Fig. 7.7.

Type 4 configurations were calculated to have significantly higher energies than any other arrangement. These have not yet been observed experimentally.

The double diamond seen by MFM in Fig. 7.6 is likely to be an adaption of Type 2-1 or Type 2-3 with a 360° DW. This will increase the energy significantly but these types of walls are generally very stable and a magnetic field opposite to the direction of magnetisation in the surrounding domains must usually be applied to unwind the wall structure. This configuration was not simulated here.

Despite the attributing preferential formation of Type 2 junctions as a result of energy associated with the junction, the analysis as it stands contains an inaccuracy. Looking at the edges of wires in each model, end domains can be observed, and these will interact and contribute to the overall energy. Attempts were made in the course of this project to remove end domains by calculation of the reverse field needed to be added such that the total magnetic field at the edge of the simulation becomes zero.

The junction energy calculations as they stand do, however, provide a means of comparing their likelihood to appear and may assist in future studies of their relative abundance, similar to that which has been performed in ASI systems. Alternate approaches based on the literature could be studied in future work. The concept of negative effective temperature as calculated by observation of the proportion of defects in the ground state could be attempted, taking the number of Type 3 junctions carved into the regular, stable lattice of Type 2 [1]. However preliminary work would be needed to confirm the true ground state, whether sequential Type 2-1/2/3/4 junctions (diamonds in opposite junctions) or vortex (alternating Type 2-1/3) or another combination. This could be investigated as with ASIs in directly magnetic imaging an array after growth, before application of a field and nucleation of domain walls/creating onion states [4], [5].

7.3 Photoemission Electron Microscopy

7.3.1 Establishing array behaviour

Fig. 7.11 defines the key directions that are relevant to all photoemission electron microscopy (PEEM) images shown here. This includes the direction of initial saturation fields (horizontal direction in images), and the PEEM sensitivity direction to sample magnetisation (represented in blue and red for opposite vertical directions). Samples are summarised in §4.6. Briefly, rings were made from 5 nm thick permalloy (coated with 2 nm Al), were either of 4 μm diameter and 400 nm track width or 2 μm diameter and 200 nm track width, and had either 10% or 50% overlap between neighbouring rings. This smaller thickness array was used to ensure de-pinning and saturation fields that were compatible with the PEEM electromagnetic cartridge (see §4.6.1). Saturating

fields were 100Oe and in-plane rotating fields were applied at a frequency of 10Hz unless otherwise specified.
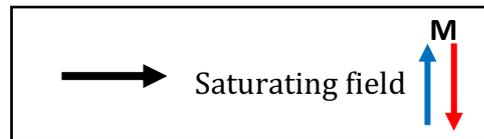

Figure 7.11. Convention for PEEM imaging. Saturating fields are unidirectional along the horizontal axis of the page and sensitivity/contrast is along the vertical axis. Red and blue arrows denote the measured magnetisation along the sensitivity axis.
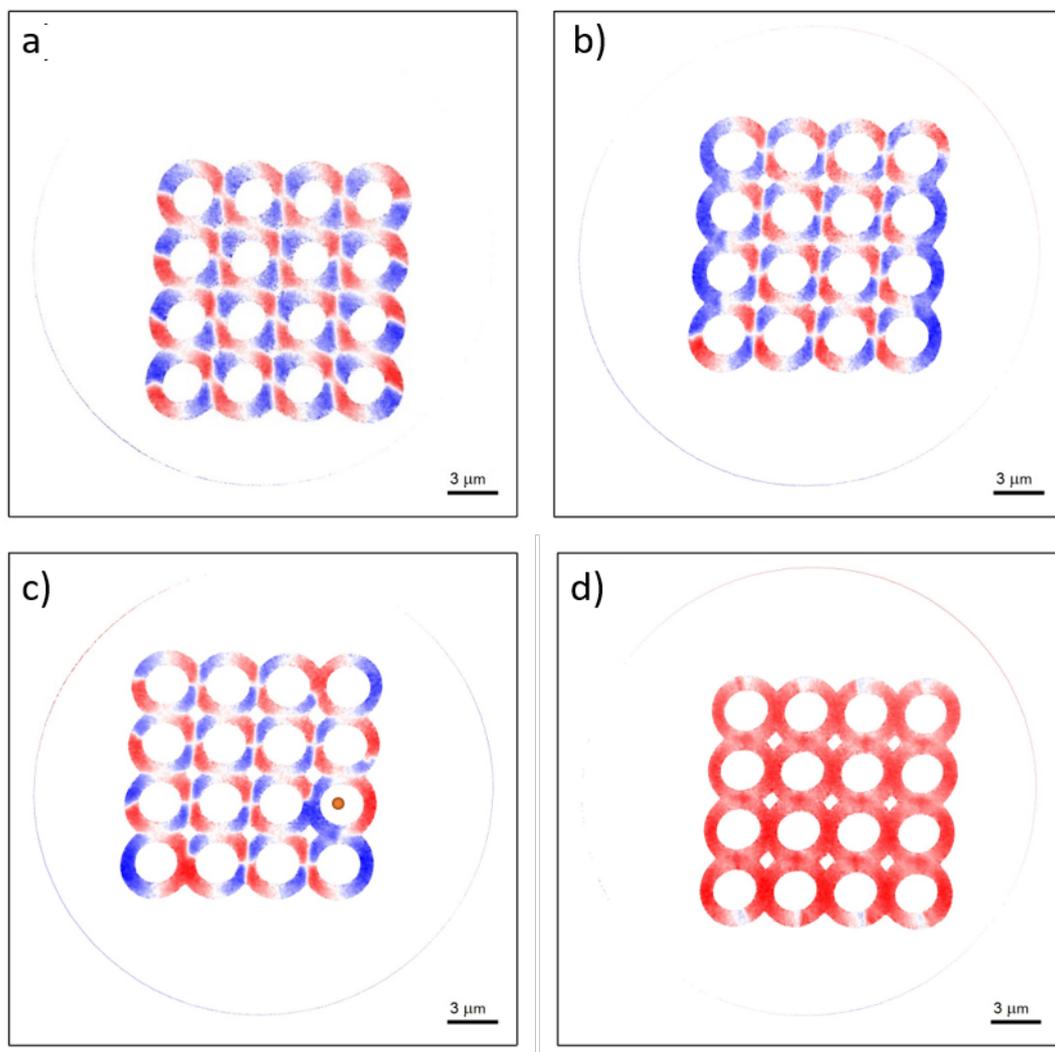

Figure 7.12. PEEM images of a 4 x 4 interconnected nanoring array with rings of 4µm diameter, 400nm track width and 50% overlap. (a) following saturation field pulse and (b) after a subsequent 50 cycles of 25Oe rotating field. (c) with a saturating field pulse then 40Oe rotating field applied for 50 cycles. Of note is the

Figure 7.12 shows images of a 4 x 4 array of rings with 4 µm diameter, 400 nm track width, 50% overlap. Figure 7.12a) shows the configuration immediately following application of a saturation field pulse. Here, DWs sit in opposite junctions along the saturation field direction, as observed previously by MFM (Fig. 7.1). The different contrast mechanism of PEEM shows the DWs very differently to MFM though. Domain mapping, like that carried out in §7.1 shows the ring junctions to have been Type 2-2 and 2-4 where DWs are present and Type 2–1 and 2-3 in those without. The difference in colour appearance between these and the micromagnetic modelling in Fig. 7.10 is from the difference in sensitivity axis.

Figure 7.12b) shows a PEEM image of the same structure after subsequent application of 50 cycles of 25Oe rotating field. This had promoted propagation of a DW down opposite outer edges of the array without experiencing pinning at junctions to create ¾ states along the vertical edges; the number of domain walls in the system, however, was preserved. This field strength appears to have been too low to move DWs that were initialised in junctions. That there are different ring types on the edges and corners, specifically the corners of one of the diagonals of the array, following a low field rotation matches micromagnetic modelling predictions such as in §5.4.1. The comparison to the 3 x 3 array with a low applied field is well replicated, however there are free standing DWs observed in corner rings. Modelling showed that affected corner rings convert to vortex rather than remain with a free standing DW.

Fig. 7.12c) shows the same array now following a saturation field pulse and then 40Oe field amplitude applied for 50 rotation cycles. The top right and bottom left rings are seen as being in oppositely oriented vortex states. Vortex states are also produced elsewhere in the array, such as the ring marked with an orange dot. On the left edge of the array (and the remaining edge ring on the right), there are again freestanding DWs . Most rings were in the onion state but the overall DW population here was lower than the saturation (Fig. 7.12a) and low field (Fig. 7.12b) cases.

Fig 7.12d) shows the array after application of a rotating 67.5 Oe field amplitude for 50 cycles (following a saturation field pulse). Though the image colour is almost completely red, this still shows all rings to be in the onion state with DW positions aligned to the final field direction – this was 90° compared to the saturating field direction (Fig. 7.12a). 67.5 Oe is clearly strong enough to maintain the maximum DW population achieved originally with saturation.

Figure 7.13. PEEM images of a 4 x 4 interconnected nanoring array (the same as the structure in Fig. 7.12) following a saturating field pulse and then after each successive application of a single 40Oe applied rotating field cycle. The orange dot in '10th cycle' highlights a ring that changes orientation over the following cycles. . The convention for the progression of further cycles in this thesis is along each row before moving down a row to the next.

Fig. 7.13 shows a series of images collected after successive 40Oe field cycles, following an initial saturating field pulse. In between some cycles, conversions between states can

be seen. For example, the ring highlighted with the orange dot between cycles 10-13 changes orientation. This doesn't occur with every ring or with every cycle, demonstrating a degree of stochasticity.

7.3.2 8 x 8 Arrays

Figure 7.14 shows PEEM images of an 8 x 8 ring array (4μm diameter, 400nm track width, 50% ring overlap) following a saturation field pulse and then 30 rotations at various field amplitudes. Between 1Oe and25Oe, the magnetic configuration of the array is largely unchanged save for DW propagation through opposite sides to create vortex or ¾ state rings, as seen for 4 x 4 arrays above under low fields (Fig. 7.12a) and b)).

At 27Oe, the magnetic configuration appears to be have become more complex, which indicates the onset of the intermediate field regime. This complexity continues through to 36Oe, albeit with different magnetic configurations at each field. From 39Oe onwards, the images mostly show the array retained the onion along the saturation axis arrangement in the bulk. Some of the fields above this occasionally showed more complex arrangements similar to those at 27-39Oe, which shows the influence of stochastic phenomena in these rings. This also shows that the rings are connected in their magnetic behaviour, and not just physically. Individual events of DW pinning in the bulk array are never wholly isolated, for example 61.5Oe shows a 'paired' behaviour in that neighbouring rings are not in onion states. The wider complexity seen elsewhere is likely to be in response to multiple localised frustration or pinning events in the array. It is also possible that individual events influence multiple rings through a cascade sequence, a phenomenon possible in artificial spin ices [6], [7].

The nature of cycle-by-cycle evolution was explored further in Fig. 7.15, in which images are shown following successive cycles or 39Oe rotating field, following a saturation pulse and then 30 initial cycles of 39Oe with the degaussing offset and 30 cycles without (note that the degaussing/offset field offset was applied after saturation for all images from this point).
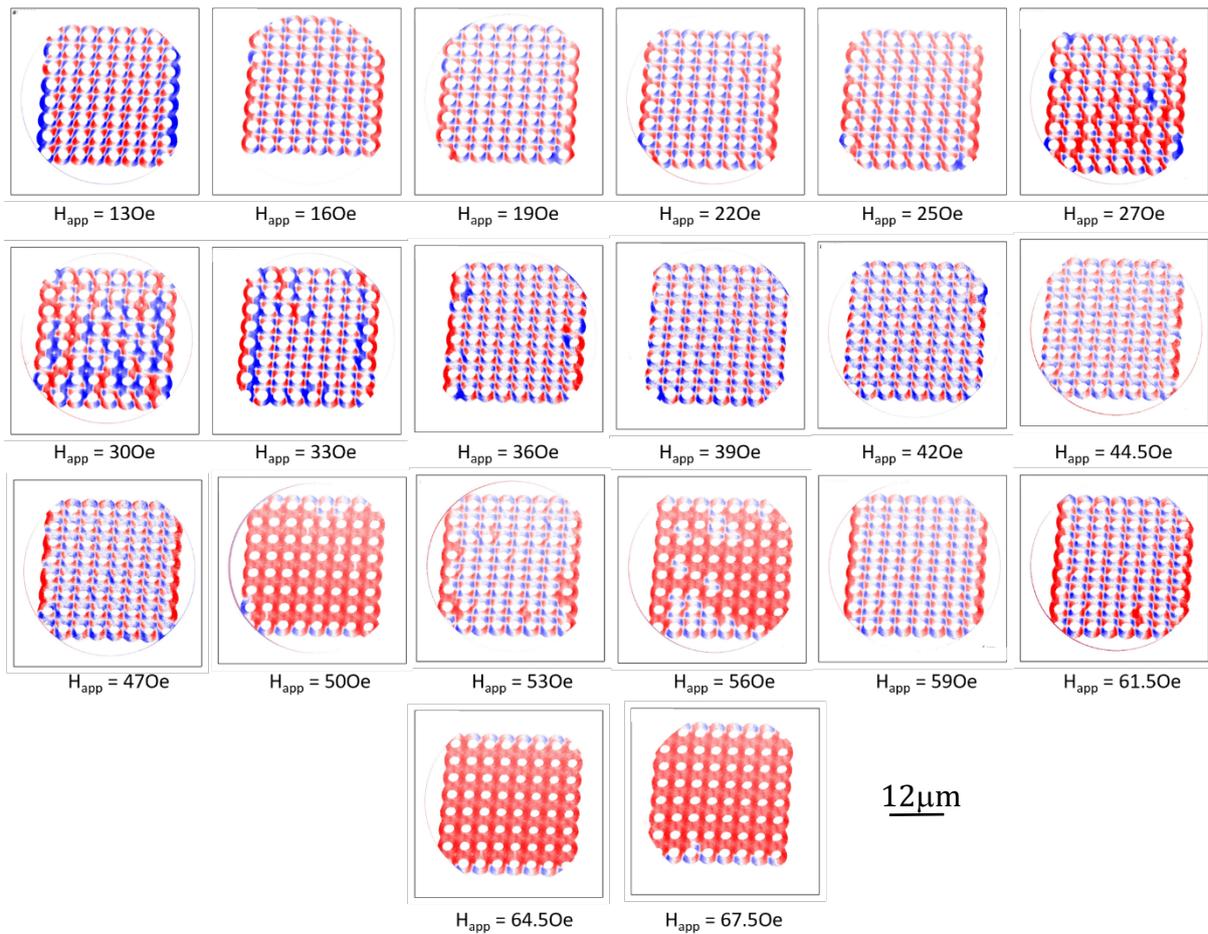
Figure 7.14. Series of final magnetisation states imaged with PEEM on 8 x 8 ring arrays after the application of a saturating field and then 30 rotations of various indicated fields. Rings are 4µm diameter, 400nm track width, 50% overlap and 5nm thickness
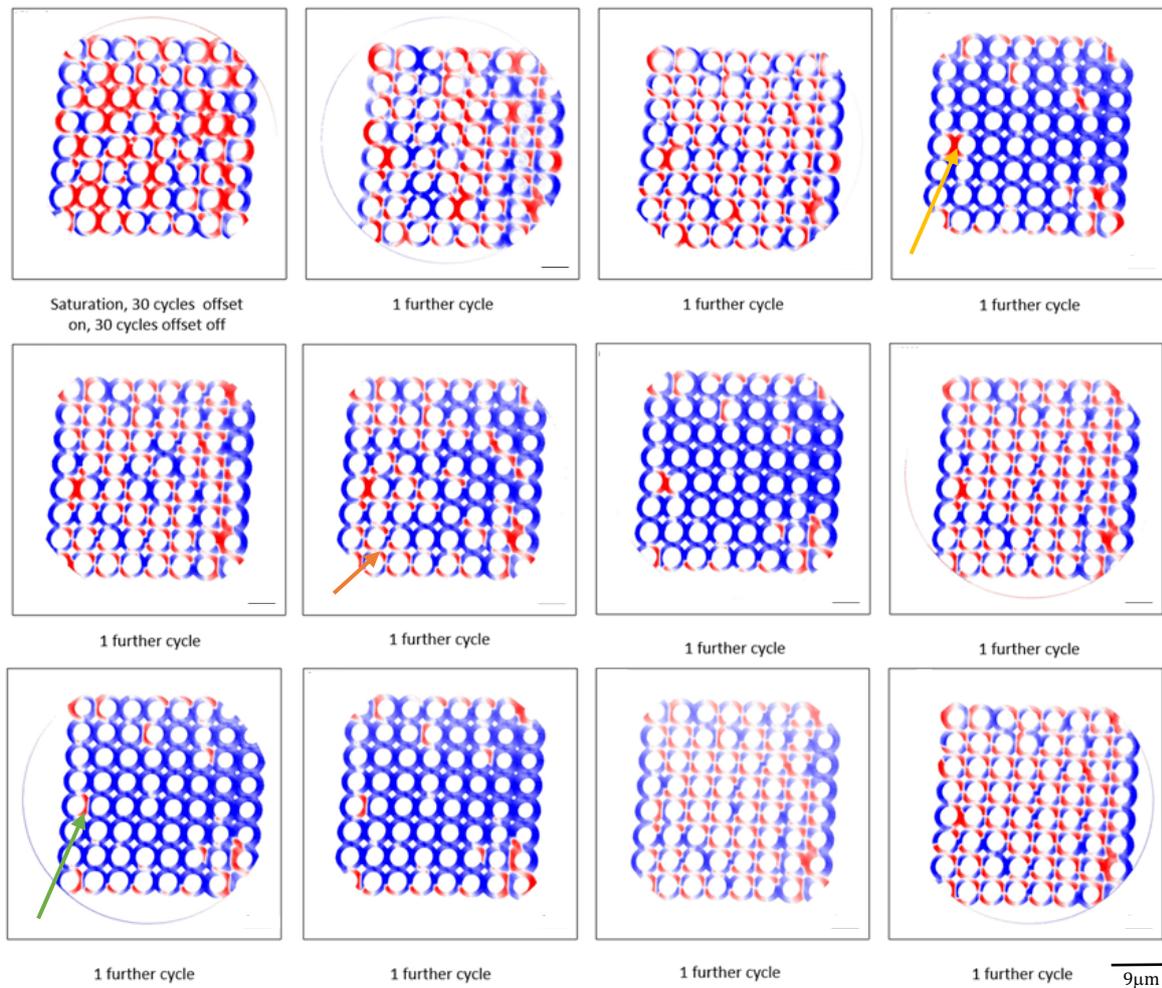
Figure 7.15. PEEM images of an 8 x 8 interconnected ring array (4µm diameter, 400nm track width, 50% overlap and 5nm thickness) after saturating field pulse then 60 cycles at 39Oe rotating magnetic field (top left). This is followed by 11 further individual cycles of rotating field.

The progress of magnetic configuration change in Fig. 7.15 shows significant changes in the array overall on most field cycles but with some local regions being more resistant to change. For example, the pair of vortex states halfway up the left side of the array (yellow arrow) is very robust, although one converts to an onion state later (green arrow) demonstrating DW repopulation of the ring. The multi-ring motif of 'blue' sensitivity indicated by the orange arrow in Fig. 7.15 also remains in place throughout all images. These are likely to be a defect that is consequence of fabrication noise in the details of these junctions, indicating a likely spatial dispersion of pinning barriers across an array.

7.3.3 25 by 25 Arrays

A 25 x 25 array was imaged, which matches the size of individual arrays within the larger array used in PNR and MOKE experiments (§6.1 and §6.2).
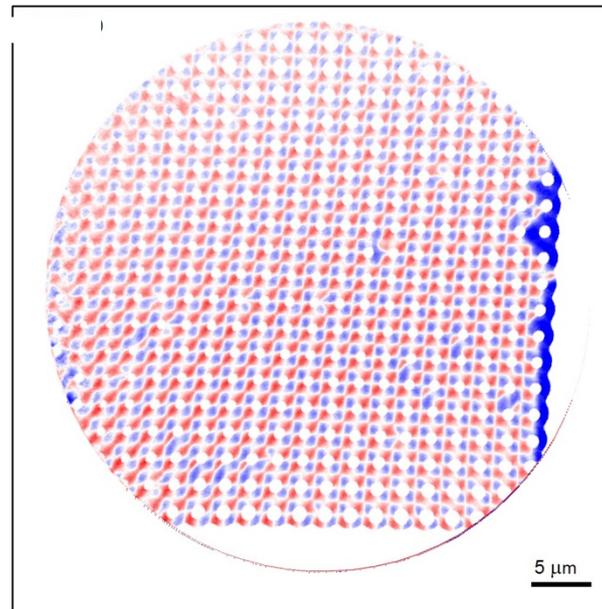

Figure 7.16. PEEM image of a 25 by 25 interconnected ring array (4µm diameter, 400nm track width, 50% overlap) following the application and removal of a saturating field.

A PEEM image following application then removal of a saturating field is shown in Fig. 7.16, the array is in general onion state, but this is punctuated by some ¾ states and the edges are a combination of ¾ and rotated onions. Whilst ¾ states distort the local orientation of moments and can have some effect on adjacent rings, there appears to be no longer range effects from this. The creation of these ¾ states was possibly from local effects pinning moments as reversal or relaxation occurred.
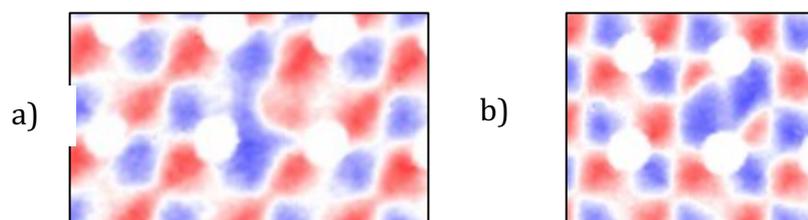
a)

b)

Figure 7.17. (a) Subsection of the array from figure 7.30 showing an irregular arrangement of domain walls leading to an appearance of a domain 'spilling over' into an adjacent ring. (b) A second subsection of the array from figure 7.30 showing an irregular arrangement of domain walls also leading to an appearance of a domain 'spilling over' into an adjacent ring.

Fig. 7.17 shows some more detailed analysis of regions of Fig. 7.16. The extended blue region in Fig. 7.17a) appears to be two DWs that have not completely combined in the shared junction but remain at the arms of the right-hand ring. The extended blue region in Fig. 7.17b) resulted from distorted domains in rings.
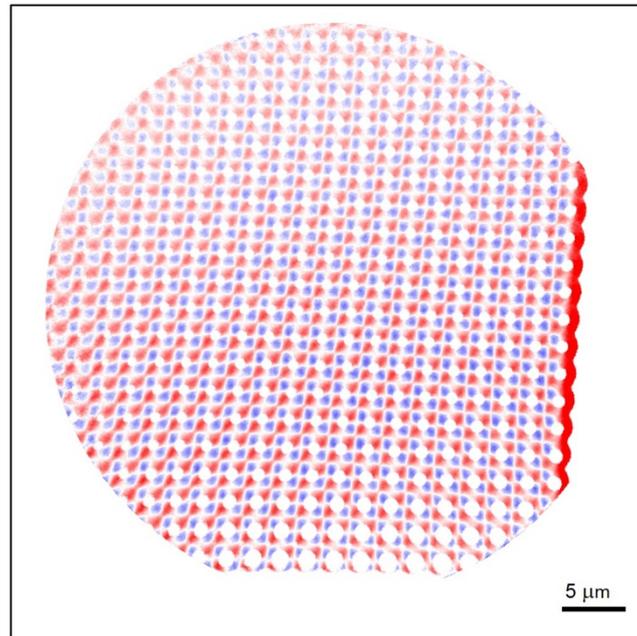

Figure 7.18. PEEM image of a 25 x 25 interconnected ring array (4µm diameter, 400nm track width, 50% overlap) following the application of a saturating field and then 30 field rotations of 13Oe amplitude and 1.5 Oe offset and then 30 rotations of 13Oe rotating field alone.

Figure 7.18 shows a PEEM image after saturation (the same as used for Fig. 7.17) and 60 cycles of 13Oe field amplitude. Almost all rings in the array appear to be in the onion state, the only exceptions being those along the right-hand edge; these have again formed ¾ states, as seen with smaller arrays above. It was not possible to capture both left- and right-hand array edges with the PEEM system.
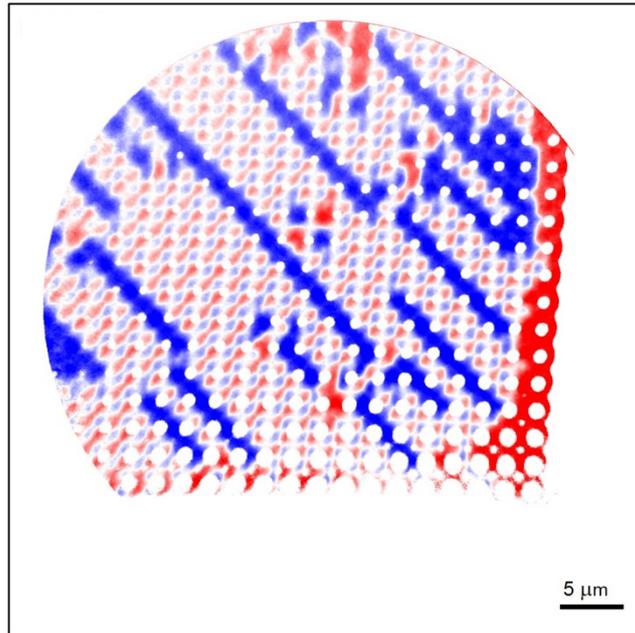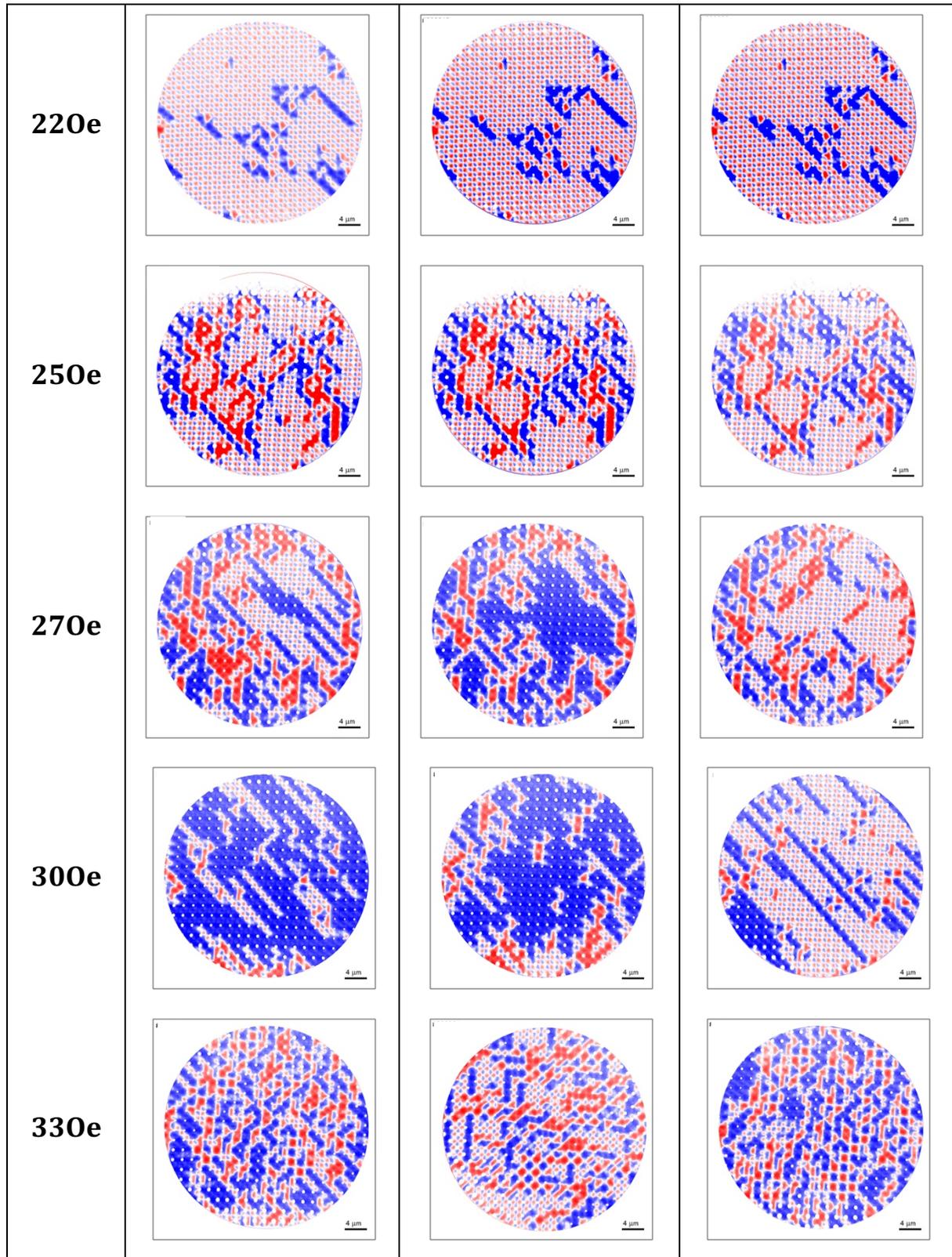
Figure 7.19. PEEM image of a 25 x 25 interconnected ring array (4µm diameter, 400nm track width, 50% overlap) following the application of a saturating field and then 30 field rotations of 30Oe amplitude and 1.5Oe offset and then 30 rotations of 30Oe rotating field alone. Note that this image suffered from focussing issues.

Use of a larger amplitude rotating field of 30Oe amplitude (Fig. 7.19) results in a more uneven magnetic configuration across the array. In particular, there are strings of moment alignment running diagonally through the array. These are remarkably similar to the appearance with magnetic imaging techniques of Dirac strings in artificial spin ices [6]–[9], where chains of continuously aligned moments are present between quasi-monopolar vertices formed as a result of frustration as the ASI system relaxes. The domains in this image are mapped in detail in later in this chapter (§7.4.4) in order to understand the nature of the domain strings more clearly.

Figure 7.20 shows sets of three PEEM images obtained at particular field amplitudes, with the first image obtained following a saturation pulse and 30 field cycles with field offset, and the following two images each after another 30 field cycles without the offset applied. This time, a 25 x 25 array of 2 µm diameter, 200 nm rings with 50 % overlap was used.

22Oe			
25Oe			
27Oe			
30Oe			
33Oe			
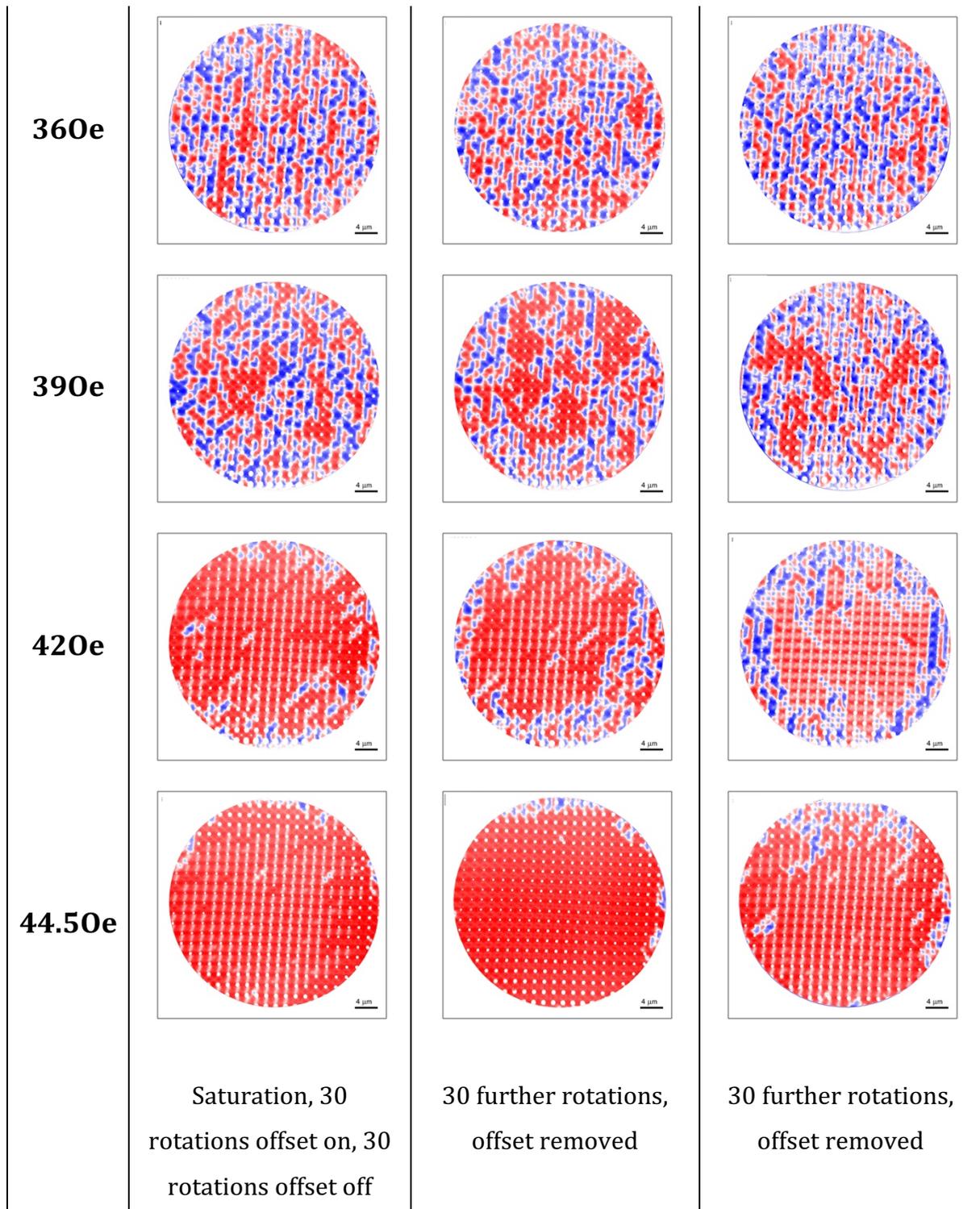
Figure 7.20. Series of three PEEM images taken from part of a 25 x 25 square array of 2μm interconnected rings (200nm wide wires, 50% overlap) following saturating pulse, and then batches of (1st column) 30 rotations at the indicated rotating field strength + 1.5Oe then 30 rotations at indicated field strength. (2nd column) 30 further rotations at indicated field, 90 total cycles. (3rd column) 30 further rotations, 120 total cycles. Scale bars are 4μm.

The PEEM images in Fig 7.20 again show the pattern of near-uniform onion states at low fields, complex magnetic configurations at intermediate fields and the uniform magnetisation (onion states) at high field amplitudes. The 'Dirac' like strings increase in number and size as the field strength increases from the low fields. This indicates their formation is likely to be governed by a few, individual DW de-pinning events. This is further supported by the appearance of both 'blue' and 'red' strings in Fig. 7.20, which indicates that the strings can be generated on either half of a field cycle. As the field progresses through the intermediate regime, the strings gradually disappear and the magnetisation becomes more disordered, presumably as DW propagation becomes more widespread across the array. At higher fields, the saturation of onion states indicates is consistent with the coherent DW motion discussed after performing MOKE experiments (§6.2).

At low fields (22Oe and 25Oe), successive cycles do not appear to change the magnetic configuration of rings. In these cases, it would appear that the lowest energy pinning sites have been overcome and all DWs have become pinned. A similar behaviour at high field (44.5Oe) is instead likely to be due to all DWs overcoming all junctions, as noted above. Interestingly, these PEEM images do not show vortex states in the quantities that would be expected for these to explain the large reduction in magnetisation seen in PNR (Fig. 6.3) and MOKE (Fig. 6.10) measurements. A detailed analysis of the magnetisation in the Fig. 7.20 images and its significance to the previous PNR and MOKE outcomes is given in §7.3.7 below.

7.3.4 Mapping PEEM

Figure 7.21 shows a full domain arrow map of a subsection of the saturated and relaxed 25 x 25 array from Fig. 7.18. this subsection is randomly sampled, given the homogeneity of onion states. Arrows clearly demonstrate the presence of onion states aligned with the saturating field direction.

Figure 7.21. Arrows showing the magnetic domain configuration for an array of 2μm nanorings having undergone a saturating field pulse (PEEM image taken from Fig. 7.18 and copied here for clarity).

Fig 7.22 shows ring mapping for a subsection of a 2μm array (PEEM image shown for reference in Fig. 7.22a) that has had 120 total rotations at 3Oe applied after saturation (30 with degaussing offset on).

Figure 7.22. (a) Reference PEEM image to be mapped in the indicated subsection (taken from Fig. 7.20. – 30Oe following 120 rotations). (b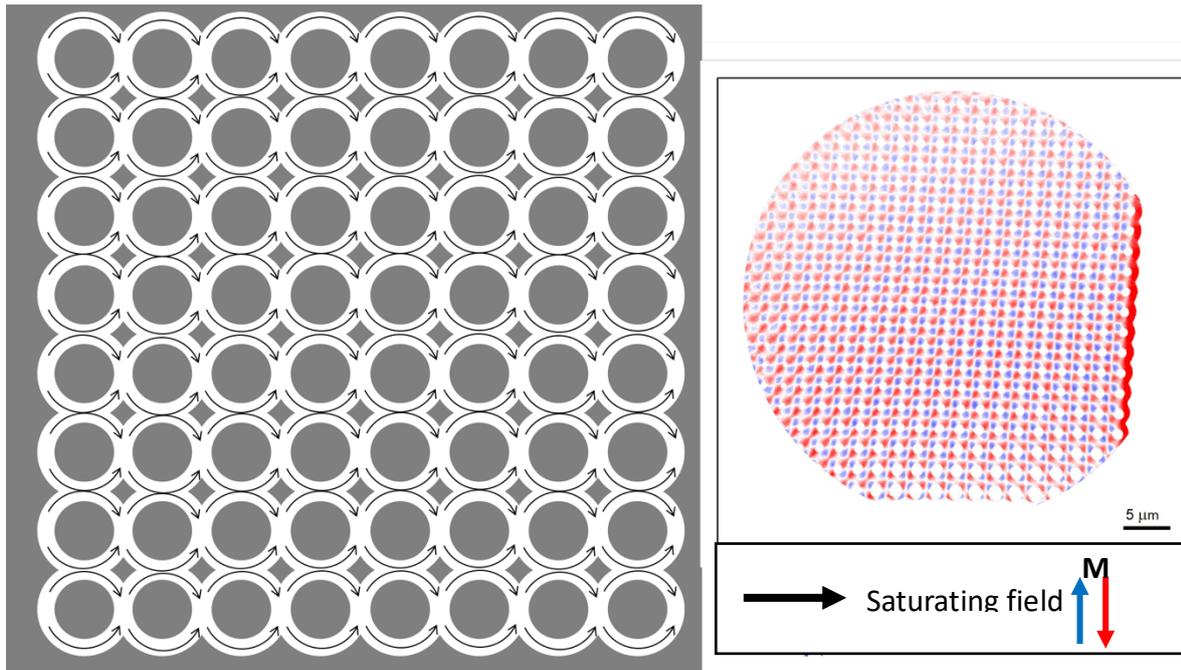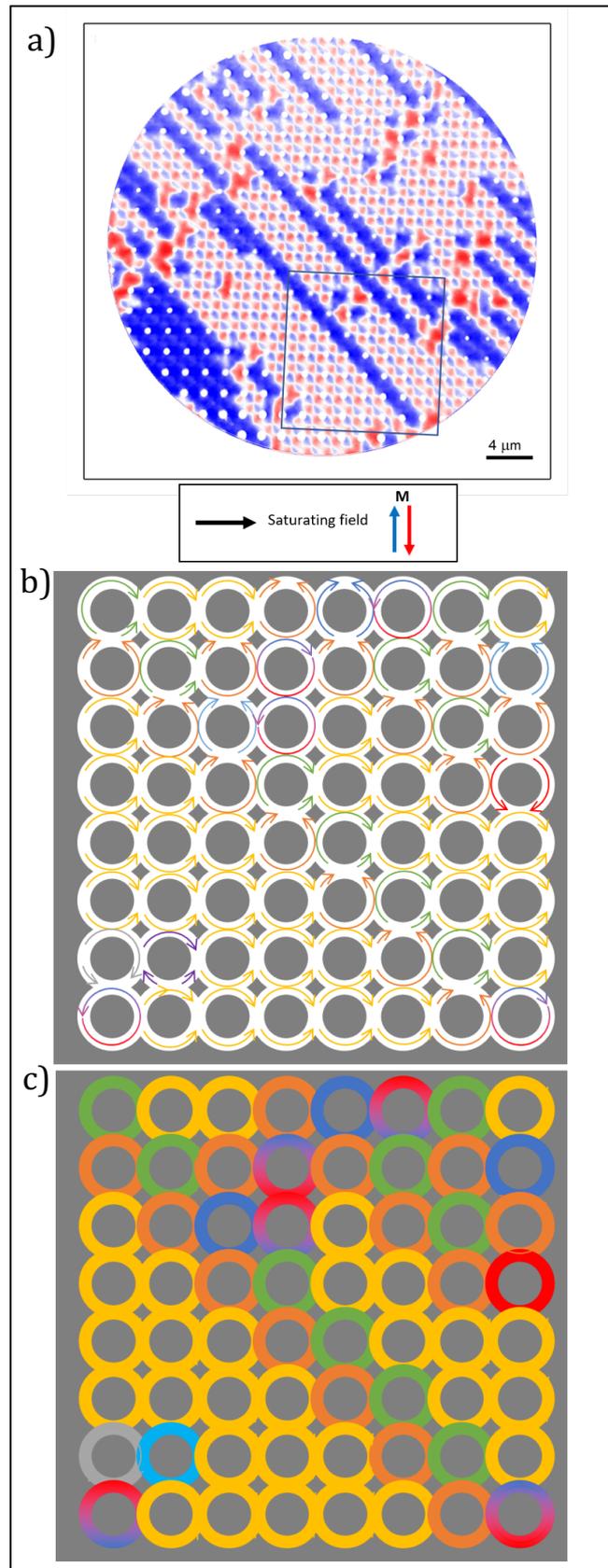) Arrows showing the magnetic domain configuration for an array of 2μm nanorings having undergone a saturating field pulse (PEEM image taken from Fig. 7.18 and copied here for clarity). Colours have been assigned to like states. (c) colour map of each ring

This approach has allowed 'super-domains' of ring states to be observed. The diagonal strings are revealed to be a boundary between pairs of ¾ ring states of opposing chirality (green and orange in Fig. 7.22b). The string terminates with a vortex, which may be indicative of a dependency between the two. Diagonal strings in other images always terminate with a vortex state ring but vortices are also often present separately from the strings. Vortices are often paired with another of the opposite chirality, as with those in the 4th column from the left in Fig. 7.22a). This may suggest that a single vortex ring state would cause frustration and that this can be avoided with the opposing vortex state nearby, with ¾ ring states found adjacent to a vortex ring that allow transition to surrounding onion state configuration without local frustration. An initial ¾ state could then 'propagate' a string of ¾ states that are paired with their anti-chiral equivalent as a drive to minimise the total energy in the region.

Although the strings are not visible in images from higher field amplitude rotations in Fig. 7.20, such as at 39Oe, mapping of the magnetic configurations in Fig. 7.23 show that vortices are never present in isolation. This image also shows that 40 of the analysed 64 rings were in a vortex state (18 clockwise and 22 anti-clockwise vortex states).

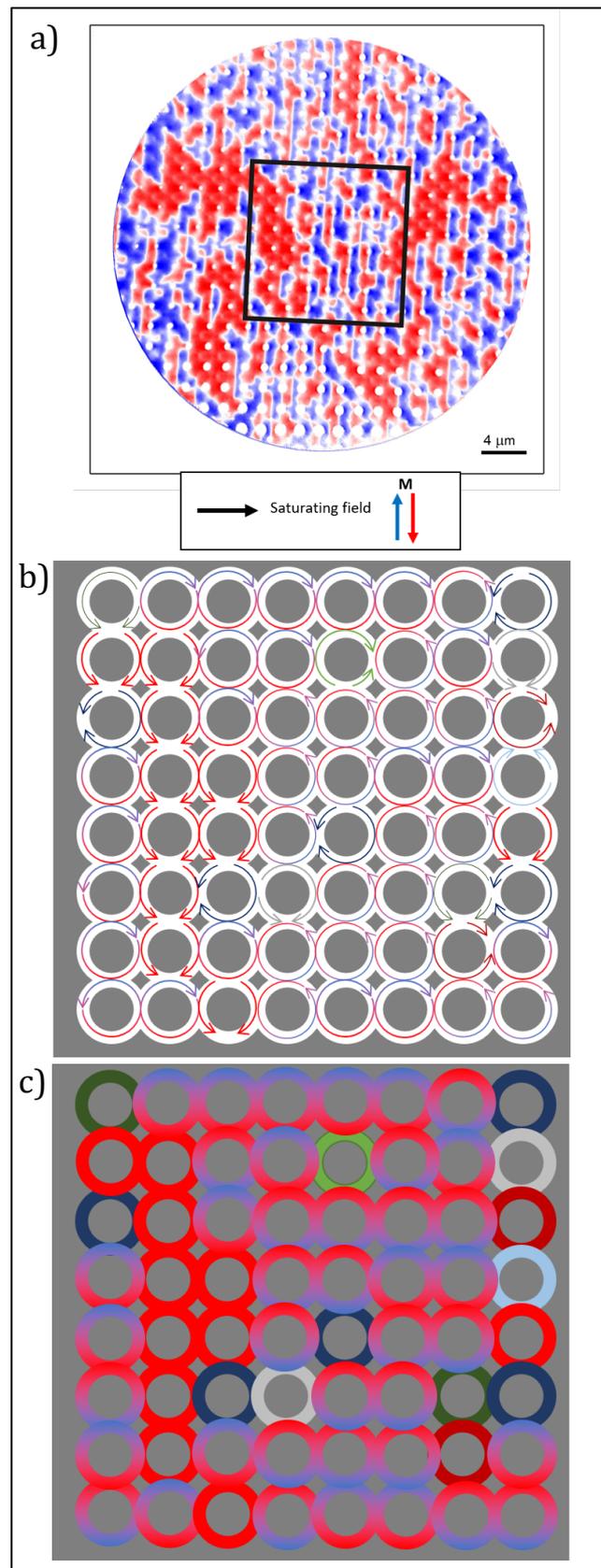**Figure 7.23 (a) Reference PEEM image to be mapped in the indicated subsection (taken from Fig. 7.20. – 39Oe applied rotating field with 120 total rotations) (b) Arrows showing the magnetic domain configuration for an array of 2µm nanorings having undergone a saturating field pulse (PEEM image taken from Fig. 7.18 and copied here for clarity). Colours have been assigned to like states. (c) colour map of each ring**

The problem of motifs such as shown in Fig. 7.17 are commonplace, and often what has been termed a vortex arguably contains domain walls. An example of this is shown in Fig. 7.24. A quasi-vortex is formed in the central ring though there is a visual 'spill over' of domains from the right. The central ring appears to still have 2 DWs so would not be an actual vortex. This region of continuous 'up' aligned magnetisation with the adjacent ring could be similar to one of the irregular junction types found in MFM analysis. These quasi-vortexes/false vortexes were often found during mapping in Fig. 7.23, though were not the majority.
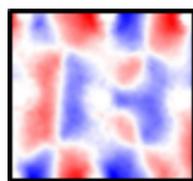
Figure 7.24. False vortex motif obtained from the reference PEEM image in figure 7.23a).

7.3.5 Trigonal Arrays

Figure 7.25 shows PEEM images of a seven-ring trigonal array (4 μm diameter rings, 400 nm track width, 50% overlap) after field rotation of 22Oe and 44.5Oe amplitudes. These arrays are difficult to quantify due to the competition between DWs to simultaneously coexist in the central ring, although micromagnetic modelling was also inconclusive for 7 ring hexagonal arrays (see §5.5.1). The modelling highlighted the difficulties too with having short wire regions between junctions in losing the definition of separate junctions. The arrays used experimentally appeared to suffer from this lack of definition and, as with the modelling, narrower track widths would be preferable for delineating junctions and reducing the effects of DW-DW interactions.

Figure 7.25. PEEM images of two 7-ring hexagonal arrays (4 µm diameter rings, 400 nm track width, 50% ring overlap) following application of (a) saturating field pulse then30 rot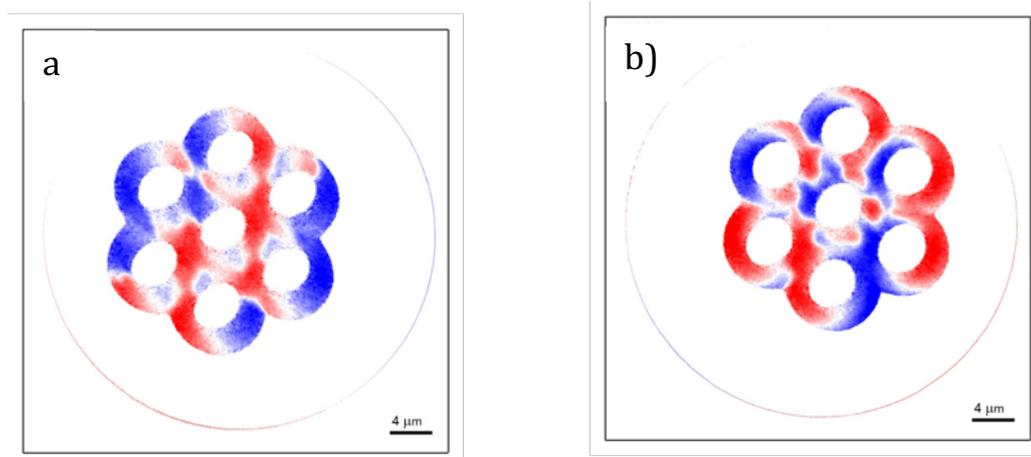ations at 23.5Oe and 30 rotations at 22Oe. (b) Saturating field pulse then 30 rotations at 46Oe and 30 rotations at 44.5Oe.

After 22Oe applied rotating field (Fig. 7.25a), the magnetic configuration is particularly difficult to distinguish, although the continuous domains at the left and right array edges are again seen. With the larger field of 44.5Oe (Fig. 7.25b), the outer rings show almost complete vortex states but with distortions and opposite domains within the central ring. This complexity suggests that the premise of simple vortex creation assumed in the creation of the analytical model in §5.5.2 is not as straightforward as envisaged. This does not discount the analytical model but places limits on the likely accuracy of its predictions.

Larger hexagonal arrays with narrower (200nm track width, 2µm diameter, 50% overlap) tracks were imaged following successive batches of rotations with progressively higher fields as with the same experiment on square arrays Fig. 7.20. The results of this experiment is presented in the same format as Fig 7.20 in Fig. 7.26.

39Oe			
42Oe			
44.5Oe			
47Oe			
50Oe			

| | Saturation, 30 rotations offset on, 30 rotations offset off | 30 further rotations, offset removed | 30 further rotations, offset removed |
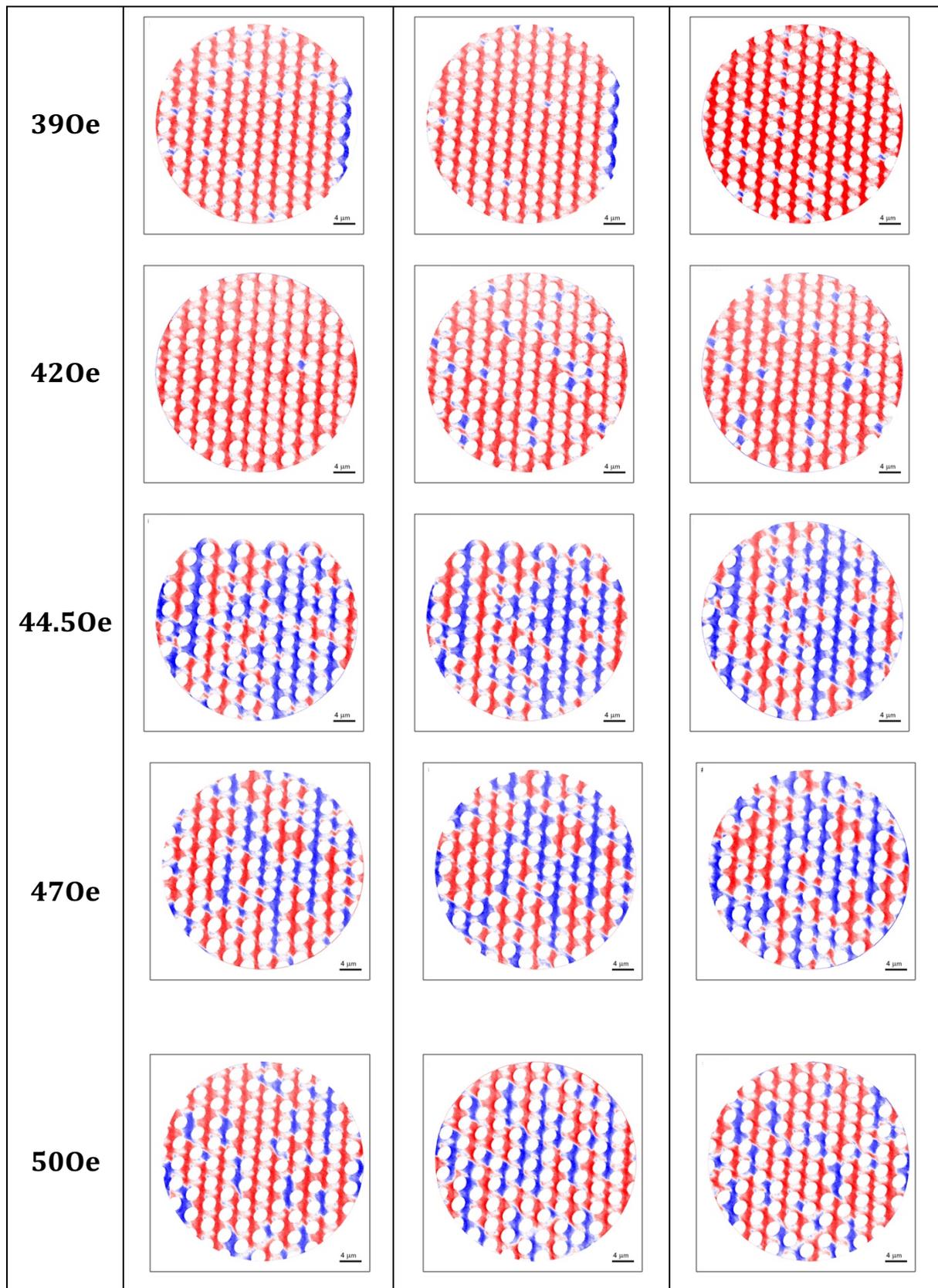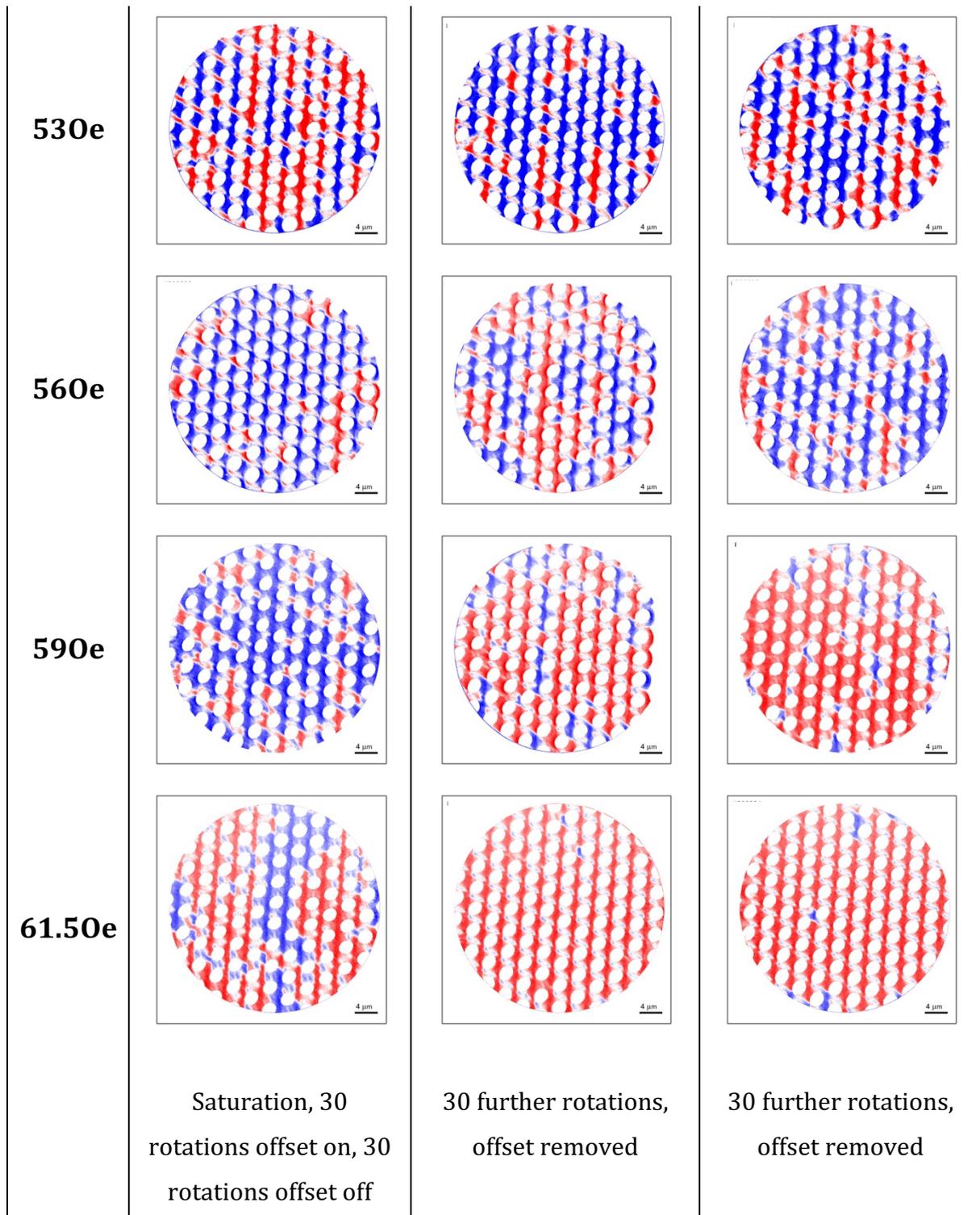
Figure 7.26. Series of three PEEM images taken from part of a 25 x 25 trigonal array of 2μm interconnected rings (200nm wide wires, 50% overlap) following saturating pulse, and then batches of (1st column) 30 rotations at the indicated rotating field strength + 1.5Oe then 30 rotations at indicated field strength. (2nd column) 30 further rotations at indicated field, 90 total cycles. (3rd column) 30 further rotations, 120 total cycles. Scale bars are 4μm.

Images from the lowest field used, 39Oe, show no significant change with subsequent rotations, as has been seen with all other arrays investigated here earlier. Rings were in the onion state with the whiter regions in rings showing the location of DWs. Some rings showed a small region of reversed magnetic domains, although there is no obvious pattern to their locations in the array.

At the highest field, 61.5Oe, the final two images suggest no significant change but the domain like behaviour of the array in the first image implies a change from saturated and relaxed state. This suggests that this field does not quite result in fully deterministic behaviour. The intermediate fields again show increasingly variable behaviour from the lowest field considered, with DWs changing position and magnetic configurations changing through the repeated images, until the more coherent type of DW motion starts to dominate at higher fields.

It is significant that this complex, dynamic and (at intermediate fields) stochastic behaviour is again observed but this time in a trigonal, rather than a square, array. This suggests that the phenomena studied could be relatively general and do not require very specific geometries to be observed, although it is likely that the exact geometric form of an array would alter the array's behaviour.

7.3.6 Linear Chain

Several linear chains were fabricated but here a study of a ten-ring linear chain is presented (Fig. 7.27). Rings had 4μm diameter, 400nm track width and 50% overlap. These structures proved useful in allowing a clear observation of magnetic configuration changes between successive single cycles.
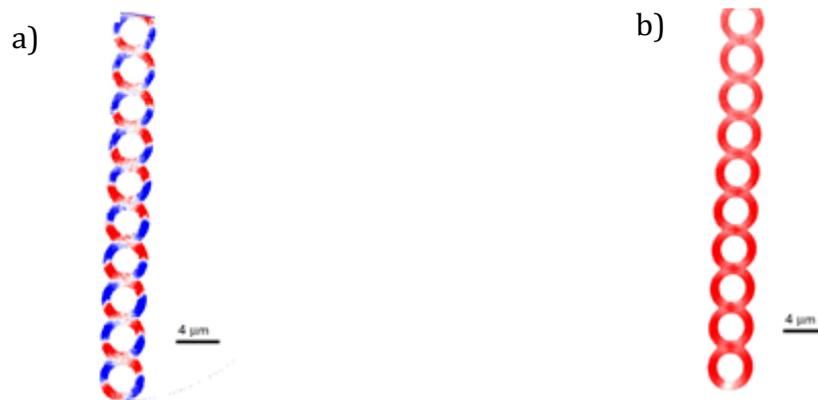

Figure 7.27. PEEM images from a linear chain of interconnected nanorings (4μm diameter, 400nm track width and 50% overlap) following application of (a) a saturating field pulse and (b) saturating field pulse then 30 rotations of 67.5Oe with degaussing offset applied.

The chain was imaged following a saturating pulse (Fig. 7.27a) and then after application of a rotating field amplitude of 67.5Oe (30 rotations, offset on; Fig. 7.27b). Both images show rings fully populated in the onion state, although domain rotation due to differences between the saturation field and final rotating field directions resulted in the walls being in positions 90° different within the rings. Micromagnetic (§5.2) and analytical (§5.3) modelling showed central rings in the chain would always convert to a vortex state if one of its onion states became trapped and the other de-pinned from its junction. This shows that 67.5Oe was enough to cause the DWs to propagate around the rings approximately coherently and overcame pinning at junctions.

Vortex state formation was seen at lower rotating field amplitudes, e.g. for 47.5Oe (Fig. 7.28). The vortex states of the top eight rings here had alternating windings, which ensured low energy (Type 2-1/2-3) junctions and no magnetic frustration. The lowest three rings were all in vortex states with clockwise chirality. This shows that complete

depopulation of an interconnected system is possible, although 30 further rotations at the same field without a saturation step resulted in almost all rings having the onion state configuration (Fig. 7.28b). This most likely resulted from DWs nucleated in the adjacent rings with identical vortex chirality in Fig. 7.28a).
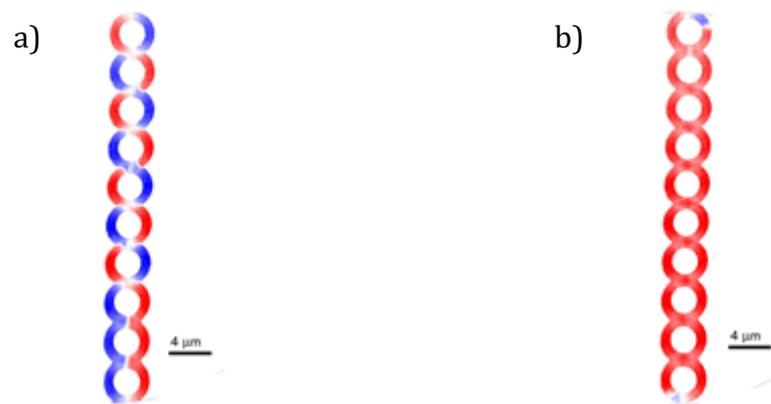
Figure 7.28. PEEM image of a linear chain of interconnected nanorings following application of a (a) saturating field pulse then 30 rotations at 47.5Oe, suspected to be an intermediate field (b) 30 further rotations at 47.5Oe.

7.3.7 ImageJ analysis

ImageJ software [10] tools were used to enable quantification of the magnetisation of PEEM images. This was achieved by selecting the splitting an image of a structure into its RGB components, to give three new greyscale images of the Red, Green and Blue channels. A threshold function was then applied to convert the Red and Blue channel images to binary images (i.e. each pixel became 1 or 0). The total count of above-threshold pixels for these channels allowed calculations of magnetisation to be performed, and without a significant contribution from the background. The information from the Green channel was discarded.

Three normalisation methods were used to cover the various situations in the images. For arrays that were largely onion states oriented along the PEEM sensitivity axis, normalised magnetisation ($M_{normalised}$) was calculated as the number of pixels of the

predominate colour (e.g. Red, $N_{red\ pixels}$) divided by the total number of like-colour pixels in a fully onion state array ($N_{total\ pixels}$), i.e.:

$$M_{normalised} = \frac{N_{red\ pixels}}{N_{total\ pixels}} \qquad \text{Equation 7.1}$$

This was particularly the case at high fields, close to deterministic DW propagation conditions.

For arrays that consisted predominantly of onion state rings oriented in the saturating field direction, $M_{normalised}$ was calculated as saturation magnetisation minus the difference in red and blue pixels divided by the total number of pixels in the array, i.e.:

$$M_{normalised} = 1.0 - \frac{abs(N_{red} - N_{blue})}{N_{total\ pixels}} \qquad \text{Equation 7.2}$$

This approach was needed at low fields, where there had been relatively little alteration from onion states oriented in the saturation field direction.

Lastly, for more mixed arrays that had a substantial balance of red/blue regions because they are all vortex or balanced ¾ states, $M_{normalised}$ was calculated as the difference in red and blue pixels divided by the total number of pixels in the array, i.e.:

$$M_{normalised} = \frac{abs(N_{red} - N_{blue})}{N_{total\ pixels}} \qquad \text{Equation 7.3}$$

This was necessary in the intermediate field region, where magnetisation configurations were very mixed.
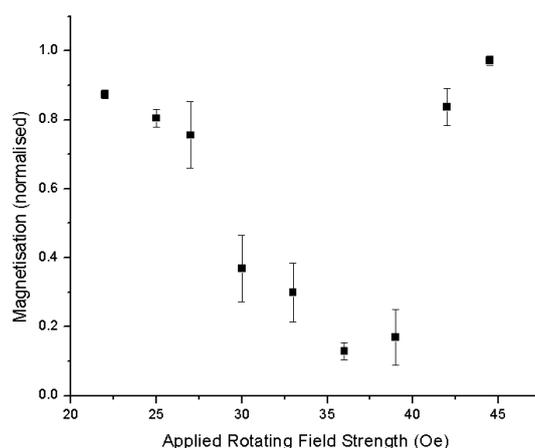
Figure 7.29. Average magnetisation calculated from PEEM images in Fig. 7.20 as a function of applied rotating field strength. Error bars show standard error.

The data from Fig. 7.20 for a square array of 25 x 25 rings of 2μm diameter, 200nm track width and 50% overlap were analysed to obtain magnetisation as a function of rotating magnetic field (Fig. 7.29). This includes a contribution of three images per field amplitude value. This plot shows a non-monotonic variation in magnetisation that is remarkably similar to magnetisation-field characteristic from PNR experiments (Fig. 6.3). The array magnetisation again is at (or close to) saturation for low and high fields but goes through a minimum at intermediate fields. What is most significant here is that the minimum magnetisation is closer to zero (and may reach zero if further data were available), which agrees with the PNR measurement. Combined with inspection of the PEEM images, this also resolves the previous apparent contradiction of zero magnetisation (measured by PNR) while still having DWs present (measured by MOKE, e.g. Fig. 6.10). PEEM colour maps show that there are indeed a significant proportion of vortex states at the minimum-magnetisation point (e.g. Fig. 7.23) but other states (e.g. ¾ states) that contain DWs are present but with roughly equal proportions of opposite magnetisation result in an overall reduction of array magnetisation. There is a degree of long-range ordering or clusters of alike states in images, but the overall effect is a near-zero minimum magnetisation. This means that rather than considering the reduction in array magnetisation as simple depopulation of onion into vortex states, PEEM imaging

shows that reality is more complex and involves an increase in randomness, albeit with a degree of ordering due to geometric constraints.

8 x 8 arrays following successive batches of applied rotating field were also subject to ImageJ analysis. Fig. 7.30 shows reference PEEM images and associated colour maps, with the legend for reference in Fig. 7.30. Two analyses were performed on the reference images – one with all rings and one that excluded edge and corner, the latter of which had a propensity rotate 90° while remaining as onion state. This increases the number of blue pixels and erroneously reports an increase in magnetisation.
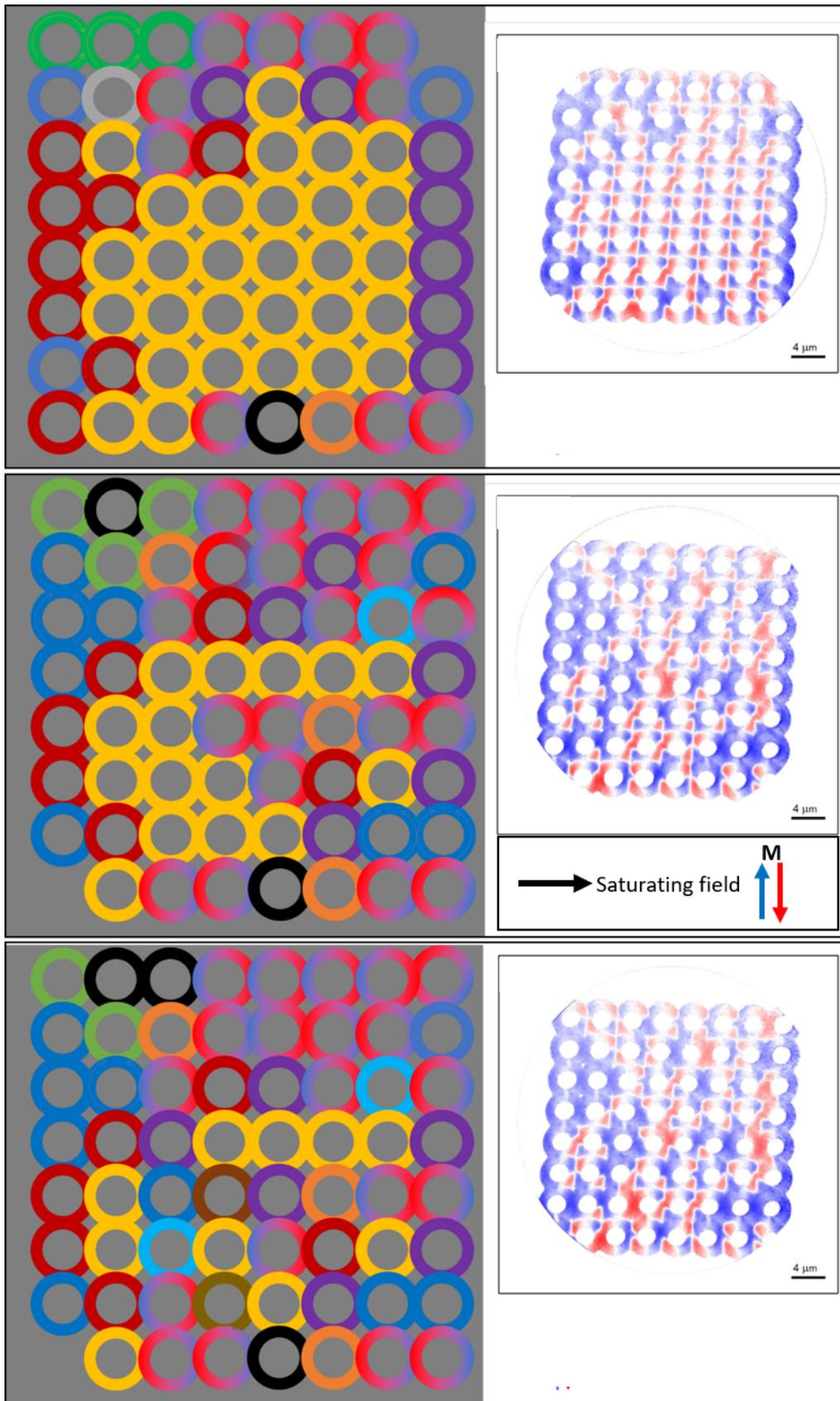
Figure 7.30. Colour map and reference PEEM images for an 8 x 8 square array subject to saturating field pulse then successive (by row) batches of 30 rotations at 27Oe applied rotating field strength.
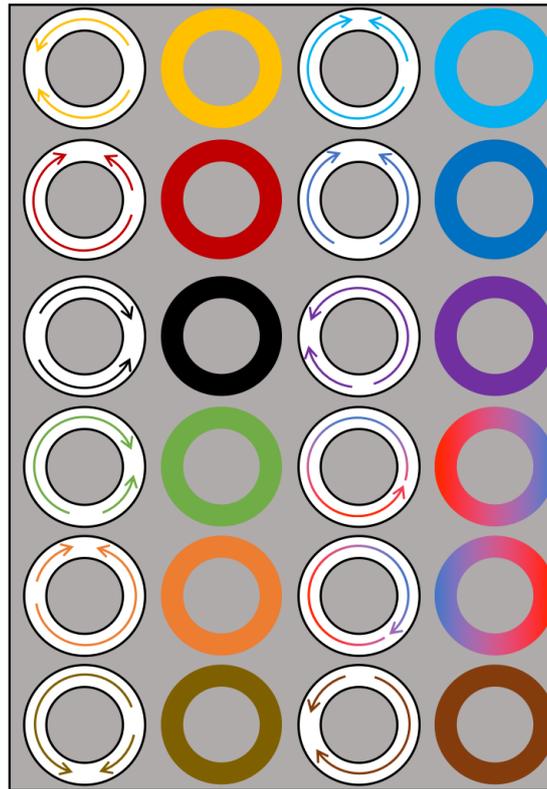
Figure 7.31. Legend of ring colour to corresponding domain arrangements for Fig. 7.30
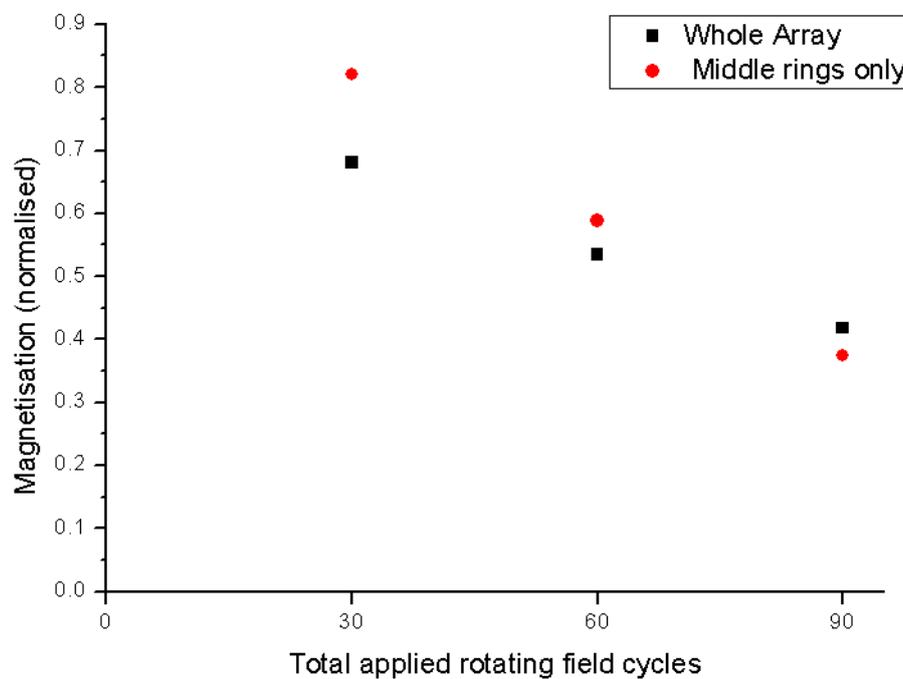
Figure 7.32. Normalised magnetisation as calculated by ImageJ pixel analysis on three PEEM images of an 8 x 8 array (from Fig 7.30) following indicated number of rotations at 27Oe. Black squares are measured from images as they were taken, and red circles are measured from the middle 36 rings.

Based on the colour map, equation 7.2 was used to calculate normalised magnetisation for the first two points as these are predominantly onion states aligned with the saturation axis. Equation 7.3 is used for the third image as the number of vortex and ¾ states increase. These results are plotted in Fig. 7.32, which shows a decrease in normalised magnetisation with successive batches of applied rotating field. This corresponds with an increase in the number of vortex states as well as an increase in the randomness of the array as seen by the reduction in yellow onion states from the colour map.

This analysis lends strength to the notion that apparent depopulation seen in PNR magnetometry is a result of complete randomness in the ensemble as well as an increase in vortex states as measured with MOKE.

7.4 Summary

MFM imaging was used to image DW topology within the interconnected nanoring array following saturating field pulses as well as intermediate fields. DWs in the former were arranged regularly in opposing junctions with the visual appearance of a diamond, as predicted by micromagnetic modelling in §5.

With the application of an intermediate rotating field, DW positions were no longer regularly arranged, often found in adjacent junctions creating "¾ states" named after the new relative sizes of domains. Vortex state creation was also possible, with some rings found to contain no DWs. There were also new types of DW arrangement beyond the diamond and empty junctions that were found following the saturating field pulse.

Wide field PEEM imaging was used to observe larger sample sizes of interconnected rings as well as cycle to cycle behaviour. Low field and high field behaviours of general retention of DW populations was observed in large square and trigonal arrays of interconnected rings. In intermediate field regimes, the visual appearance of the array was towards frustration, as seen by the increase in red/blue contrast and development of domains of aligned magnetisations. Chains of like magnetisation could also be found which had a similar visual appearance to Dirac strings in ASIs. Observation of linear chains could imply from that combination in junctions, repopulation and annihilation of DWs as predicted by micromagnetic modelling took place.

A reduction in total array moment measured by experimentation is suggested to take place by a combination of two mechanisms. The first is this onion to vortex conversion, physically reducing the number of DWs. This has been observed in arrow maps such as in Figs. 7.22 or 7.23 and also in linear chains of interconnected rings (Fig 7.28a). The second is the high degree of frustration in the intermediate array, for example in intermediate field values in the field sweep in Fig. 7.20. Without frustration, for example if the array was saturated and relaxed and onions were arranged regularly, the summation of magnetisation contributions from DWs in individual elements would give a normalised value of approximately 1. When frustration is induced and ¾ states are obtainable and onions may exist oriented 90° to the 'regular' axis that existed at saturation, the net effect of summation of individual contributions is a reduction from

the normalised maximum. This is a direct result of emergence in interconnected nanoring arrays and explains why an experimental measurement reliant on dynamic movement of walls, MOKE, produces a different value to one that relies on a measurement of a static system, PNR.

ImageJ quantification of different contrasts in PEEM gives credit to this hypothesis. Using this method, it was possible to quantify the degree of visual frustration and showed for square arrays a non-monotonic variation that fell to near zero normalised magnetisation, as with PNR.

Whilst imaging helped characterise and explain experimentally measured behaviour of interconnected nanoring arrays, the discovery that the array is an novel method for obtaining artificial spin ice behaviour was a by-product of the investigation. From this, a different path for functionality of the array can be realised.

Whereas obtaining a true ground state in ASIs is difficult, the interconnected nanoring array was found with imaging to exist in an ordered ground state following saturation and relaxation. An advantage of this interconnected system is the ability to produce new final states and junction types in situ with a full range of external parameters. Here, external field strength was trialled extensively to produce unique final states. There is no conceivable reason why a constant strength rotating applied field with a different external input, temperature being the most obvious, cannot be explored in the same manner.

ASI applications are varied and abundant. One large direction of research identified in literature review was into thermodynamic simulators – systems that probe thermodynamic principles by observing degeneracy in ASIs as conditions are varied [11]–[17]. The analogous nature of the interconnected nanoring array to ASIs, the unique advantages it offers and the wealth of information it can provide mean the system could become a key member of the pantheon of ASI based thermodynamic simulators.

On reflection, the beauty of the imaged array, especially combined with computer colourisation, is extraordinary. The complexity of larger arrays would require a lifetime, or at least a dedicated PhD programme, to characterise by hand. However, this complexity demonstrates the ability of the interconnected array to realise functionality

through stochasticity. By exerting control on the extent of stochasticity, for example by changing wire dimensions or junction overlaps, the configuration of the array after application of a rotating field can be probabilistically controlled. This is similar to weighting of connections in a reservoir computation architecture as highlighted in literature review. An interconnected array that used a different method to control stochasticity, perhaps by fabrication of the array on a network of current lines that can be turned on or off to control local magnetic field, may be an excellent candidate for realising low power reservoir computing hardware. That local control could tailor the weightings of nodes, as outlined in literature review of reservoir computing, to realise the requirements of a reservoir layer.

7.6 References

[1]   J. C. Gartside *et al.*, "Realization of ground state in artificial kagome spin ice via topological defect-driven magnetic writing," *Nat. Nanotechnol.*, vol. 13, no. 1, pp. 53–58, 2018.

[2]   Y.-L. Wang *et al.*, "Rewritable artificial magnetic charge ice," *Science (80-.).*, vol. 352, no. 6288, pp. 962 LP – 966, May 2016.

[3]   R. F. Wang *et al.*, "Artificial 'spin ice' in a geometrically frustrated lattice of nanoscale ferromagnetic islands," *Nature*, vol. 439, no. 7074, pp. 303–306, 2006.

[4]   J. P. Morgan, A. Stein, S. Langridge, and C. H. Marrows, "Thermal ground-state ordering and elementary excitations in artificial magnetic square ice," *Nat. Phys.*, vol. 7, no. 1, pp. 75–79, 2011.

[5]   C. Nisoli, "On thermalization of magnetic nano-arrays at fabrication," *New J. Phys.*, vol. 14, no. 15pp, p. 35017, 2012.

[6]   E. Mengotti, L. J. Heyderman, A. F. Rodríguez, F. Nolting, R. V Hügli, and H.-B. Braun, "Real-space observation of emergent magnetic monopoles and associated Dirac strings in artificial kagome spin ice," *Nat. Phys.*, vol. 7, no. 1, pp. 68–74, 2011.

[7]   R. V Hügli *et al.*, "Artificial kagome spin ice: Dimensional reduction, avalanche control and emergent magnetic monopoles," *Philos. Trans. R. Soc. A Math. Phys. Eng. Sci.*, vol. 370, no. 1981, pp. 5767–5782, 2012.

[8]   S. Ladak, D. E. Read, W. R. Branford, and L. F. Cohen, "Direct observation and control of magnetic monopole defects in an artificial spin-ice material," *New J. Phys.*, vol. 13, 2011.

[9]   L. J. Heyderman and R. L. Stamps, "Artificial ferroic systems: Novel functionality from structure, interactions and dynamics," *J. Phys. Condens. Matter*, vol. 25, no. 36, pp. 363201–29, 2013.

[10]   "Rasband, W.S., ImageJ, U. S. National Institutes of Health, Bethesda, Maryland, USA, https://imagej.nih.gov/ij/, 1997-2018."

[11]   A. Farhan *et al.*, "Thermally induced magnetic relaxation in building blocks of artificial kagome spin ice," *Phys. Rev. B*, vol. 89, no. 21, p. 214405, 2014.

[12]   L. Anghinolfi *et al.*, "Thermodynamic phase transitions in a frustrated magnetic metamaterial," *Nat. Commun.*, vol. 6, 2015.

[13]   A. Schumann, P. Szary, E. Y. Vedmedenko, and H. Zabel, "Magnetic dipole configurations in honeycomb lattices: Order and disorder," *New J. Phys.*, vol. 14, 2012.

[14]   Z. Budrikis *et al.*, "Domain dynamics and fluctuations in artificial square ice at finite temperatures," *New J. Phys.*, vol. 14, no. 14, 2012.

[15]   L. Yu *et al.*, "Monte Carlo simulation on a new artificial spin ice lattice consisting of hexagons and three-moment vertices," *AIP Adv.*, vol. 7, no. 8, p. 85211, 2017.

[16]   C. Nisoli *et al.*, "Ground state lost but degeneracy found: The effective thermodynamics of artificial spin ice," *Phys. Rev. Lett.*, vol. 98, no. 21, 2007.

[17]   Z. Budrikis *et al.*, "Disorder strength and field-driven ground state domain formation in artificial spin ice: Experiment, simulation, and theory," *Phys. Rev. Lett.*, vol. 109, no. 3, 2012.

Chapter 8 – The End?

"If I have seen further it is by standing on the shoulders of giants" – Sir Isaac Newton

8.0 Introduction

In §8.1, the conclusion of this thesis recaps experimental work, results obtained and the outcomes from this programme of research. §8.2 then considers possible future activity and the important questions that remain.

8.1 Key findings and conclusions

Arrays of interconnected soft ferromagnetic nanowire rings have been shown to have emergent properties in their ensemble DW population when DW propagation through the ring junctions is stochastic. DW motion was driven by in-plane rotating fields and the array DW population was found to be a strong function of field strength. This work introduces the interconnected ferromagnetic nanoring array as a new magnetic nanodevice archetype for exploring emergence, frustration and appears to be a hardware platform well suited to supporting types of neural network.

Micromagnetic modelling showed that DW pinning at a junction or passage through a junction could lead to a loss or gain in overall DW population in an interconnected system. An analytical model was developed based on these loss and gain mechanisms to describe the emergent equilibrium DW population in interconnected ring arrays . The model assumed each ring to either be in an 'onion' state, with two DWs, or a 'vortex' state, with no DWs with the rates of DW loss and gain determined by the array geometry and the probability of DWs overcoming the pinning potential at junctions between rings. The model was updated in this work to account for configurational effects, and predicted a non-linear dependence of DW population on the DW de-pinning

probability, and that a minimum in DW population would be achieved for mid-range values of de-pinning probability in large arrays. Achieving these experimentally would be interesting for their potential use as the reservoir component of reservoir computing.

Polarised neutron reflectometry (PNR) was used to quantitatively measure the magnetisation of permalloy rings in square arrays that had been saturated and then subject to in-plane rotating magnetic fields of different strengths. PNR showed magnetisation to be a strong function of applied field strength and went through a minimum (reaching zero) at mid-range field values, similar to the analytical model predictions of DW population.

MOKE experiments further substantiated this behaviour by measuring static and dynamic DW populations and vortex state population through 25 rotations of magnetic field. These measurements again identified non-monotonic variation in DW populations further highlighting the presence of emergent behaviour, including a minimum in DW population where there was also a predicted maximum in vortex state population. This was found readily in extremely large square arrays (approximately 2.5×10^7 rings) and also in smaller 2 x 2 (4 ring), 5 x 5 (25 ring) and 8 x 8 (64 ring) arrays. These finite arrays showed a marked difference in the strength of the applied rotating field required to find DW population minima.

The cycle to cycle variation in each state showed that the DW populations tended towards a value, supporting the modelled hypothesis of a dynamic system in equilibrium. The observed change in DW population over a few or many field cycles (depending on the experimental conditions) demonstrated the property of 'fading memory' that is important for reservoir computing applications.

Some differences between the MOKE and PNR data were surprising. The maximum vortex population from the same array was measured to be at approximately 43Oe by MOKE but 50Oe by PNR. The DW population measured by MOKE did not fall to zero, unlike the magnetisation in PNR. This apparent contradiction was resolved with imaging of the magnetic configurations by photoemission electron microscopy (PEEM) and magnetic force microscopy (MFM).

MFM provided the first real image of an interconnected array which was found in its simplest saturated and relaxed state to be generally like the array modelled micromagnetically. The DWs formed a diamond arrangement within junctions and these were readily imaged on 26 x 26 square arrays and found, before application of a rotating field, to arrange themselves in regular lines in junctions on opposing sides of rings. MFM images also started to highlight that a wider range of magnetic configurations could be found in rings than simply the onion and vortex states assumed in the analytical model. Rings could be in the onion or vortex states but also in '¾' states of DWs separated by just 90° of a ring, and that these ¾ states often appeared together in lines.

MFM imaging showed that the characteristics of junctions in these arrays was strikingly similar to those of vertices in artificial spin ices, leading to the identification of the interconnected array as an alternate candidate to traditional ASIs. Previous studies of ASIs have generally considered static states whereas this study has focussed on dynamical properties of the ring arrays. Micromagnetic modelling of all junction types possible based on classification of vertex types in square ASIs allowed the energetics of junction types to be explored. This provided an explanation for the predominance of the diamond state formation seen where two DWs met in a junction. Much like ASI systems, despite this favourability there exists non-zero probabilities that higher energy junctions of different type are found as a result of emergent interactions between constituent parts of the system.

With PEEM, a clear distinction between low, intermediate and high field behaviour of arrays was obtained. In the intermediate field regime, the extent of frustration appeared to change non-monotonically with the strength of the applied field. An ImageJ macro was used to quantify this visual frustration and extracted a normalised magnetisation vs. field strength dependence that was similar to results found experimentally with PNR and MOKE. The PEEM imaging showed that, in the intermediate field regime, the presence of vortices and a disposition to a heavily frustrated arrangement of rings with magnetisations in different orientations led to the array magnetisation tending towards zero at its minimum, as a function of applied rotating field strength. This occurred while there were still DWs in the system, thus reconciling the previous PNR and MOKE field characteristic measurements.

PEEM was also used to image the response of linear ring chains and trigonal arrays of rings. The linear chains allowed changes in ring states to be observed in detail. The DW population dependence on rotating field amplitude showed a similar characteristic to the square arrays studied earlier, and the analytical modelling of the appropriate structure.

8.2 Future direction of research

Whilst this thesis uncovered some of the novelty of interconnected nanoring arrays, multiple paths for future research were unexplored and many questions left unanswered. Some specific examples are outlined, though this list is far from exhaustive.

The similarity to ASI systems means the substantial body of ASI research could be used to inform studies of interconnected nanoring arrays. The rotating applied field can replace techniques such as thermalisation during fabrication popularised by Morgan *et al.* [1], [2]. Whilst artificial spin ices remain an excellent playground for studying statistical mechanics of frustration/thermodynamics [3]–[7], and have a degree of tuneability from material used or array geometry, interconnected nanoring arrays benefit from the simplicity to be 'reprogrammed' with an external field in situ.

Observing the as-grown state of artificial spin ices was a noteable advance, showing ground state ordering with isolated changes – or excitations from the ground state [8]. This arises from each island existing at every thickness through growth, thus being free to thermally fluctuate when very thin. At a certain thickness, the energy barrier to reversal becomes so large as to freeze the state of the island at that point. This tends the system towards the ground state in the ensemble. It is a one shot process that is destroyed by the application of an external field. Similarly, the interconnected ring array should be studied in the as-grown state at the next opportunity for magnetic imaging to confirm the true ground state of the system.

As seen in studies of ASIs, inter-island spacing affects the relative population of vertex type [9]. Future PEEM work on interconnected arrays could continue to look at the effects of ring size, track width and ring overlap and quantify the abundance of various

states. It would also be interesting to perform on PEEM images a statistical analysis of junction types similar to that with ASIs in Schumann *et al* [10]. This study also predicts hard/easy axis affects domains in artificial spin ice, so does changing the geometry of the ring from symmetric circle to an oval have a similar biasing effect? The simplicity of this change may make it appropriate for a project student to explore.

A desire to watch the evolution of interconnected arrays as magnetic fields were applied was expressed following imaging with PEEM. One advantage of MTXM over PEEM is that this is possible (MTXM needing only photons to construct an image). Therefore, it would be recommended if the evolution of emergence is to be understood further and for micromagnetic simulations to be further experimentally verified, for beamtime to be applied for utilising MTXM. Progression from onion to vortex and vice versa would be an initial experimental goal. From there, a wealth of possibilities could be explored: watching single or clusters of rings as rotating fields are applied to watch DWs attempt to depin from junctions and quantify the probability of success at each junction as a function of varying field strength stands out as an initial candidate. A recent approach by Morley et al. [11] used MTXM to watch motion of magnetic charges using heating elements arranged around ASI structures on a Si_3N_4 membrane. Using excitations from an applied field and/or injected heating pulses, emergent magnetic monopoles could be observed in these structures in semi-real time. Similarly Zeissler et al. investigated the 'random walk' of monopoles through a spin ice lattice [12] and Farhan et al. have recently published work showing real time monopole movement in a 3D ASI system [13].

The Functional Materials – Magnetics group at Sheffield have worked towards an alternate approach to modelling of DW population from the relatively simple analytical model critiqued in this thesis. A phenomenological model has started be developed that simply gives a probability to DWs passing through junctions. This could be a highly useful in developing an understanding of how local processes evolve into wider configurational changes across arrays.

Future MOKE experiments could build upon the protocols developed here to investigate applying changing fields without a saturation step between in order to investigate the robustness of response to particular field values and how array behaviour is influenced by its history.

There exists scope for collaboration with research groups that have a strong focus on ASIs, perhaps with a view to improving computing type applications. Gartside *et al.* [14] have explored the use of MFM to force ground state formation in Kagome lattices where it was unobtainable. The magnetisation of the MFM tip is used to manipulate islands that are frustrated so that they reach a ground state. Whilst the saturated and relaxed interconnected nanoring array found a true stable state to be obtainable in the whole array, the reverse concept of using an MFM tip to force frustration may be useful. Biasing of the array could be carried out to try and influence the end state after a rotating field protocol is applied. Bias functions are a concept in reservoir and other recurrent neural network computing types, further improving the candidacy of the interconnected array. Other methods to achieve biasing or weighting changes to neuron connections that could be explored are:

- Changes in local geometry. For example, masking part of the array, metallising with thermal evaporation, removing the mask and then metallising again to create regions of different thickness. Topological frustration has been investigated elsewhere (e.g. [15])
- Creating patterns that induce a bias or rich landscape for frustration (e.g. [9], [16]) or with local reductions or increases in track width and/or thickness to create a 3D array (e.g. [13])
- Further increasing stochasticity – addition of notching will impede motion that not only requires a higher field to overcome but can also change chirality/type of DWs as they de-pin.

Chapter 3 highlighted the recurrent artificial neural network approach of reservoir computing as an exciting development that can tackle beyond Moore's Law/non-Von Neumann developments and problems.

There is great potential for the interconnected ferromagnetic nanoring array to realise reservoir computing hardware. The system has a high degree of connectivity, neuron-like behaviour between nodes (junctions) and the characteristic of an input – reservoir – output sequence. Interactions between neighbouring magnetic rings can transform stochastic behaviour of DW pinning at individual ring junctions into a reliable ensemble behaviour. "Hidden interactions" in the reservoir could provide required computation that is read out with a MOKE system measuring normalised magnetisation following

application of the rotating magnetic field. Adjusting the strength of such a field affords tuneability to the reservoir, and PEEM showed evidence of fading memory and recurrence in the system in that the end state after one set of inputs is highly likely to influence the response to the next input. Further work is suggested to look at varying the strength of the applied field with two-steps (i.e. two field strengths) before reading out the end state. If there is a different response to the two-step procedure compared to just applying the second step, then it will be shown that the input history directly affects the response, further reinforcing the candidacy for the interconnected array. It would also be interesting to consider what else could be used as a data input with an interconnected array, wires carrying spin-polarised currents that bias fields to regions of the array, as an example. Further to this there exists the possibility to explore other methods of data output, such as magnetoresistance measurements, given the good interface that this could provide with conventional CMOS circuitry.

8.3 References

[1] J. P. Morgan, A. Stein, S. Langridge, and C. H. Marrows, "Magnetic reversal of an artificial square ice: Dipolar correlation and charge ordering," *New J. Phys.*, vol. 13, 2011.

[2] C. Nisoli, "On thermalization of magnetic nano-arrays at fabrication," *New J. Phys.*, vol. 14, no. 15pp, p. 35017, 2012.

[3] C. Nisoli *et al.*, "Ground state lost but degeneracy found: The effective thermodynamics of artificial spin ice," *Phys. Rev. Lett.*, vol. 98, no. 21, 2007.

[4] P. E. Lammert *et al.*, "Direct entropy determination and application to artificial spin ice," *Nat. Phys.*, vol. 6, no. 10, pp. 786–789, 2010.

[5] W. R. Branford, S. Ladak, D. E. Read, K. Zeissler, and L. F. Cohen, "Emerging Chirality in Artificial Spin Ice," *Science (80-.).*, vol. 335, no. 6076, pp. 1597 LP – 1600, Mar. 2012.

[6] A. Farhan *et al.*, "Thermally induced magnetic relaxation in building blocks of artificial kagome spin ice," *Phys. Rev. B*, vol. 89, no. 21, p. 214405, 2014.

[7] A. Farhan *et al.*, "Direct observation of thermal relaxation in artificial spin ice," *Phys. Rev. Lett.*, vol. 111, no. 5, 2013.

[8] J. P. Morgan, A. Stein, S. Langridge, and C. H. Marrows, "Thermal ground-state ordering and elementary excitations in artificial magnetic square ice," *Nat. Phys.*, vol. 7, no. 1, pp. 75–79, 2011.

[9] I. Gilbert *et al.*, "Emergent ice rule and magnetic charge screening from vertex frustration in artificial spin ice," *Nature Physics*, vol. 10, no. 9, pp. 670–675, 2014.

[10] A. Schumann, P. Szary, E. Y. Vedmedenko, and H. Zabel, "Magnetic dipole configurations in honeycomb lattices: Order and disorder," *New J. Phys.*, vol. 14, 2012.

[11] S. A. Morley *et al.*, "Thermally and field-driven mobility of emergent magnetic charges in square artificial spin ice," vol. 1, pp. 1–10, 2018.

[12] K. Zeissler *et al.*, "The non-random walk of chiral magnetic charge carriers in artificial spin ice," *Sci. Rep.*, vol. 3, p. 1252, 2013.

[13] A. Farhan *et al.*, "Emergent magnetic monopole dynamics in macroscopically degenerate artificial spin ice," *Sci. Adv.*, vol. 5, no. 2, 2019.

[14] J. C. Gartside *et al.*, "Realization of ground state in artificial kagome spin ice via topological defect-driven magnetic writing," *Nat. Nanotechnol.*, vol. 13, no. 1, pp. 53–58, 2018.

[15] J. Drisko, T. Marsh, and J. Cumings, "Topological frustration of artificial spin ice," *Nat. Commun.*, vol. 8, no. May 2016, pp. 1–8, 2017.

[16] D. Shi *et al.*, "Frustration and thermalization in an artificial magnetic quasicrystal," *Nat. Phys.*, vol. 14, no. 3, pp. 309–314, 2018.

Appendix

A1 Mumax scripts

A1.1 Basic application of a rotating field

//Define the mesh

CellXY:=4
CellZ:=20

SetGridsize(7800/CellXY, 4000/CellXY, 20/CellZ)
*SetCellsize(CellXY*1e-9, CellXY*1e-9, CellZ*1e-9)*

//Material Parameters

Msat   =860e-3
Aex   = 13e-12
alpha   = 1

//Geometry

setgeom(imageShape("http://172.16.68.165:35360/Richard/PNGs/4um400nmhalfoverla p.png"))
saveas(geom, "imageShape")

//Initial Field
m = uniform(0,1,0)

//Define field angle limits and step
xmax := 510
xstep := 15

//Define how often to save magnetisation state and field strength/direction
TableAdd(B_ext)
Autosave(m,3e-09)
TableAutoSave(3e-09)

//Set initial angle and field strength
x   := 90
*B_ext = vector(0.0050*cos(x*pi/180),0.0050*sin(x*pi/180),0)*

//Relax system

```
relax()

//A loop to control field position
for x:=90; x<=xmax; x+=xstep{
        B_ext = vector(0.0050*cos(x*pi/180),0.0050*sin(x*pi/180),0)
        run(12e-09)


}
```

A1.2 Repopulating a two-ring array

```
//Define the mesh

CellXY:=4
CellZ:=20

SetGridsize(7600/CellXY, 4000/CellXY, 20/CellZ)
SetCellsize(CellXY*1e-9, CellXY*1e-9, CellZ*1e-9)

//Material Parameters

Msat    = 715e3
Aex     = 13e-12
alpha   = 1


TableAdd(Edens_demag)
TableAdd(Edens_exch)
TableAdd(Edens_Zeeman)
TableAdd(Edens_total)

//Geometry

setgeom(imageShape("http://172.16.68.165:35360/Richard/PNGs/4um400nmhalfoverlap.pn
g") )
saveas(geom, "imageShape")

defregion(0,(xrange(0,inf)))
defregion(1,(xrange(-inf,0))) // left ring

m.setRegion(0,uniform(0,1,0))
m.setRegion(1,vortex(1,-1))

xmax  :=  500
xstep :=  10

TableAdd(B_ext)

Autosave(m,2e-09)
TableAutoSave(2e-09)


x     := 90
```

```
B_ext = vector(0.012*cos(x*pi/180),0.012*sin(x*pi/180),0)
relax()
```

```
for x:=90; x<=xmax; x+=xstep{
B_ext = vector(0.012*cos(x*pi/180),0.012*sin(x*pi/180),0)
run(12e-09)
}
```

A1.3 Initialising quadrants in a simulated junction

```
//Define the mesh

CellXY:=4
CellZ:=20

SetGridSize(3476/CellXY, 1800/CellXY, 20/CellZ)
SetCellSize(CellXY*1e-9, CellXY*1e-9, CellZ*1e-9)

//Material Parameters

Msat    = 800e3
Aex     = 13e-12
alpha   = 1


TableAdd(Edens_demag)
TableAdd(Edens_exch)
TableAdd(Edens_Zeeman)
TableAdd(Edens_total)

//Geometry

setgeom(imageShape("http://172.16.68.165:35360/Richard/PNGs/Junction.png") )
saveas(geom, "imageShape")

//regions

defregion(1, (xrange(0, inf).intersect(yrange(0,inf))))  // right upper
defregion(2, (xrange(-inf, 0).intersect(yrange(0,inf)))) // left upper
defregion(3, (xrange(0,inf).intersect(yrange(-inf,0))))  //right lower
defregion(4, (xrange(-inf,0).intersect(yrange(-inf,0)))) // left lower

//magnetisation

m = uniform(1, 0, 0)  // no need to normalize length

//Initialise one region

m.setRegion(1,uniform(-1,0,0))
m.setRegion(2,uniform(-1,0,0))
m.setRegion(3,uniform(1,0,0))
m.setRegion(4,uniform(1,0,0))
```

```
save(m)
relax()
save(m)
tablesave()
```

A2.1 Original analytical model

The analytical model as created by Mahmoori uses equation A1 to create plots in §5. This was updated to a new form in equation 5.5.

$$W = 1 - \frac{\sum_1^m C_n \left(1 - P_{pass}^n\right)\left(P_1 P_{pass} + P_2 P_{pass}^2 + \cdots P_n P_{pass}^n\right)}{\sum_1^m C_n \left(P_{pass} + P_{pass}^2 + \cdots P_{pass}^n\right)} \qquad Equation\ A1$$

A2.2 Creating structures in RAITH

Arrays were fabricated via electron beam lithography as described in §3.XXX. A vast variety of arrays types have been fabricated of differing general composition (i.e. square, trigonal etc) and geometries. RAITH incorporates a vector drawing function for making shapes, with built in functions to generate circles, polygons, rectangles etc.

A ring in RAITH is created with the circle drawing tool. The ring radius is chosen such that

$$r_{nanoring} = \frac{d - w}{2} \qquad Equation\ A2$$

where d is the desired ring diameter and w is the track width. The tickbox for 'Fill' is unchecked and the 'Width' set to w.

Arrays are simply and quickly created using the 'Duplicate > Matrix' function under 'Modify.' Select the array dimensions for U and V (e.g. for a 25 by 25 matrix set U and V to 25, or for a simple single duplication set U or V to 1). Then choose a base vector that represents the translation operation that is desired.

A3 MOKE

A3.1 Obtaining results from MOKE

- To maximise the number of rings sampled, a collimated (parallel) beam is preferable. Remove the condenser and objective lenses from the beam path.
- With the beam correctly aligned and the sample mounted flat, movement in and out of the XYθ stage is all that is needed to direct the beam onto the photodiode.
- Follow Standard Operating Procedure to choose analyser and quarter wave plate angles.
- Import field files to '*MOKE Analyser*´ software. You may need to recalibrate the electromagnet and create your own field files. An Excel workbook to create field files with 25 rotations has been left in the SCAMMD server to help with this.
- Follow SOP to run field protocol on the sample and download Kerr Voltage results
- On a different PC, with the .dat files obtained via experimentation, run the MATLAB script Find_Peaks.m. A copy has been left on the SCAMMD server and is also visible in Appendix XXX
- Find_Peaks.m asks the filename (e.g. "30Oe.dat" – ensure you are in the same directory as the file you wish to process) and outputs a plot of Kerr Voltage-Time with peaks and troughs marked and a dat file "*Peaks_and_Troughs_of_*(filename)"
- The dat file has two columns that are the Kerr Voltages of Peaks and Troughs (respectively)
  - You may need to adjust the value of the variable "*Min_Separation*" to ensure all peaks and troughs are recorded in the plot. It is fine if there are 'phantom' points (markers where there isn't a peak) that are highlighted.
- Copy the data in the dat file into the '*Array_Results_Master*' template that can be found on the SCAMMD server.
  - The tab '*Paste Here*' is annotated with instructions to take results from the dat file and align them in cells in the '*Peaks + Troughs*' tab.
  - These are linked to corresponding cells in '*Averages*,' '*Amplitudes*' and '*Vortex*' that can be plotted as desired.

A3.2 Edge defect MOKE

Additional MOKE experimentation was carried out for a defect square structure. The experimental programme investigated one such array to check the characteristic behaviour relative to full square arrays.
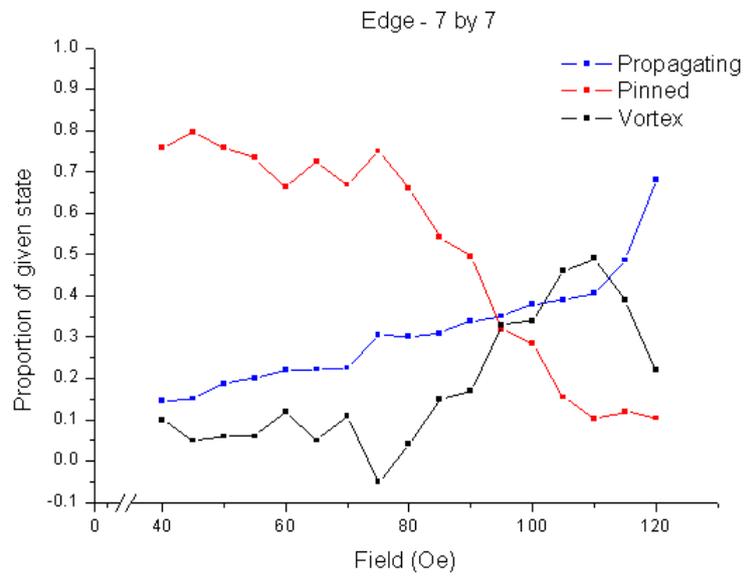

Figure A.1. Plot of relative calculated populations of propagating and pinned onion states and vortex states in a 7 by 7 square array of interconnected edge-only nanoring arrays following the application of 25 rotations at the indicated field.
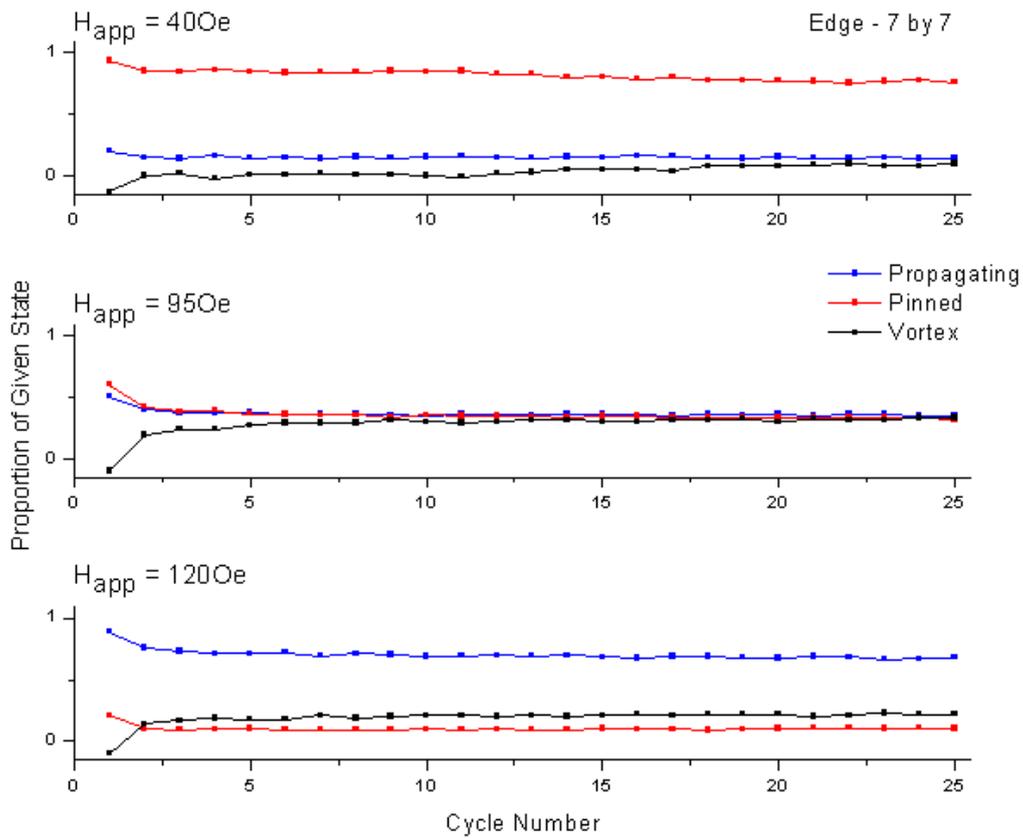
Figure A.2. Population changes in a 7 by 7 square array of interconnected edge-only nanoring, at low, intermediate and high field regimes as increasing cycles of rotating field are applied at indicated values. 25th cycle values correspond to figure 6.21.

This showed non-monotonic variation at a relatively high field (comparable to results from a 2 x 2 square array).

A.4 Further MFM on 2 by 2 arrays

This section presents some further MFM imaging on non-infinite 2 by 2 arrays of 2μm rings. These were chosen as initial analytical modelling had presented them as a special case that would always depopulate at low applied fields. Micromagnetic modelling showed that two rings on one of the diagonals would convert to vortex but the others would be trapped as onions.

MFM imaging on 2 by 2 arrays was successfully carried out on arrays that had two field protocols –30Oe and 55Oe. MOKE magnetometry in §6.2.3. later assessed both fields as low fields where propagation was inhibited.
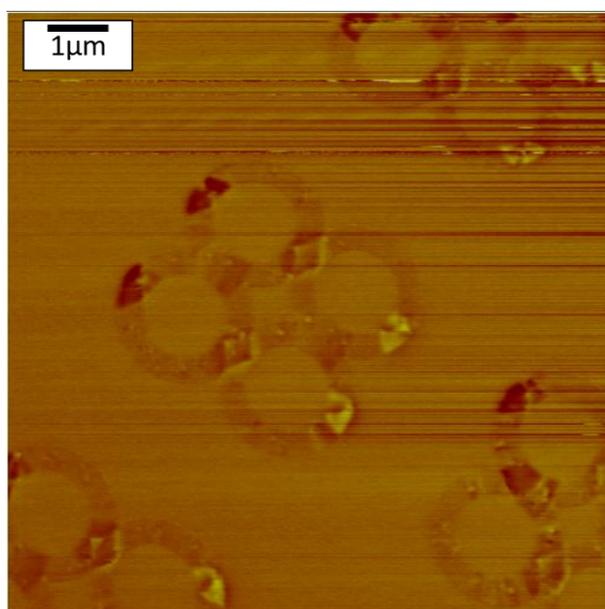

Figure A.3. MFM image of 2 by 2 arrays following 25 applied field rotations at 30Oe.

Figure A.3 has a 2 x 2 array that appears similar to micromagnetic models of a 2 x 2 array following saturation then relaxation (i.e. the first frame of each 2 x 2 array simulation). It is interesting that one array returned to this saturation state after application of a 'low' field – other arrays clearly demonstrate some movement of DWs and pinning in junctions. It is plausible that DWs were pinned in the extremes of rings by some geometric defect. Referencing MOKE magnetometry on these arrays, 30Oe was found to produce very little propagating type behaviour. It can be inferred from this image that the field was too low to depin walls from junctions leading to retention in general of DWs. There was no annihilation of corner rings, as predicted by

micromagnetic modelling. On closer inspection of free-standing DWs, there is frustration in that similar magnetic charges can be found in the same domain of each half of the ring. That is to say that arrow mapping would find both ends of an onion half have the same charge as evidenced by similar MFM contrast (light regions when followed around the ring meet another light region). This is not universal in the array of interest, the bottom left ring maps as expected. The non-triviality of the final state points to a high degree of frustration despite the initial simplicity presented.
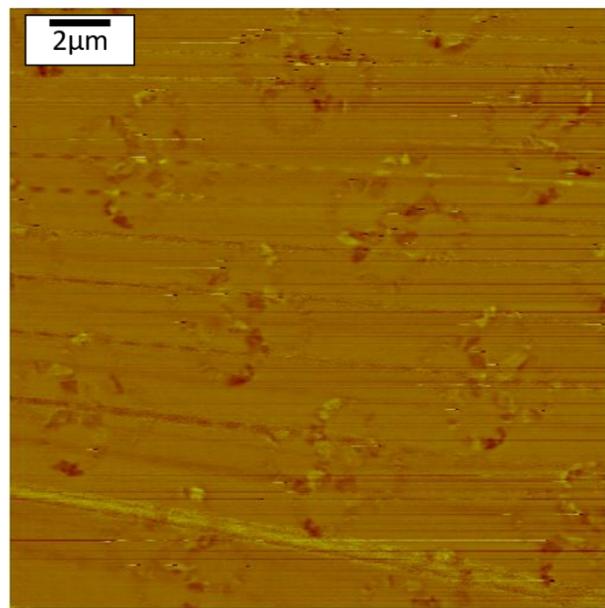

Figure A.4. MFM image of 2 by 2 arrays following 25 applied field rotations at 55Oe.

Fig. A.4 suffers from poor image quality but potentially demonstrates a limitation of using MFM for characterisation of these structures. Tracks in many of these arrays show lots of contrast suggesting non-uniform magnetisation or many out-of-plane interactions within track segments.